# FAST-WAKING AND LOW-VOLTAGE THERMOELECTRIC AND PHOTOVOLTAIC CMOS CHARGERS FOR ENERGY-HARVESTING WIRELESS MICROSENSORS

A Dissertation
Presented to
The Academic Faculty

by

Andrés Blanco

In Partial Fulfillment
of the Requirements for the Degree
Doctor of Philosophy in the
School of Electrical and Computer Engineering

Georgia Institute of Technology
August 2017

# FAST-WAKING AND LOW-VOLTAGE THERMOELECTRIC AND PHOTOVOLTAIC CMOS CHARGERS FOR ENERGY-HARVESTING WIRELESS MICROSENSORS

Dr. Gabriel A. Rincón-Mora
School of Electrical and Computer Engineering
*Georgia Institute of Technology*

Dr. Hua Wang
School of Electrical and Computer Engineering
*Georgia Institute of Technology*

Dr. Farrokh Ayazi
School of Electrical and Computer Engineering
*Georgia Institute of Technology*

Dr. Sung Ha Kang
School of Mathematics
*Georgia Institute of Technology*

Dr. Saibal Mukhopadhyay
School of Electrical and Computer Engineering
*Georgia Institute of Technology*

Date Approved: July 14,2017

# ACKNOWLEDGEMENTS

First of all, I would like to acknowledge the guidance given to me by my advisor, Professor Gabriel Alfonso Rincón-Mora. I thank him for his dedication and patience throughout my PhD program. Without him, this research would not have been possible.

I also thank my dissertation and proposal committee members, Dr. Farrokh Ayazi, Dr. Saibal Mukhopadhyay, Dr. Hua Wang, and Dr. Sung Ha Kang for their invaluable feedback and support.

I would also like to thank my colleagues at the Georgia Tech Analog, Power, and Energy Lab, Luke Milner, Dongwon Kwon, Suhwan Kim, Orlando Lazaro, Rajiv Damodaran Prabha, Karl Peterson, Carlos Solis, Josh Cowan, Kowshik Murali, Jun-Yang Lei, Nan Xing, Siyu Yang, and Amy Wilson, for, both our many technical discussions, and their friendship throughout this journey.

I am extremely grateful to Mr. Paul Emerson, Dr. Rajarshi Mukhopadhyay, and Texas Instruments for supporting this research and providing the resources necessary for a successful PhD program.

Thank you to my friends and family whose love and encouragement have made this not only possible, but much easier. To my mother, Lelia Rivera Martinez, my father, Dr. Arturo Blanco Plard, and my siblings, Lelimar, Viviana, and Gustavo, for their unconditional love and support. To Daniel and Janet Hansen for their invaluable advice and encouragement. And to Mari Rodriguez who kept me close to home.

Finally, I would like to thank Danielle Hansen who has provided an endless amount of love, encouragement, and strength throughout this process.

# TABLE OF CONTENTS

# LIST OF TABLES

# LIST OF FIGURES

# SUMMARY

The small size of wireless microsystems allows them to be deployed within larger systems to sense and monitor various indicators throughout many applications. However, their small size restricts the amount of energy that can be stored in the system. Current microscale battery technologies do not store enough energy to power the microsystems for more than a few months without recharging. Harvesting ambient energy to replenish the on-board battery extend the lifetime of the microsystem. Radio frequency (RF) energy harvesting extracts energy from electromagnetic radiation, but current technology does not extract enough power. Although kinetic energy harvested through piezoelectric or electrostatic transducers could produce enough power for the system, vibrations are not always available or persistent. Harvesting from light or thermal proves more promising because of their abundance and steady availability.

Although light and thermal energy are more practical in some applications than other forms of ambient energy, they nevertheless suffer from long energy droughts. Additionally, due to the very limited space available in the microsystem, the system cannot store enough energy to continue operation throughout these energy droughts. Therefore, the microsystem must reliably wake from these energy droughts, even if the on-board battery has been depleted. The challenge here is waking a microsystem directly from an ambient source transducer whose voltage and power levels are limited due to their small size. Starter circuits must be used to ensure the system wakes regardless of the state of charge of the energy storage device.

The purpose of the presented research is to develop, design, simulate, fabricate, test and evaluate CMOS integrated circuits that can reliably wake from no energy conditions and quickly recharge a depleted battery. Since the battery is depleted during startup, the system must use the low voltage produced by the energy harvesting transducer to transfer energy. However, the low gate drive available results in low efficiency charging during this phase, so the system should start to a small capacitor to minimize the duration of the low efficiency phase. Once the small capacitor is charged, it can supply a high efficiency charger that can efficiently transfer energy to the larger battery. Systems in the literature today charge the battery during startup, which results in prolonged wake times or add a bulky additional inductor to start to a temporary supply, which leads to an impractical system size. The presented system has the fastest normalized wake time while reusing the inductor already present in the battery charger for startup, therefore, minimizing the overall footprint of the system.

This dissertation presents the background motivation, theoretical analysis, design procedures, and experimental results from prototypes of a fast self-starting energy harvesting system. The first chapter describes the background and applications of wireless microsystems and energy harvesting sources. Chapter 2 introduces a task-scheduling algorithm whose aim is to minimize the size of the on-board battery and describes the theoretical motivation of minimizing wake time and a design strategy to reduce wake time. Chapter 3 presents, compares, and evaluates state of the art low voltage starters. Chapter 4 introduces a novel starter circuit and provides the design procedure and experimental performance. This starter circuit reuses the battery charging inductor to quickly charge a temporary supply without affecting efficiency during steady

state charging. Chapter 5 describes an improved starter circuit, which addresses the limitations of the starter presented in the previous chapter. Specifically, robustness is improved by giving the starter the ability to operate from a slow rising, resistive input source and charge the output capacitor to higher voltages when compared with its predecessor. Chapter 6 integrates the starter circuit into a complete harvesting system and details the operation of the system and the circuit blocks that make the system operational. A prototype of the system was fabricated, and experimental results are presented that validate the system and are used to compare with the state of the art. Finally, Chapter 7 concludes the dissertation by summarizing the findings, the major contributions, technical limitations and future direction of this research.

# CHAPTER 1

# ENERGY-HARVESTING MICROSYSTEMS

## 1.1 Applications

Modern technological advances have allowed the design and creation of systems in the millimeter or less scale. Due to their small size, these microsystems can be deployed within larger systems to sense and monitor various indicators in biomedical, industrial, and military applications [1]-[22]. Biomedical applications include wearable electrocardiograms [1], [2], and implantable pacemakers [3], [4]. The intraocular pressure sensor in Figure 1.1 can be implanted into the anterior chamber of the eye to continuously monitor pressure leading to improved treatment regiments, assessment of medication schedule compliance and vision loss prevention [5], [6]. The implantable blood glucose monitor in Figure 1.2 senses blood glucose levels inside the body and transmits the data to an external reader [7].

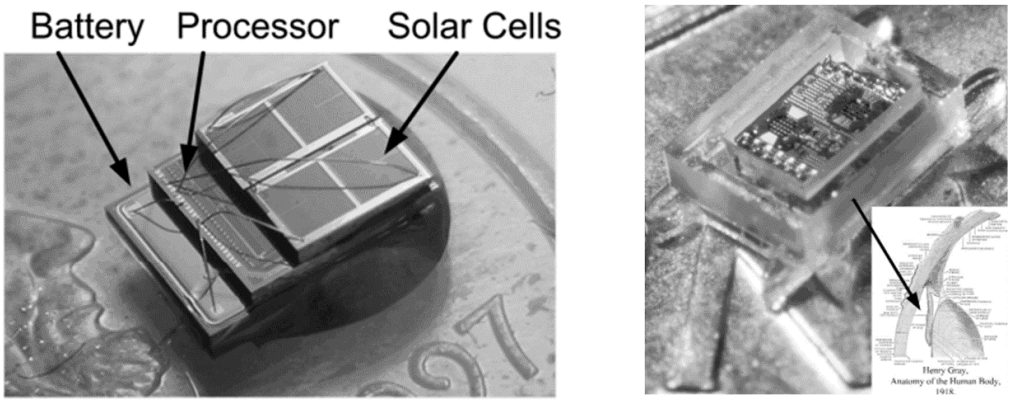


(a) (b)

**Figure 1.1. (a) Stacked self-powered sensor system [5] © 2010 IEEE and (b) implantable intraocular pressure monitor [6] © 2011 IEEE.**

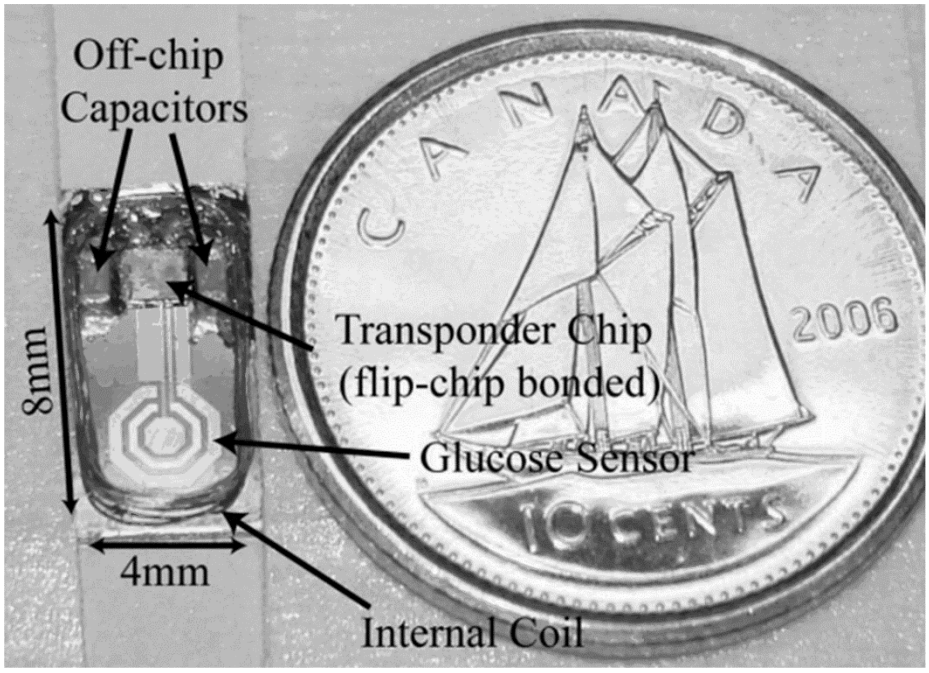


**Figure 1.2. Implantable, wireless powered blood glucose sensor [7] © 2009 IEEE.**

The miniaturization of mechanical and electronic systems has enabled the design and prototyping of microrobots that could one day assist in minimally invasive surgeries [8]. Smart drug delivery microsystems using biodegradable chips could treat hormone deficiencies, chronic pain, or other long-term ailments by releasing pulses of doses at intervals after implantation [9]. These drug delivery systems could increase the efficiency of treatment by delivering more concentrated doses to the affected areas without damaging the rest of the body [10], [11]. A network of tiny sensors that monitors a patient's sleep can diagnose sleep disorders without disturbing sleep due to their small size [12].

Microsystems also find many applications outside of the biomedical field. Micro aerial vehicles can provide operations in hazardous environments. For example, these tiny, insect-like vehicles can lead a search and rescue within collapsed buildings, conduct explorations in a nuclear plant during a radiation leak, or provide reconnaissance and

surveillance for the military [13]. Microsystems can also provide in-tire pressure sensor for vehicles that monitors load and tire wear-out. Tracking the health of a tire would help prevent blowouts by informing the user when preventative maintenance or replacement is required [14], [15].

## 1.2 Technological Challenges

Although modern microsystems have significantly reduced their operating power requirements, the limited size restricts both the available power that can be delivered to the system and the amount of energy that can be stored. A restriction on the available power reduces the functionality and performance of the system. For example, increasing processing speed or wireless transmission data requires higher levels of power. Additionally, a limited amount of stored energy restricts the system's lifetime or increases maintenance cost, since the depletion of the energy storage unit leads to the system's death or requires a recharge.

The most common power source for microelectronics is the electrochemical battery. The technologies in Table 1.1 are some of the most common types of electrochemical batteries. Nickel-cadmium batteries have a high number of charge cycles at 1500, but the lowest weight energy density and power density [23]. This means that although this technology can be charged many cycles before significant performance degradation, the battery itself does not hold much energy and cannot produce as much power as other electrochemical technologies. Additionally, nickel based batteries have a relatively high self-discharge rate, which means it loses a large amount of capacity on its own whether in use or on the shelf.

Although nickel-metal hydride provides high energy and power density with a moderate amount of charge cycles, Li-ion and Li-polymer provide even larger densities with similar number of charge cycles. Furthermore, lithium based batteries have a charge efficiency greater than 99.8%, meaning that only 0.2% of energy is lost during the charging process. With an efficiency as low as 66 – 70%, nickel based batteries can lose up to 34% of energy inside the battery during charging. These losses are inherent to the battery and are in addition to circuitry used for power conversion. A drawback of Li-ion and Li-polymer batteries is that they need to be pulse-charged, requiring a special charging circuit or auxiliary battery whereas NiMH batteries can be directly connected to an energy source without requiring complex charging circuits [23].

**Table 1.1. Comparison of electrochemical batteries.**

| Technology | Weight Energy Density (Wh/kg) | Power Density (W/kg) | Cycles | Charge Efficiency |
|---|---|---|---|---|
| NiCd | 42 | 150 | 1500 | 70%–90% |
| NiMH | 100 | 250 – 1000 | 1000 | 66% |
| Li-ion | 165 | 1800 | 1200 | 99.9% |
| Li-polymer | 156 | 3000 | 500-1000 | 99.8% |

An alternative to electrochemical batteries are supercapacitors, which can have over 500,000 charge cycles [24] and 3000 W/kg [25] power densities. In addition to having more charge cycles, the charging profiles of supercapacitors are more flexible than batteries, allowing for deep or shallow discharges without much loss in performance. However, a large drawback of supercapacitors is a high self-discharge rate. At a loss of around 5.9% per day, supercapacitors are not ideal for long term energy storage, but are more appropriate as short term power supplies. Supercapacitors share their charge-

voltage relationship with regular capacitors, meaning that their voltage level is nearly linear with their charge level. Therefore, if the charging circuit requires a minimum voltage on the supercapacitor, the charge stored below this voltage level cannot be used. This restriction reduces the useable amount of energy in a supercapacitor.

An additional form of energy storage for wireless microsystems is the fuel cell. Micro fuel cells, typically fueled by hydrogen or methanol can be fabricated on silicon wafers alongside the integrated circuit it powers [26]. Direct methanol fuel cells (DMFC) can have as much as 10 times more energy density than Li-ion or Li-polymer batteries [27]. Although they hold much more energy than electrochemical batteries, fuel cells are not recharged, but instead are refueled, which may not be practical for microsystems. Additionally, fuel cells have much lower power densities than lithium based batteries and typically cannot produce the peak power level demanded by the microsystem. Therefore, micro fuel cells are often combined with batteries in a hybrid system so that the fuel cell's high energy density complements a battery's high power density [28]. It should be noted that although the battery supplies the system's immediate power needs, the system's total energy needs, and therefore its average power, is supplied by the fuel cell. Because of the fuel cell's limited output power, special power management circuits must be used to ensure the maximum amount of power is being extracted from the cell since the fuel inside will be spent regardless [29], [30]. This results in a nearly constant power extracted from the cell regardless of the microsystem's immediate power needs. The hybrid system would allow the battery to provide the extra power or absorb the excess power in the system.

Nuclear batteries provide up to five or six orders of magnitude higher energy density than electrochemical batteries or micro fuel cells. The high energy density combined with a very low self-discharge rate leads to extremely long lifetimes, up to hundreds of years in some cases [31]. Additionally, nuclear batteries are extremely resilient regardless of ambient conditions, producing near constant performance under severe temperature, pressure or electromagnetic fields [32], [33]. One type of nuclear battery, a betavoltaic cell, uses silicon to capture the kinetic energy released from a radioactive isotope, potentially allowing integration with the rest of the microsystem [31], [32]. Unfortunately, nuclear batteries remain an expensive solution due to the difficulty of extracting and operating the radioactive isotopes [33]. Furthermore, although the energy density is very high, their maximum power is extremely limited, with microscale devices producing less than 100 nW [31].

While Lithium batteries and supercapacitors deliver the necessary instantaneous power to the microsystem, their energy density is too low for extended applications. In other words, they would discharge before the intended life of the system. Fuel cells and nuclear batteries hold orders of magnitude more energy, but fuel cells need manual refueling and nuclear batteries produce far too little power for a practical wireless system. Although a combination of high energy dense fuel cells or nuclear batteries alongside high power dense electrochemical batteries or supercapacitors can both produce the required power levels of wireless microsystems and extend the energy lifetime of the system, the limitation of fuel cells and nuclear batteries persists. An attractive alternative is to harvest energy from the immediate environment of the microsystem to recharge an auxiliary battery or supercapacitor. Transducers converting light, thermal, or kinetic

energy can produce the necessary average power while maintaining a small form factor. Since the energy consumed by the system comes from the environment, and not an on-board device, the lifetime of the system, in terms of energy requirements, is extended indefinitely.

## 1.3 Ambient Energy

Harvesting ambient energy from a tiny transducer can extend the lifetime of a wireless microsystem indefinitely while maintaining a practical size for miniaturized applications. Advances in microelectromechanical systems (MEMS) have allowed the creation of tiny transducers that could produce practical power levels for wireless microsystems. By continually replenishing the system with the power it requires, energy harvesters remove the need of an energy storage device, replacing it instead with a much smaller energy cache, which delivers short bursts of power that the energy harvester alone cannot provide. Possible forms of ambient energy that can be harvested for wireless microsystems include kinetic, radio frequency (RF), light, and thermal energy.

### 1.3.1 Kinetic Energy

Kinetic energy transducers convert energy in the form of motion into electrical energy and, generally, use one of three transduction mechanisms: electrostatic, piezoelectric or electromagnetic. Electrostatic transducers, in general, extract energy from a parallel plate capacitor, whose capacitive properties are altered by motion. Piezoelectric harvesters derive their power from materials whose molecules polarize when the material is deformed or bent due to vibrations. Finally, electromagnetic transducers take

advantage of the fact that when a coil moves in a static magnetic field, it produces an electromotive force (EMF), which can be harvested as electrical energy.

*Electrostatic Transducers:*

Electrostatic transducers, in essence, are pre-charged capacitors, in which one plate is stationary and the other moves with the applied motion. In these transducers, mechanical energy from motion works against the electrostatic force stored as charged in the parallel plates. For example, the proof mass in the transducer in Figure 1.3 moves with vibrations with respect to the stationary anchor [34]. If the proof mass and stationary anchor are pre-charged with opposite polarities, the electrical force will try to pull them together. When motion is applied that opposes the electrical force, i.e. pulls the plates apart, the mechanical energy is transferred into electrical energy [35]-[48]. With applied forces typical of microsystem applications, tiny electrostatic transducers can harvest around 1 – 50 $\mu W/cm^3$ [35], [49], [50].

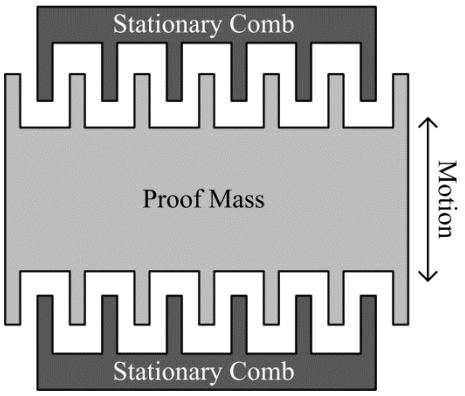


**Figure 1.3. Diagram of a MEMS electrostatic transducer.**

*Piezoelectric Transducers:*

Materials that exhibit the piezoelectric effect offer another way of harvesting kinetic energy from vibrations. When a strain is applied to a piezoelectric material, the molecules inside the material are deformed and become electrically polarized [34]. This

polarization creates an electric field inside the material, which translates to a voltage across the terminals of the device. If a proof mass is applied on one side of a piezoelectric cantilever while the other side is anchored, a vibration applied to it will cause the cantilever to bend, as shown in Figure 1.4 [51]. Straining the material will transfer some of the mechanical energy from the vibration into elastic strain energy, i.e. bending the material, and the rest into the electric field that generates a voltage. An energy harvesting circuit can then extract energy from this voltage [52]-[62] in the range of 16–375 $\mu W/cm^3$ [50], [52], [53].

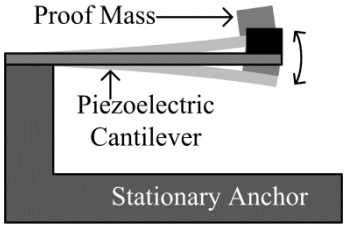


**Figure 1.4. Diagram of a piezoelectric cantilever.**

*Electromagnetic Transducers:*

A third method of harvesting kinetic energy from vibrations is to use an electromagnetic transducer. According to Faraday's Law of Induction, a changing magnetic field inside a coil or conductor will induce an electromotive force across the conductor. A coil moving with respect to a stationary magnet will experience a changing magnetic field, and therefore will produce an electromotive force or voltage across its terminals [54]-[67]. Miniaturized coils attached to a beam, as in Figure 1.5 [56], move with vibrations within a stationary magnet producing 55–215 $\mu W/cm^3$ [56], [60] of electrical power.

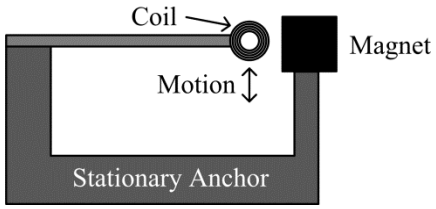


**Figure 1.5. Diagram of electromagnetic vibration harvester.**

### 1.3.2 RF Energy

With the increased use of wireless data transmission in everyday life, harvesting power from unused transmissions in the radio frequency (RF) band is becoming more attractive [68]-[79]. However, significant obstacles still remain, as power levels remain well below practical uses, typically below 100 nW/cm$^2$ when the receiving antenna is within 100 meters of the power source [80]. Larger distances prove to be even more impractical since the power per unit area decreases quadratically with distance from the source [81]. Additionally, harvesting energy from multiple sources is difficult since antennas typically can receive only a single narrow frequency band while sources generate radiation across the entire RF spectrum.

### 1.3.3 Light Energy

With the abundance of light in many microsystem applications and light's high energy density, harvesting energy from light remains a popular and viable method of powering microsensors [82]-[97] Harvesting energy from the sun in outdoor applications can produce 0.15 – 10 mW /cm$^2$. Using artificial light in indoor applications results in significantly less harvested power, around 10 – 100 μW/cm$^2$, but enough to power a wireless microsensor [5], [6], [98]. Additionally, the ability to integrate the photovoltaic

cell in the same silicon chip as the rest of the system using the same process leads to decreased costs when compared to other energy harvesting transducers [99], [100].

### 1.3.4 Thermal Energy

Electrical, mechanical, and chemical process create waste heat as they are not perfectly efficient. In many situations, this wasted heat can be re-captured and converted into electrical energy. Using thermoelectric generators, a small part fraction of the wasted heat can power wireless microsensors in factories, vehicles, oil rigs, or other applications in which there is a large temperature difference between the system and the outside environment [33], [101]-[119]. An emerging application for thermoelectric generators is wearable or implantable medical devices. The difference in temperature between the human body and ambient air is around 10 – 15 °C [120], although not all of the temperature difference falls across the transducer. Nevertheless, wearable sensors could harvest this thermal energy and power the system with about 20 μW [121]. More generally, microscale thermoelectric generators produce about 1–100 $\mu W/cm^2$ [122], [123] per degree Celsius.

### 1.3.5 Comparison

Harvesting ambient energy from the sources in Table 1.2 to supply wireless microsensors can extend the lifetime of the microsystem by replenishing the on-board battery. In the current state of the art, RF energy harvesting does not produce enough power to sustain a sensor throughout its lifetime. Although kinetic energy harvested through piezoelectric or electrostatic transducers could produce power levels up to 375 $\mu W/cm^3$ of power, vibrations are not always available or persistent. Photovoltaic cells

and thermoelectric generators produce similar power levels when compared to kinetic energy transducers, but their energy sources tend to be more constant and abundant. For example, sunlight and indoor lighting are typically available for hours at a time. In the case of thermal energy, because of the slow nature of temperature changes, temperature differences are inherently available for long periods of time. The combination of abundance and steady availability make light and thermal energy ideal for harvesting in wireless microsystems.

**Table 1.2 Comparison of Energy Harvesting Sources**

| Source | Transduction Mechanism | Estimated Power |
|---|---|---|
| Light | Photovoltaic Effect | 1 – 388 $\mu W/mm^3$ |
| Thermal | Seebeck Effect | 1 – 30 $\mu W/°C/mm^3$ |
| Vibrations | Electrostatic | 1 – 50 $\mu W/mm^3$ |
| | Piezoelectric | .01 uW – 3.5 $\mu W/mm^3$ |
| | Electromagnetic | 0.6 $\mu$W – 2.2 $\mu W/mm^3$ |
| RF Energy | Antenna | < 1 $nW/mm^3$ |

## 1.4 DC Sources

Although harvesting energy from vibrations could produce enough power for microsystems, vibrations are not always available. Two practical alternatives are light and thermal energy, which are ubiquitous across microsystem applications. Light energy is harvested primarily using semiconductors as free charges are created when light is absorbed in the material. The Seebeck effect is exploited to harvest thermal energy when a temperature difference is imposed across a material. Although both harvesting sources use very different mechanisms, the challenges involved with both, namely low output

power and low output voltage for tiny transducers, allow similar, though not the same, solutions.

### 1.4.1 Photovoltaic Cells

The abundance of light across applications of microsystems makes photovoltaic cells an attractive and practical source of energy. Because electrons in semiconductors are can be freed by receiving a relatively low amount of energy, called the bandgap energy, light hitting a semiconductor releases a large amount of electrons [124]. When an electron is freed, it leaves a positively charged absence, called a hole, in its original atom. Both the electron and the hole can now move across the material. In a general semiconductor, the free electron will recombine with the hole after a short and the energy will be lost to thermal dissipation.

Minority carriers, i.e. electrons in p-type and holes in n-type semiconductors, have a finite lifetime before the carrier loses its energy and recombines with one of the relatively numerous majority carriers. However, separating the pair before recombination produces a net charge across the semiconductor, which can be used to produce electrical current. The electric field created in the depletion regain of a PN junction, as in Figure 1.6, could separate an electron-hole pair. If the minority carrier created by the photon is within one diffusion length, $L_N$ or $L_P$, of the junction and its built-in electrical field $\varepsilon_{BI}$ in Figure 1.7, the field will attract the minority carrier and sweep it across the junction while blocking the majority carrier. However, statistically the minority carrier will not travel much further than its diffusion length before recombination, so pairs created further from the junction will not be separated and will not produce electrical energy.

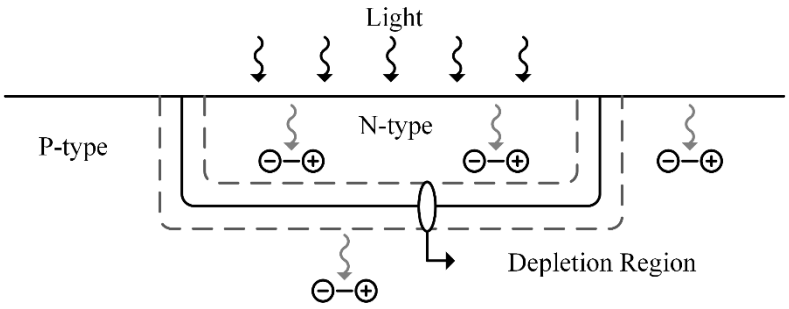


**Figure 1.6. Electron-hole pairs created due to light incident on a PN junction.**

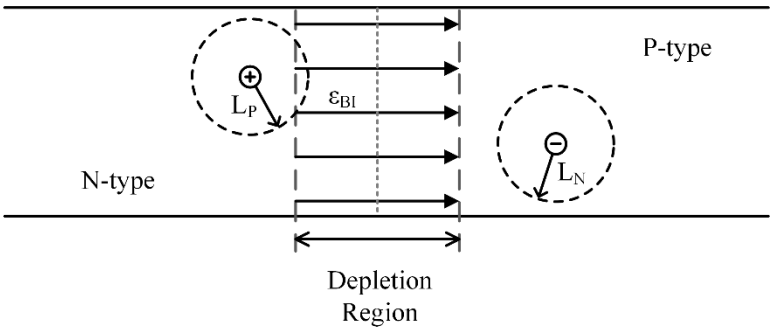


**Figure 1.7. Minority carriers diffusing near a depletion region.**

As electrons in the p-type region are swept to the n-type region, the n-type region accumulates negative charge. Similarly, as holes from the n-type are swept to the p-type region, a positive charge accumulates in the p-type region. As charge across the junction increases, a new electrical field, i.e. a voltage, forms in the opposite direction of the built-in field. As the built-in field is neutralized, majority carriers begin to cross the junction in the opposite direction of the photocurrent. Therefore, at equilibrium, the PN junction has a positive voltage, called the open-circuit voltage, with no net current or power flowing out of the cell. To extract energy, a load is connected to draw photovoltaic current so less current flows into the diode. The model in Figure 1.8 illustrates that as the load at $v_{PV}$ draws more of the photocurrent, $i_{PH}$, the diode $D_{PV}$ conducts less and the voltage is lowered. If too much current is drawn, all the photocurrent flows out of the cell; with no

voltage formed, no power is drawn. At the other extreme, if no current is drawn, all the photocurrent flows through the diode and again, no power is drawn. Therefore, a conditioning circuit must be used so that the energy from the cell is extracted at its maximum power point where a balance is reached between the cell voltage and current.

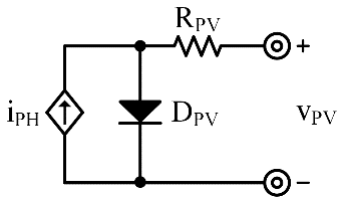


**Figure 1.8 Photovoltaic cell model.**

Because of the small size of microscale devices, the amount of light absorbed by the exposed semiconductor is also small. For example, each of the low cost, integrated CMOS photovoltaic cells in Figure 1.9 are as small as 70 μm on each side [100]. Furthermore, because semiconductors have relatively high resistance, smaller cells, routed by highly conductive metal, are typically connected in parallel to reduce the equivalent resistance and increase efficiency. Although efficiency is improved, the metal routing reduces the amount of exposed semiconductor and, therefore, the power generated [99]. Additionally, many microsystems applications are indoor, where light comes from low intensity, artificial sources. Therefore, both the photocurrent and diode voltages are relatively small. Microscale photovoltaic cells produce 300 – 450 mV of open circuit voltage and 1 – 100 μW of power from indoor light [125], [126].

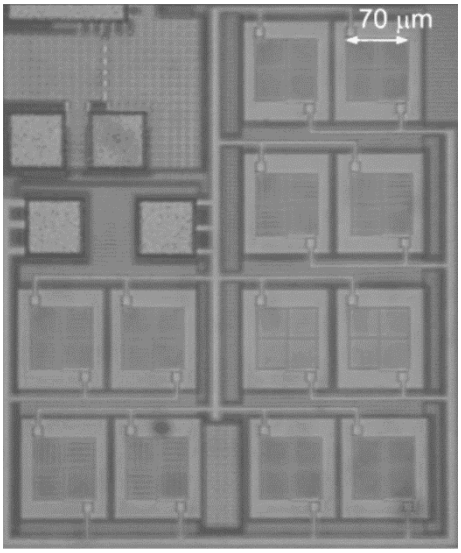


**Figure 1.9. Integrated CMOS cell for powering microsystems [100].**

### 1.4.2 Thermoelectric Generators

As a material is heated, it acquires more thermal energy and its particles are more likely to diffuse [127]. If a thermal gradient or difference in temperature exists across a material, as it does in Figure 1.10, charged particles, if free to move, will tend to diffuse into the cold region. Likewise, particles in the colder region will diffuse towards the hotter region. However, because the hotter charges have more thermal energy, they will tend to diffuse more than their colder counterparts. This difference in energy causes a net movement of hot charged particles to the cold region creating an accumulation of charge in the colder region. The accumulation of charge translates to a voltage, which is proportional to the temperature difference across the material. The proportionality constant between voltage and temperature, named the Seebeck coefficient, depends on the material used and the absolute temperature of the device.

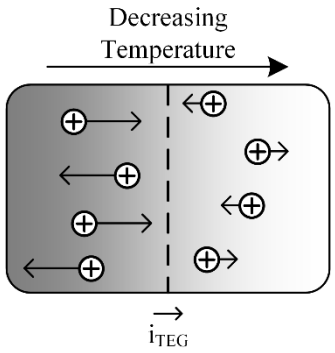


**Figure 1.10. Positive charges diffusing towards higher temperatures.**

The ability to fabricate semiconductors with either hole (positive) or electron (negative) majority charge carriers makes semiconductors an ideal material to harvest energy using the Seebeck effect. In a semiconductor with a hole majority, or p-type material, both holes and electrons move in the direction of decreasing temperature. However, since the number of positive charges (holes) overwhelms the number of free electrons, a net positive charge is observed on the cold side of the material. Conversely, in an electron majority semiconductor, or n-type material, electrons overwhelm holes, and a negative charge is created on the cold side. Placing an n-type material next to a p-type material and connecting two ends together, as in Figure 1.11, creates a net voltage across the free terminals of the n- and p-type materials. Since charges in both materials move in the same direction, but with opposite electrical polarity, a positive charge accumulates in the cold end of the p-type material, while a negative charge accumulates on the cold end of the n-type material.

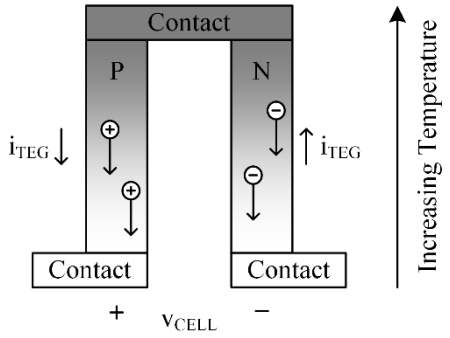


**Figure 1.11. Single thermoelectric generator cell with P and N sections.**

The voltage produced by each cell, $v_{CELL}$, is tiny, on the order of 200 μV/K [108], [110], [112], [115], [116], so a practical energy harvesting device would contain many of these cells in series, where the number of cells is limited by the total area and the minimum size of each cell. Modern fabrication processes have allowed the creation of tiny cells, in the order of 35 by 35 μm. The small area of the cell allows for a dense array of many thermoelectric cells, as shown in Figure 1.13, which produces 80 mV/K with 210 Ω series resistance [123]. In addition to the limited voltage produced by each cell, the electrical resistance of the semiconductors limits the generated power as shown in Figure 1.12. When an electrical load is connected across $v_{TEG}$, current is drawn from the thermoelectric generator, but some power is lost to $R_{TEG}$. As the current increases, more power and voltage is lost to the resistance, until finally no power is available at the output. Therefore, as is the case with a photovoltaic cell, the harvesting circuit must draw power at or near the transducer's maximum power point so it does not draw either too much or too little current.

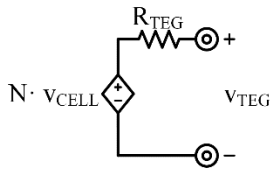


**Figure 1.12. Model of a thermoelectric generator.**

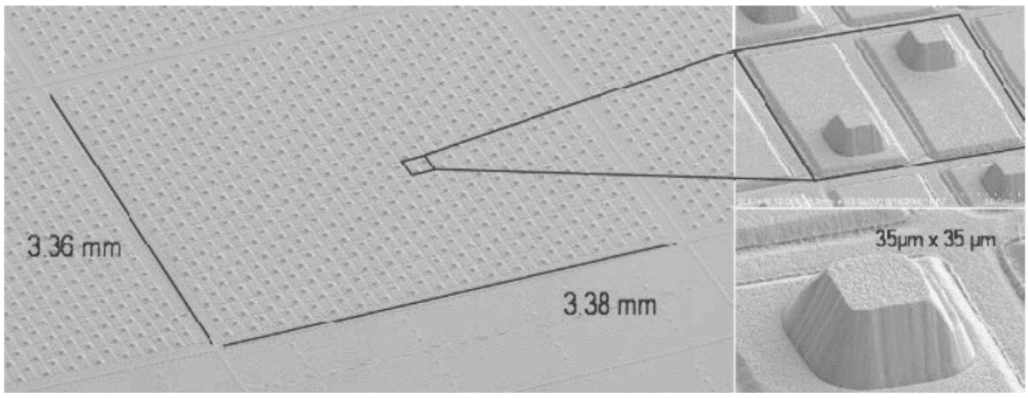


**Figure 1.13. Miniature, stacked thermoelectric generators [123].**

## 1.5 Microsystem Wake-up

Distributed wireless microsensors sense, process, and transmit data across a network to a base station, which then uses the information to make intelligent decisions regarding the larger system or infrastructure [20]. The microsystem in each node can essentially be divided into the blocks in Figure 1.14: an energy source, power management, sensors, data processing and storage, and communications. The energy source and power management blocks work together to provide the necessary voltage and power required by the individual blocks. The energy source provides the total energy consumed by the microsystem throughout its lifetime whereas the power management block delivers the instantaneous power while supplying a regulated voltage. Since the energy sources are not persistent, the microsystem will experience energy droughts in

which it will need to either survive from the on-board energy storage or enter a sleep state in which the system wakes when the energy source returns.

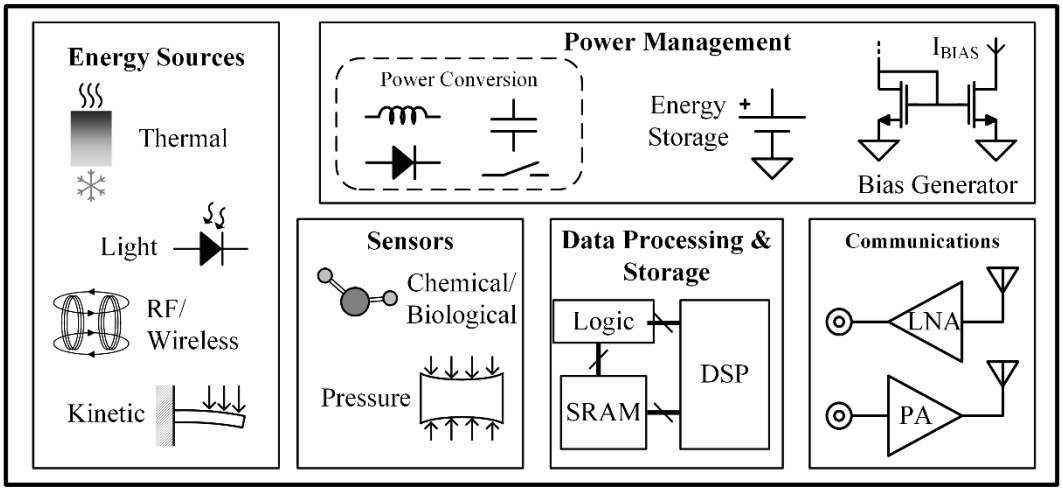


**Figure 1.14. Functional component diagram of wireless microsensor.**

### 1.5.1 Voltage Requirements

Because the size constraint of the microsystem requires the energy source to be tiny, the voltage produced by the energy source transducer is small [125], [128]. Therefore, the power management block must step up or boost the input voltage to a level high enough that the functional blocks can operate correctly. The requirement of each block is different as each is composed of a combination of digital, analog and radio frequency (RF) circuits. Circuits in wireless microsystems consist mainly of CMOS transistors that require a minimum supply voltage to function. Signal amplification limits the supply voltage of digital circuits, as the gain reduces with decreasing supply. Threshold and overdrive voltages limit the supply of analog circuits, as these limit the bandwidth and accuracy. Furthermore, voltage swing and signal-to-noise ratio add an extra requirement on the supply, particularly in radio frequency (RF) blocks. Even the boosting circuits used in the power management block must be supplied with a voltage

sufficient to turn transistors fully on and off during operation, which makes the minimum supply dependent on the threshold voltage.

By operating in the subthreshold regime, the supply voltage of a digital gate can be below the transistor threshold voltage. Since the transistors operate in weak inversion, drain current follows an exponential relationship with input voltage, beginning at its leakage current and increases with gate voltage. For digital gates, signal amplification or restoration occurs when the gain across the circuit is greater than one. As a signal is passed through cascaded gates, the signal is amplified by each gate according to their gain. If the gain is less than one, the signal will be attenuated and possibly lost. Therefore, the supply voltage must be enough so that gain of each stage remains above one.

For an ideal MOSFET transistor, the minimum supply for the simplest digital circuit, an inverter, is about 36 mV at room temperature [129], [130]. However, this value does not consider process variations, specifically asymmetry between the NMOS and PMOS transistors. Any asymmetry moves the inverter away from the ideal, maximum-gain bias point of half the supply voltage. Assuming a standard deviation of the threshold voltage of 32 mV for each type of transistor, the minimum supply increases to 250 mV [129]-[133]. It should be noted that this minimum supply voltage ensures operation, but not performance. For example, the maximum operating frequency decreases with supply voltage, so the required speed of the circuit may dictate a higher supply voltage. Furthermore, the minimum supply voltage is temperature dependent, so ensuring the circuit operates at all desired temperatures requires inserting margin that will increase the supply past 250 mV.

The digital inverter also serves as a simple, high gain analog amplifier [134], [135]. However, although the inverter provides gain at 36 mV supply voltage for theoretical transistors and at 250 mV taking into account process variations, the supply voltage must be high enough to allow voltage swings that overcome noise present in the system with sufficient margin. The largest voltage swing a non-switching, linear, CMOS amplifier can provide is the supply voltage. Therefore, the output signal of the amplifier will, at maximum, swing between the supply voltage and ground. Since real circuits insert noise into the signal, the larger the signal swing, the stronger the signal strength will be compared to the injected noise. Therefore, the signal-to-noise ratio (SNR) increases with supply voltage and is poor at low supply voltages.

As the supply voltage decreases, the bandwidth, or speed, of CMOS circuits also decreases. The transition frequency of a transistor represents the maximum frequency at which the transistor still provides gain above unity [136]. In the above-threshold regime, the transition frequency, increases linearly with gate voltage bias. However, in subthreshold, the transition frequency, increases exponentially with gate voltage bias. Therefore, bandwidth falls rapidly in the subthreshold region and becomes a limiting factor when reducing the supply voltage.

Finally, wireless microsensors rely on radio frequency (RF) transmission to communicate with the central node or other nodes in the network. This communication requires driving an antenna at an RF carrier frequency along with the modulated (data) signal with a power amplifier. To transmit the required distance while maintaining signal quality, the power amplifier must deliver sufficient power, which increases quadratically with supply voltage [137]. Although switching, non-linear power amplifiers can provide

higher power levels to the antenna, the supply voltage still limits the output voltage swing, causing output power to decrease rapidly with the supply voltage. Therefore, the minimum supply voltage for RF transmitters is dictated by the amount of power required to drive the antenna.

### 1.5.2 Wake-up Conditions

Although harvesting energy from the environment can extend the lifetime of a microsystem, the energy source will not always be available. In the case of outdoor light, sunlight is not constant during the day and is not present at night. In indoor light applications, lights may be turned off during the day or overnight. Even temperature differences may go away when machinery is turned off for downtime or maintenance in an industrial application; in the case of wearable devices, the ambient temperature may change when moving between indoors and outdoors. When the energy source to the microsystem disappears for extended periods of time, the system can only operate from the energy storage device. However, due to the very limited space available in the microsystem, the system cannot store enough energy to continue operation throughout energy droughts. Therefore, the microsystem must be able to come back online, or wake, when the energy source returns. The challenge with waking a microsystem after long droughts is that the energy storage device, or battery, may be depleted and cannot provide the voltage and power necessary to the power management block in order to restart the system. A starter circuit, with a lower minimum supply voltage, must provide the voltage and power to the power management block, and charge the battery so that full operation can resume.

## 1.6 Summary

The continued reduction in the size of microelectronic devices has allowed the creation of systems in the millimeter or less scale. Their small size allows these microsystems to be deployed within larger systems to sense and monitor various indicators throughout many applications. In addition to their small size, advances in circuit designs have allowed the circuits to consume less power while performing the necessary functions. However, the limited size still restricts both the power that can be delivered to the system loads and the amount of energy that can be stored. Current microscale battery technologies do not store enough energy to power the microsystems for more than a few months. Harvesting ambient energy to supply wireless microsensors can extend the lifetime of the microsystem by replenishing the on-board battery. RF energy harvesting extracts energy from electromagnetic radiation, but current technology limits the extracted power levels well below what microsensors require. Although kinetic energy harvested through piezoelectric or electrostatic transducers could produce enough power for the system, vibrations are not always available or persistent. Harvesting from light or thermal proves more promising because of their abundance and steady availability.

Although light and thermal energy are more steady and constant than other forms of ambient energy, they unfortunately suffer from long energy droughts. Additionally, due to the very limited space available in the microsystem, the system cannot store enough energy to continue operation throughout these energy droughts. Therefore, the microsystem must reliably wake from these energy droughts, even if the on-board battery has been depleted. The challenge here is waking a microsystem directly from an ambient

source transducer whose voltage and power levels are limited due to their small size. Starter circuits must be used to ensure the system wakes regardless of the state of charge of the energy storage device.

# CHAPTER 2

# ENERGY-HARVESTING AND DROUGHT-RECOVERING WIRELESS MICROSYSTEMS

Wireless microsensors can add life-, cost-, and energy-saving intelligence to larger systems by sensing ambient conditions [6], [14], [90], [98], [138]. The key to their ubiquity is miniaturization because space in modern and emerging applications is increasingly scarce. Tiny onboard batteries, however, store little energy, and in the case of super capacitors, also leak considerable power [24]. Therefore, harnessing ambient energy is often a requirement for these microsystems. Still, ambient energy, $E_A$, is not constant and not always available [139], [140]. When ambient energy is present, miniaturized transducers might only produce 1 of the $100\mu W/mm^2$ that the highest power-producing devices can [6], [90]. So with $E_A$, the harvesting source $v_H$ in Figure 2.1 feeds a maximum power-point (MPP) charger that replenishes a battery, $C_B$, with enough energy to supply the system. The power supply [141], [142] then draws and conditions power to satisfy the sensor, digital-signal processor (DSP), power amplifier (PA), and other system components. The central processor (CP) assesses the state of the system to determine which blocks to activate and which to disable.

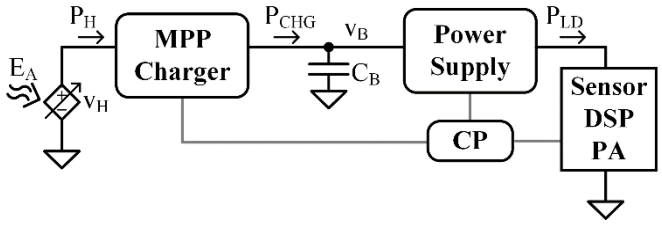


**Figure 2.1. Energy-harvesting wireless microsensor system**

Since $v_H$ does not always output power $P_H$, the battery must be large enough to store the energy that the system requires across harvesting droughts. Or, if allowed to drain, which is more practical because drought periods can be long and batteries suffer from self-discharge, the system should recover fast enough when the ambient energy returns to leverage input power is available before $E_A$ again fades. Critical design considerations here are size and wake time. But for a small battery, load power should be low. A low task schedule minimizes the size of the battery while maximizing the use of the input power. A small battery, however, drains across harvesting droughts, so the system must be able to survive and quickly recover energy droughts to continue sensing and transmitting data.

## 2.1 Low-Energy Task Schedule

Tasks performed by the microsensor, including sensing, processing data, and sending data require power and energy to be delivered to the system load. This energy must first be delivered to and stored by the battery $C_B$, since $P_H$ is not enough to fully satisfy the load on its own. Scheduling multiple tasks at a time requires the battery to hold the sum of the energies required by each task. Therefore, to minimize how much energy the battery $C_B$ stores at any given time, the system should schedule no more than one task at a time, and a task should only occur when $C_B$ has enough energy to sustain it. This way, the task with the largest energy usage dictates the energy capacity of the battery instead of the sum of all tasks. Reducing the required battery capacity means decreasing its volume and the overall size of the microsystem.

In a microsensor, the main tasks performed are typically sensing, processing, and transmitting processed data. The first task is to acquire a measurement of the external

information, for example a temperature or pressure reading, using a sensing transducer. The transducer converts the measurement into an electrical signal which must be processed and stored into a local memory. Since the storing event constitutes the recording of the data point, processing and storing must occur immediately after the data is available from the transducer or the data point will not be recorded. Therefore, sensing, processing, and storing should be considered as a single, combined task that cannot be divided or rearranged. Sensing, processing, and storing the data requires electrical power and energy, which is supplied by $C_B$. Once data is stored, it must then be transmitted, which also requires power and energy from $C_B$. Transmitting data usually requires more energy, $E_T$, than sensing events (sensing, processing, and storing) do with $E_S$.

Since a transmitting event requires more energy, and therefore, more time to charge the battery, scheduling multiple sensing events between transmissions leads to the system sensing and processing more data points within a given time period. For this, the system can monitor $C_B$'s voltage $v_B$ as a way of determining when $C_B$ stores enough energy to sustain a task. As soon as $C_B$ collects sufficient energy, the system executes the task. So, when the harvester charges $C_B$ to the sensing threshold $V_{S(TH)}$, like Figure 2.2 indicates and Figure 2.3 shows at 180 ms, the system senses, processes, and stores data. Since $C_B$ supplies the sensor and microelectronics involved in this process, the event discharges $C_B$ below $V_{S(TH)}$. After the sensing event, the system allows the harvester to recharge $C_B$, so $v_B$ rises. When $v_B$ again reaches $V_{S(TH)}$ at 200 ms, the system senses again and the sequence repeats (and loops in Figure 2.2) the N times that the application requires.

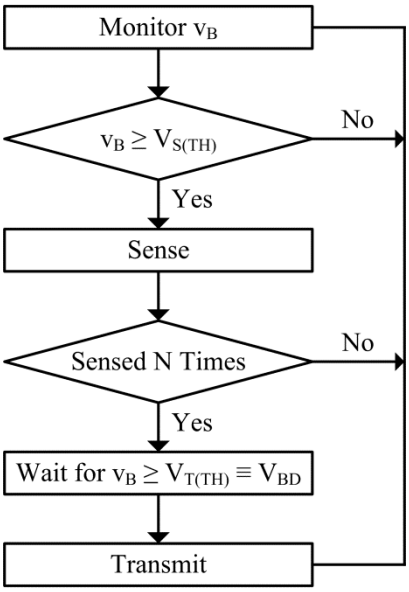


**Figure 2.2. Proposed low-energy "just-enough" task schedule flow chart.**

After sensing N times, the system waits and the harvester charges $C_B$ until $v_B$ reaches the transmission threshold voltage $V_{T(TH)}$. Since transmissions are usually the most power-consuming task in the system, $V_{T(TH)}$ corresponds to the highest energy level that $C_B$ should hold. The smallest $C_B$ that will hold this energy will do so at the highest voltage possible, which corresponds to the breakdown voltage $V_{BD}$ of the circuit. So when $v_B$ reaches $V_{BD}$, which happens at 350 ms in Figure 2.3, the power amplifier transmits the information collected across N sensing events. Since $C_B$ supplies the transmitting circuits, the transmitting event will discharge $C_B$ to its minimum voltage $V_{MIN}$. Each event should not discharge $C_B$ below the energy and corresponding voltage, $V_{MIN}$, required to keep the system operational. Therefore, $v_B$ drops to $V_{MIN}$ after every transmission and sensing event in Figure 2.3.

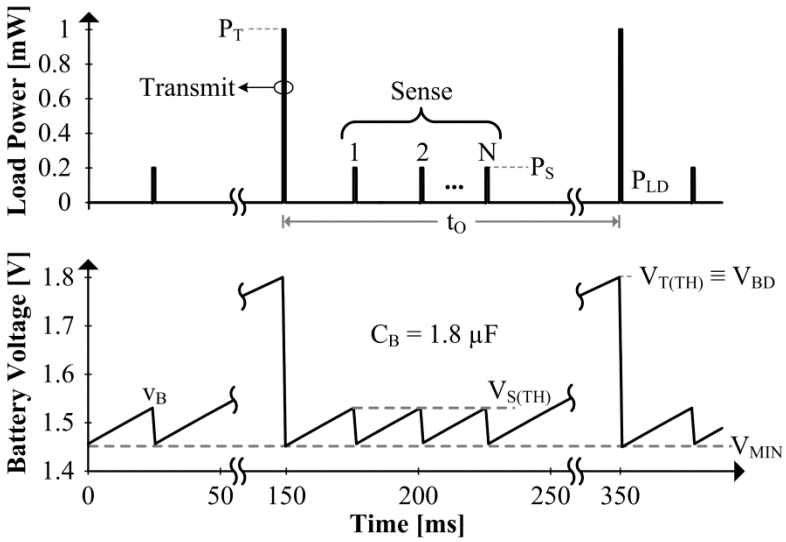


**Figure 2.3. Power train and corresponding battery-voltage simulation.**

By waiting for $v_B$ to reach sensing and transmission thresholds $V_{S(TH)}$ and $V_{T(TH)}$, the system automatically adjusts the time $t_O$ between transmissions to keep average load power $P_{LD(AVG)}$ and power losses $P_{LOSS}$ at the level the harvesting source $v_H$ supplies with $P_H$:

$$P_H = P_{LD(AVG)} + P_{LOSS}\,. \tag{2.1}$$

This means that the consumed power, on average, is equal to the input power. If $t_O$ were fixed so that $P_{LD(AVG)}$ was also constant, any excess input power would not be used. If the input power were to go below the load power plus losses, the battery would deplete and the system would cease to operate until the battery could be recharged. By using the "just enough" low-energy task schedule, the consumed power always matches the available input power thereby maximizing the system's resources.

The application of the microsystem and the state of the art of supporting technologies dictate the thresholds and values required to operate the system. CMOS circuits, for example, can sustain up to 1.8–4.5 V and consume 11 nW when idling, 2–50

μJ when sensing, and 38 nJ–58 μJ when transmitting [6], [14], [98], [138], as Table 2.1 shows. Chargers can deliver 0.15%–0.7% of the power drawn from a 40–500 mV source during startup and 87% from higher voltages in steady state [11]-[13]. Although startup does not affect the time the battery requires to charge when enough ambient energy is present (in Figure 2.3), low startup efficiency extends the time needed to recover from harvesting droughts.

**Table 2.1 Power Levels in the State of the Art**

| Parameter | | Range | Reference |
|---|---|---|---|
| Harvesting Source | $v_H$ | 40–500 mV | [143] |
| Harvesting Source Power | $P_H$ | 1–1000 μW/mm$^2$ | [6], [90] |
| Idle Power | $P_{IDLE}$ | 11 nW | [98] |
| Sense Energy | $E_S$ | 2–50 μJ | [14], [138] |
| Transmission Energy | $E_T$ | 38 nJ–58 μJ | [6], [14] |
| Breakdown Voltage | $V_{BD}$ | 1.8–4.5 V | [144] |
| Startup Efficiency | $\eta_{ST}$ | 0.15%–0.7% | [143] |
| Steady-State Efficiency | $\eta_{SS}$ | 87% | [87] |

## 2.2 Downtime Operation, Analysis, and Design

The charger in Figure 2.1, like most harvesting chargers [87], monitors the power it delivers, $P_{CHG}$, and adjusts to ensure it maximizes the delivered power. This entails operating the harvesting transducer at or near its maximum power point (MPP) and minimizing losses incurred in the charger. When $P_{CHG}$ falls below the threshold level in which it can supply the load, $P_{LD}$, the system will turn off the Power Supply block. Note that this threshold level, $P_{TH}$ in Figure 2.4, is slightly larger than $P_{LD}$, since the charger must supply both the load and the losses incurred in the Power Supply block. Because the

transmission circuits are turned off during this time, no communication is possible when $P_{CHG}$ falls below $P_{T1}$. Because of this, the system should transmit a system-offline report before it switches the power supply, and therefore the load circuits, off. This report requires the battery to hold sufficient extra charge to send one transmission when the input power disappears.

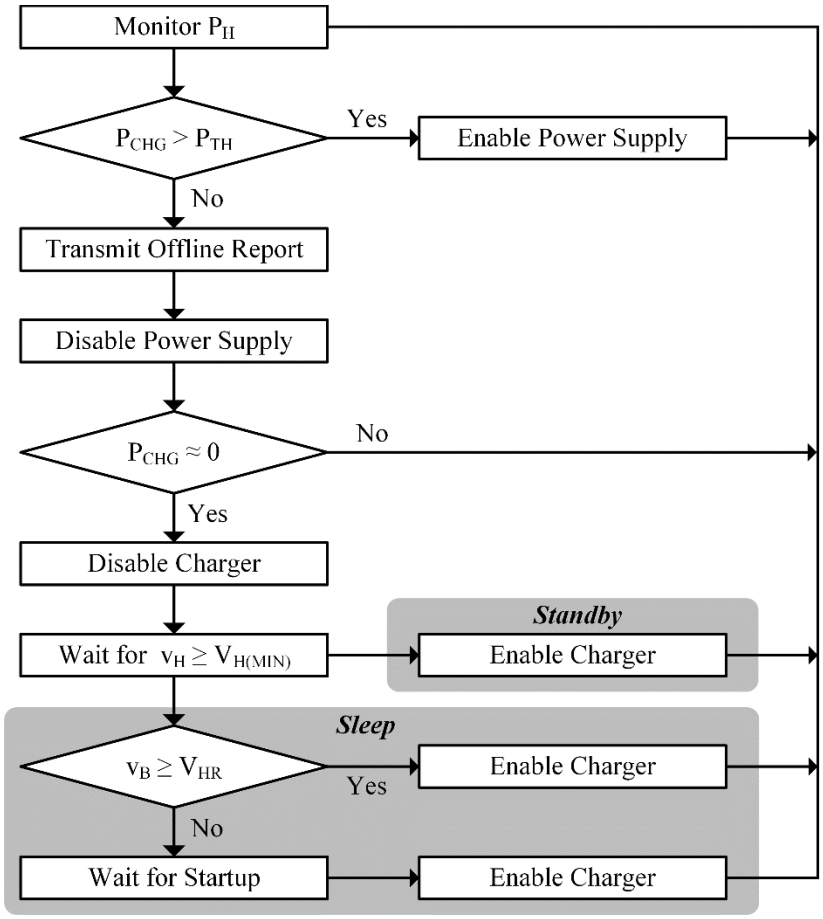


**Figure 2.4. Proposed downtime flow chart.**

Once the report is sent, the central processor (CP) then disables the power supply that feeds the sensor, DSP, PA, and other blocks until $P_{CHG}$ climbs back to $P_{TH}$. During this time, as long as $P_{CHG}$ is greater than zero, the battery continues charging. But if $P_{CHG}$ falls further to zero, the harvesting power $P_H$ is no longer able to sustain the charger's losses. When this occurs, the central processor shuts the charger to enter standby or sleep

mode until $v_H$ recovers to the minimum level $V_{H(MIN)}$ from which the charger can draw and output power. The system could be designed for either standby or sleep mode during droughts. During standby, the system never turns completely off and must depend on the battery continuously providing a low, standby, power. In sleep mode, the system goes into a low power mode at first, but in this case the battery is allowed to completely discharge at which point, no power is consumed.

### 2.2.1 Standby

When designed for standby, the battery $C_B$ must be large enough to keep $v_B$ from ever falling below the headroom level $V_{HR}$ that the charger requires to operate. This way, the microsystem can immediately resume operation when input power returns. Although most circuits are turned off during the outage, low-power survival blocks in the central processor, which monitor the available input power and detect when it has returned, still operate. Since these circuits remain on, the battery discharges, albeit slowly. Furthermore, electrochemical batteries and supercapacitors experience self-discharge, which means they lose charge even when not in use. Therefore, the battery must have the capacity to provide enough energy for the survival blocks during the entire drought in addition to the energy it will lose due to self-discharge.

When the input power disappears, the battery will be somewhere between completely charged at $V_{BD}$ and its operational minimum, $V_{MIN}$. Since being charged to $V_{BD}$ at the beginning means the battery will have the highest energy possible throughout the drought, it has the best chance to remain above $V_{HR}$ if it begins at $V_{BD}$. Therefore, the battery being charged at $V_{MIN}$ at the beginning of the drought will be the worst-case condition for standby operation and will be used for design purposes. When the system

detects that the input power is no longer enough to charge the battery at 0.25s in Figure 2.5, the power amplifier sends an offline transmission, which discharges $C_B$ quickly by one $E_T$. After that, survival blocks and self-discharge continue to discharge $C_B$ until the drought ends at 7200 s. At 7200 s, the battery voltage $v_B$, nears the headroom voltage $V_{HR}$, which means that a longer drought for this particular design would discharge the battery to a point below where the system could recover from. This means that the battery must be designed such that it holds at least the capacity necessary to remain above $V_{HR}$ for the longest expected drought for its application.

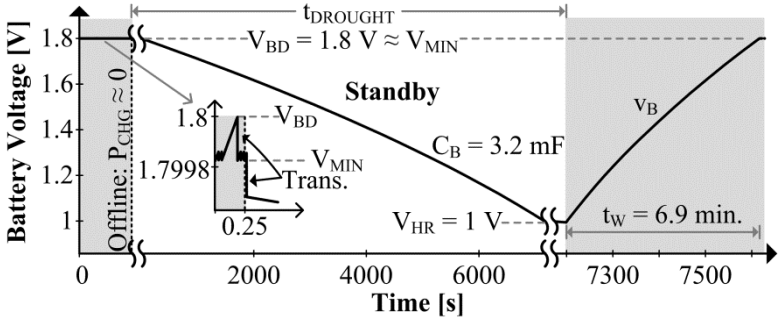


**Figure 2.5. Standby simulation.**

Just before sending an offline report at 0.25 s in Figure 2.5, the battery should store enough energy above $V_{HR}$ to sustain the transmission $E_T$ and supply survival blocks $E_Q$ and the battery's self-leakage $E_{LK}$ across the longest possible drought, which can be hours or longer [139]. In addition, the battery must hold enough energy for the normal operation transmissions, another $E_T$. In order to minimize the space the battery occupies, $v_B$should be at its maximum voltage, $V_{BD,}$ just before a normal operation transmission is sent. Therefore, between $V_{HR}$ and $V_{BD}$, the battery should hold $E_{LK}$ and $E_Q$ for survival, $E_T$ for an offline transmission report, and another $E_T$ for normal operation transmission.

In the case of a super capacitor, its energy is proportional to the capacitance and the square of the voltage:

$$E_B = 0.5 C_B {v_B}^2 \tag{2.2}$$

So to hold $E_{LK}$, $E_Q$, and two $E_T$'s, the battery's capacitance must be:

$$C_B \equiv \frac{2E_T + E_Q + E_{LK}}{0.5\left({V_{T(TH)}}^2 - {V_{HR}}^2\right)} = \frac{2E_T + P_Q T_{DR} + P_{LK} T_{DR}}{0.5\left({V_{BD}}^2 - {V_{HR}}^2\right)}. \tag{2.3}$$

From the values in Table 2.1, $C_B$ can be 3.2 mF when $E_T$ is 1 μJ, $P_Q$ is 0.5 μW, $P_{LK}$ is negligibly lower, $T_{DR}$ is 2 hours, $V_{BD}$ is 1.8 V, and $V_{HR}$ is 1 V. Because of the drought's long duration, $T_{DR}$, $E_Q$ at 3.6 mJ is by far the largest contributor to $C_B$'s size. Since the larger $E_Q$ is stored between $V_{HR}$ and $V_{MIN}$, and the smaller $E_T$ is stored between $V_{MIN}$ and $V_{BD}$, $V_{MIN}$,

$$V_{MIN} = \sqrt{\frac{E_T + P_Q T_{ON} + P_{LK} T_{ON}}{0.5 C_B} + {V_{HR}}^2}. \tag{2.4}$$

will be very close to $V_{BD}$. This is why $v_B$ remains near 1.8 V during transmissions in Figure 2.5.

After the drought, when $v_H$ is back at or above $V_{H(MIN)}$, the central processor enables the charger whose output maintains $v_B$ above $V_{HR}$. The system then waits across wake time $t_W$ until $C_B$ has enough energy

$$0.5 C_B \left({V_{MIN}}^2 - {V_{HR}}^2\right) \tag{2.5}$$

above $V_{HR}$ at $V_{MIN}$ to send an offline transmission and supply survival blocks with $P_Q$ and the battery's self-leakage $P_{LK}$ across another drought. The central processor also waits for $P_{CHG}$ to reach $P_{TH}$ to enable the power supply, and in doing so, brings the system back online. Since the charger delivers a $P_H \eta_{SS}$ portion of $P_H$, where $\eta_{SS}$ is steady-state

efficiency, $v_B$ can reach $V_{MIN}$ in 6.9 minutes when $C_B$ is 3.2 mF, $V_{MIN}$ is 1.8 V, $V_{HR}$ is 1 V, $P_H$ is 10 µW, and $\eta_{SS}$ is 87%:

$$t_W = \frac{0.5C_B\left(V_{MIN}{}^2 - V_{HR}{}^2\right)}{P_{CHG}} = \frac{0.5C_B\left(V_{MIN}{}^2 - V_{HR}{}^2\right)}{P_H\eta_{SS}}. \quad (2.6)$$

### 2.2.2 Sleep

When designed for sleep, the battery is allowed to drain completely during an energy drought. The battery should therefore hold the energy necessary to sustain an offline transmission $E_T$ and supply survival blocks with $P_Q$ and the battery's self-leakage $P_{LK}$ across a transmission period $T_T$. But since the drought can begin just after a transmission starts, the drought could begin one $E_T$ below the battery's maximum capacity. For sleep, however, the transmission time is so short that survival block power consumption and battery self-discharge are negligible. $C_B$ can therefore be 1.8 µF when $E_T$ is 1 µJ, $T_T$ is 1 ms, $P_Q$ is 0.5 µW, $V_{BD}$ is 1.8 V, and $V_{HR}$ is 1 V:

$$C_B \equiv \frac{2E_T + E_Q + E_{LK}}{0.5\left(V_{T(TH)}{}^2 - V_{HR}{}^2\right)} = \frac{2E_T + P_Q T_T + P_{LK} T_T}{0.5\left(V_{BD}{}^2 - V_{HR}{}^2\right)} \approx \frac{2E_T}{0.5\left(V_{BD}{}^2 - V_{HR}{}^2\right)}. \quad (2.7)$$

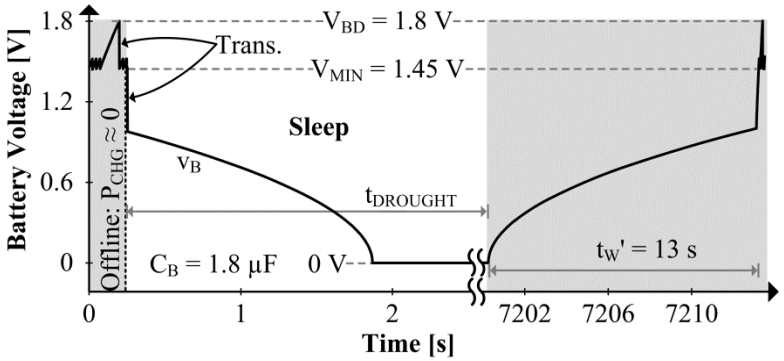


**Figure 2.6. Sleep simulation.**

Like in standby, the central processor enables the charger when $v_H$ is back at or above $V_{H(MIN)}$. When the battery collects the energy for an offline transmission and $P_{CHG}$

surpasses $P_{TH}$, the minimum input power required to charge, the processor enables the power supply and the system. Contrasting with a standby-designed system where $v_B$ remains above $V_{HR}$ throughout the drought, in a sleep system, the battery charges from 0 V, not from $V_{HR}$. This means that initially there is no power, voltage, or energy available from the battery, so the charger must, initially, derive power from $v_H$, which can be so low at 40–500 mV that startup efficiency $\eta_{ST}$ is often less than 0.7% [128], [143], [145].

While the battery voltage, $v_B$, is below $V_{HR}$, the charger operates with efficiency $\eta_{ST}$, and when it surpasses $V_{HR}$, it transfers power with efficiency $\eta_{SS}$. In other words, the charger first delivers a $P_H\eta_{ST}$ fraction of $P_H$ to raise $v_B$ to $V_{HR}$ and then a $P_H\eta_{SS}$ portion to raise $v_B$ to $V_{MIN}$ [145]. So with 1.8 μF, for example, $V_{MIN,}$

$$V_{MIN} = \sqrt{\frac{E_T}{0.5C_B} + {V_{HR}}^2}\,. \tag{2.8}$$

is 1.45 V when $E_T$ is 1 μJ and $V_{HR}$ is 1 V. The wake time for a sleep system, $t_W'$, can therefore be 13 s when $P_H$ is 10 μW, $\eta_{ST}$ is 0.7%, and $\eta_{SS}$ is 87%:

$$t_W' = \frac{0.5C_B{V_{HR}}^2}{P_H\eta_{ST}} + \frac{0.5C_B\left({V_{MIN}}^2 - {V_{HR}}^2\right)}{P_H\eta_{SS}}. \tag{2.9}$$

## 2.3 Temporary Supply

One way to accelerate the wakeup process is to supply the charger with a voltage above its minimum headroom level $V_{HR}$ with a smaller temporary supply $C_T$ [128], [143].To achieve this, $C_T$ is charged quickly above $V_{HR}$ from a low $v_H$ and with $\eta_{ST}$. Even with a low efficiency, the small size of the capacitor still allows for a fast charging time. With $C_T$ supplying the charger with a voltage higher $V_{HR}$, the charger transfers power to the main battery $C_B$ with the much higher efficiency $\eta_{SS}$ and therefore $C_B$ charges faster.

The temporary supply, $C_T$, however, should only feed the charger until the battery reaches $V_{HR}$ because, once $C_B$ reaches $V_{HR}$, the battery can supply the charger.

The purpose of the voltage supply to the charger is to supply gate-drive and quiescent power $P_C$ lost in the controller, which is a $P_H k_C$ portion of the $P_H$ drawn. Across one switching cycle $T_{SW}$, $C_T$ should therefore store this controller energy $E_C$ or $P_C T_{SW}$ above $V_{HR}$:

$$C_T \equiv \frac{E_C}{0.5\left(V_{BD}{}^2 - V_{HR}{}^2\right)} = \frac{P_H k_C T_{SW}}{0.5\left(V_{BD}{}^2 - V_{HR}{}^2\right)}. \tag{2.10}$$

Switch and parasitic series resistances, however, consume another $P_H k_R$ fraction. So of the $P_H - P_H k_R$ delivered, $C_T$ receives $P_H k_C$ and $C_B$ charges with $P_H - P_H k_R - P_H k_C$ or $P_{CB}$. Since $C_T$ is continuously being discharged to supply $P_H k_C$, it must be recharged once it falls to $V_{HR.}$ $v_B$ in Figure 2.7 therefore charges with $P_{CB}$ to $V_{HR}$ in $t_{B(HR)}$, across which time $C_T$ recharges N times:

$$N = \frac{t_{B(HR)}}{T_{SW}} = \frac{0.5 C_B V_{HR}{}^2}{T_{SW} P_{CB}} = \frac{0.5 C_B V_{HR}{}^2}{T_{SW}\left(P_H - P_H k_R - P_H k_C\right)}. \tag{2.11}$$

Unfortunately, resistive, or Ohmic, losses are higher when using $C_T$ because the charger passes more power at $P_H$ than without $C_T$ at $P_H - P_H k_C$, so $\eta_{SS}$ with $C_T$ is $(P_H k_C)k_R/P_H$ or $k_C k_R$ lower: $\eta_{SS} - k_C k_R$.

When first waking with startup efficiency $\eta_{ST}$, however, $C_T$ should charge just high enough above $V_{HR}$ to supply the gate-driver and quiescent losses $E_C$:

$$V_{T1} = \sqrt{\frac{E_C}{0.5 C_T} + V_{HR}{}^2} = \sqrt{\frac{P_H k_C T_{SW}}{0.5 C_T} + V_{HR}{}^2}. \tag{2.12}$$

So when waking, the temporary supply, $C_T$, charges to $V_{T1}$ with $P_H \eta_{ST}$ and the battery, $C_B$, first charges to $V_{HR}$ with $P_{CB}$ or $P_H(\eta_{SS} - k_C k_R)$ and then to $V_{MIN}$ with $P_{CHG}$ or $P_H \eta_{SS}$:

$$t_W'' = \frac{0.5C_T V_{T1}^{\,2}}{P_H \eta_{ST}} + \frac{0.5C_B V_{HR}^{\,2}}{P_H(\eta_{SS} - k_C k_R)} + \frac{0.5C_B\left(V_{MIN}^{\,2} - V_{HR}^{\,2}\right)}{P_H \eta_{SS}}. \qquad (2.13)$$

Following the same example, $C_T$, N, $V_{T1}$, and wake time $t_W$" can be 71 pF, 1040, 1.8 V, and 220 ms when $T_{SW}$ is 100 µs and $k_C$ and $k_R$ in $\eta_{SS}$ are 8% and 5%.

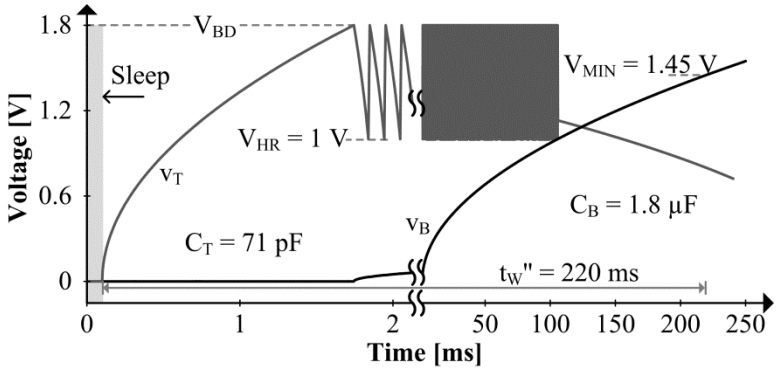


**Figure 2.7. Wake simulation with and without temporary supply $C_T$.**

## 2.4 Design Tradeoffs

Although modern survival circuits consume very little power, they still discharge the battery $C_B$ across long harvesting droughts [146]. Super capacitors suffer more because they have higher self-discharge rates [24]. Unfortunately, keeping $C_B$ charged above the minimum headroom level $V_{HR}$ that circuits need to operate across these outages requires substantial capacitance, and as a result, volume and wake time, as Figure 2.8 states. This is why sleep mode saves space, because while asleep, $C_B$ can drain. This way, $C_B$ and wake time can be 1800× and 1880× lower after a 2-hour drought when allowed to sleep than when kept in standby.

The challenge with sleeping is waking with a drained $C_B$ and a millivolt source. This is because chargers output less than 0.7% of the power drawn when supplied from 40–500-mV [143]. The problem with this is a long wake period. A smaller temporary

battery $C_T$ can help because $C_T$ charges quicker, and with $C_T$'s $v_T$ above $V_{HR}$, the charger is more efficient (at 87% [87]) and therefore faster. This way, $C_T$ delivers the energy lost in the controller. In the example cited, wake time is 59× times shorter with only 0.004% more capacitance for $C_T$.

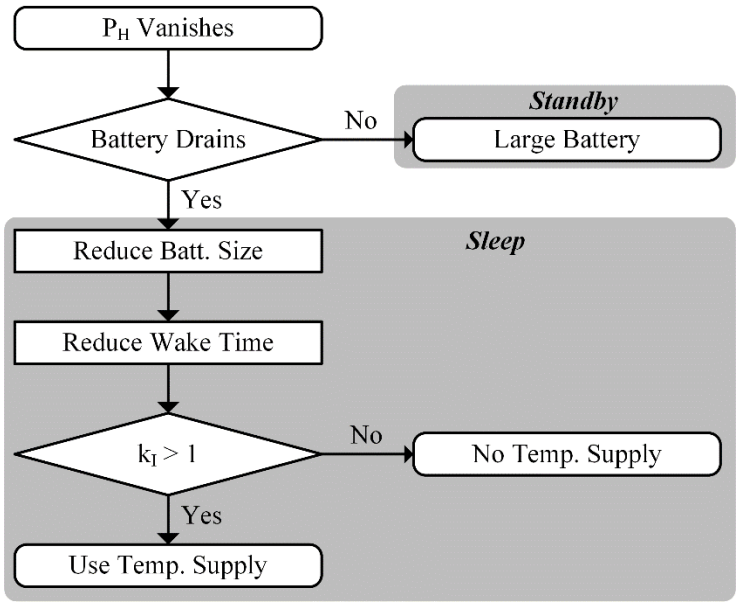


**Figure 2.8. Wake design flow chart.**

In practice, startup efficiency $\eta_{ST}$ determines wake time $t_W'$ without $C_T$, steady-state efficiency $\eta_{SS}$ sets the counterpart $t_W''$ with $C_T$, and $k_C k_R$'s reduction in $t_W''$ is normally insignificant. Wake improvement factor $k_I$ with $C_T$ therefore reduces to

$$k_I \equiv \frac{t_W'}{t_W''} \approx \left(\frac{\eta_{SS}}{\eta_{ST}}\right)\left(\frac{V_{HR}}{V_{MIN}}\right)^2 . \qquad (2.14)$$

In other words, improvement $k_I$ hinges on how much $\eta_{SS}$ overwhelms $\eta_{ST}$ and how little $V_{MIN}$ surpasses $V_{HR}$. Because with lower $\eta_{SS}$, the losses that $C_T$ supplies climb, so $C_B$ receives less power. And with a higher $V_{MIN}$, $C_B$ requires more time to charge. This is

why $C_T$ reduces wake time (i.e., $k_I$ exceeds 1) in Fig. 9 when $\eta_{SS}/\eta_{ST}$ outweighs $(V_{MIN}/V_{HR})^2$ and $k_I$ is 59× in the example cited, which represents a typical case.

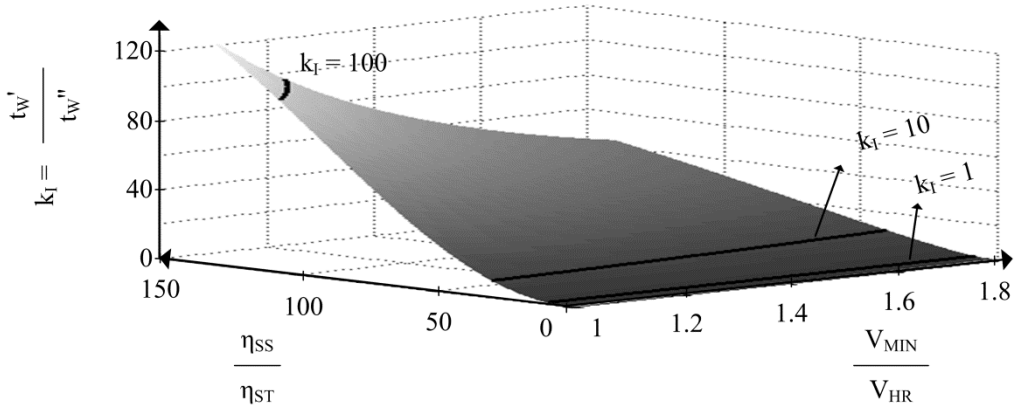


**Figure 2.9. Wake-time improvement factor.**

## 2.5 Summary

To keep onboard batteries small, microsystems should perform only one task at a time, and do so as soon as stored energy is sufficient to sustain a task. This way tasks are distributed across time and are performed in between charging periods. The "just enough" low-energy task schedule algorithm minimizes the size of the required battery by only requiring the battery to store enough charge for one task at any given time. When ambient energy vanishes, the system stops receiving input power and is unable to charge the battery. Therefore, tasks cannot be scheduled and the system must enter either a standby or sleep mode. Designing for a system that goes into standby mode requires that the battery hold enough charge during droughts so that the system can continue operation when the input power returns. Unfortunately, droughts can be so long that this survival battery capacity dominates and dictates the total battery size, leading to larger and costlier systems. Alternatively, a system that goes into sleep mode allows the battery to

completely drain when input power is not present. By removing the need for extra capacity, microsystems that allow sleep reduce battery size by 1800× and wake time by 1880×. Additionally, by using a temporary supply during wake-up, the initial inefficient startup is only applied to a much smaller capacitor, whereas the battery charges with the much higher efficiency steady state charger. With only 0.004% additional capacitance for a temporary supply, the system can wake 59× faster from a no-charge condition. This way, with the low-energy "just-enough" schedule, analytical methods, and design process proposed here, smaller energy-harvesting sensor systems can sustain more events more frequently and recover from harvesting droughts more quickly.

# CHAPTER 3

# LOW-VOLTAGE STARTERS IN THE STATE OF THE ART

Although harvesting energy from the environment can replenish the system battery, the power available by these transducers can be intermittent. Light and thermal energy could disappear for hours at a time. Power hungry components in the microsystem can drain the battery during these energy droughts. When the battery is drained below the system headroom voltage, the system loses its supply. Once the energy source returns, the energy harvester must draw power from the source to re-create a voltage supply. While miniaturized DC energy sources produce tens to hundreds of millivolts, CMOS circuits require higher voltages for proper operation. Therefore, a boosting converter is required to increase the voltage from the energy source to supply the system and charge the battery. However, even these boost converters require a minimum voltage supply to operate. Starter circuits in energy harvesters either allow the converter to transfer energy with low supplies, albeit with low efficiency, or create a temporary supply for the converter while the battery is initially being charged.

During startup, a supply can be created by directly charging the battery [145], [147]-[150] with low efficiency energy transfers. However, because of the relatively large energy capacity of the on-board battery, the time required to charge the battery to a CMOS-compatible voltage is extensive. During the time in which the battery voltage is below the minimum supply of the steady-state power converter, the energy transfer to the battery is low due to both the limited power extracted from the power source and the low efficiency of the startup process. Once the battery reaches the minimum supply voltage,

the harvester extracts higher power levels at high efficiencies [151]. Therefore, for fast startup and high overall efficiency, the energy capacity of the battery should be minimized, which reduces the power available to microsystem.

In order to decouple the power requirements of the battery with the startup restrictions, the starter can instead charge a smaller capacitor, which serves as a temporary supply. Starting up to a smaller capacitor allows for faster startup and creates a supply for the maximum power point charger, which means the battery begins high efficiency charging even when its voltage is below the minimum required supply. Since the startup time is now significantly reduced, the on-board battery can be designed so it is large enough to deliver the necessary power to the system without significantly extending startup. However, state of the art temporary supplies require an additional switched-inductor power converter to charge the startup capacitor [128], [152]. Since the inductor is typically off-chip, the system size is significantly increased.

The challenge in creating a supply with a drained battery is that the voltage available from the energy source is below the minimum supply voltage of a switched inductor boost converter. Therefore, the system requires a low voltage starter that allows the harvester to draw energy and charge the battery. State of the art starters consist of conventional boost converters operating near sub-threshold, replacing the energizing transistor with a mechanical switch, amplifying the input voltage with a transformer, or driving a charge pump with an LC or ring oscillator. While the boost converter offers the best performance in terms of startup time and efficiency, its minimum input voltage is much greater than what a tiny transducer can generate. The transformer starter operates at extremely low voltage, but adds large and costly components to the system. Using a

mechanical switch relies on vibrations, which may not be available or predictable in the system. An LC oscillator also increases the component count and system size, while the ring oscillator starter is limited by the variations in the fabrication process.

## 3.1 Switched-Inductor Boost Converter

Because the voltages produced by tiny DC transducers are below the requirements of CMOS circuit blocks inside a microsystem, a boosting converter must be used to increase the voltage that charges the on-board battery. Boost converters temporarily store energy in inductors or capacitors and transfer the energy through switches to achieve a higher voltage. Although switched-capacitor charge pumps provide high boost ratios at low input voltages, their large number of switches degrades efficiency [153]. Switch inductor boost converters require a higher voltage supply to operate, but can transfer energy at much higher efficiency for a wide boosting ratio. Additionally, once the converter is started, the switched inductor can use its high output voltage to supply its own circuits.

### 3.1.1 Operation

The switched inductor in Figure 3.1 transfers energy by first increasing the current in inductor $L_X$. When $M_E$ turns on, a positive voltage is applied across $L_X$ so the current in the inductor, $i_L$, begins to climb. Once $i_L$ reaches its peak, $M_E$ turns off and $L_X$ continues to conduct into $C_{SW}$ so the switching node, $v_{SW}$, rises. The inductor current will continue to increase as long as a positive voltage is impressed across the inductor. However, when $v_{SW}$ surpasses the input voltage, the voltage across $L_X$ becomes negative and the current begins to fall. When $v_{SW}$ reaches a diode drop, $v_D$, above $v_B$, diode $D_D$

turns on and allows current $i_L$ to flow into $v_B$. Because diodes only conduct in one direction, $D_D$ prevents reverse current out of the battery so it is not discharged by the converter. Since $v_{OUT}$ is greater than $v_I$, the inductor current continues to decrease as $D_D$ conducts and energy is transferred into the output.

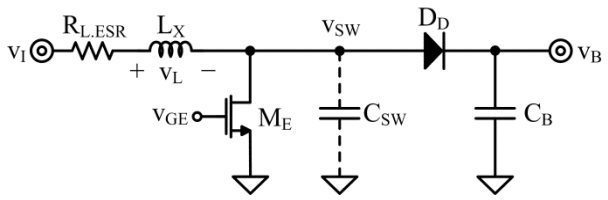


**Figure 3.1. Schematic of switched-inductor boost converter.**

### 3.1.2 Analysis

When a positive voltage, $v_{GE}$, is applied to the gate of transistor $M_E$, $v_{SW}$ is pulled to the ground node, during $t_E$ in Figure 3.2. Since $M_E$ is turned on, a positive voltage across $L_X$ increases its current, $i_L$, with a slope of

$$\frac{di}{dt} = \frac{v_L}{L_X}. \tag{3.1}$$

If $v_{GE}$ is sufficiently above the transistor's threshold voltage, $V_{TH}$, the voltage across $M_E$ is close to zero, so $v_L$ becomes $v_I$. Conducting for a duration of $t_E$, with an inductor voltage $v_L$ close to $v_I$, results in an inductor peak current of $i_{L(PK)}$ at the end of the energizing phase. At this point, the converter has transferred

$$E_L = 0.5 L_X i_{L(PK)}^2 \tag{3.2}$$

of energy into the inductor.

When $v_{GE}$ returns to zero at the end of the energizing phase, the inductor continues to conduct current, but the only component that can conduct current during this time is $C_{SW}$. Once $M_E$ opens, the inductor first transfers energy to $C_{SW}$,

$$E_{C.SW} = 0.5C_{SW}(v_B + v_D)^2, \tag{3.3}$$

until $v_{SW}$ reaches a diode voltage above $v_B$, at which point $D_D$ begins to conduct. The inductor current now begins to flow into the battery and charges $v_B$ during the de-energizing time $t_D$. Once the inductor current is drained, the energy stored in the inductor during the energizing phase is transferred to the battery in addition to the charge flowing out of $v_I$ during $t_D$, so that the total energy transferred to the battery is

$$E_B = 0.5L_X i_{L(PK)}{}^2 + 0.5 i_{L(PK)} v_I t_D. \tag{3.4}$$

After the end of the de-energizing phase, the converter waits until the beginning of the next charging cycle, with period $T_{SW}$, to begin energizing the inductor again.

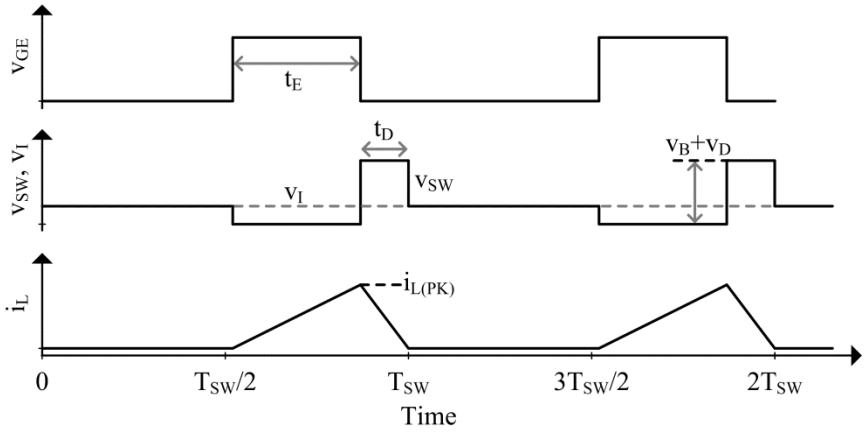


**Figure 3.2. Operational waveforms of boost converter.**

### 3.1.3 Evaluation

If the system battery is initially discharged, the harvester source is the only available voltage to drive $M_E$. However, because tiny transducers produce low voltages, the current capability of $M_E$ is limited. $M_E$ must conduct enough current so that the inductor has enough energy to charge $C_{SW}$ to a diode voltage above the target output voltage. Increasing the width of $M_E$ improves current capability, but also increases $C_{SW}$

producing limited returns. Therefore, the minimum supply of switched-inductor boost converters remains close to the threshold voltage of $M_E$ [154] and lowering the supply requires reductions in the threshold voltage [111]. Unfortunately, reducing the threshold voltage of transistors increases their leakage currents, so that the switches cannot be truly turned off. Therefore, further reductions of threshold voltages do not lead to reductions in minimum supplies.

Nevertheless, boost converters can charge a battery from input voltages as low as 0.6V when the input is the only supply available [155], [156]. At steady-state, when the output voltage is high enough to be used as a supply, the boost converter can operate with input voltages below 20 mV. Furthermore, boost converters can achieve efficiencies as high as 83-87% [87], [154] in steady state with output-to-input voltage ratios between 5 and 50. Although the initial efficiency of a boost converter is low, it can still charge a 500 nF battery to 1.2 V in 4.2 ms from a 0.65 V [154] input source while only using a single inductor.

## 3.2 Motion Activated Switch

To overcome the threshold voltage limitation of a switched-inductor boost converter, the energizing transistor, $M_E$, can be replaced with a mechanical switch. The mechanical switch can be a switch-button operated by a person [157]. However, this type of system would require costly periodic monitoring and maintenance of each wireless microsensor node. If vibrations or other forms of ambient kinetic energy are available to the system, a motion-activated micromechanical switch can replace a pushbutton and energize the power inductor without direct human interaction [128]. Since these vibrations would occur at seemingly random and infrequent time intervals, reliable and

timely startup would be difficult to achieve. Nevertheless, mechanical switches do not have voltage requirements to turn on, so they enable ultra-low voltage startup.

### 3.2.1 Operation

After a prolonged energy drought, in which the system battery completely depletes, the charger in Figure 3.3 cannot operate because $v_B$ is not high enough to switch $M_E$ on and off. When vibrations occur in the system, switch $S_M$ in Figure 3.3 is activated and closes causing $v_H$ to drop across $L_{ST}$ and $R_{ST.ESR}$. A positive voltage across the inductor causes its current $i_L$ to rise while the mechanical switch is closed. However, because of the long duration of vibrations, the inductor current will eventually rise to the point where the voltage drop across the total series resistance will reach the input voltage $v_H$. Since all the voltage will be dropped across the resistors, no voltage will fall across the inductor, and the current will stop rising.

When the vibration causes the mechanical switch to open, the current in the inductor will charge the switching node, $v_{SW}$, until it surpasses a diode voltage above $v_T$, which is initially zero. As the diode conducts, the temporary supply, $C_T$, charges with the energy stored in the inductor, until the inductor completely depletes into $C_T$. If enough energy was transferred to $C_T$, $v_T$ will rise above the minimum voltage required to operate the controller block and the charger. The system then begins charging the battery, $C_B$, from the harvesting source using $L_X$ for the switched-inductor charger.

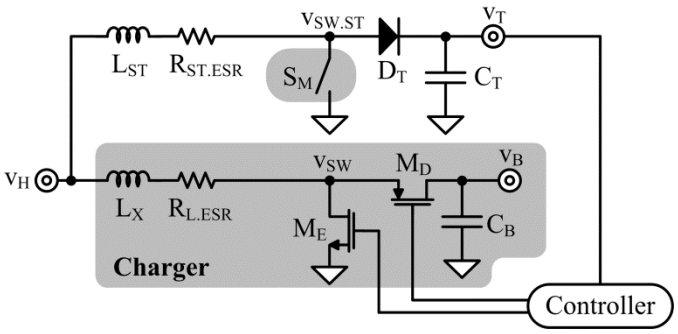


**Figure 3.3. Schematic of motion-assisted starter.**

### 3.2.2 Analysis

When a vibration in the system causes the mechanical switch, $S_M$, to short, a positive voltage, beginning at $v_H$, falls across $L_{ST}$ and $R_{ST.ESR}$. Initially the current through the inductor, $i_L$ in Figure 3.4, is zero, so no voltage falls across the resistance but instead falls across the inductor. However, since the inductor has a positive voltage, its current begins to rise and some of the voltage now falls across the resistance, reducing the inductor voltage. The inductor current continues rising, following a negative exponential function, with its slope reducing with time. Since the vibration period $t_{VIB}$ is much greater than the time constant of $L_X$ and $R_{ESR}$, the inductor current will settle to

$$i_{L(PK)} = \frac{v_I}{R_{TOT}}\left[1 - e^{-\left(R_{TOT}/L_{ST}\right)t_{VIB}}\right] \approx \frac{v_I}{R_{TOT}}, \qquad (3.5)$$

where $R_{TOT}$ is the sum of $R_{ST.ESR}$ and the resistance of $S_M$. The inductor current remains at $i_{L(PK)}$, during $t_{VIB}$ in Figure 3.5, until the vibration allows $S_M$ to disengage. During the second half-period of the vibration, $S_M$ opens and the energy stored in $L_{ST}$ charges the switching node, $v_{SW.ST}$, until it surpasses $v_T$ by a diode voltage, $v_D$.

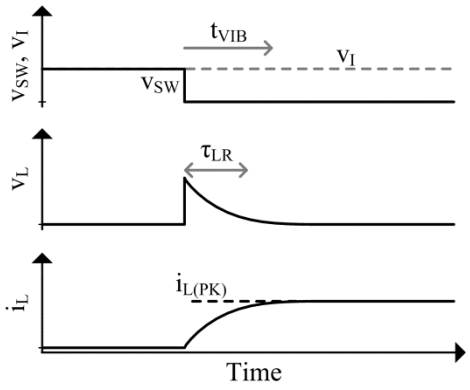


**Figure 3.4. Initial response to mechanical switch closing.**

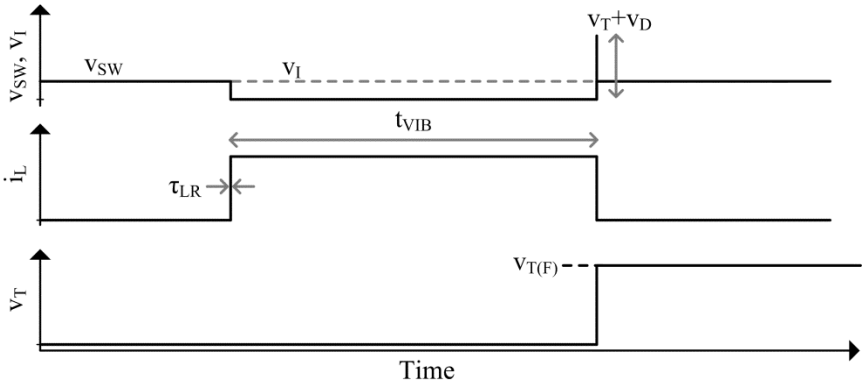


**Figure 3.5. Charging of $C_T$ after complete vibration cycle.**

When $D_T$ turns on, the energy in $L_{ST}$, will transfer to $C_T$ with some energy lost to $D_T$. The energy lost to $D_T$,

$$E_D = Q_D v_D = Q_T v_D = C_T V_{T(F)} v_D \tag{3.6}$$

is proportional to the charge flowing through the diode, $Q_D$, and the voltage dropped across it, $v_D$. Since $D_T$ and $C_T$ are in series, the charge flowing through these components are the same, so the charge flowing into $D_T$ is proportional to $C_T$ and the change in voltage during this time, $v_{T(F)}$. The energy transferred to $C_T$ is therefore

$$E_T \equiv 0.5 C_T v_{T(F)}^{\ 2} = 0.5 L_{ST} i_{L(PK)}^{\ 2} - C_T v_{T(F)} v_D \equiv E_L - E_D . \tag{3.7}$$

Since the inductor current has settled to its peak current at $v_I/R_{TOT}$, the energy transferred

to $C_T$, and therefore its final voltage, is dependent on the input voltage. Therefore, to achieve a required $v_{T(F)}$, the minimum input voltage will be

$$v_{I(MIN)} = R_{TOT}\sqrt{\frac{C_T}{L_{ST}}\left(v_{T(F)}{}^2 + 2v_{T(F)}v_D\right)}. \tag{3.8}$$

### 3.2.3 Evaluation

Replacing a transistor with a motion activated mechanical switch eliminates the threshold voltage requirement of a switched-inductor boost converter. Energizing the inductor with a mechanical switch can reduce the minimum input voltage of the converter to 35 mV [128], charging a 470 pF temporary supply to 1V. Since only one charging event occurs per vibration cycle, charging the battery during startup is not practical because of its larger capacity. Therefore, an extra inductor is required to charge the smaller temporary supply during startup. Adding an additional inductor that only operates during startup is a significant increase in cost and size to the microsystem.

Furthermore, predictable and reliable startup is difficult to achieve with this technology. Since the mechanical switch uses vibrations to transfer energy, the system must wait at least half a vibration cycle for the mechanical switch to close and open. Typical ambient vibrations are in the 50-300 Hz frequency range [158], which translates to a .01-1 s startup time. However, this estimate assumes constant vibrations, particularly during energy droughts that may not be available in all applications. In applications where vibrations are constant and persistent, harvesting kinetic energy may be a more practical solution. Furthermore, if the mechanical switch cannot be turned off during steady state, periodic switching of $S_M$ pulls current from $v_H$, degrading efficiency and input power.

## 3.3 Amplifying Transformer-Based Oscillator

Another method of bypassing the threshold voltage limitations of conventional boost converters is to use a transformer with a large turns ratio. When a voltage is applied to one side of the transformer, a voltage appears on the secondary side equal to the primary voltage times the turns ratio. Therefore, a theoretical transformer could inherently create a boosted version of the input voltage. However, real transformers cannot, on their own, boost DC voltages, since this would imply the current on each side would increase indefinitely. Switches are required on both sides of the transformer so that the voltages across the primary and secondary sides are, on average, zero. Fortunately, integrating the transformer into an oscillator performs both tasks of boosting the input voltage while ensuring the average terminal voltages are zero [148], [149].

### 3.3.1 Operation

A transformer can create a large voltage at its output by amplifying its input voltage by its windings turns ratio, N. Furthermore, incorporating the transformer into a positive feedback loop, as in Figure 4.1, removes the need of a controller, as the feedback causes oscillations and periodic energy transfer to the battery [113], [148], [149], [159]. Depletion mode transistor, $M_{DEP}$, is on initially even with zero volts across its gate and source. With $M_{DEP}$ on, a positive voltage, $v_H$ falls across the primary winding $L_P$ so its current, $i_P$ in Figure 3.6, begins to rise. Because $L_P$ and $L_S$ are magnetically coupled, the current in the secondary side, $i_S$, also begins to rise. As $i_S$ rises and is positive, $v_{OSC}$ and $v_G$ climb, increasing $M_{DEP}$'s gate drive. However, as $v_{OSC}$ continues to climb, the voltage across $L_S$ eventually reverses polarity so that $i_S$ and $i_P$ fall until they too reverse direction.

A negative current at $i_S$ begins to discharge $v_{OSC}$ and $v_G$ until $v_G$ becomes negative and shuts off $M_{DEP}$. $v_{OSC}$ becoming negative again reverses $i_S$'s polarity and current begins to flow out of the secondary side charging $v_{OSC}$ to the positive direction. Eventually $v_{OSC}$ and $v_G$ become positive and turns $M_{DEP}$ back on. This completes a full oscillation cycle that is continually repeated by the circuit.

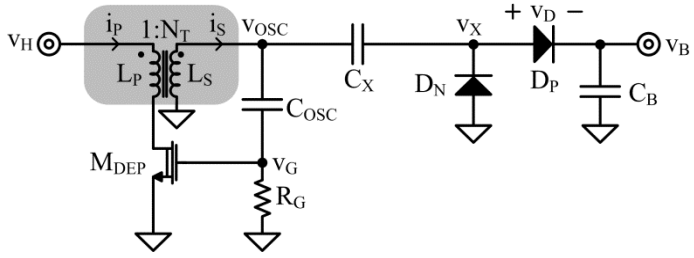


**Figure 3.6. Schematic of amplifying transformer-based oscillator.**

The oscillation at $v_{OSC}$ is a sinusoid that cannot directly charge a battery, which stores a DC, or constant polarity, voltage. Therefore, a rectifying charge pump composed of $C_X$, $D_N$ and $D_P$ is added to the oscillator for charging. When $v_{OSC}$ is negative, $D_N$ turns on and clamps $v_X$ to ground. $C_X$ then stores the negative peak at $v_X$ until $v_{OSC}$ becomes positive. As $v_{OSC}$ climbs, $C_X$ adds the voltage stored to it, so when $v_{OSC}$ reaches its positive peak, $v_X$ reaches twice that amount and charges $C_B$ through $D_P$ up to that voltage. The pre-charge of $C_X$ during the negative half cycle and the addition during the positive half cycle give the charge pump a gain of two which is in addition to the gain provided by the transformer turns ratio.

### 3.3.2 Analysis

The transformer and oscillator create a sinusoid, $v_{OSC}$ in Figure 3.7, with an amplitude of the input voltage times the turn ratio, $N_T$. This amplitude must be enough to turn $M_{DEP}$ on and off. Since $M_{DEP}$'s threshold voltage is negative, any positive voltage

turns the transistor on. However, $v_G$ must go sufficiently negative so that the gate-source voltage is below its threshold voltage. Alternatively, a requirement could be imposed on $M_{DEP}$ such that the absolute value of its threshold voltage is within the expected amplitude of $v_G$. Another requirement for the oscillator is to charge the battery to its target voltage. The output of the starter circuit will be a diode voltage, $v_D$, below the amplified input voltage, so that the minimum input voltage is

$$v_{IN(MIN)} = \frac{v_B + v_D}{2N_T}. \tag{3.9}$$

Therefore, an increase in turns ratio allows further reduction in input voltage. However, larger turns ratio result in physically larger transformers, which impedes integration.

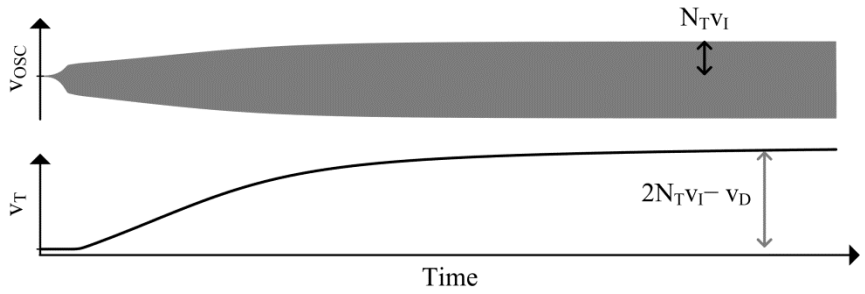


**Figure 3.7. Operational waveform of transformer-based oscillator.**

### 3.3.3 Evaluation

With its inherent turns ratio gain, a transformer can significantly reduce the minimum input voltage of a DC sourced energy harvester. With a turns ratio of 60, a minimum input voltage below 40 mV can be achieved [148], [149]. The transformer can also be reused in steady state to charge the battery with a more efficient configuration, although efficiencies remain close to 40% [149]. Additionally, adding a transformer, especially one with a large turns ratio, greatly increases the size of the system. Although

some volume can be saved by reusing the transformer, its low conversion efficiency when compared to a conventional boost limits its practical applications.

## 3.4 Linear LC Oscillator

An alternative approach to reducing the minimum input voltage of an energy harvester is to first boost the voltage used as gate drive for the switches in the boost converter. Using a similar technique as the amplifying transformer, an oscillation can be created using an inductor and capacitor in the form of an LC tank and regenerating amplifier. Then, a simple charge pump can increase the voltage from the amplitude of the oscillation. Once a higher voltage is achieved, a simple ring oscillator can provide the signal necessary to turn the energizing switch in the boost converter on and off. For faster startup, the LC oscillator drives an auxiliary boost converter to quickly charge a temporary supply that feeds a controller. Although this system would require more components than a transformer based oscillator, the startup circuits do not consume significant amounts of power, so they can be designed for a lower volume when compared with a transformer.

### 3.4.1 Operation

When $v_H$ recovers from an energy drought, the LC oscillator in Figure 3.8 begins to transfer energy between the inductors, $L_P$ and $L_N$, and capacitor $C_{OSC}$. If $v_P$ is higher than $v_N$, $M_N$ will turn on and pull $v_N$ low, turning $M_P$ off. Since $v_N$ is now low, a positive voltage falls across $L_N$, and its current increases, charging $C_{OSC}$. As $C_{OSC}$ charges, $v_N$ begins to rise with respect to $v_P$, until $v_N$ surpasses $v_P$, and $L_N$'s current begins to decrease. When $v_N$ rises past $v_P$, $M_P$ turns off and pulls $v_P$ low, turning $M_N$ off. Like the

first half cycle, $v_P$ being pulled low creates a positive voltage across $L_P$, which causes its current to rise. As its current rises, $L_P$ charges $C_{OSC}$ until $v_P$ surpasses $v_N$ and a new oscillator cycle begins.

Because of the circuit's linear and symmetric operation, the inductors energize and de-energize with amplitude of $v_H$. Therefore, the amplitude of $v_P$ and $v_N$ is also $v_H$. Since the input voltage is too low to directly drive a switch in the boost converter, the amplitude of these signals must be increased. Feeding $v_P$ and $v_N$ into a charge pump before supplying the boost converter increases its level enough to operate a power transistor. After a high voltage is produced by the charge pump, a second oscillator, at the converter switching frequency, drives an energizing switch, $M_{SE}$ in Figure 3.8, in the auxiliary boost converter. $D_T$ provides the de-energizing path that charges $C_T$ and creates a temporary supply for the main charger composed of $L_X$, $M_{CE}$ and $M_D$.

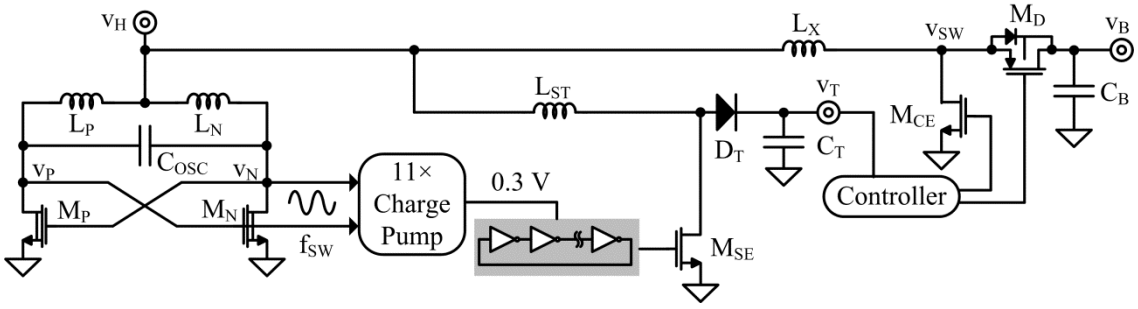


**Figure 3.8. Schematic of linear LC oscillator**

### 3.4.2 Analysis

An LC oscillator can operate as long as the gain of its positive feedback loop remains above one. In Figure 3.8, the cross coupled pair consisting of $M_P$ and $M_N$ provide the positive feedback to the LC tank since they pull whichever node is lower towards ground and provide a high impedance to the higher node, allowing it to go even higher.

At equilibrium, when $v_P$ equals $v_N$, their equivalent impedance is $-1/g_m$. However, the LC tank also adds impedance in parallel to the cross-coupled pair so that the total conductance between $v_P$ and $v_N$ is

$$G_P = sC_{OSC} + \frac{1}{R_{ESR.OSC} + L_{OSC}} - g_m , \tag{3.10}$$

where $L_{OSC}$ is the series combination of $L_P$ and $L_N$ and $R_{ESR.OSC}$ is the equivalent resistance in $L_P$ and $L_N$. For positive feedback, the total conductance, $G_P$, must be negative. This requires

$$g_m > \frac{R_{ESR.OSC}}{R_{ESR.OSC}^{\ 2} + \frac{L_{OSC}}{C_{OSC}}} \approx \frac{R_{ESR.OSC} C_{OSC}}{L_{OSC}} . \tag{3.11}$$

If $M_N$ and $M_P$ operate in the above threshold region, the minimum supply voltage becomes

$$v_{IN(MIN)} = \frac{R_{ESR.OSC} C_{OSC}}{K_N L_{OSC}} + V_{TN} , \tag{3.12}$$

where $K_N$ and $V_{TN}$ are the MOSFET transconductance coefficient and threshold voltage respectively.

Even if the input voltage is high enough for the LC oscillator to operate, the oscillator does not provide gain to the input. The sinusoidal outputs must still be amplified by a charge pump to be used to supply a switched-inductor boost converter. A switched-capacitor charge pump boosts voltages by precharging a capacitor, and then superimposing an additional voltage as in Figure 3.9. The charge pump capacitor $C_C$ is initially charged to $v_I$ with its bottom plate connected to ground. During the second phase, $C_C$'s bottom plate is connected to the input voltage and its top plate is connected to

the output. The result is an output voltage equal to the sum of the precharged capacitor voltage and the input voltage.

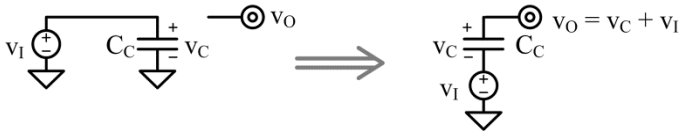


**Figure 3.9. Simplified operation of switched-capacitor charge pump.**

Changing the position of the capacitor requires series switches that must be turned on and off during each phase as in Figure 3.10. Control of these switches requires at least an oscillator and enough gate drive to overcome leakage currents of out-of-phase switches. Fortunately, subthreshold currents increase exponentially, so even a small gate drive produces a current large enough to overcome leakage. Higher order effects such as drain induced barrier lowering (DIBL) cause the leakage current of a transistor to increase with the voltage across it [160], thereby limiting the minimum input voltage of the charge pump to about 100 mV [145], [147]. If the input to the LC oscillator is around 50 mV, the amplitude of $v_P$ and $v_N$ are also 50 mV, but their peak-to-peak voltages are 100 mV, which is enough to drive a charge pump.

The switches in Figure 3.10 implement the same function as was shown in Figure 3.9, but indicate how the top and bottom plates are switched between nodes. During the first phase, switch $S_1$ connects the top plate to the input voltage and $S_4$ connects the bottom plate to ground. While $C_C$ pre-charges to the input voltage, $S_2$ and $S_3$ remain open and block the output voltage. During the second phase, $S_1$ and $S_4$ open, and $S_3$ connects the top plate to the output while $S_2$ connects the bottom plate to the input voltage. The speed at which CC pre-charges and discharges into the output is determined by the

current drive of the switches, which is determined by the gate drive voltage for MOSFET switches.

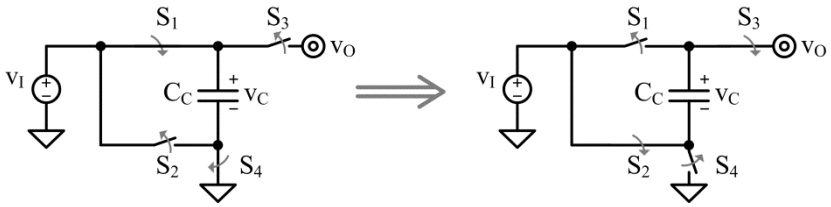


**Figure 3.10. Implementation of voltage doubler with ideal switches.**

Cascaded, low voltage charge pumps, such as the implementation in Figure 3.11, operate by adding several stages in series so that the output of each stage becomes the input to the next. Each stage pre-charges a flying capacitor, $C_{FLYi}$, through a diode or diode-connected transistor, $M_{Di}$, while the bottom plate of the capacitor is grounded using the signal generated by the LC oscillator. During the next phase, the bottom plate of the capacitor is pushed up to the input voltage so that the top plate reaches the pre-charged voltage plus the input voltage and becomes the supply for the next stage. Consecutive stages operate in opposing phases so that while one is pre-charging, the other is discharging into its output. Cascading stages allows for higher output voltages that can better drive power switches. Furthermore, using later stages as supplies to drive the charge pump switches, $M_{Si}$, reduces the voltage drops across the diodes, increasing the voltage gain of the charge pump. Once the charge pump output voltage reaches the minimum supply for the switched-inductor boost converter, the controller enables the converter and begins charging the temporary supply.

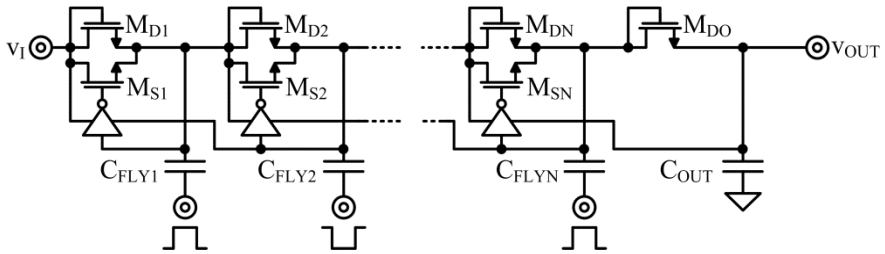


**Figure 3.11. Transistor implementation of low voltage charge pump.**

### 3.4.3 Evaluation

Creating a sine wave with an LC oscillator and then rectifying and boosting the signal through a charge pump can create enough gate drive for a switched inductor power converter to operate from a very low voltage. If native, i.e. zero-threshold, devices are used in the oscillator, the minimum supply can be as low as 50 mV [152]. With just 50 mV at its input, this system can charge a 4.7 nF temporary supply to 0.8 V in 15 ms. However, the LC oscillator requires two inductors and the charge pump supplies an auxiliary converter which requires an inductor in addition to the one used to charge the battery. Although inductors can be much smaller than a transformer, this technology requires three inductors in addition to the inductor in the battery charger.

## 3.5 Ring Oscillator Driven Starter

A simpler, more compact solution to operating a boost converter at low input voltages is to use a digital ring oscillator to create a switching signal that is boosted by a switched-capacitor charge pump. The advantage of a ring oscillator over an LC oscillator is that no external inductors or capacitors are required. Instead, the ring oscillator is composed solely out of CMOS transistors, allowing for a much more compact solution. Similar to the LC oscillator approach, the input voltage feeds the oscillator directly,

which then drives a charge pump. The charge pump need not rectify the signal since the oscillator can be designed to switch near the desired converter switching frequency. Because the oscillator is a simple digital circuit, it suffers from the same limitations as any other digital gate, mainly reduced gain and speed at lower supplies, and sensitivity to mismatches between NMOS and PMOS transistors. Post-processing techniques can reduce the sensitivity by adjusting the threshold voltage of the transistors to correct for variations in the fabrication, although this extra processing step increases the cost of fabrication of the system.

### 3.5.1 Operation

When the input voltage, $v_H$, to the system in Figure 3.12 returns, the ring oscillator begins operation by sending a periodic digital signal to the charge pump. The four-stage charge pump then increases the amplitude of the digital signal, so that when it reaches the gate of $M_{SE}$, its amplitude is enough to switch $M_{SE}$ fully on and off. With the ability to drive $M_{SE}$, the system can then energize the inductor $L_X$ with $M_{SE}$, and de-energize into $C_T$ through $D_D$. As $C_T$ climbs, the body diode of $M_B$ conducts and $v_B$ follows a diode voltage below $v_T$. Once $v_T$ surpasses its target voltage, the controller is enabled and charging continues using $M_{CE}$ and $M_D$ to energize and de-energize the inductor. When the controller is enabled, $M_B$ is turned on so that $v_T$ and $v_B$ are shorted. Further charging is then shared between $C_T$ and $C_B$.

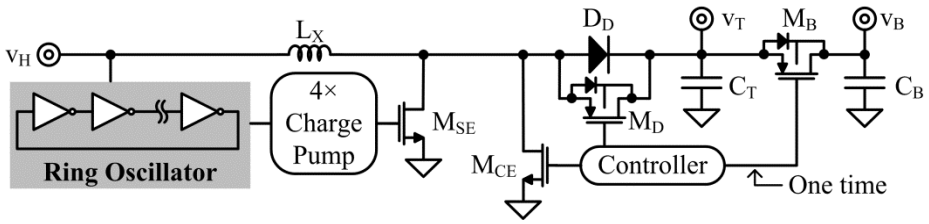


**Figure 3.12. Schematic of ring oscillator driven starter.**

The ring oscillator in Figure 3.12 consists of cascaded stages of digital CMOS inverters. The output of each inverter in the oscillator in Figure 3.13 is connected to the input of the following stage, except for the last inverter whose output returns to the input of the first inverter. To ensure oscillations, the circuit requires an odd number of inverter stages. If the input to the first inverter, $v_{I1}$, is low, its output, $v_{I2}$, is high. Similarly, the input of every odd-numbered stage in the oscillator would be low and their outputs high. Since the oscillator only works for an odd number of total stages, the last stage would also have a low input and a high output. However, since the output of the last stage is the input to the first, the last stage would cause $v_{I1}$ to go from low to high. This transition would then propagate across the stages until $v_{I1}$ flips again. This results in the internal nodes, $v_{I1}$ to $v_{I(N)}$ to toggle between $v_{DD}$ and ground with a period equal to twice the total propagation delay across all the stages, since the signals must transition from high to low and then from low to high to complete one cycle.

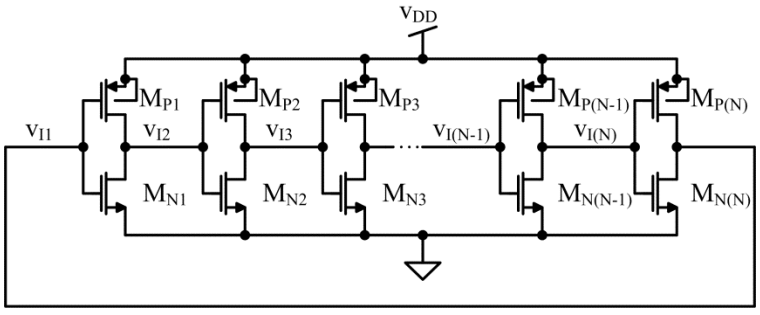


**Figure 3.13. Schematic of CMOS ring oscillator.**

### 3.5.2 Analysis

The minimum supply of a ring oscillator driven system will be determined by the oscillator. Since the oscillator is composed cascaded CMOS inverter stages, it will operate correctly as long as each individual inverter has enough voltage headroom. By operating in the subthreshold regime, the supply voltage of an inverter can be below the transistor threshold voltage. Since the transistors operate in weak inversion, their drain current follows an exponential relationship with respect to input voltage, beginning at its leakage current,

$$I_{OFF} = \mu_n C_{OX} \phi_T^{\,2} \frac{W}{L} \frac{1-\kappa_n}{\kappa_n} e^{\left(-\kappa_n V_{TH} / \phi_T\right)}, \tag{3.13}$$

and increases with gate voltage:

$$I_D = I_{OFF} e^{\kappa_n V_{GS} / \phi_T} \left(1 - e^{-V_{DS} / \phi_T}\right) \tag{3.14}$$

The leakage current $I_{OFF}$ is a function of mobility ($\mu_n$), oxide capacitance ($C_{OX}$), thermal voltage ($\phi_T$), transistor width (W), length (L), threshold voltage ($V_{TH}$), and capacitive-divider coefficient ($\kappa_n$). Drain current, $I_{D,}$ increases with gate-source ($v_{GS}$) and drain-source ($v_{DS}$) voltages.

For digital gates, signal amplification or restoration occurs when the gain across the circuit is greater than one. As a signal is passed through cascaded gates, the signal is amplified by each gate according to their gain. If the gain is less than one, the signal will be attenuated and possibly lost. Therefore, the supply voltage must be enough so that gain of each stage remains above one. For each stage in the ring oscillator, the inverter in Figure 3.14 has gain

$$A_{INV} = \frac{\partial v_o}{\partial v_{in}} = \frac{\partial i_o}{\partial v_{in}} \frac{\partial v_o}{\partial i_o} = \left(g_{mn} + g_{mp}\right)\left(\frac{1}{g_{dsn} + g_{dsn}}\right) \tag{3.15}$$

where $g_{mn}$ and $g_{mp}$ are the transconductances for $M_N$ and $M_P$ respectively and $g_{dsn}$ and $g_{dsp}$ are the output conductances of $M_N$ and $M_P$ respectively.

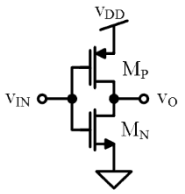


**Figure 3.14. Schematic of CMOS inverter circuit.**

The transconductance of a transistor is defined as the change in output current for a given change in input voltage, which for an NMOS in the subthreshold region is given by

$$g_{mn} = \frac{\partial i_{dn}}{\partial v_{in}} = \frac{\kappa_n}{\phi_T} I_{OFFN} e^{\kappa_n V_{IN} / \phi_T}\left(1 - e^{-V_O/\phi_T}\right). \tag{3.16}$$

The transconductance of a PMOS transistor is given by (3.16), substituting the appropriate subscripts to reflect PMOS parameters. Similarly, the output conductance

$$g_{dsn} = \frac{\partial i_{dn}}{\partial v_o} = \frac{1}{\phi_T} I_{OFFN} e^{\kappa_n V_{IN} / \phi_T} e^{-V_O/\phi_T} \tag{3.17}$$

expresses the change in output current with respect to output voltage. Substituting (3.16) and (3.17) into (3.15) and setting $V_{IN}$ and $V_O$ to half of the supply voltage (where the gain is maximum) produces the gain of the inverter:

$$A_{INV} = \left(\frac{\kappa_n + \kappa_p}{2}\right)\frac{1 - e^{-V_{DD}/2\phi_T}}{e^{-V_{DD}/2\phi_T}}. \tag{3.18}$$

Reducing the supply voltage increases the output conductance of both transistors, which

causes an overall decrease in gain. Figure 3.15 plots the simulated transfer function of an inverter for various values of supply voltage, $v_{DD,}$ with the axes normalized to the supply voltage. Setting the gain from Equation (3.18) equal to one and solving for $v_{DD}$, reveals a minimum supply voltage of

$$v_{DD(MIN)} = 2\phi_T \ln\left(\frac{\kappa_n + \kappa_p + 2}{\kappa_n + \kappa_p}\right). \tag{3.19}$$

For an ideal MOSFET, where κ is one, $v_{DD(MIN)}$ is $1.4\phi_T$, or about 36 mV at room temperature [129], [130]. However, this value does not consider process variations, specifically asymmetry between the NMOS and PMOS transistors. Any asymmetry moves the inverter away from the assumed maximum-gain bias point of half the supply voltage, essentially shifting the plots in Figure 3.15 to the left or the right so that the high gain region occurs outside of the maximum voltage, $v_{DD}$. Assuming a standard deviation of the threshold voltage of 32 mV for each type of transistor, the minimum supply increases to 250 mV [129]-[133]. For voltages lower than 250 mV, there is no guarantee that the inverter will produce gain greater than one.

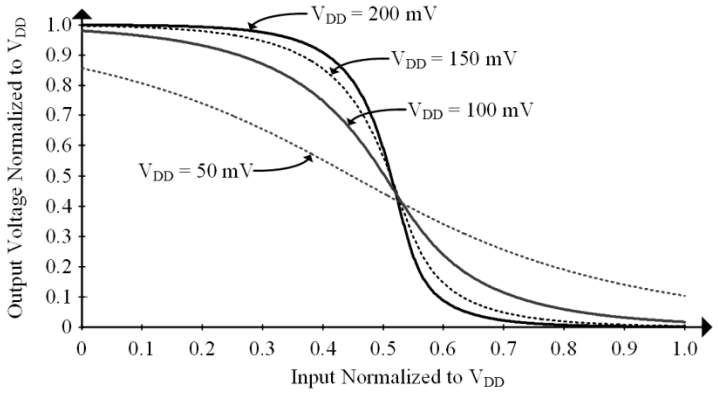


**Figure 3.15. Transfer function of inverter for various supply voltages normalized to $V_{DD}$.**

Since assymetries in inverters due to statistical variations in fabricaton processed dictate the minimum supply voltage of a ring oscillator, reducing or eliminating the asymmetry would allow for lower voltage operation. However, creating more predictable or less varying fabrication processes is impractical since no process is completely repeatable. Fortunately, after the circuit is fabricated, the threshold voltages of the transistors can be altered to make the inverters more symmetric. By applying a high voltage, $v_{PROG}$ in Figure 3.16, to the body of the PMOS in the inverter, positive charges are injected into the oxide of $M_P$ [147]. These injected charges remain trapped in the gate oxide and permanently increase the threshold voltage.

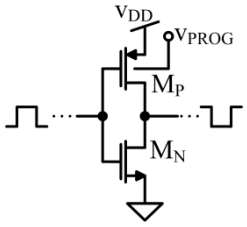


**Figure 3.16. Threshold voltage programming of ring oscillator inverter.**

By increasing the PMOS threshold voltage until the PMOS drive matches the NMOS drive, the asymmetries can be minimized so that the minimum input voltage is reduced. If a triple-well process is used, where the body of the NMOS transistors need not be the chip substrate, the NMOS threshold voltage can also be altered. If an additional well is not available, the PMOS must be designed to be systematically stronger than the NMOS, so that the programming reduces the PMOS strength to match the NMOS. In steady state operation, the body of the PMOS should be connected to the supply voltage, and the body of the NMOS should be connected to ground. Finally, since the input voltage is reduced, the signal that drives the charge pump is reduced, so more stages are required inside the charge pump. In addition to requiring a higher voltage ratio,

since the driving signal in the charge pump is lower, switches do not completely turn on and off, and significant voltage is dropped across the switches. Therefore, the threshold-adjusted system in Figure 3.17 requires a thirty-stage charge pump even though the gain across it is less than thirty [145].

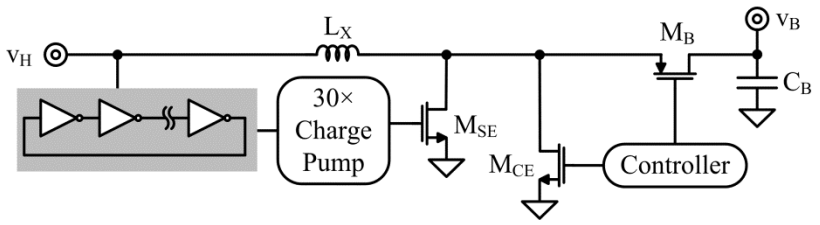


**Figure 3.17. Schematic of threshold adjusted ring oscillator driven starter.**

### 3.5.3 Evaluation

Ring oscillators operating at low supply voltages can drive switched-capacitor charge pumps to boost input voltages. Since the oscillator consists of a chain of inverters, the minimum operating supply voltage is the same for an inverter. Considering process variations, the minimum supply of a ring oscillator is limited to 200-300 mV [129]-[133]. Post fabrication threshold tuning can be applied to each inverter in the oscillator to compensate for die-to-die process variations, reducing the supply voltage to 80-95 mV [145], [147]. However, post fabrication tuning can be expensive, since it adds testing time to each integrated circuit. With each IC requiring around 60 minutes for a 34% decrease in supply voltage, a significant cost is added to the system with limited benefits. Additionally, since the second stage of the system, a charge pump, operates in the subthreshold region, the current drive capability is small, so charging is inefficient and slow. Once a supply voltage is created, however, the system can supply a switched-inductor boost converter, which can charge the battery more efficiently.

## 3.6 Comparison

Low voltage starters in the state of the art aim to reduce the minimum input voltage of energy harvesting boost converters. While switched-inductor boost converters are limited by the threshold voltage its power switches, once a high supply is available, they provide the highest efficiency and integration of all technologies. Replacing a power switch in the converter with a mechanical switch removes the threshold voltage limitation, but adds a requirement that a human physically presses a button to reset the system. Alternatively, a motion-activated microelectromechanical (MEMS) switch can be used to make the system completely autonomous from human interaction. However, the MEMS switch requires vibrations to occur periodically and consistently after an energy drought, which is not practical in many applications. An amplifying transformer inherently boosts the input voltage by its turns ratio, so it produces one of the lowest startup voltage. However, adding a bulky transformer is contrary to the goal of minimizing system size for ubiquity. An LC oscillator starter also operates from low voltages, but requires three additional off-chip inductors that are used during startup only. Finally, a charge-pumped ring oscillator driving a boost converter is limited by process variations, so reducing the minimum supply requires costly post-fabrication tuning.

Table 3.1 quantifies the comparison among the state of the art starter circuits. As expected, a conventional boost converter requires the highest input voltage, but charges its output capacitor with the highest equivalent current, $I_{EQ}$. The equivalent current, $I_{EQ}$, is defined here as the average current required from each technology to charge its output capacitor, $C_T$ to its target voltage, $v_{TAR}$ within startup time, $t_{ST}$. Technologies that allow for an ultra-low input voltage, i.e. transformer, MEMS switch, and LC oscillator, require

bulky and costly extra components and, in the case of the MEMS switch, an external force in the form of vibrations. Of these, the transformer offers the highest $I_{EQ}$, but its expected size is also the largest of the technologies. Although threshold tuned ring oscillators can operate as low as 80 mV, its extensive and expensive post-processing adjustment makes the system impractical, and with an $I_{EQ}$ of only 8 nA is also the slowest technology. Finally, the most compact solution, the natural ring oscillator, is limited to 330 mV and although the output capacitor, $C_T$ is not reported, $I_{EQ}$ is expected to be low since the charge pump in the system operates in the subthreshold region, which means its current capability will be low.

**Table 3.1. Comparison of low-voltage starters in the state of the art.**

| ` | **Boost Converter [154]** | **X-Former [149]** | **MEMS Switch [128]** | **LC Osc. [152]** | **Ring Oscillator** | |
|---|---|---|---|---|---|---|
| | | | | | **Tuned [145]** | **Natural [150]** |
| **$V_{H(MIN)}$** | 0.65 | 40 mV | 35 mV | 50 mV | 80 mV | 330 mV |
| **$C_T$** | 500 nF | 10 nF | 470 pF | 4.7 nF | 30 pF | – |
| **$V_{TAR}$** | 1.2 V | 1.2 V | 1 V | 0.8 V | 1.3 V | 1.8 V |
| **$t_{ST}$** | 4.2 ms | 4.9 ms | 3 ms | 15 ms | 4.8 ms | 1.2 s |
| **$I_{EQ}$** | 143 µA | 2.45 µA | 157 nA | 251 nA | 8 nA | – |
| **Magnetics** | 4.7 µH | 1:60 X-Former | 22 µH<br>22 µH<br>MEMS<br>Switch | 2 µH<br>2 µH<br>100 µH<br>27 µH | 6.8 µH | – |
| **Volume** | **4 $mm^3$ | 175 $mm^3$ | 150 $mm^3$ | **16 $mm^3$ | **4 $mm^3$ | 4 $mm^3$ |
| **Technology** | 0.35 µm | 0.13 µm | 0.35 µm | 65 nm | 65 nm | – |

## 3.7 Summary

Starter circuits in the state of the art are able to wake microsystems from voltages as low as 35 mV. However, to achieve such low voltages, bulky components, such as a transformer, or relying on external vibrations are required. In wireless microsystems, system size is of critical importance and adding large components for startup is impractical. Relying on vibrations is risky, since many applications will not have dependable or periodic sources of kinetic energy, and those that do, might be better served harvesting kinetic energy instead. Reductions on the minimum supply can also be made by using post processing adjustments, but these are time consuming and expensive. Furthermore, startup, as achieved by the state of the art, is either slow, because they aim to charge the battery directly with an inefficient converter, or large since they charge a smaller temporary supply with an additional boost converter. Therefore, an ideal startup circuit adds no external components to the system, charges a temporary supply for fast wake, and only uses components found in modern CMOS processes.

# CHAPTER 4

# NONLINEAR LC-OSCILLATING CMOS STARTER

State of the art starters operating from low input voltages increase the system cost by adding large off-chip components or requiring post-fabrication tuning. The proposed low-voltage starter re-uses the inductor of the battery charger to charge a startup capacitor that acts as a temporary supply while the battery is discharged. Minimizing extra components used for startup reduces the impact of the circuit on the system while the use of a temporary supply allows for fast and efficient charging of the battery. Charging the high energy-density battery from no-charge conditions without a temporary supply becomes impractical in an energy harvesting system, since the starter draws only a fraction of the power available to the harvester. Instead, charging a smaller, temporary supply provides the voltage necessary for high efficiency energy transfer quickly. Using a temporary supply allows the energy harvester to charge the battery from no-charge conditions in the minimum amount of time.

## 4.1 Operation

The proposed system in Figure 4.1 starts from the low voltage available in $v_H$ and charges $C_T$ to be used as a temporary supply for the controller. Using the voltage and power available from $v_T$, the controller drives switches $S_B$ and $S_E$ to charge the system battery $C_B$. During steady state or battery charging mode, the controller turns off the starter through $v_{OFF}$ and monitors $v_T$ to ensure that the minimum voltage requirement is maintained. While the controller block is not operational during startup, $S_E$ and $S_B$ must

be turned off so that the battery does not steal energy from $C_T$. Therefore, the controller ensures that the gate drive signals keep the switches off until the supply is ready. Using NMOS transistors allows the switches to be turned off with zero volts. However, an NMOS implementation for $S_B$ requires a boosted gate drive when charging the battery, since its gate must be at least a threshold voltage above the battery. PMOS transistors do not require a higher voltage to be turned on, but applying zero volts to its gate will cause the switch to turn on during startup.

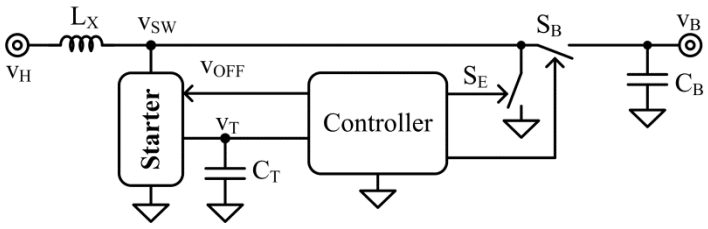


**Figure 4.1. Proposed harvester system with starter and temporary supply.**

The starter in Figure 4.2 re-uses the battery charging inductor $L_X$ to oscillate and rectify energy from the input voltage, $v_H$, to charge $C_T$ when no voltage is initially available at $v_T$ or $v_B$. Transistor $M_{SEN}$ is used to ground $v_{SW}$ to create a positive voltage across $L_X$. The higher the inductor voltage, $v_L$, the higher the inductor's current, $i_L$, will reach. The maximum voltage that can be applied across $L_X$ is $v_H$ and can only occur when $v_{SW}$ is zero. However, $M_{SEN}$'s resistance will limit how low $v_{SW}$ can go. Therefore, $M_{SEN}$ must have a low on-resistance to maximize the current and energy that can be stored in the inductor. To that end, $M_{SEN}$'s gate is connected to the maximum available voltage before startup, $v_H$, and a low threshold voltage transistor is used. Other transistors in the circuits can have low threshold voltages, but reducing their thresholds will have a smaller effect on the starter's overall performance.

The role of $M_{PD}$ and $M_{PO}$ is to rectify the oscillating node $v_{SW}$. When $v_{SW}$ rises above $v_T$, $M_{PD}$ and $M_{PO}$ turn on and conduct current into $v_T$ to charge $C_T$. $M_{PLDY}$, $R_{DLY}$, $R_G$, and $M_{NR}$ create the positive feedback necessary to sustain oscillations. Since $M_{NR}$'s gate, $v_{DLY}$ is derived from $v_{SW}$, which is initially low, $S_{PoR}$ must initialize the circuit so that $v_E$ is initially zero and $M_{SEN}$ is on. $S_{PoR}$ is only needed during the first cycle, since once the starter begins oscillations, $M_{NR}$ functionally replaces $S_{PoR}$. Once enough oscillations have charged $C_T$ so that $v_T$ passes its target, the controller turns off the starter by applying the $v_{OFF}$ signal to $M_{OFF}$'s gate, preventing $M_{NR}$ from turning on. Once the starter is on, $S_E$ and $S_B$ form a high efficiency boost converter that can charge $C_B$ from $v_H$.

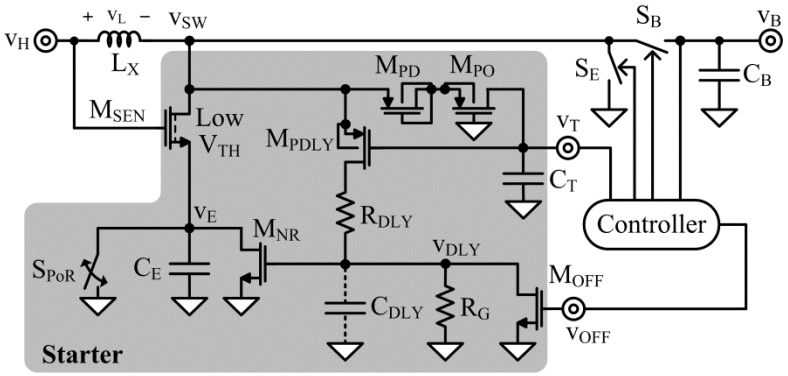


**Figure 4.2. Schematic of harvester system.**

### 4.1.1 Starter

The starter circuit begins operation when the power-on-reset switch in Figure 4.3a is closed to reset $C_E$. With $v_E$ at zero volts, $M_{SEN}$'s $v_{GS}$ voltage becomes $v_H$, which, if above its threshold voltage, is enough to turn the transistor on. Once $M_{SEN}$ is on, it pulls $v_{SW}$ towards ground which creates a positive voltage across $L_X$. The positive voltage causes $i_L$ to rise and consequently, the inductor current charges $C_E$ until $v_E$ reaches $v_{E(PK)}$ in Figure

4.4, around 0.13 µs. $v_{E(PK)}$ corresponds to the voltage at $v_E$, at which the starter can no longer energize $L_X$. Specifically, as $v_E$ rises, $M_{SEN}$'s gate-source voltage reduces, until $M_{SEN}$ can no longer conduct $i_L$, which occurs when $v_E$ reaches $v_{E(PK)}$. Since $M_{SEN}$'s gate voltage is $v_H$, $v_{E(PK)}$ is around a threshold voltage below $v_H$. When $v_E$ reaches its peak, $i_L$ stops increasing and reaches $i_{LPK(0)}$, in Figure 4.4.

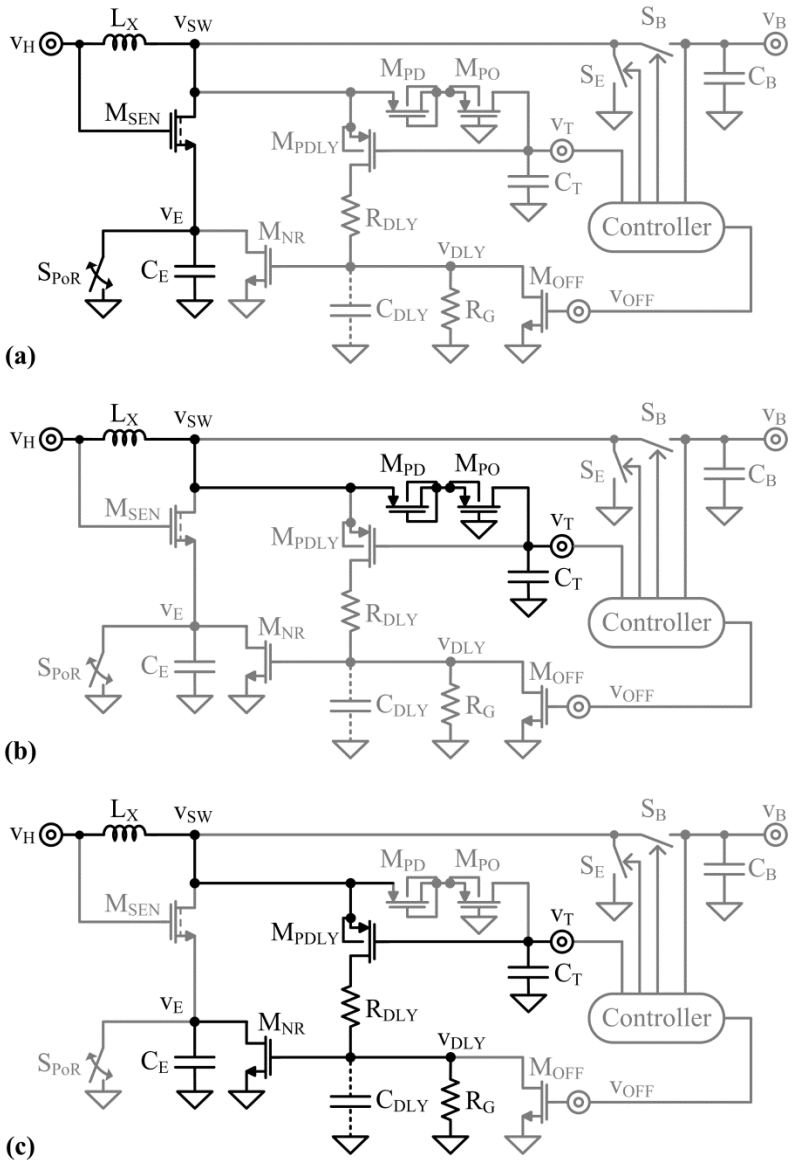


**Figure 4.3. Operation of switched-inductor starter circuit throughout the (a) energizing phase, (b) de-energizing phase, and (c) reset phase.**

Once $v_E$ reaches a threshold voltage below $v_H$, $M_{SEN}$ turns off so it cannot conduct $i_L$. The inductor current instead begins charging the parasitic capacitance in node $v_{SW}$. As the capacitance charges, $v_{SW}$ rises above $v_H$, creating a negative voltage across the inductor. With a negative voltage, the inductor's current begins to decrease just after reaching its peak, $i_{L(PK0)}$ in Figure 4.4. As $v_{SW}$ continues to rise, transistors $M_{PD}$ and $M_{PO}$ in Figure 4.3b begin to turn on. Since $M_{PO}$'s gate is connected to ground, it requires its gate voltage to rise a threshold voltage, $V_{TP}$, above ground to turn on. $M_{PD}$'s gate is connected to its drain, which means it requires its source, $v_{SW}$, to climb above its drain by another threshold voltage. By requiring $M_{PD}$'s source voltage to climb above $v_T$, current is only allowed to flow into $C_T$, thus preventing reverse discharge. In all, $v_{SW}$ needs to rise above $2V_{TP}$, with respect to ground, during the first cycle before $M_{PD}$ and $M_{PO}$ turn on. In later cycles, when $v_T$ is above a $V_{TP}$, $M_{PO}$'s source voltage will automatically be at least a threshold voltage above its gate, so $v_{SW}$ need only rise a $V_{TP}$ (from $M_{PD}$) above $v_T$ to turn on $M_{PD}$ and $M_{PO}$. Once the transistors begin conducting, energy from $L_X$ is transferred to $C_T$ and $v_T$ rises.

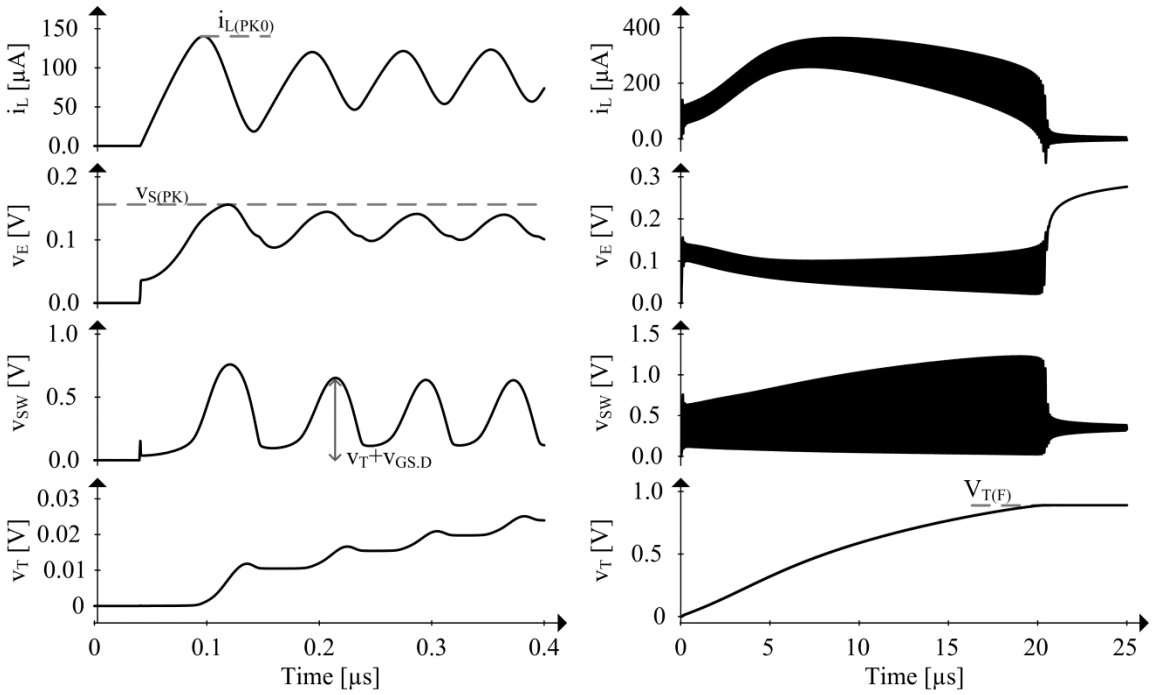


**Figure 4.4. Operational waveforms of starter circuit.**

While $M_{PD}$ and $M_{PO}$ conduct, $v_{SW}$ is at least a threshold voltage above $v_T$. Since $M_{PDLY}$'s gate voltage is $v_T$ and its source voltage is $v_{SW}$, its gate-source voltage is above its threshold voltage, so it also conducts. $M_{PDLY}$ begins to charge $v_{DLY}$ through $R_{DLY}$ as shown in Figure 4.3c. As $v_{DLY}$ rises, $M_{NR}$ turns on and discharges $C_E$, bringing $v_E$ and $v_{SW}$ low so that $M_{SEN}$ turns on again beginning another energizing event. Since $v_{DLY}$ is charged through $R_{DLY}$ and $C_{DLY}$ adds capacitance to the node, $v_{DLY}$ only charges after a time delay. This delay allows some of the inductor energy to transfer to $C_T$ before $C_E$ is reset. While $C_E$ is being discharged, and then while $L_X$ energizes, $R_G$ partially discharges $v_{DLY}$ so that $M_{NR}$ turns off and allows $L_X$ to charge $C_E$.

As oscillations continue, $C_T$ charges and $v_T$ rises. However, as $v_T$ continues to increase, the inductor current falls faster during de-energizing since the voltage across it becomes larger. On the other hand, the energizing events change very little since the positive voltage applied across the inductor is, at maximum, $v_H$, which does not change

during startup. Eventually, the inductor loses more energy to $C_{SW}$, during the de-energizing phase than what it gains during the energizing phase. After this point, $C_T$ no longer receives energy, so $v_T$ remains at $V_{T(F)}$. Since $M_{PD}$ and $M_{PO}$ no longer turn on, $M_{PDLY1}$ and $M_{PDLY2}$ also remain off so that $v_E$ is no longer reset and oscillations stop.

### 4.1.2 Battery Charger

Once $v_T$ reaches the controller's minimum supply voltage requirement, the system can deactivate the starter by turning $M_{OFF}$ on. By shorting $v_{OFF}$ to ground, further oscillations are stopped since $M_{NR}$ can no longer turn on to reset $C_E$. With the starter off, the controller in Figure 4.5 can control $S_E$ and $S_B$ to transfer energy from $v_H$ to $v_B$. By turning on $S_E$, a positive voltage, $v_H$, is applied across $L_X$ so that the inductor current increases until it reaches $i_{L(PK)}$. Because the gate drive to $S_E$ is much higher than $M_{SEN}$'s gate drive during startup, the inductor can energize to a higher current more efficiently.

After $i_L$ reaches its peak, $S_E$ is turned off, and $L_X$ charges $v_{SW}$'s parasitic capacitance until $v_{SW}$ surpasses $v_B$ and $S_B$ is turned on. With $S_B$ on, the inductor de-energizes into $v_B$ and charges $C_B$. Since the controller and gate drivers of $S_E$ and $S_B$ draw current from its supply, $v_T$, $C_T$ discharges as the charger operates. Therefore, when $v_T$ is discharged below a threshold, around 1 V in Figure 4.6, the controller sends an energy packet during $t_{CH.T}$ to $C_T$ by energizing through $S_E$, but de-energizing through $M_{PD}$ and $M_{PO}$ by not engaging $S_B$. This keeps $v_T$ high enough to continually operate the controller and battery charger. Once $v_T$ reaches its threshold requirement, battery charging resumes during $t_{CH.BAT}$ in Figure 4.6.

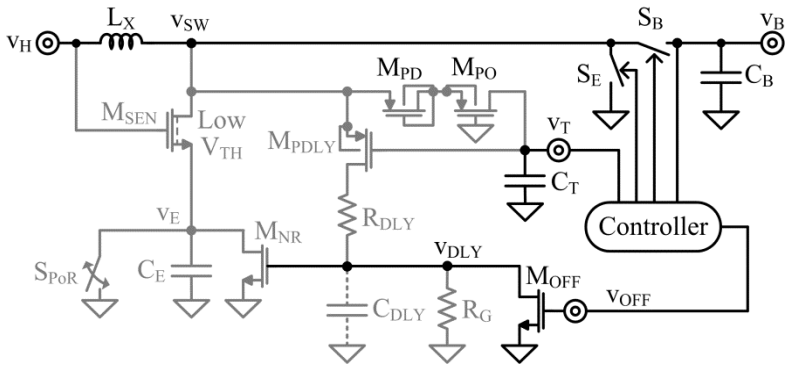


**Figure 4.5. Operation of switched-inductor battery charger.**

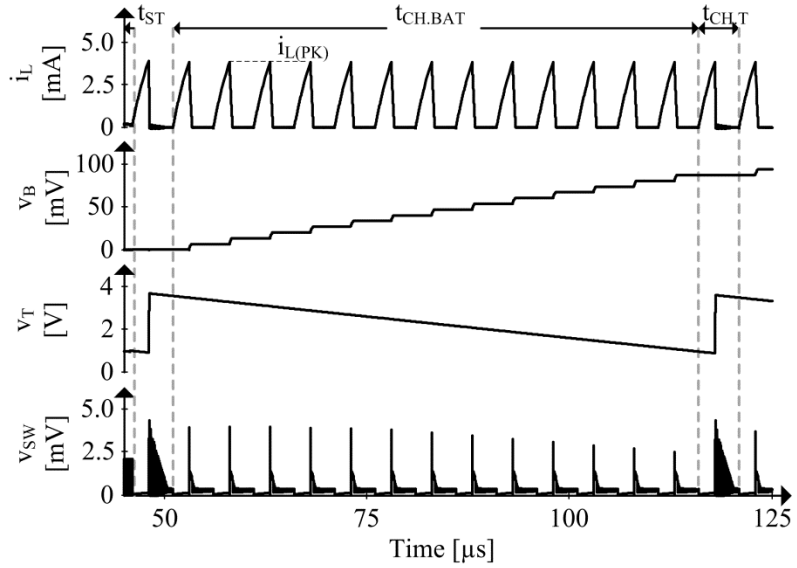


**Figure 4.6. Simluated steady-state waveforms of the harvester.**

## 4.2 Integrated Circuit Design

Since decreasing the size of microsystems increases their application space, it is of critical importance that component of the microsystem is miniaturized and integrated. Since discrete components are much larger than integrated devices, the proposed oscillating starter was designed in a 180-nm CMOS process to ensure an overall small system size. The key design goal for the starter is ensuring oscillations, while maintaining a low minimum input voltage. The minimum input voltage must also take into account

that $v_T$ must charge to its target voltage, which is high enough to supply a system controller. The power switches, $S_E$ and $S_B$ in Figure 4.5, were also designed in the design in the CMOS process. When enabled, the switches must be able to transfer power to the battery, $C_B$, efficiently. Both the starter and battery charger must be designed with the constraint that all off-chip components, including the inductor and the battery itself, must maintain a small form factor, to not significantly increase the system size.

### 4.2.1 Starter

The starter begins oscillating cycles with $L_X$ being energized through $M_{SEN}$. In order for $M_{SEN}$ to conduct, its gate-source voltage must be above its threshold voltage. During the energizing phase, its gate is at $v_H$ and its source, $v_E$, is approximately zero, so $M_{SEN}$'s threshold voltage must be below $v_H$. To drive current into $C_T$, the inductor current $i_L$ must surpass $M_{SEN}$'s drain current. This means $v_E$ must rise enough so that $M_{SEN}$'s gate drive reduces to the point where it can no longer sustain $L_X$'s current. This occurs when $v_E$ rises to $v_H$–$V_{TN}$. The period between when $v_E$ is at its minimum until it rises enough to close $M_{SEN}$ is determined by how long it takes for $C_E$ and $C_{SW}$ to charge through $L_X$, which can be approximated as a quarter period of an LC tank. A quarter LC period corresponds to the time it takes for the energy in the inductor to transfer to the capacitor, so that energizing time is approximately

$$t_E \approx \frac{t_{LC}}{4} = \frac{2\pi}{4}\sqrt{L_X\left(C_E + C_{SW}\right)}. \tag{4.1}$$

During the energizing phase, the inductor receives energy from the harvesting source, but loses energy to $C_E$, $M_{SEN}$, switching node capacitance $C_{SW}$. The inductor charges $C_E$ to $v_{E(PK)}$ to complete the energizing phase, and, in doing so, loses

$$E_{E(E)} = 0.5C_E v_{E(PK)}^{\ 2} = 0.5C_E(v_H - V_{TN})^2 . \quad (4.2)$$

Furthermore, after the energizing phase is complete, $C_{SW}$ must be charged to $|2V_{TP}|$ so that the reset phase can begin, so the energy in $C_{SW}$, $E_{SW(E)}$, is

$$E_{SW(E)} = 0.5C_{SW}(2V_{TP})^2 \quad (4.3)$$

to $C_{SW}$. Since $M_{SEN}$ has resistance $R_{DS(SEN)}$, conducting $i_L$'s current during the energizing phase loses

$$E_{SEN(E)} = \int_0^{t_E} i_{SEN}^{\ 2} R_{DS(SEN)} dt \approx \frac{i_{L(PK0)}^{\ 2} R_{DS(SEN)} t_E}{3} . \quad (4.4)$$

So, for $L_X$ to have energy at the end of the energizing phase and at the beginning of the reset phase, the input source must supply the inductor with $E_{H(E)}$, more energy than $C_{SW}$, $C_E$, and $M_{SEN}$ consume, requiring

$$E_{H(E)} > E_{SW(E)} + E_{E(E)} + E_{SEN(E)} . \quad (4.5)$$

Finally, a total charge of $q_H$ is supplied by $v_H$ to charge $C_E$ and $C_{SW}$ to their respective voltages. Since the charge delivered to a capacitor is equal to its capacitance times the difference between initial and final voltages, the charge extracted from $v_H$ can be calculated by finding the charge delivered to the capacitors. The energy required to provide this charge,

$$E_{H(E)} = q_H v_H = (C_{SW} 2V_{TP} + C_E \Delta v_E) v_H , \quad (4.6)$$

must be supplied by $v_H$. Therefore, $v_H$ must be high enough for $E_{H(E)}$ to not only charge $C_{SW}$ and $C_E$ but also supply what $M_{SEN}$ consumes. This is why $M_{PD}$ and $M_{PO}$ are small, to keep $C_{SW}$ and its uncollectable energy small.

For oscillations to persist, $M_{NR}$'s gate voltage $v_{DLY}$ must rise high enough after each energizing period $t_E$ to reset $M_{NR}$ and start another energizing event. Additionally, $v_{DLY}$ must reach its target ($M_{NR}$'s threshold voltage) before $L_X$ exhausts its energy. Once $L_X$ exhausts its energy, it would start discharging $C_{SW}$ and $C_{DLY}$ would stop charging before $M_{NR}$ can reset. In other words, $v_{DLY}$'s delay, $t_{DLY}$, must be shorter than $L_X$'s exhaust time $t_{EX}$ when drained across $v_H$ and $v_{SW}$:

$$t_{DLY} < t_{EX} = L_X\left(\frac{\Delta i_L}{\Delta v_L}\right) = L_X\left(\frac{\Delta i_L}{v_{SW} - v_H}\right) \tag{4.7}$$

For this, $L_X$ first charges $C_{SW}$ from $v_{E(PK)}$ to the greater of $2V_{TP}$ above ground or $V_{TP}$ above $v_T$. Once $v_{SW}$ is high enough to turn on $M_{PD}$ and $M_{PO}$, $M_{PDLY1}$ and $M_{PDLY2}$ also turn on and begin charging $v_{DLY}$. $L_X$, then charges $C_{DLY}$ via $R_{DLY}$ with some current flowing instead into $R_G$. Because $R_G$ steals part of the current that would otherwise charge $C_{DLY}$, $v_{DLY}$ does not reach all the way to $v_{SW}$. $v_{DLY}$ therefore reaches 90% of the voltage-divided fraction of $v_{SW}$ that $R_{DLY}$ and $R_G$ set after roughly 2.3 RC time constants $t_{RC}$:

$$\Delta v_{DLY} \approx v_{SW}\left(\frac{R_G}{R_{DLY} + R_G}\right)\left[1 - e^{-\left(\frac{t_{DLY}}{t_{RC}}\right)}\right]. \tag{4.8}$$

$M_{PDLY1}$ and $M_{PDLY2}$'s series resistance is designed to be much lower than $R_{DLY}$, so that the resistance that determines the final time constant, $t_{RC}$, is $R_{DLY}$ in parallel with $R_G$. Therefore, $C_{DLY}$ charges with time constant:

$$t_{DLY} \approx 2.3t_{RC} \approx 2.3(R_{DLY} \parallel R_G)C_{DLY} \tag{4.9}$$

Since $M_{NR}$ resets the system before $v_{DLY}$ can reach 100% of $v_{SW}$'s voltage-divided fraction, $t_{DLY}$ is about $2.3t_{RC}$.

When the system first starts and $C_T$ is discharged, $C_{SW}$ must charge from zero to $M_{PD}$ and $M_{PO}$'s two source–gate voltages $2v_{SGP}$. $L_X$ therefore drains with a voltage, $2v_{SGP} - v_H$. $v_{DLY}$, which charges from $v_{SW}$, must then rise above $M_{NR}$'s threshold voltage $V_{TN0}$ for $M_{NR}$ to turn on and reset $C_E$. This means, the voltage-divided fraction that $R_{DLY}$ and $R_G$ set from $v_{SW}$'s $2v_{SGP}$ must be greater than $V_{TN0}$:

$$2v_{SGP}\left(\frac{R_G}{R_{DLY}+R_G}\right) > V_{TN0} \tag{4.10}$$

and $v_{DLY}$ must rise above $V_{TN0}$ across $t_{DLY}$ before $L_X$ depletes during $t_{EX}$ when drained with $2v_{SGP} - v_H$.

Once $M_{NR}$ engages, $v_E$ and $v_{SW}$ are pulled low, so that $v_{DLY}$ stops charging. With $R_G$ drawing current from $C_{DLY}$, $v_{DLY}$ begins to discharge. $M_{NR}$ should then reset $M_{SEN}$ across $t_{RES}$ before $R_G$ discharges $C_{DLY}$ across $t_{DIS}$:

$$t_{RES} \approx 2.3C_S\left(R_{DS(SEN)} \parallel R_{DS(NR)}\right) < t_{DIS} \tag{4.11}$$

where $R_{DS(SEN)}$ and $R_{DS(NR)}$ are $M_{SEN}$ and $M_{NR}$'s resistances and $t_{RES}$ is roughly 2.3 time constants of $C_E$, $R_{SEN}$, and $R_{NR}$. $R_G$ should then drain $C_{DLY}$ before the energizing event ends. So about 2.3 time constants of $R_G$ and $C_{DLY}$ must elapse before $t_E$:

$$t_{DIS} \approx 2.3R_G C_{DLY} < t_E . \tag{4.12}$$

### 4.2.2 Battery Charger

Since the power available to energy harvesters from ambient sources is small, power conversion, from the input to the battery, must have high efficiency in order to provide the maximum power possible to the load. Switched-inductors provide high conversion efficiency across a wide input to output ratio, but they require an established supply to

operate correctly and efficiently. Therefore, after the starter has charged the temporary supply, the system controller can turn it off, and the switched inductor in Figure 4.7 can begin charging the battery.

When the system is ready to charge the battery, $M_{B1}$, through $v_{GP}$, is turned on, and remains on as long as battery charging continues. Energizing switch, $M_E$, controlled by $v_{GN}$, begins the charging cycle by pulling the switching node, $v_{SW}$, to ground, which increases the current in the inductor. When $M_E$ is turned off, the inductor current charges the parasitic capacitance at $v_{SW}$, causing $v_{SW}$ to rise. Once $v_{SW}$ rises past $M_{B2}$'s gate-source voltage above $v_B$, $M_{B2}$ turns on and begins draining the inductor into the battery. Because $M_{B2}$'s gate is tied to its drain, it acts as a diode and only conducts as long as the inductor current is positive. As the inductor current reduces, it eventually reaches zero, and $M_{B2}$ turns off, marking the end of one charging cycle.

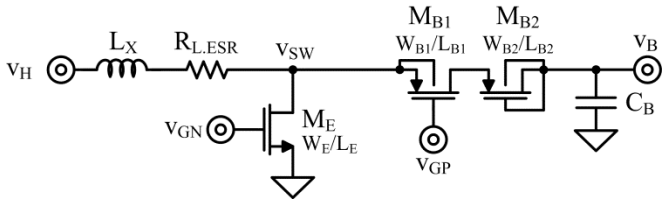


**Figure 4.7. Schematic of battery charger.**

In order to maximize the converter efficiency, the dominant losses must be identified and minimized. When the inductor energizes, its current, $i_L$, flows through $R_{L.ESR}$ and $M_E$'s on-resistance, $R_{DS(E)}$, each causing conduction losses. During the de-energizing phase, the inductor current flows through $M_{B1}$ and $M_{B2}$ with conduction losses coming from $R_{L.ESR}$, $M_{B1}$'s on-resistance, $R_{DS(B)}$ and $M_{B2}$'s gate-source voltage, $v_{SG(B2)}$. Furthermore, when transistors are turned on, their gate capacitance is charged to the

system's supply voltage. These gate-drive losses are due to the fact that charge is drawn from the supply voltage each switching cycle.

During the energizing phase, $M_E$ turns on and conducts $i_L$, which begins at zero and climbs linearly with a slop of $v_E/L_X$, where $v_E$ is the voltage across the inductor during this phase. $M_E$, which is designed for low loss, has a small drain-to-source voltage, so it resides in the triode region and can be modeled as a resistor with resistance $R_{DS(E)}$. The inductor's equivalent series resistance (ESR), $R_{L.ESR}$ also causes energy losses when the inductor is conducting. Therefore, when the inductor current linearly increases to $i_{L(PK)}$ in $t_{E.B}$ with period $T_{SW}$, the conduction power loss is:

$$P_{C(E)} = i_{E(RMS)}{}^2 R_E = \frac{i_{L(PK)}{}^2}{3}\frac{t_{E.B}}{T_{SW}}\left(R_{L.ESR} + R_{DS(E)}\right). \tag{4.13}$$

Additionally, the energy required to turn on $M_E$ is equal to the voltage applied to its gate, $V_G$, times the total charge delivered to its parasitic gate capacitance. Since this energy is lost every switching cycle, the gate drive power losses due to $M_E$ is

$$P_{GD(E)} = C_E V_{GD}{}^2 f_{SW} = \frac{W_E L_E C_{OX}'' V_G{}^2}{T_{SW}}. \tag{4.14}$$

Since the gate drive losses increase with $M_E$'s width, $W_E$, a smaller switch would consume less gate drive losses. However, $M_E$'s conduction loss, $P_{C(E)}$, increases with its drain resistance $R_{DS(E)}$, which is inversely proportional to $W_E$. Therefore, while a smaller $W_E$ reduces gate drive losses, it would also increase conduction losses. Minimizing the total losses including gate drive and conduction loss produces the optimal value of $W_E$. Since increasing the transistor length increases both gate drive and conduction losses, the minimum length allowed by the semiconductor fabrication process should be used for maximum efficiency.

When the inductor is draining into the output capacitor, $C_B$, current conducts through $M_{B1}$ and $M_{B2}$. Since $M_{B1}$'s gate is connected to ground, its gate-source voltage is large enough to maintain the transistor in the triode region, so it acts as a resistor with resistance $R_{DS(D)}$. The combination of the losses from $M_{B1}$ and the inductor's ESR are derived exactly as the conduction losses during the energizing phase, replacing the appropriate resistances and the energizing time, $t_{E.B}$ with the de-energizing time, $t_{D.B}$:

$$P_{C(MB1)} + P_{C(L)} = \frac{i_{L(PK)}^{2}}{3}\frac{t_{D.B}}{T_{SW}}\left(R_{DS(B1)} + R_{L.ESR}\right). \tag{4.15}$$

However, this does not include the loss incurred by $M_{B2}$, whose gate is connected to its drain. Since its gate-to-source voltage is equal to its drain-to-source voltage, $M_{B2}$ operates in the saturation region and cannot be modeled as a simple resistor. Instead, the drain current, $i_D$, of a transistor in the saturation region increases quadratically with source-gate voltage, $v_{SG}$. Since the drain current of $M_{B2}$ is known (the inductor current), its source-drain voltage (equal to its source-gate voltage) can be found by solving $M_{B2}$'s quadratic drain current equation for $v_{SG}$:

$$v_{SD(B2)} = v_{SG(B2)} = \left|V_{TP}\right| + \sqrt{\frac{i_D}{k'\left(\frac{W_{B2}}{L_{B2}}\right)}}. \tag{4.16}$$

Since $M_{B2}$'s source-drain voltage is not constant with current, it cannot be modeled as an ideal diode. Its drain-source voltage is not linearly dependent on current, so it cannot be modeled as a resistor either. Therefore, the power lost must be calculated as the average of the product between the drain-source voltage and the drain current. To simplify the calculation, the average is only taken during the de-energizing time, $t_D$,

which is when $M_{B2}$ conducts, and then extended across the switching period so that the conduction loss in $M_{B2}$ becomes

$$P_{C(MB2)} = \frac{1}{T_{SW}} \int_0^{t_D} v_{SG} i_L dt = \frac{2}{5\sqrt{k'\left(\frac{W_{B2}}{L_{B2}}\right)}} t_{D.B} i_{L(PK)}^{3/2} + \left(\frac{i_{L(PK)}}{2}\right)\left|V_{TP}\right|. \quad (4.17)$$

Therefore, the total conduction loss during the de-energizing phase, $P_{C(D)}$, includes the ohmic losses in $R_{L.ESR}$ and $M_{B1}$'s $R_{DS(B1)}$ as well as $M_{B2}$'s conduction loss:

$$P_{C(D)} = P_{C(MB1)} + P_{C(L)} + P_{C(MB2)}. \quad (4.18)$$

Since $M_{B1}$ remains on after startup, it does not incur any gate drive losses after the initial switching. Additionally, $M_{B2}$ is turned on by the inductor charging the switching node parasitic capacitance, $C_{SW}$, which does not incur additional losses. However, after the inductor drains its current into the output, $v_{SW}$ remains at the output voltage, meaning $C_{SW}$ holds charge around $v_B$. This imposes a negative voltage across $L_X$, even if its current has reached zero. A negative voltage causes the inductor to begin conducting current in the negative direction until $C_{SW}$ has been discharged below $v_H$ and a positive voltage causes the inductor current to begin to rise and ultimately charge $C_{SW}$ again.

The oscillation between $L_X$ and $C_{SW}$, known as ringing, continues until the parasitic resistance $R_{L.ESR}$ consumes the original energy that $C_{SW}$ held,

$$E_{CSW(R)} = C_{SW} V_B^2. \quad (4.19)$$

Since a wider $M_{B2}$ adds parasitic capacitance to $C_{SW}$, $M_{B2}$ must be sized to minimize the total loss including its conduction loss and $E_{CSW(R)}$. Additional stray capacitance on the chip and printed circuit board (PCB) contribute to $C_{SW}$, so these should be minimized to improve efficiency.

## 4.3 Low-voltage Starter Prototype

A prototype of the proposed starter was created using a 180-nm CMOS process and a 2-layer, FR4 printed circuit board. The goal of the prototype was to validate the design and simulations of the proposed starter circuit in the context of an energy harvester. Since the main purpose was to test the starter circuit, the system controller was implemented off-chip and on the printed circuit board. Additional test circuits on the board were also used to measure the operation and performance of the starter, and to some extent, the harvesting system. However, off-chip components that would be required in a final system, such as the inductor, input capacitance and battery, were selected to provide maximum performance while only occupying the practical size expected in wireless microsystems.

### 4.3.1 Harvesting System

The proposed harvester circuit in Figure 4.8 was developed, designed and fabricated in a Texas Instruments 180-nm CMOS process. The 600 × 250-$\mu m^2$ CMOS die in Figure 4.8b integrates the oscillating starter in Figure 4.9, the startup capacitor $C_T$, and the power transistors $M_E$ and $M_{B1}$–$M_{B2}$. The printed circuit board (PCB) in Figure 4.8c embeds the fabricated microchip, the 100-μH inductor $L_X$, the controller, the 100-nF battery $C_B$ in, and test circuits used to evaluate the system. Operationally, the starter charges $C_T$ until $C_T$ stores enough energy for the controller to operate $M_E$ and $M_{B1}$. Afterwards, $M_E$ energizes $L_X$ from the harvesting source $v_H$ and $M_{B1}$–$M_{B2}$ drains $L_X$ into $C_B$ in alternating cycles. The purpose of the diode-connected transistor $M_{B2}$ is to block reverse battery current that would otherwise drain $C_B$. Here, the power converter that $M_E$, $M_{B1}$, $M_{B2}$, and the

controller realize is for test purposes only, to show how the starter affects the dc-sourced harvester it supports.

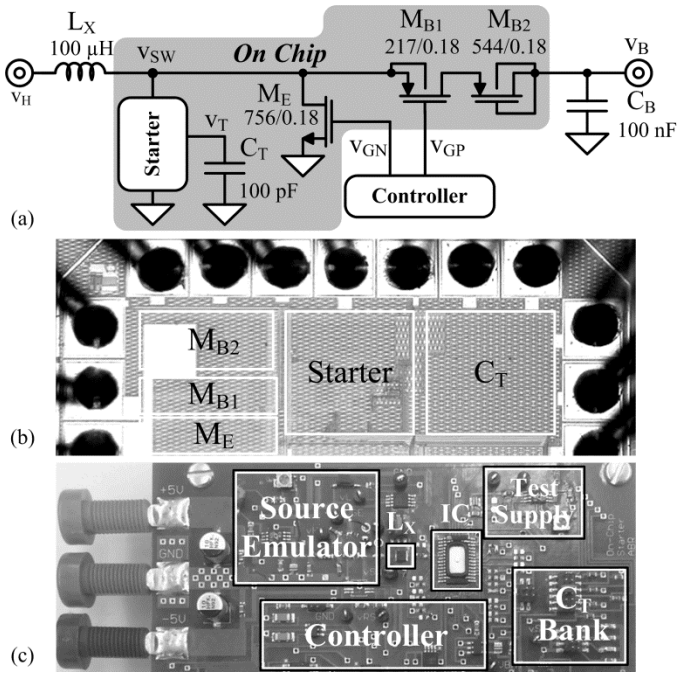


**Figure 4.8. Prototype harvesting (a) system, (b) die and (c) printed circuit board.**

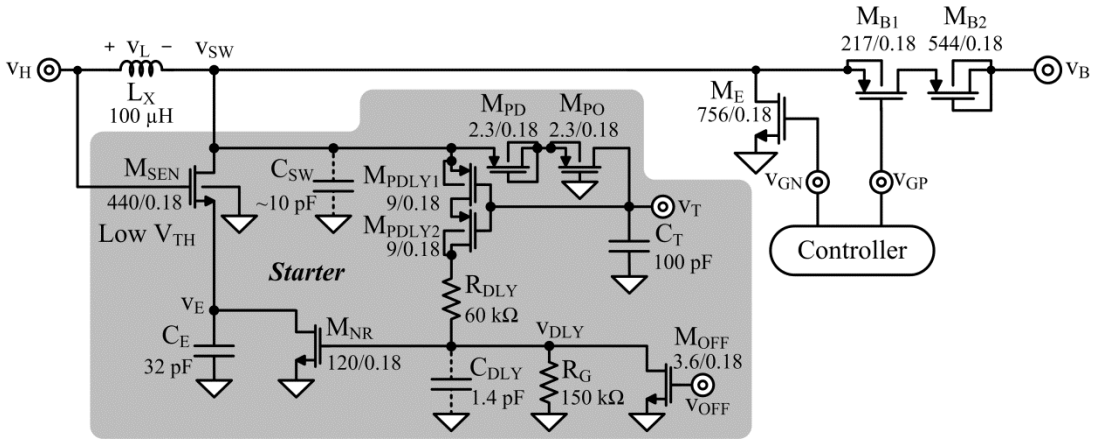


**Figure 4.9. Schematic of prototyped starter circuit and harvester.**

A simple controller for the power converter was implemented on the printed circuit board (PCB). Its main purpose was to facilitate the transition between startup and

steady-state battery charging. To this end, an external voltage reference, $V_{REF}$, an external oscillating square wave, $v_{OSC}$, and the starter's output voltage, $v_T$, were fed into the controller shown in Figure 4.10. An external reset signal, $v_{RST}$, was used to ensure proper initialization of the controller. Before any measurements are taken, $v_{RST}$ should be held high until the system is ready to be tested, at which point $v_{RST}$ is brought low. The controller, then, generates the starter disabling signal, $v_{OFF}$, $M_E$'s gate-controlling signal, $v_{GN}$, and $M_{B1}$'s gate-controlling signal, $v_{GP}$. Note that $v_{GP}$ in Figure 4.8a is not inverted, therefore the PCB controller outputs a high voltage when $M_{B1}$should be off, and a low voltage when $M_{B1}$should be on. Since $M_{B1}$ is off during startup, a high signal must be applied to $M_{B1}$'s gate, even though a supply voltage is not available. Since the goal of this prototype is to test the starter circuit and its effect on the system during the battery charging phase, this issue was not addressed in this design cycle. Instead, a test supply, which was always on, was used for the controller.

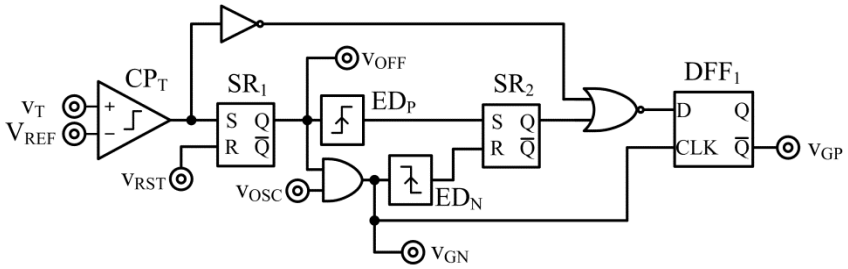


**Figure 4.10. Schematic of off-chip experimental controller.**

By comparing $v_T$ and $V_{REF}$ through comparator $CP_T$, and then latching this signal through S-R latch $SR_1$, the controller indicates that the starter should turn off, by applying a high voltage to $v_{OFF}$, once $v_T$ surpasses $V_{REF}$ as shown in Figure 4.11. When $v_{OFF}$ goes from low to high, the positive edge detector, $ED_P$, sends a short pulse, setting the output of S-R latch $SR_2$ high. Since both inputs to the NOR gate at this point are high, the "D"

input to $DFF_1$ remains low. Since $v_{OFF}$ is now high, once $v_{OSC}$ arrives, the AND gate allows $v_{OSC}$ to propagate across it, generating $v_{GN}$. In other words, $M_E$'s gate is simply $v_{OSC}$ when $v_{OFF}$ is high, and always low when $v_{OFF}$ is low. $V_{GN}$ also becomes the "CLK" signal to $DFF_1$. When $v_{GN}$ goes high for the first time, the "D" input to $DFF_1$ is low, so $v_{GP}$ remains high, and $M_{B1}$ off. Therefore, $L_X$ is energized through $M_E$, but with $M_{B1}$ off, the inductor current drains into $C_T$ through $M_{PD}$ and $M_{PO}$, charging $v_T$ one more time. This is why $v_T$ rises just after the first falling edge of $v_{GN}$ in Figure 4.11. This guarantees that the losses incurred to $v_T$ due to the controller and gate drivers do not discharge $C_T$ below its minimum threshold.

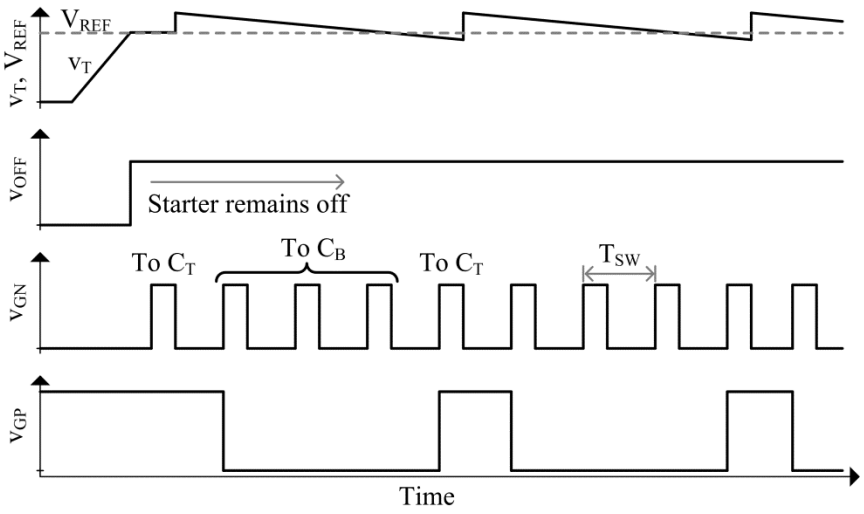


**Figure 4.11. Operational waveforms of PCB controller.**

When $v_{OSC}$ goes low, the negative edge detector $ED_N$, resets $SR_2$ so that its "Q" output remains low throughout operation. Therefore, $DFF_1$'s "D" input would then be controlled solely by the output of $CP_T$. While $v_T$ remains above $V_{REF}$, $v_{GP}$ is kept low, so that energy packets are delivered to the battery, $C_B$. Since losses incurred by the controller and gate drivers cause $v_T$ to fall, it must be periodically refreshed and recharged. When $v_T$ falls below $V_{REF}$, $DFF_1$'s output changes state and pulls $v_{GP}$ high,

turning off $M_{B1}$ and directing energy packets to $v_T$, until $C_T$ charges past $V_{REF}$. Since $v_T$ can fall below $V_{REF}$ at any point during operation, it must wait until the next $v_{GN}$ cycle to receive energy. This is why $v_T$ in Figure 4.11 continues falling below $V_{REF}$ until the next $v_{GN}$ falling edge. To prevent $v_T$ from falling below $V_{T(MIN)}$, the lowest $v_T$ could fall before the system ceases to operate correctly, $V_{REF}$ must be chosen so that $V_T$ does not fall from $V_{REF}$ to $V_{T(MIN)}$ in one switching cycle, $T_{SW}$, due to losses, $I_{LOSS}$.

$$V_{REF} > V_{T(MIN)} + \frac{I_{LOSS} T_{SW}}{C_T}. \tag{4.20}$$

The off-chip implementation of the edge detectors is shown in Figure 4.12. The positive edge detector in Figure 4.12a creates a pulse when its input voltage, $v_{IN}$, changes state from low to high. $v_{IN}$ is connected directly to one input of an AND gate, while the other input is connected to a delayed, inverted version of $v_{IN}$. When $v_{IN}$ is initially low, one input to the AND gate is low, while the other is high. When $v_{IN}$ transitions to the high state, so does one of the inputs of the AND gate, and while the inverter tries to flip the other input of the AND gate low, the resistor and capacitor pair delay its transition so that both AND gate signals are high momentarily. This produces a pulse at the output, $v_O$, whose duration is approximately the RC time delay constant.

The negative edge detector in Figure 4.12b has a similar operation, but the AND gate is replaced by a NOR gate so that the output is only high when both inputs to the NOR gate are low. This implies that the pulse is generated when the input transitions from high to low, while the delayed, inverted signal remains low for a short period. Like the positive edge detector, this overlap period is approximately equal to the RC time constant created by the resistor-capacitor pair.

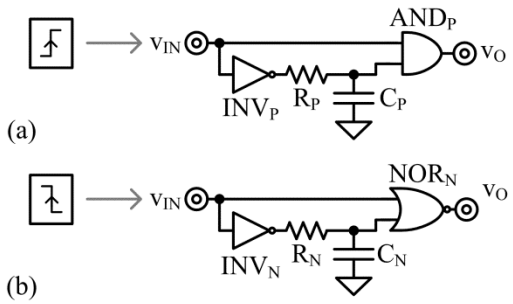


**Figure 4.12. Schematic of off-chip (a) positive and (b) negative edge detectors.**

### 4.3.2 Initializing Startup

Simulations showed that the oscillating starter circuit required a switch, $S_{PoR}$ in Figure 4.2 to reset the capacitance $C_E$ in order to begin oscillations. Fundamentally, for a slow rising $v_H$, $v_E$ will follow $v_H$ so that there is no voltage across the inductor. Once $v_H$ settles to its final voltage, $v_E$ remains high, so that $M_{SEN}$ remains off, the inductor voltage is zero, and no current is conducted. By momentarily shorting $v_E$ to ground, $M_{SEN}$ is turned on, and the input voltage, $v_H$, falls across the inductor, which increases its current.

While creating a pulse that is long enough to reset $C_E$, but short enough so it does not affect operation can easily be implemented in simulations, it is not practical in hardware experiments. Therefore, in experiments $S_{PoR}$ remains on long enough that the inductor current rises until the total series resistance limits its current. When $S_{PoR}$ is dis-engaged, oscillations begin and the starter charges the output $C_T$. As a more practical alternative, experiments also showed that oscillations could be initiated if $v_H$ rose fast enough. For some applications, where the energy source disappears and re-appears suddenly, a power-on-reset switch may not be necessary since the oscillator will begin on its own.

*Power on Reset:*

Initializing the oscillator with a power on reset switch begins when a switch connected to $v_E$ in Figure 4.9 is turned on and shorts $v_E$ to ground. With a positive voltage, $v_H$ across $L_X$, the inductor current rises until the voltage drop across the switch's resistance and the inductor's equivalent series resistance, $R_{L.ESR}$, reaches $v_H$. In other words, as the inductor's current increases, so does the voltage dropped across series resistances until all of the voltage available falls across the resistors instead of the inductor. When the voltage across the inductor, $v_L$, reaches zero, the inductor current no longer rises, and remains at a fixed current until the switch is turned off. This is why $i_L$ begins at 1.4 mA in Figure 4.13 during $t_{PoR}$.

When the power-on-reset switch is turned off, the inductor current charges $C_E$ until $v_E$ rises enough to turn off $M_{SEN}$. With $M_{SEN}$ off, the inductor begins charging the switching node's parasitic capacitance, $C_{SW}$, causing $v_{SW}$ to rise, around 0.15 µs in Figure 4.13. As $v_{SW}$ rises, $M_{PD}$ and $M_{PO}$ turn on, and the inductor drains into $C_T$. Due to the relatively large current caused by the power-on-reset switch, $v_T$ is charged about 340 mV within 100ns, during the first de-energizing phase. However, once the oscillator turns on, the inductor current reduces, and $C_T$ charges at a much slower pace, charging the remaining 500 mV in about 40 µs.

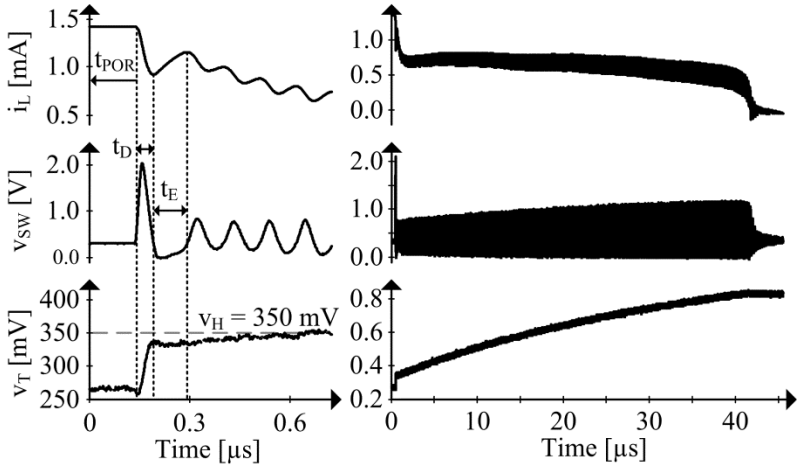


**Figure 4.13. Measured waveform of the oscillating starter using a power on reset switch.**

*Stepped Input:*

Requiring a switch to turn on before startup, when there is not enough voltage headroom to activate a controller or fully turn on a switch, may not be practical for most applications. Through experiments, an alternative way of activating the oscillator was discovered when the input voltage increased from zero to the oscillator's minimum voltage requirement faster than the charging time of $C_E$. Since $C_E$ charges through $L_X$, the charging time for $C_E$ can be approximated as a quarter cycle of a LC tank period or

$$t_S \approx \frac{2\pi\sqrt{L_X C_S}}{4}. \tag{4.21}$$

Fulfilling this requirement implies that when $v_H$ rises, $C_E$ remains discharged so that $v_E$ remains at or near zero. With $v_E$ near zero, a positive voltage, $v_H$, is applied across the inductor and $i_L$ begins to rise. With a positive current in $i_L$ and $v_H$ high enough to turn on $M_{SEN}$, the starter is able to begin and sustain oscillations. So, when $v_H$ rises within 250 ns in Figure 4.14, the starter can oscillate and charge $C_T$ until $v_T$ rises to about 500 mV within 40µs.

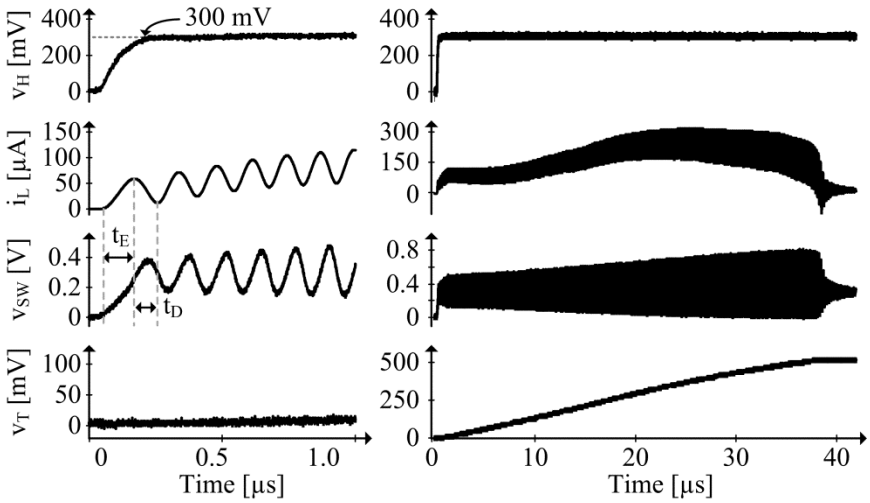


**Figure 4.14. Measured waveform of the oscillating starter with a stepped input.**

Although starting with a stepped input instead of a power-on-reset switch may be slower, since the switch induces a larger initial current, the additional switch may prove to be impractical. An electronic switch is not expected to be reliable, since the available voltage, $v_H$ is not enough to properly operate CMOS circuits. A mechanical switch, which has no voltage requirement, could be used, but would require vibrations to activate or human interaction, which is not an option in most microsystem applications. Additionally, the high current drawn during $t_{PoR}$ may be incompatible with the small, low-power producing transducers found in wireless microsystems. Therefore, requiring a stepped input, although itself imposing requirements onto the system, is preferred over adding a power-on-reset switch.

## 4.4 Measured Performance

The performance of the prototyped starter and system was evaluated to validate the simulated performance as well explore its limitations and advantages. Key performance metrics for the starter include minimum input voltage, startup time, and startup

efficiency. Furthermore, since the output of the starter should supply the system controller, the maximum output voltage for a given input level, also affects overall system performance. Finally, since the starter circuit will ultimately share the inductor of the battery charger, measuring the impact the starter has on the charger during steady state is critical. Therefore, the efficiency of the battery charger was measured with and without an attached starter to confirm the viability of reusing the inductor.

### 4.4.1 Starter Performance

As Figure 4.14 demonstrates, the starter energizes and drains $L_X$ in alternating cycles when $v_H$ rises to 300 mV to charge $C_T$ to 500 mV in 38 µs. The system starts as long as $v_H$ ramps to its target within 250 ns, before $L_X$ and $C_E$ have a chance to drain with resonance. To determine the minimum operating voltage of the oscillator, the output voltage was connected to the input voltage in order to sustain oscillations and the input voltage was reduced slowly until oscillations stopped. The oscillations were initiated by stepping the input to 0.6 V within 250 ns. As shown in Figure 4.15, the oscillations persisted for input voltages above 255 mV. This means that the starter circuit can oscillate with input voltages as low as 255 mV while charging its output to the same voltage level.

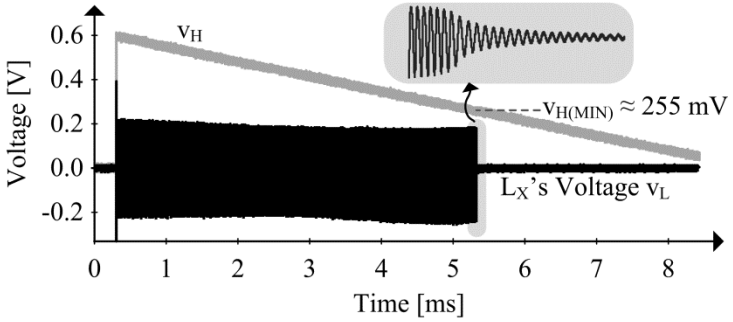


**Figure 4.15. Measured starter waveforms when $C_T$ is a pre-charged battery.**

Notice in Figure 4.14 that the system stops charging the output capacitor, $C_T$, when $v_T$ reaches 500 mV. This happens because at first, $L_X$ energizes more than it drains to build current $i_L$ in $L_X$. However, as oscillations continue and $C_T$ charges, the inductor drains more than it receives so $i_L$, on average, begins to decrease. To test the functionality of the starter circuit, the output node was left open-circuited with $C_T$ connected. After the input ramped up, the oscillator charged $C_T$ to its maximum voltage, $v_{T(F)}$ in Figure 4.16, which increases with input voltage $v_H$. When connected to a drained $C_T$, the starter can charge the output to 320 mV from a 250 mV input and to 1.55V from a 450 mV input voltage, as Figure 4.16 shows. This means, the system charges $C_T$, but only to the extent that $v_H$ allows. At its lowest input voltage, the gain is approximately equal to unity, indicating that at this point the oscillator begins to transfer energy to its output. As $v_H$ increases, the starter's gain increases from just above one to 3.7 V/V when the input voltage is 450 mV.

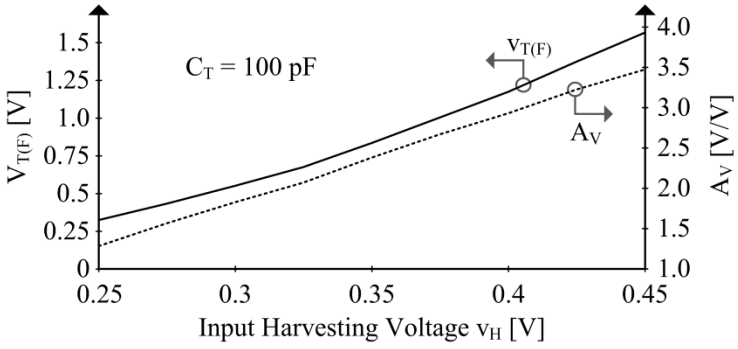


**Figure 4.16. Measured final startup voltage and gain across $v_H$.**

The input-to-output voltage relationship is nearly independent of $C_T$, as Figure 4.17 shows, with only a ±2.5% variation across 0.1–1.6 nF of $C_T$. Since varying the output capacitance $C_T$ does not change $v_{T(F)}$, the starter transfers more energy with increased capacitance, but with a limited output voltage. So irrespective of the energy

needed to charge $C_T$, the effective gain of the system from $v_H$ to $C_T$'s final voltage $V_{T(F)}$ is 1.28–3.47 V/V.

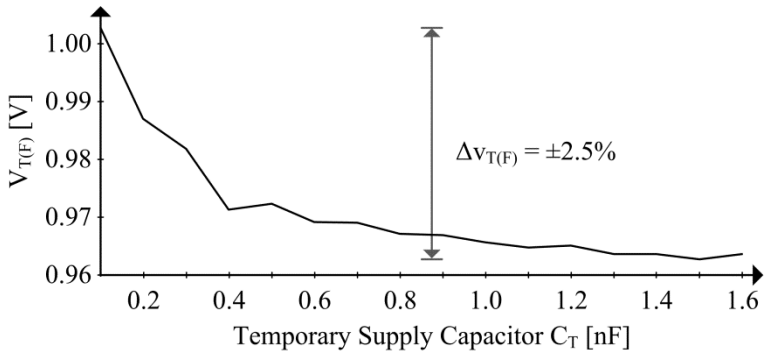


**Figure 4.17. Measured final startup voltage across $C_T$.**

Startup time measures the amount of time it takes the oscillator to charge $C_T$ to $V_{T(F)}$ once $v_H$ surpasses the minimum input voltage of the starter circuit. Since $V_{T(F)}$ rises with $v_H$, startup time is expected to increase with $v_H$ as well, since the starter will ultimately charge $v_T$ to a higher voltage. This is why startup time, $t_{ST}$, increases with $v_H$ in Figure 4.18. For input voltage ranging 250–450 mV at $v_H$ startup time spans 44–93 µs. Startup efficiency, $\eta_{ST}$ measures the ratio of output energy to input energy during the startup phase. During the startup time, the output capacitor, $C_T$, receives 0.15% to 0.65% of the energy that $v_H$ sources. Power-conversion efficiency across startup is low because the system lacks the gate drive necessary to keep conduction losses low. With lower losses, $L_X$ would have been able to draw and deliver more power. Since $M_{SEN}$'s gate drive increases with $v_H$, losses are lower for higher values of input voltage, so startup efficiency increases with $v_H$.

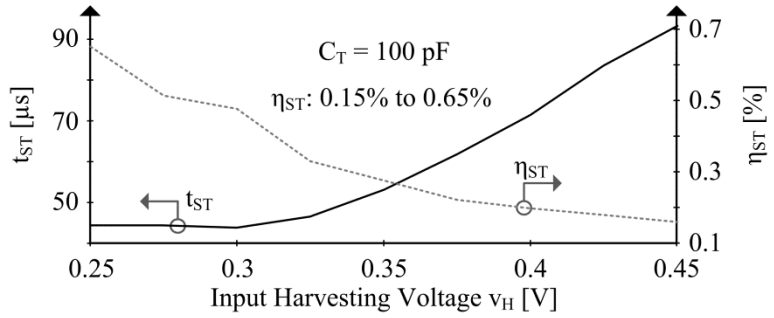


**Figure 4.18. Measured startup time and conversion efficiency across $v_H$.**

For higher values of $C_T$, the starter must deliver more charge to the output capacitor. Since the output voltage remains the same across $C_T$, the charge delivered to it is equal to the capacitance times the final voltage. Since charge increases linearly with capacitance, $t_{ST}$ in Figure 4.19 also increases linearly with $C_T$. For an output capacitance between 0.1 to 1.6 nF, $t_{ST}$ rises from 64 to 783 µs. Startup efficiency, on the other hand, does not vary with increasing $C_T$. Since output energy increases linearly with $C_T$, input energy must also increase linearly with $C_T$ to maintain a constant $\eta_{ST}$.

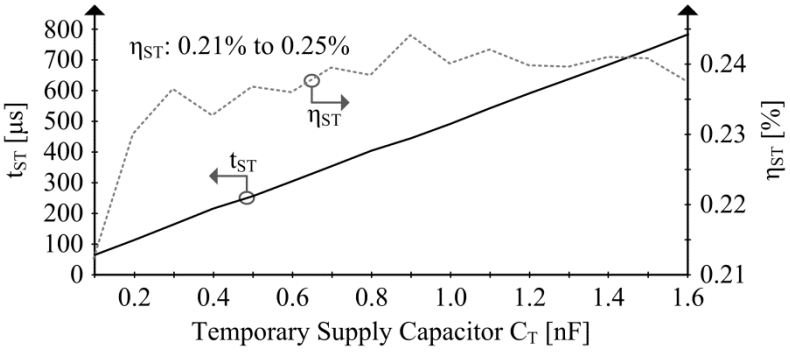


**Figure 4.19. Measured startup time and conversion efficiency across $C_T$.**

### 4.4.2 System Performance:

Once the starter circuit charges $C_T$ to a reference voltage after $t_{STRT}$, the boost converter consisting of $M_E$, $M_{PD}$, and $M_{PO}$ transfers energy to $C_B$. For testing purposes, the reference voltage, $V_{REF}$, to which $C_T$ would charge, was set to 0.7 V for a 350 mV input

voltage. After $v_T$ is charged to $V_R$, the system controller turns the oscillator off and, through the boost converter, sends one energy packet to $C_T$ to ensure $v_T$ does not fall below its target as in Figure 4.20. After this energy transfer, the controller engages ME to energize $L_X$ to $i_{L(PK)}$, and then turns $M_E$ off so that the inductor drains its energy into the battery, $C_B$.

The boost converter continues to transfer energy to $C_B$ with a period $T_{SW}$ set to 16 μs. During the first several cycles, where $C_B$ is discharged, the inductor de-energizing time is slower and time-varying. This is due mainly to two factors. First, since the energy stored in a capacitor increases quadratically with its voltage, sending constant energy packets will cause larger voltage increases when its initial voltage is lower. This is why $v_B$ rises more during the first cycle in Figure 4.20 than it does in its third cycle. Since the de-energizing time decreases with increasing $v_B$, as $v_B$ rises, $i_L$ decreases faster from its peak. Second, since $v_B$ is initially zero, most of the voltage dropped during the de-energizing time is due to $M_{PD}$ and $M_{PO}$. Since their voltages vary with current, as $i_L$ reduces during its first cycle, the voltage across $L_X$ also reduces so $L_X$ drains slower. Therefore, as the battery charges, $v_B$ becomes the dominant voltage and $i_L$ reduces faster and linearly.

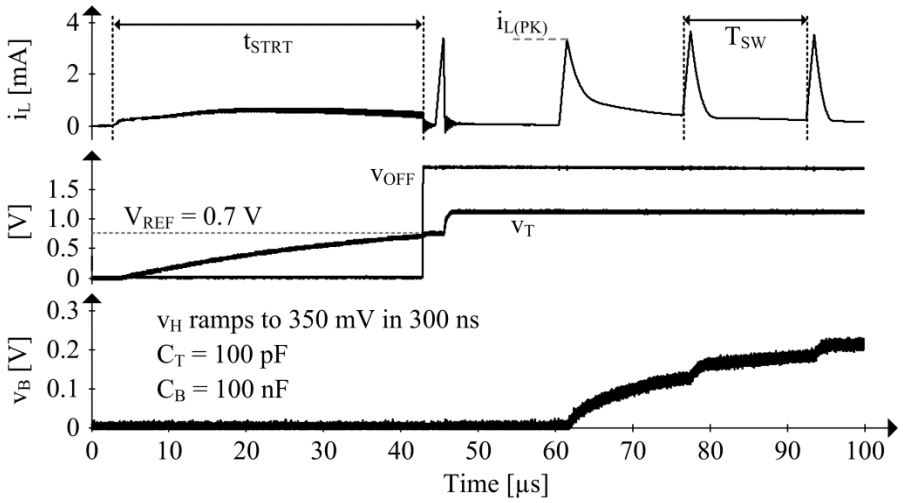


**Figure 4.20. Measured startup, transition, and steady-state waveforms.**

The main design goal of the boost converter was to transfer energy to the battery as efficiently as possible. Unfortunately, sharing the switching node with the starter means that the starter circuit will add to the parasitic capacitance at $C_{SW}$ and cause extra losses. However, the starter should not cause excessive additional losses in the system. Figure 4.21 shows the charging efficiency at different input power levels. Three setups were used to evaluate the effect of the starter circuit. The first setup tested a power stage that did not have a starter connected to it, so it only included $M_E$, $M_{PD}$, and $M_{PO}$. The second setup included the same isolated power stage with a starter circuit connected externally, through the PCB. Finally, the most realistic setup consisted of a power stage and starter circuit connected inside the integrated circuit (IC).

The aim of doing three setups is that the isolated power stage represents the ideal system, in which the starter circuit consumes no power. Therefore, efficiency is at a maximum. Since connecting a starter circuit inside the IC is not possible after it has been fabricated, a copy of the power stage was fabricated with a starter attached to it. However, since the power stages will not be identical, the losses in the converter will be

somewhat different. Therefore, the original, isolated power stage is connected to a starter circuit externally so that the losses due to the power converter are identical. The printed circuit board (PCB) connection introduces more capacitance at the switching node, which is a pessimistic degradation in efficiency, while the internal connection represents a more practical solution. Comparing the three setups proves to be the fairest evaluation of losses due to the starter circuit.

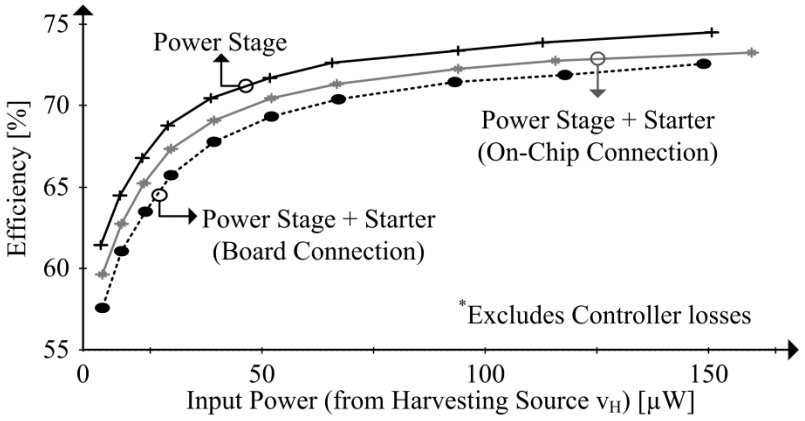


**Figure 4.21. Measured steady-state power-conversion efficiency.**

Without the starter and in steady state, $M_E$ and $M_{B1}$–$M_{B2}$ in Figure 4.9 charge $C_B$ with 62% to 74% of the 10–160 μW that the system receives from the harvesting source $v_H$, as Figure 4.21 shows. The reduction in efficiency due to connecting the starter is 1.8%. The reason for this loss is the energy lost to charging $C_E$ and the additional capacitance that the starter adds to $v_{SW}$. For one, $C_E$ partially drains $L_X$ because $M_E$ in Figure 4.9 first discharges $C_E$ through $M_{SEN}$ when $M_E$ energizes $L_X$. With $C_E$'s $v_E$ nearly at 0 V, $v_H$ closes $M_{SEN}$ to draw current from $L_X$ and charge $C_E$. Charging $C_{SW}$ similarly draws power from $L_X$, which is why adding board capacitance to $v_{SW}$ raises the loss in Figure 4.21 to 3.9%. Note that, even after $v_{OFF}$ closes $M_{OFF}$, $M_{PDLY1}$, $M_{PDLY2}$, and $R_{DLY}$ do not dissipate much of $L_X$'s energy because $C_T$'s $v_T$ keeps $M_{PDLY1}$ and $M_{PDLY2}$ off.

### 4.4.3 Discussion

One way to boost the input voltage to sufficiently high levels to operate CMOS switches is with a transformer [149]. And with a low-loss transformer, the system can convert and transfer power efficiently in steady state. Unfortunately, a low-loss transformer is, in relative terms, bulky and expensive. Although transistors powered from 300–400-mV supplies are resistive, they can still steer currents and transfer power. In fact, ring oscillators in [132], [133], [150], [154], [161] can drive CMOS transistors to switch capacitors that generate a voltage that is high enough to then energize and drain an inductor into a battery. And by tuning N- and P-channel MOS threshold voltages to balance, the network can operate with an 80-mV input [145], [147], as Table 4.1 shows.

LC oscillators can similarly operate with a 50-mV supply [152]. The problem here is that resistances are so high at 50–330 mV and switched capacitors so inefficient that initializing the system requires 1.2–15 ms. Plus, the LC oscillator requires two 4-μH inductors and tuning threshold voltages is prohibitively expensive in practice. Although the prototyped system starts from 250 mV from Figure 4.16, $v_H$ in Table 4.1 is 300 mV because performance is more comparable to the state of the art when $C_T$'s final voltage $V_{T(F)}$ is 0.55 V.

In [128], motion opens and closes an electromechanical MEMS switch that energizes and drains an inductor into 470 pF until the capacitor's voltage is high enough to drive a CMOS transistor. Since motion drives the MEMS device, the system can start from a 35-mV input. The drawback here is motion, because vibrations are not always available, and when they are, the period is long, so starting the system can require 3–20

ms. Plus, the switching interruptions that motion causes in steady state reduce how much power the system can output.

**Table 4.1. Performance summary and the state of the art.**

| | X-Former [149] | MEMS Switch [128] | LC Osc. [152] | Ring Oscillator | | This Work |
|---|---|---|---|---|---|---|
| | | | | Tuned [145] | Natural [150] | |
| $V_{H(MIN)}$ | 40 mV | 35 mV | 50 mV | 80 mV | 330 mV | 300 mV |
| $C_T$ | 10 µF | 470 pF | 4.7 nF | 30 pF | – | 100 pF |
| $V_{TAR}$ | 1.2 V | 1 V | 0.8 V | 1.3 V | 1.8 V | 0.55 V |
| $t_{ST}$ | 4.9 s | 3 ms | 15 ms | 4.8 ms | 1.2 s | 44 µs |
| $^{*}I_{EQ}$ | 2.45 µA | 157 nA | 251 nA | 8 nA | – | 1.25 µA |
| $\eta_{ST}$ | – | – | – | – | – | 0.50% |
| Other | 1:60 X-Former | 22 µH 22 µH MEMS Switch | 2 µH 2 µH 100 µH 27 µH | 6.8 µH | – | 100 µH |
| Vol. | 175 $mm^3$ | 150 $mm^3$ | $^{**}$16 $mm^3$ | $^{**}$4 $mm^3$ | 4 $mm^3$ | 4 $mm^3$ |
| Tech. | 0.13 µm | 0.35 µm | 65 nm | 65 nm | – | 0.18 µm |

Although the prototyped starter and harvester system proved to be functional, significant limitations were seen in the performance of the circuit. First, the starter circuit was not able to initiate oscillations on its own, and instead relied on an external force to jumpstart it. Additionally, once the starter was oscillating, its rectified output voltage remained limited. For low output voltages, where the circuit could still oscillate, the starter exhibited low gain and was not able to charge its output capacitor significantly above its input. Despite the limitations, the prototyped starter circuit was able to charge

its output capacitor within 100 μs for a 100 pF capacitor and within 1 ms for a 1 nF capacitor. It in fact had the second highest equivalent current, $I_{EQ}$, after the transformer based starter. Equivalent current here is defined as $C_T V_{TAR}/t_{ST,\ which}$ is a normalized measure of how fast the starter charges a capacitor, $C_T$, to a target voltage, $V_{TAR}$. Furthermore, the maximum output voltage or startup efficiency did not show a dependence on the output capacitor. And even though the startup efficiency was less than 1%, such a small startup time allows the system to quickly leave the startup phase, and begin high efficiency battery charging.

## 4.5 Summary

The starter presented here charges a temporary supply by rectifying oscillations from a non-linear LC oscillator. By charging a smaller, temporary supply, instead of the battery, startup time can be greatly reduced, and high efficiency steady state charging can be achieved much faster. Although the efficiency of the prototyped starter was found to be less than 1%, the amount of energy that is required by the output capacitance is so small that the starter can still charge it quickly. Once the output is charged, it can supply a high efficiency charger that can take over. Therefore, the key to high efficiency charging during wake periods in energy harvesting systems is to keep the load on the starter circuit low, so it is not used for long periods of time.

The prototype of the DC-sourced low voltage starter confirmed that reusing the inductor of the power converter already present in wireless microsystems minimizes the impact of the starter circuit on the overall system. The main benefit of the low voltage oscillator is allowing integration while only degrading efficiency by 1.8% during steady-state. Furthermore, charging a temporary supply instead of the on-board battery during

startup allows the system to reach steady-state in less than 100 μs. This allows the harvester to draw more energy, increasing the lifetime and functionality of the wireless microsystem. One limitation of this technology is that the harvesting source must rise within 300 ns for the system to start, which is not always possible. The voltage of the input source also limits the starter's final voltage. These restrictions, however, are not necessarily insurmountable, plus, fast start-up applications are emerging, like when office lights or car headlights first shine on a miniaturized photovoltaic cell.

# CHAPTER 5

# ROBUST BOOTSTRAPPING STARTER

Since tiny DC energy harvesting transducers produce only hundreds of millivolts, while electronic circuits require volts, the harvesting system must boost, or increase, the input voltage. Typical power converters can easily achieve this by transferring energy using an inductor and a low resistance switching network and the voltage provided by the battery to control and drive the switches. However, since ambient energy sources can vanish long enough for the battery to deplete, the system must wake from the low input voltage and produce a high voltage supply. Before the high voltage is produced, the power converter is not operational, and the system instead must rely on a starter circuit. Once a high voltage is established, however, the power converter can use it as a supply and accelerate wake time. Although the starter presented in Chapter 4 operated from input voltages as low as 250 mV, it only produced one volt at its output when its input reached 375 mV.

Another drawback of the presented starter circuit is that it could only start if the input voltage rose quickly. Although some applications could potentially meet this requirement, many more situations use slow changing ambient sources. Additionally, extra capacitance, $C_{IN}$ in Figure 5.1, is typically added at the input voltage node to reduce the ripple voltage and improve conversion efficiency. This added capacitance, along with the transducer's limited power, slows the rising rate of the voltage and prevents the starter from oscillating. Therefore, to expand the application space of the oscillator as well as reduce its impact and requirements on the overall system, it must be able to start regardless of the rise time of its input.

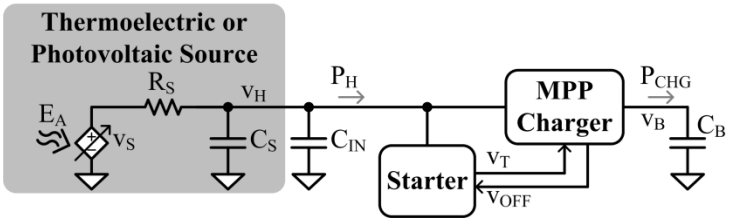


**Figure 5.1. Thermoelectric energy-harvesting charger system.**

## 5.1 Increasing Gain and Robustness

In order to maximize the application space of a starter circuit, it must operate at the lowest voltage possible, produce a high output voltage, and be robust enough to operate with a realistic transducer. The starter circuit presented in the previous chapter suffered from low voltage gain and, therefore, produced a limited output voltage. The reason for the limited output was that only a fraction of the inductor current actually reached the output node. To increase the output voltage, more of this current must be steered to the output. The presented circuit also required a stepped input or an initializing switch to operate, which limits its usefulness in many applications. To overcome this limitation, a linear, self-starting, LC oscillator can be used to jump start the oscillating core. Since the jump starter can begin oscillating before the core is ready to charge the output, it may cause the starter to prematurely draw power from the transducer, lowering its voltage and ultimately stalling the startup process. Therefore, the starter requires a reset circuit, which detects a possible stalled condition and attempts to start again after a short period of time.

### 5.1.1 Charging

The oscillating starter presented in Chapter 4 could not charge its output, vT, to a high voltage because most of the power drawn from the source was consumed by the energizing circuit instead of being directed to the output. The starter, shown in Figure 5.2

with the addition of $M_{FB}$, energized the inductor through $M_{SEN}$, $C_S$, and $M_R$. As the inductor current, $i_L$, increases, $v_E$ begins to rise until $M_{SEN}$ can no longer conduct the additional current. At this point, $M_{SEN}$ enters the saturation region, which means $M_{SEN}$ conducts a fixed amount of current. However, since $v_{SW}$ remains below $v_H$, $i_L$ continues to increase. The difference in current between $i_L$ and the saturation current of $M_{SEN}$ initially charges $C_{SW}$ until $M_{PD}$ and $M_{PO}$ conduct and eventually is rectified into the output capacitor. As $v_T$ and $v_{SW}$ rise, more of this excess current, $i_{REC}$ in Figure 5.2, must be expended to charge $C_{SW}$. The maximum voltage $v_{SW}$ can reach occurs when all of $i_{REC}$ is delivered to $C_{SW}$ and no excess energy is left to charge $C_T$. Therefore, $i_{REC}$ determines how high the starter can charge $v_T$, since it is $i_{REC}$ and not $i_L$ which charges $C_{SW}$ to $v_{SW}$'s maximum possible voltage.

Completely shutting off $M_{SEN}$ during the de-energizing phase would then allow nearly all of $i_L$ to be available as $i_{REC}$. To this end, $M_{FB}$ in Figure 5.2 is added to the oscillator so that when $v_{SW}$ rises, it turns off $M_{SEN}$. When $v_{SW}$, which is connected to $M_{FB}$'s gate, rises above $v_E$ by $M_{FB}$'s threshold voltage, $M_{FB}$ conducts current and pulls $v_E$ towards $v_H$. As $v_{SW}$ continues rising, $M_{FB}$'s drain resistance lowers and the connection between $v_H$ and $v_E$ becomes stronger until $v_E$ is approximately equal to $v_H$. At this point, $M_{SEN}$'s gate-source voltage is near zero and the transistor is in the cutoff region. With $M_{SEN}$ off, all of $i_L$ flows into $i_{REC}$. $M_{FB}$ remains on until $M_R$ turns on and pulls $v_E$ to ground causing $M_{SEN}$ to turn on and pull $v_{SW}$ low, until $M_{FB}$ turns off.

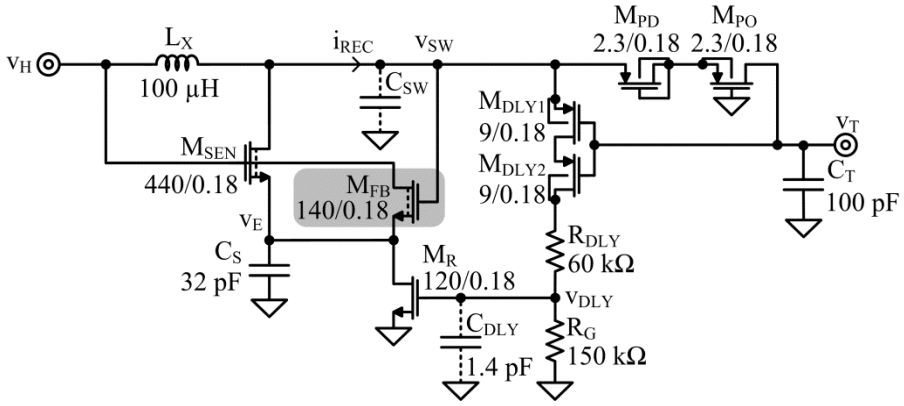


**Figure 5.2. Schematic of starter with gain enhancing $M_{FB}$.**

In the oscillator without $M_{FB}$, the inductor current, shown in Figure 5.3a, remains well above $i_{REC}$ throughout the oscillator's operation. And with only a tiny fraction of the available inductor energy reaching the output, $v_T$ only rises to a final output voltage of 0.55 V when the input voltage is 0.3 V. With the addition of $M_{FB}$, $i_{REC}$ in Figure 5.3b increases to $i_L$ during the de-energizing phase, so more energy is available to the output. This allows the starter to charge $C_T$ to a final output voltage, $V_{T(F)}$, above 4V. Therefore, without $M_{FB}$, the oscillator produces a gain of 1.7 V/V while producing a gain greater than 13 V/V with $M_{FB}$.

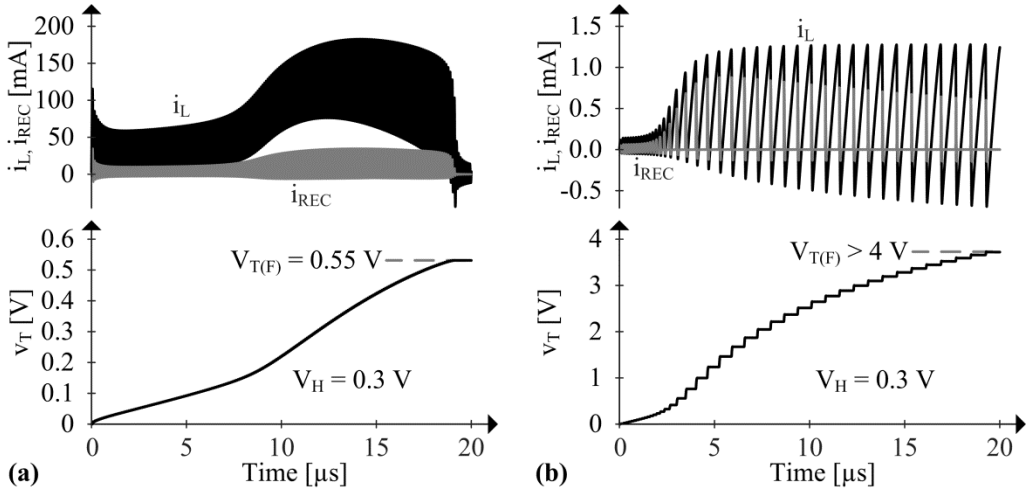


**Figure 5.3. Waveforms showing starter charging capability (a) without and (b) with $M_{FB}$.**

When $v_T$ is around 0.5 V in Figure 5.3a, the inductor current peaks to around 170 µA while $i_{REC}$ only reaches 32 µA. This causes $v_T$ in Figure 5.4a to rise only 2.6 mV when $i_{REC}$ is delivered to $C_T$ in each cycle and about 10 mV over four cycles across 0.4 µs. With the addition of $M_{FB}$, $i_{REC}$ in Figure 5.4b rises to and follows $i_L$ so that all the inductor's energy is available to $C_T$. This allows an increase of 140 mV in one cycle and 400 mV over three cycles and across 1 µs. Comparing the waveforms in Figure 5.4 makes clear that the addition of $M_{FB}$ causes the oscillator to deliver more energy in each cycle so that less charge time and cycles are required to reach the starter's target voltage.

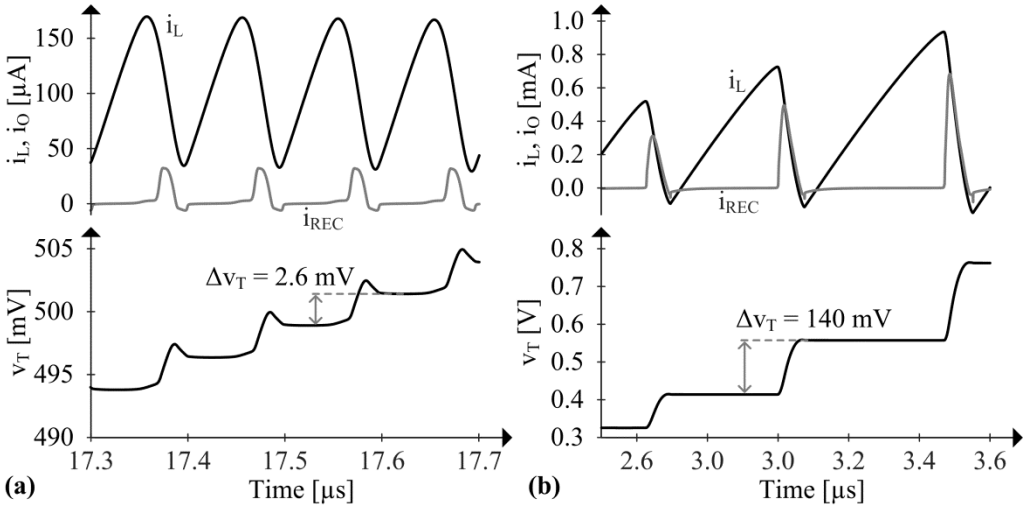


**Figure 5.4. Waveforms showing starter charging capability (a) without and (b) with $M_{FB}$ when the output voltage $v_T$ is around 0.5V.**

By adding one transistor to the existing technology, the gain can be increased by nearly a factor of eight when the input voltage is 0.3 V. Additionally, since the required target voltage is around 1 V, the improved starter provides more than enough gain and output voltage by having the capability to charge its output to above 4V. Note that although $M_{FB}$ makes the oscillator more efficient, the peak current is higher than before. In other words, the oscillator will draw more instantaneous power from the source.

However, with the improved efficiency, the total energy drawn from the source is lower, while delivering more charge and voltage to the output.

### 5.1.2 Jump Starting

Another limitation of the prototyped starter, which remains in the improved gain circuit in Figure 5.2, is that it could not begin oscillations without a fast-rising input or auxiliary power-on-reset switch. The root cause of this problem is that the circuit relies on a capacitor to energize the inductor, and for slow rising inputs, the capacitor does not provide enough delay to create a voltage across $L_X$. Instead, the capacitor, $C_S$, charges along with $v_{SW}$ and $v_H$. With $v_E$ following $v_H$, $M_{SEN}$ remains off and the inductor current remains zero. To overcome this limitation, the energizing capacitor $C_S$ can be replaced with a resistor, $R_E$ in Figure 5.5, which will always draw current through the inductor if $v_H$ is high enough to turn $M_{SEN}$ on.

The oscillator in Figure 5.5 implements a self-starting oscillator by introducing an additional feedback loop. If $v_H$ is high enough to turn $M_{SEN}$ and $M_{FB}$ on, $R_E$ will draw current through $M_{SEN}$ and $L_X$. Any positive perturbation at the gate of $M_{FB}$ will cause an increase in its drain current, which will ultimately cause $v_E$ to rise. When $v_E$ rises, $M_{SEN}$'s gate-source voltage decreases, and its drain current decreases correspondingly. With less current being pulled by $M_{SEN}$, the switching node, $v_{SW}$, rises, strengthening the original perturbation. If the original perturbation were negative, the circuit would show a similar response, but in the opposite direction, ultimately driving the switching node low.

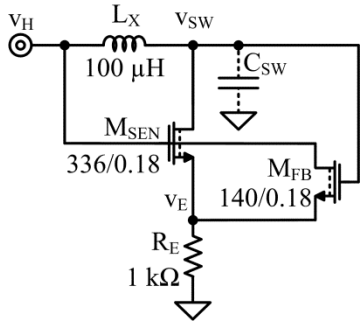


**Figure 5.5. Schematic of jump starter oscillator.**

Without the inductor, $L_X$, and capacitance, $C_{SW}$, any perturbation would cause the positive feedback loop to move strongly in one direction until the series resistance ultimately limited the current drawn from the source. In other words, positive feedback on its own does not cause oscillations. Instead, the inductor and capacitor are necessary so that energy moves back and forth in the form of inductor current and capacitor voltage. If the input voltage, $v_H$ in Figure 5.5, rises slowly enough so that $v_{SW}$ moves at the same rate, there will be no initial voltage across the inductor, and no oscillations. However, any perturbation from this state, such as noise found in all electronic circuits, will begin oscillations. For example, if $v_{SW}$ begins at $v_H$, both $M_{FB}$ and $M_{SEN}$ will conduct through $R_E$ with $L_X$ conducting $M_{SEN}$'s drain current. If $v_{SW}$ rises slightly above $v_H$, $M_{FB}$'s drain current will rise causing a rise in $v_E$, and a drop in $M_{SEN}$'s drain current. Since the inductor is conducting more current than $M_{SEN}$, the excess current will flow into $C_{SW}$ and strengthen the perturbation. As $M_{SEN}$'s current keeps reducing, more of the inductor current, $i_L$, flows into $C_{SW}$ and $v_{SW}$ rises.

However, a rising $v_{SW}$ imposes a negative voltage onto $L_X$ causing $i_L$ to fall until it reaches zero. Once $i_L$ is zero, $C_{SW}$ stops receiving energy and $v_{SW}$ is at its maximum. With a negative voltage on $L_X$, $i_L$ begins to increase, but in the negative direction, pulling

energy from $C_{SW}$. This continues until $v_{SW}$ is low enough so that $M_{FB}$ no longer pulls $v_E$ high and $M_{SEN}$ can conduct current. $M_{SEN}$ then helps discharge $C_{SW}$ and create a positive voltage across $L_X$ so that its current can increase in the positive direction. Once $i_L$ is positive again, $v_{SW}$ is at its minimum, but $C_{SW}$ begins to receive energy from $L_X$ and $v_{SW}$ begins to rise. When $v_{SW}$ reaches $v_H$, the cycle begins again.

As the input voltage, $v_H$ in Figure 5.6, rises above $M_{SEN}$'s and $M_{FB}$'s threshold voltage, $M_{SEN}$ begins conducting inductor current and $M_{FB}$ begins providing positive feedback. Once positive feedback is established, the amplitude of oscillation grows exponentially until the amplitude settles. Since more input voltage allows more energy to be stored in the inductor and then delivered to $C_{SW}$, the amplitude also increases and follows the input voltage. This is why $v_{SW}$ in Figure 5.6 continues to increase until $v_H$ settles at 300 mV and $v_{SW}$'s peak voltage at 0.85 V. Although the 50 µs rise time in the input voltage in Figure 5.6 shows a significant improvement over the requirements of the circuit presented in Chapter 4, real-life energy harvesting transducers will have a wide range of rise times. Fortunately, the jump starter circuit in Figure 5.5 oscillates regardless of input rise rate. Figure 5.7 shows simulation waveforms of the circuit with an input rising in 100 µs, 1ms and 10 ms. The circuit is able to begin oscillations at the same minimum input voltage, $v_H$, regardless of rise rate.

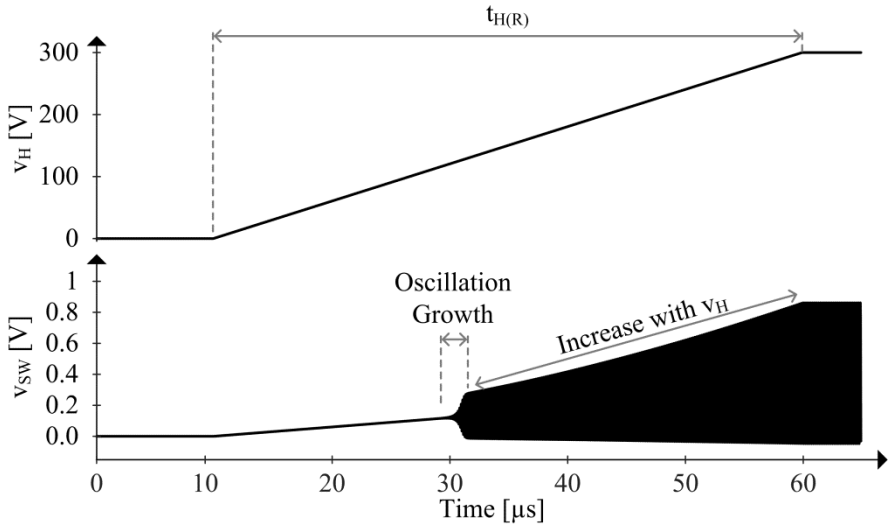


**Figure 5.6. Waveform showing self-startup of jump starter circuit with slowly rising input voltage.**

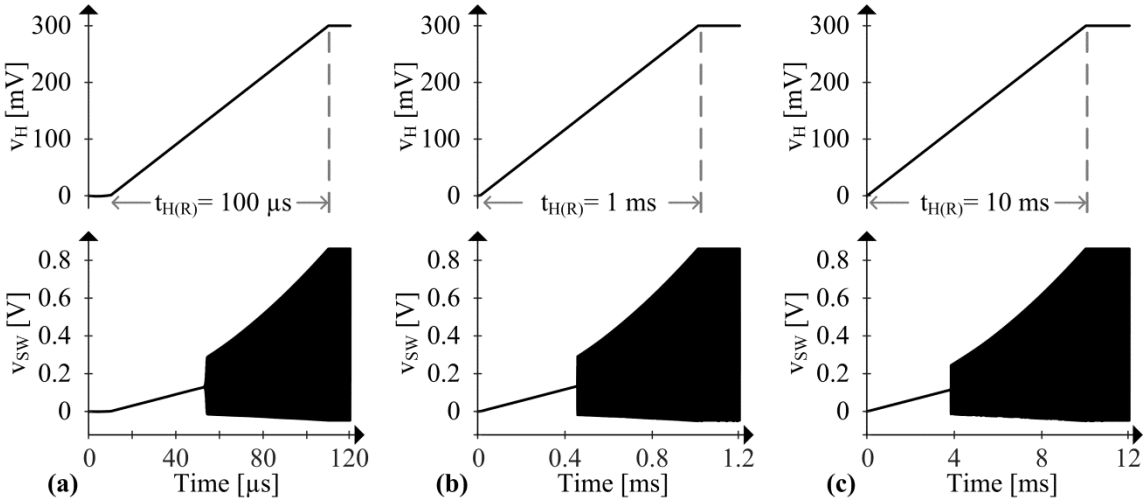


**Figure 5.7. Waveform showing jump starter circuit oscillating with input rise rates of (a) 100 µs, (b) 1ms, (c) and 10 ms.**

Note that although the jump starter oscillates from slow input rise rates, the amplitude at $v_{SW}$ is less than 1V. With the threshold voltage drop expected from a rectifier, this circuit can only charge the output capacitor to less than 0.5 V. Although decreasing $R_E$ would allow higher inductor currents and therefore more energy delivered to $C_{SW}$ and eventually $C_T$, it would cause the starter to draw a higher DC, or constant,

current from the input voltage. Since practical transducers cannot produce unlimited current, additional power drawn by the starter would cause a voltage drop at the input and prevent the starter from charging the output. However, combining the oscillator in Figure 5.2 with the oscillator in Figure 5.5 would create a high gain, self-starting oscillator that can be used as a starter circuit. The resulting circuit would simply replace $C_S$ in Figure 5.2 with a resistor $R_E$.

### 5.1.3 Resetting

With the introduction of the jump starter, the starter can now initialize oscillations and charge $C_T$ from slow rising input voltages. However, with slow rising inputs, the circuit may start oscillating prematurely. Since the starter presented in Chapter 4 only turned on with the activation of a power-on-reset switch or a fast rising input, it would only attempt to start under conditions that would guarantee startup. However, with the jump starter always on, the jump starter may turn on before $v_H$ reaches the minimum voltage of the oscillating core. As the jump starter turns on it begins drawing current. Real transducers cannot provide unlimited amounts of power and as the drawn current increases, its terminal voltage decreases. This is illustrated in the source model in Figure 5.8 where $R_S$ drops a voltage proportional to the current drawn.

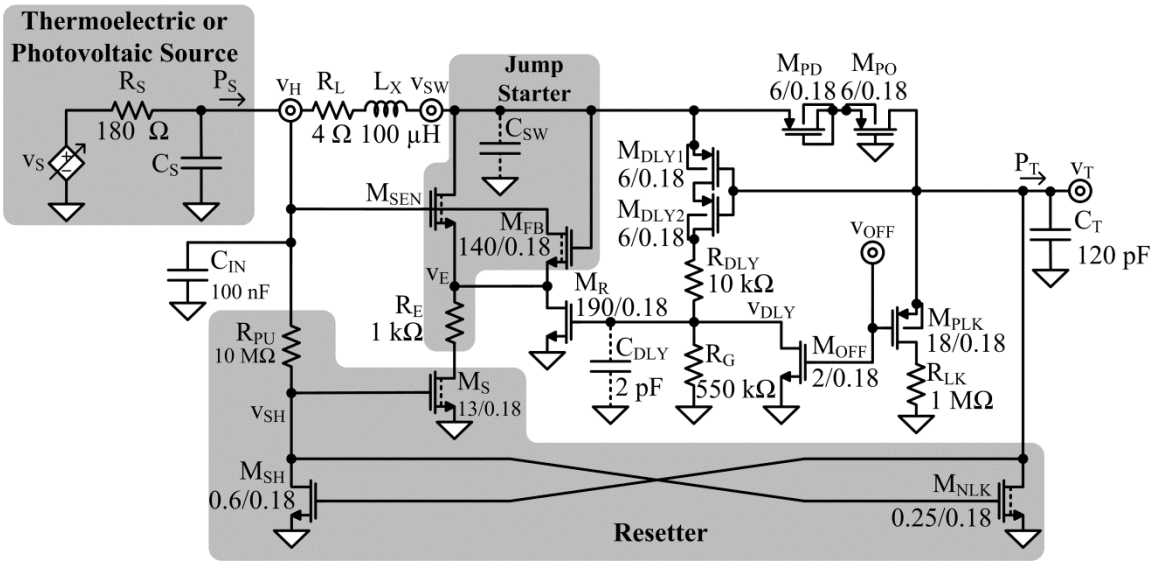


**Figure 5.8. Schematic of high-gain, self-starting oscillator with source model.**

Although the high gain starter can still produce high voltages for low inputs, if the input voltage reduces before startup completes, the output voltage will not reach its maximum level. For example, although $v_H$ in Figure 5.9 surpasses 300 mV, which according to Figure 5.3b should be enough for $v_T$ to reach 4V, $v_T$ only rises to 470 mV. When the oscillating core turns on, around 1.3 ms, the oscillator draws significant amounts of currents which cause $v_H$ to drop below the minimum input voltage, $v_{H(MIN)}$ before $v_T$ fully charges. When $v_H$ is below $v_{H(MIN)}$, the oscillator core is off, which is indicated by $M_R$'s drain current, $i_{D(MR)}$ going to zero. Although $v_H$ rises back above $v_{H(MIN)}$, $v_T$ is already above 200 mV, which means that the jump starter needs to charge $v_{SW}$ an additional 200 mV in order to start the oscillating core. However, since the jump starter has limited gain, it is unable to charge $C_{SW}$ high enough to turn $M_{DLY1}$ and $M_{DLY2}$ on and restart the oscillating core. Instead, for the remainder of the simulation, $C_T$ is weakly charged by the oscillations created by the jump starter. Additionally, since the jump starter remains on and continues drawing current, $v_H$ never reaches $v_S$.

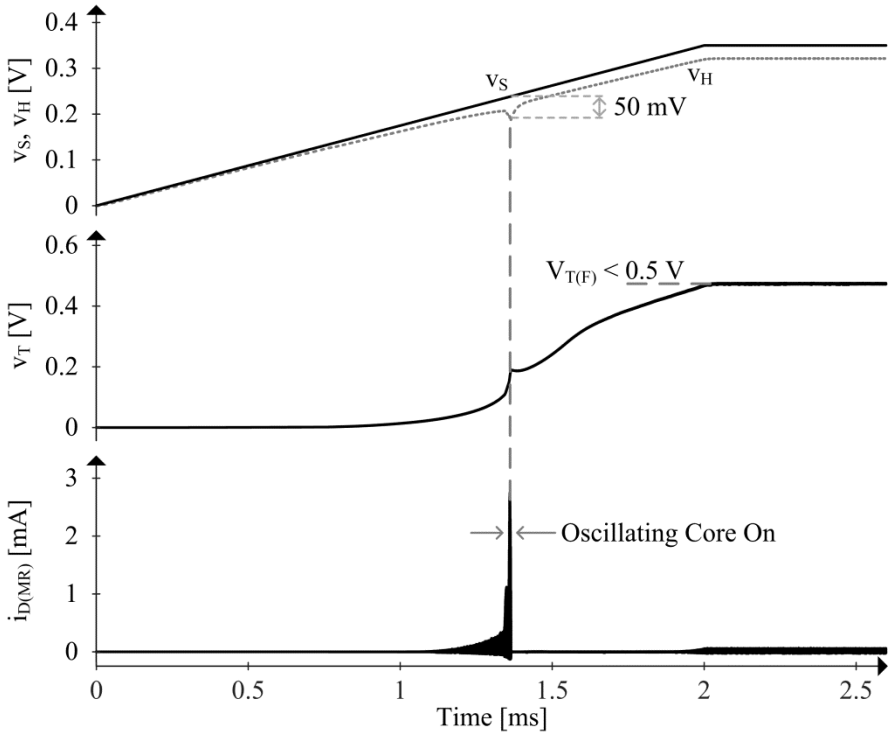


**Figure 5.9. Waveform of startup from a resistive source without reset circuit.**

To ensure that the starter reaches its target voltage for any rising input voltage, the resetter circuit in Figure 5.8 is added to the starter. The resetter has two main functions: discharge $C_T$ if $v_T$ does not reach its target and turn off the jump starter once $C_T$ begins charging. Discharging $C_T$ would allow the oscillating core to turn on after some time while $v_H$ recovers. The resetter circuit discharges the output capacitor through $R_{LK}$ and $M_{NLK}$. Turning off the jump starter while $v_T$ is not zero prevents $C_T$ from weakly charging as it does from 1.3 to 2 ms in Figure 5.9. The resetter in Figure 5.8 turns off the jump starter by enabling $M_{SH}$ when $v_T$ surpasses an NMOS threshold voltage. As $v_T$ rises, $M_{SH}$ turns on and pulls $v_{SH}$ low, turning $M_S$ off. With $M_S$ off, $R_E$ cannot conduct and the jump starter is disabled.

Running a similar scenario as Figure 5.9 with the resetter circuit allows the starter to charge the output, $v_T$ in Figure 5.10, above 1.5 V. Even with a resistive source causing

$v_H$ to fall when current is drawn, the starter circuit can charge $C_T$ to its target by disabling the oscillator when not charging and discharging the output when it has not reached its target. After the starter makes its first attempt, around 1.3 ms, $v_T$ only reaches 260 mV. However, by discharging $C_T$ and turning the oscillator off, $v_H$ can recover fully and reach $v_S$, so by the time $v_S$ settles at around 2 ms, the oscillator core can charge the output to 1.8 V. Therefore, resetting after each attempt allows the starter circuit to have more voltage at $v_H$ in its next attempt and charge $v_T$ to a higher voltage if $v_S$ continues to rise.

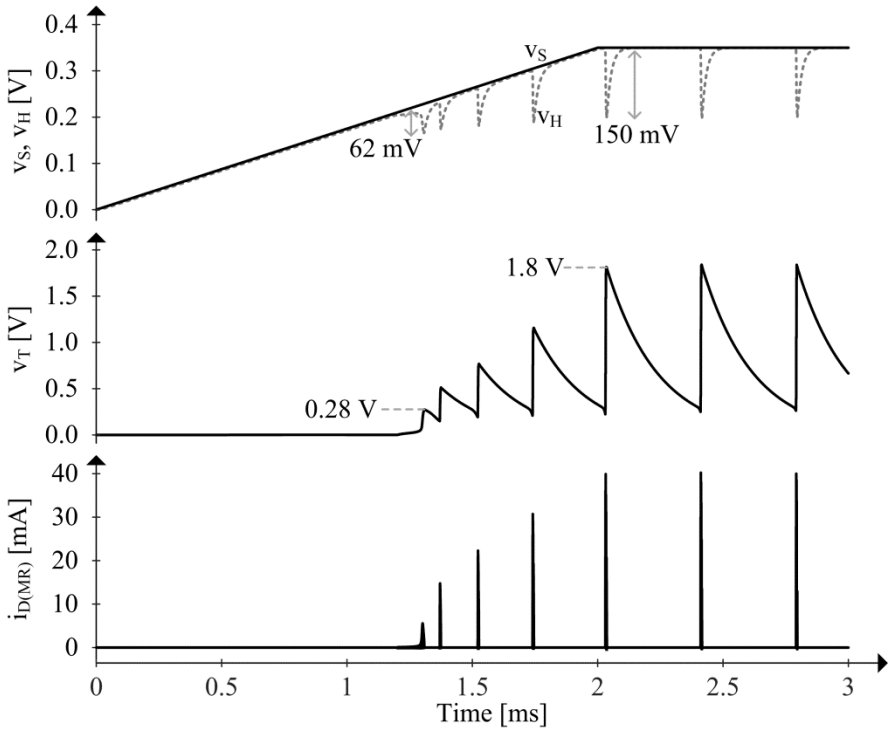


**Figure 5.10. Waveform of startup from a resistive source with reset circuit.**

## 5.2 Bootstrapping and Resetting Starter Prototype

A prototype of a starter combining the improved oscillating core, jump starter, and resetter was created using a 180-nm CMOS process and a 2-layer, FR4 printed circuit board. The goal of the prototype was to validate the design and simulations of the proposed starter circuit and verify the improvements made upon the previous prototype.

Since the previous prototype proved that the starter circuit did not affect the power conversion efficiency of the battery charger, a battery charger was not tested with this prototype. Test circuits on the board were also used to measure the operation and performance of the starter. The off-chip components that would be required in a final system, such as the inductor and input capacitance, were selected to provide maximum performance while only occupying the practical size expected in wireless microsystems. Other components which are not expected to be used in the final system or will be integrated on-chip later were selected to provide proper performance and functionality. These components were not necessarily designed for small size or low power consumption.

The switched inductor in Figure 5.8 implements the oscillating core that energizes and drains $L_X$ from a dc source, $v_S$, into a temporary supply, $C_T$. The jump starter bootstraps the circuit so oscillations that start from a low harvesting voltage $v_H$ can activate the oscillating core. The resetter restarts the oscillating core until the temporary supply reaches its target. The voltage source $v_S$, resistor $R_S$, and capacitor $C_S$ is meant to emulate a tiny thermoelectric or photovoltaic source with $R_S$ limiting the power generated by $v_S$ as a real transducer would. Input capacitance $C_{IN}$ is intentionally added to provide the starter circuit fast transient currents that would otherwise overwhelm the source. Finally, $R_L$ is the parasitic equivalent series resistance (ESR) of the inductor $L_X$, which introduces additional losses to the system.

### 5.2.1 Oscillating Core

When $v_H$ is at or above $v_{H(MIN)}$, the gate voltage of low-threshold switch $M_{SEN}$ is high enough for $M_{SEN}$ to draw current $i_L$ through $L_X$ into $R_E$. With a positive voltage across the

inductor, $L_X$ energizes from $v_S$. But as the inductor current, $i_L$, ramps (past 14.7238 ms in Figure 5.11), $R_E$'s voltage $v_E$ climbs and collapses $M_{SEN}$'s gate–source voltage. So $M_{SEN}$ opens and $i_L$ flows into $C_{SW}$ to charge $C_{SW}$ to $v_H$, which ends the energizing period $t_E$. With current energy still in $L_X$, $L_X$ then drains into $C_{SW}$ to raise $v_{SW}$ above $v_H$. If $v_{SW}$ rises two threshold voltages $2|v_{TP}|$ above $C_T$'s $v_T$: above $v_{SW(MIN)}$, diode and ground switches $M_{PD}$ and $M_{PO}$ close to deplete $L_X$ into $C_T$.

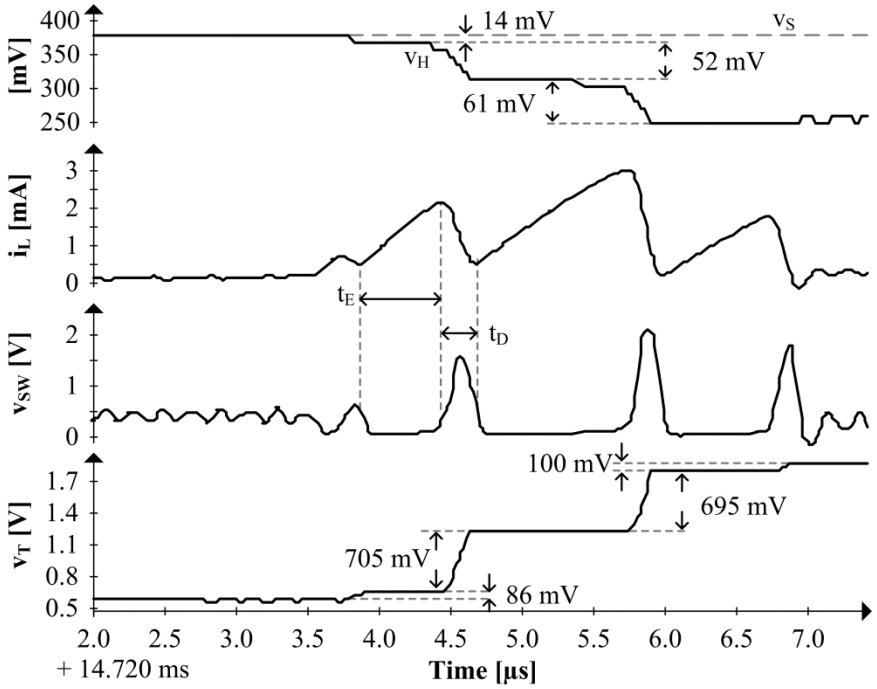


**Figure 5.11. Measured oscillating and charging waveforms.**

When $v_{SW}$ is high enough above $C_T$'s $v_T$, $M_{DLY1}$ and $M_{DLY2}$ close to steer some of $i_L$ into $C_{DLY}$. With sufficient energy, $C_{DLY}$ charges enough to close $M_R$ and re-engage $M_{SEN}$, and in so doing, drain $C_{SW}$. $v_{SW}$ therefore drops, and when $v_{SW}$ falls below $v_H$, $L_X$ begins to energize and start another cycle. But since $C_{DLY}$ and $R_G$ keep $M_R$ engaged for $t_G$, $L_X$ energizes that much longer on the second cycle so that $i_L$ peaks to a higher level.

Notice $C_{DLY}$ does not begin to charge until $v_{SW}$ rises above $v_T$ by $|v_{TP}|$. And $C_{DLY}$ does not trip $M_R$ until after $R_{DLY}$'s delay $t_{DLY}$. After $v_{SW}$ falls and $R_G$'s delay $t_G$, $R_G$ resets $M_R$'s

gate to zero. Like the oscillator presented in Chapter 4, $t_{DLY}$ should be long enough to ensure $C_T$ receives energy from $L_X$, but also shorter than the de-energizing time $t_D$. If $t_{DLY}$ is too short, the starter would still oscillate, but send less energy to $C_T$ per cycle, which would extend startup time. Conversely, if $t_{DLY}$ is longer than $t_D$, $v_{SW}$ would fall below $v_T + |v_{TP}|$ before $M_R$ turns on. This would shut $M_{DLY1}$ and $M_{DLY2}$, preventing $M_R$ from turning on and resetting $v_E$. The delay created by $R_G$ and $C_{DLY}$, $t_G$, should be shorter than the energizing time, $t_E$, so that $M_R$ turns off before de-energizing begins. Fortunately, $t_{DLY}$'s and $t_G$'s acceptable ranges are sufficiently wide to accommodate process and temperature variations in $R_{DLY}$, $R_G$, and $C_{DLY}$. Simulations confirm that $C_T$ charges to 1.4 V from 220 mV when $R_{DLY}$, $R_G$, and $C_{DLY}$ vary –50% to +100%.

$M_{PD}$–$M_{PO}$'s and $M_{DLY1}$–$M_{DLY2}$'s body diodes are head-to-head and back-to-back to block one another as $v_{SW}$ rises to $v_{SW(MIN)}$. This is important because leaking energy away from $C_{SW}$ can keep $v_{SW}$ from reaching its minimum threshold. $M_{PO}$ keeps $v_{SW(MIN)}$ from dropping below $2|v_{TP}|$ to ensure $v_{SW}$ is high enough to charge $C_{DLY}$ to at least $M_R$'s threshold voltage and re-engage $M_{SEN}$. As $v_T$ rises, $M_{PO}$ drops a lower voltage, and as a result, burns less power.

### 5.2.2 Jump Starter

For the core to oscillate, $v_{SW}$ must climb $|v_{TP}|$ above $v_T$ to close $M_{DLY1}$ and $M_{DLY2}$. $v_S$ and $L_X$ must therefore charge $C_{SW}$ above this $|v_{TP}| + v_T$ threshold $v_{SW(MIN)}$. But in addition to the energy required by the switch node capacitance, $0.5C_{SW}(|v_{TP}| + v_T)^2$, $v_S$ and $L_X$ must also supply $M_{SEN}$'s leakage and $v_S$'s and $L_X$'s ohmic losses in $R_S$ and $R_L$. For this, $L_X$ must first draw enough energy $E_L$ from $v_S$. Since $E_L$ climbs with $v_H$, $v_H$ must similarly surpass

a threshold $v_{H(MIN)}$. So to keep $v_{H(MIN)}$ low, $L_X$ and $M_{SEN}$'s off resistance should be high and $C_{SW}$, $|v_{TP}|$, $R_S$, $R_L$, $v_T$, and $M_{SEN}$'s on resistance low.

Although $M_{SEN}$'s current falls as $v_E$ rises, $M_{SEN}$ does not completely turn off. So $M_{SEN}$ leaks some of the inductor energy, $E_L$, away from $C_{SW}$. $M_{FB}$ reduces this leakage because, as $v_{SW}$ and $v_E$ climb, $M_{FB}$ shorts $M_{SEN}$'s gate–source terminals, completely turning $MS_{EN}$ off. The switching node, $v_{SW}$, and its parasitic capacitance, $C_{SW}$, therefore receive more of the inductor energy and charge to $v_{SW(MIN)}$ with less input energy. That way, a lower input voltage can charge $C_{SW}$ to $v_{SW(MIN)}$.

### 5.2.3 Resetter

Although $L_X$ loads $C_{IN}$, $v_S$ supplies much of the current that $L_X$ draws when energizing at 3.8–4.4 µs in Figure 5.11, so $v_H$ falls, but not by much. When $L_X$ drains at 4.4–4.7 µs, however, $M_{FB}$ closes and pulls additional current from $C_{IN}$. This is why $C_{IN}$ discharges and $v_H$ falls more at 4.4–4.7 µs than at 3.8–4.4 µs. The challenge with $v_H$ falling is that $v_T$ rises after $L_X$ delivers a packet to $C_T$, so $v_{SW}$ must climb to a higher threshold $v_{SW(MIN)}$. In other words, $v_{H(MIN)}$ increases with every cycle. And if $v_H$ falls below $v_{H(MIN)}$ after one cycle, $v_H$ may not be high enough to reach the higher $v_{H(MIN)}$. This can stall the circuit.

To fix this runaway problem, the starter can repeat the startup process until $C_T$ receives enough energy to supply the charger. For this, $M_{SH}$ shuts the jump starter (by opening $M_S$) each time $C_T$ charges above $M_{SH}$'s threshold $V_{TN0}$. $M_R$, however, can still help $L_X$ and $C_{SW}$ oscillate and charge $C_T$. So if $v_H$ does not fall below $v_{H(MIN)}$, like in Figure 5.11, $C_T$ can charge to its target in one or two more cycles.

If $v_H$ falls below $v_{H(MIN)}$, the core stops oscillating. This removes the load that droops $v_H$, so $v_H$ rises to $v_S$. Meanwhile, $M_{PLK}$ discharges $C_T$, so $v_{H(MIN)}$ also falls. When

$v_T$ falls low enough below $V_{TN0}$, $M_{SH}$ opens to close $M_S$ and reactivate the jump starter. These attempts continue until $v_H$ is high enough to charge $C_T$ fully. At that point, the system sends an off signal $v_{OFF}$ that disables the oscillating core so it can no longer reset. $v_{H(MIN)}$ is therefore the voltage necessary to charge $C_{SW}$ $|v_{TP}|$ above $v_T$'s reset level $V_{TN0}$ and $C_T$ to its target from $V_{TN0}$.

### 5.2.4 Stopping Oscillations

Once the starter charges $v_T$ past its target voltage, the temporary supply, $C_T$, can provide voltage and power to the rest of the system and the starter can be disabled. The starter presented in Chapter 4 could be turned off by enabling $M_{OFF}$, which shorted $v_{DLY}$ and prevented further oscillations. Similarly, $M_{OFF}$ in the starter in Figure 5.8 shuts down the oscillating core and keeps $M_R$ off. During startup $M_{PLK}$ discharges $C_T$ when $v_{OFF}$ is low. However, as $v_{OFF}$ is raised to $v_T$, which is $M_{PLK}$'s source voltage, $M_{PLK}$ is turned off and the leakage path is removed. Additionally, with $v_T$ above $V_{TN0}$, $M_{SH}$ is on, which pulls $v_{SH}$ low and disables the jump starter. With $v_{SH}$ low, $M_{NLK}$ is also off so it does not discharge $C_T$.

An off-chip comparator and reference voltage was used to detect when $v_T$ reached its target voltage of 1.8 V. As $v_T$ surpassed the reference, $V_{REF}$ in Figure 5.12, comparator $CP_T$ tripped and applied a high voltage to $v_{OFF}$. Since the comparator was used for testing purposes only, an external supply was used for it, so it was always on regardless of $C_T$'s voltage. In a final system, $v_T$ would supply $CP_T$. A comparator with hysteresis was used to avoid $v_{OFF}$ going back low when leakage or noise caused $v_T$ to reduce.

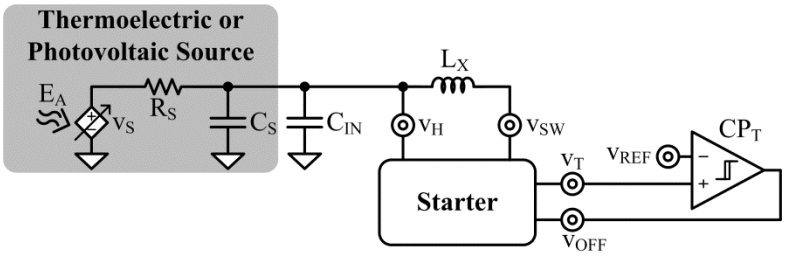


**Figure 5.12. Schematic of external components controlling the starter.**

## 5.3 Measured Performance

The 200 × 370-μm$^2$ die in Figure 5.13 integrates the bootstrapping and resetting 0.18-μm CMOS starter and the 120-pF temporary supply $C_T$ in Figure 5.8. The ambient source, transfer inductor $L_X$, and input capacitor $C_{IN}$ are off chip. A 0–400-mV source $v_S$ and a 180-Ω series resistor $R_S$ emulate the thermoelectric source. The 100-μH inductor includes 4 Ω of series resistance and occupies 2 × 1.25 × 1.45 mm$^3$. The 100-nF capacitor includes 100 mΩ of series resistance and measures 1.6 × 0.8 × 0.6 mm$^3$. For testing purposes, the board also includes an off-chip comparator that monitors $C_T$'s $v_T$ to generate the off signal $v_{OFF}$ that the charger in Figure 5.1 outputs when $v_T$ is high enough to operate the charger.

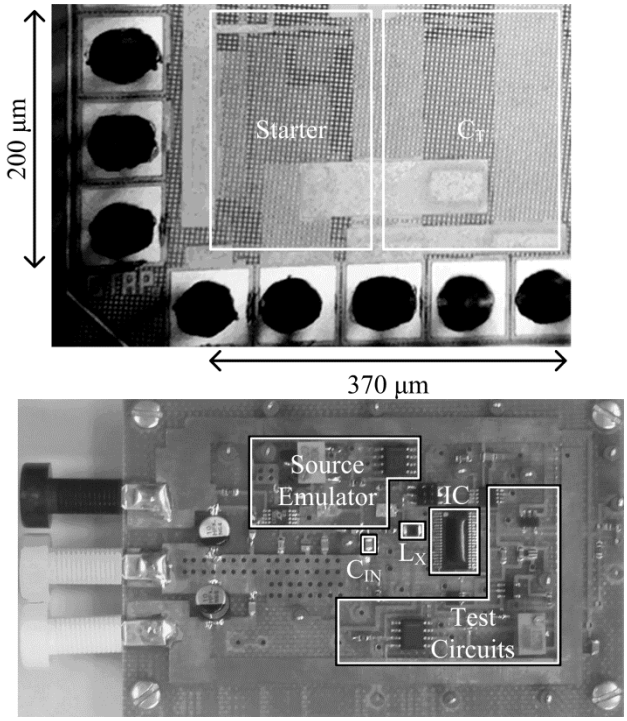


**Figure 5.13. Prototyped die and experimental board.**

### 5.3.1 Startup

One of the most important goals of this prototype was to verify the functionality of the starter and the proper operation of its three main components: the oscillating core, the jump starter and the resetter. In general the starter will go through three phases of operation: the off phase, the bootstrap phase, the reset phase and the charge phase. Additionally, if the input rises slowly enough, the starter may repeat some of the phases. The off phase encompasses the initial time where the input voltage, $v_H$, is so low that $M_{SEN}$ and $M_{FB}$ are off and there are no oscillations. During the bootstrap phase, the jump starter oscillates until the amplitude at $v_{SW}$ is large enough to engage the oscillating core. If, after the bootstrap phase, the output of the starter, $v_T$, does not rise enough, the starter moves into the reset phase and $C_T$ is discharged and the oscillator is turned off. Finally,

the charging phase occurs after a bootstrap phase only when $v_H$ is high enough so that the starter can charge $C_T$ to its target voltage.

*Off Phase:*

After a prolonged harvesting drought, the charger depletes the input capacitor $C_{IN}$ and the load empties the battery $C_B$. So when ambient energy first raises $v_S$ above ground, all nodes in the circuit are near ground. As long as $v_H$ remains below 180 mV in Figure 5.14, nothing conducts current. As long as $v_H$ remains below the threshold voltages of $M_{SEN}$ and $M_{FB}$, the starter remains off. Since no current is drawn from the input, there is no voltage dropped across $R_S$ so $v_H$ and $v_{SW}$ follow $v_S$ as $v_S$ ramps up.

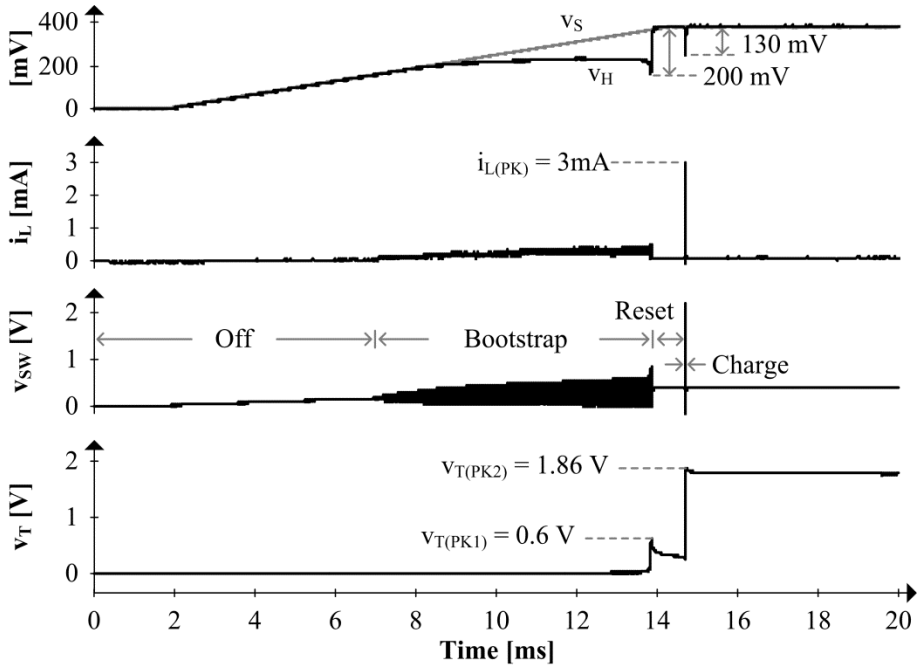


**Figure 5.14. Measured startup waveforms.**

*Bootstrap Phase:*

At and above 180 mV, $M_{SEN}$ in the starter conducts enough current to energize $L_X$, but not enough for $L_X$ to raise $v_{SW}$ to charge $C_T$ and engage $M_R$. Still, with the help of $M_{FB}$, $L_X$ depletes into $C_{SW}$ and $C_{SW}$ drains back into $L_X$. As $v_H$ rises above 180 mV, $L_X$ and

$C_{SW}$ exchange energy without drawing or delivering much power. As oscillations grow, however, the inductor peak current begins to increase. This loads the source, so that at about 9 ms, when $v_S$ is 200 mV, $v_H$ begins to droop below $v_S$. With $v_H$ just below the minimum threshold $v_{H(MIN)}$, the jump starter continues to bootstrap $v_{SW}$, so oscillations grow and loading persists, but $C_T$ still does not charge.

*Reset Phase:*

As the oscillations on $v_{SW}$ grow, $M_{DLY1}$ and $M_{DLY2}$ begin to turn on and charge $C_{DLY}$. When the energy leaked into $C_{DLY}$ is sufficiently high to engage $M_R$ in Figure 5.8, the oscillating core begins to operate. So, at 13.8 ms in Figure 5.14, $L_X$ draws considerably more energy from $v_S$ than in the bootstrapping phase. As a result, $v_H$ dips further and excess $L_X$ energy charges $C_T$ to 0.6 V. Drawing so much current from the input causes $v_H$ to drop below $v_{H(MIN)}$, so the oscillating core stops. Since $v_T$ is not high enough for the charger to operate and shut the starter, $v_{OFF}$ remains low. However, becuase $v_T$ has risen above $M_{SH}$'s threshold voltage, $M_{SH}$ shuts the jump starter. This completely removes the load on $v_H$, so that it can recover to $v_S$. $M_{PLK}$ discharges $C_T$ until $M_{SH}$ again opens at 14.7 ms to reactivate the starter. Without a load, $v_H$ is now high enough at $v_S$ to charge $C_T$ to 1.86 V. So at this point, the comparator that emulates the charger raises $v_{OFF}$ to disable the starter.

### 5.3.2 Reliable Starts

The starter incorporates three oscillators that must start and interface reliably to charge the temporary supply $C_T$. More specifically, the jump starter should start and oscillate until $v_{SW}$ is high enough to activate the oscillating core. The core must then oscillate and charge $C_T$. If $C_T$ does not reach the voltage the charger requires, the resetter must shut

and reactivate the starter and oscillate this way until $C_T$ fully charges. Once $v_T$ reaches its target voltage, the system would then shut down all three oscillators.

To determine the minimum input voltage level, $v_{H(MIN)}$, above which the starter can charge $C_T$, the input source, $v_H$ in Figure 5.15, should ramp at a rate that is much slower than the startup time $t_{ST}$ of the system. Note that in this test, $R_S$ is removed so that $v_S$ and $v_H$ are equal. This way, the impact of startup dynamics on measured readings is minimal. In the case of Figure 5.15, rise time $t_{H(R)}$ is over 0.5 s. This value is orders of magnitude greater than the 15–135 µs that the starter requires to charge $C_T$. Measurements therefore demonstrate that the starter starts with 215–222 mV across five measured sampled chips.

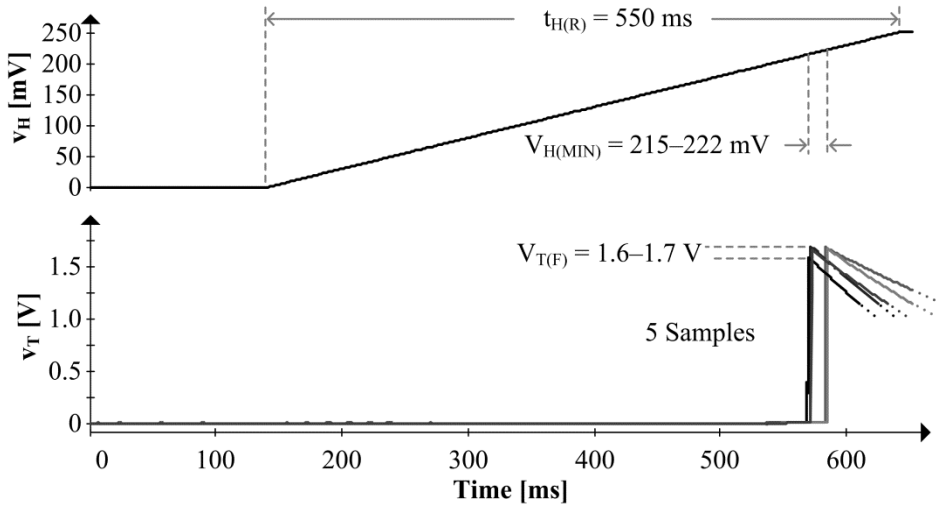


**Figure 5.15. Measured minimum input threshold.**

In the case of energy harvesters, ambient energy can vanish and reappear slowly. And in some cases, an external force or signal can suddenly inhibit and reconnect an ambient source. The system must therefore be able to start from slow- and fast-rising ramps. But to start, the input $v_H$ must surpass the 215–222-mV minimum level $v_{H(MIN)}$

that the starter requires to operate. This is why $v_H$ in Figure 5.16 rises to 250 mV in 100 ns and 1, 5, and 10 ms. In all cases, the starter charges $C_T$ to 1.8 V.

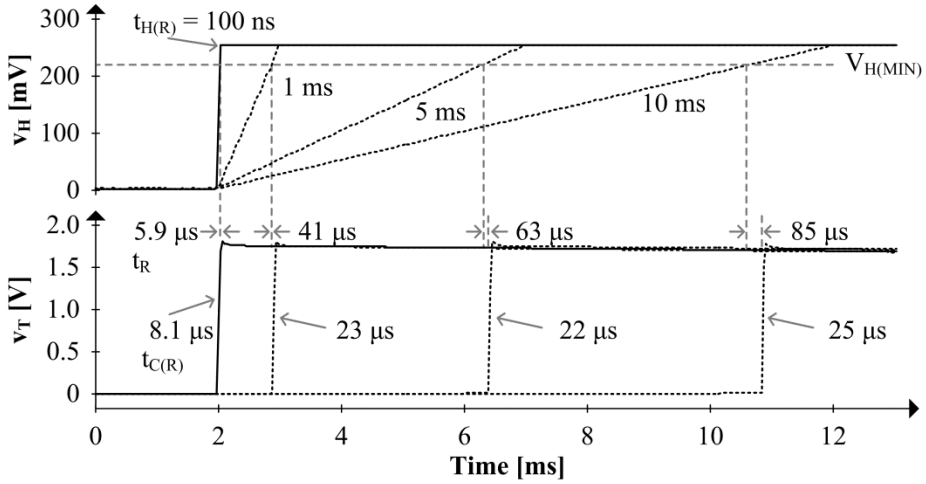


**Figure 5.16. Measured starts for 100 ns–10 ms input rise times.**

### 5.3.3 Startup Time

Startup time $t_{ST}$ is the time after $v_H$ reaches $v_{H(MIN)}$ that the system requires to charge $C_T$ to, in this case, 1.8 V. When $v_H$ rises in $t_{H(R)}$ or 1, 5, and 10 ms in Figure 5.16, for example, the starter requires $t_R$ to react and $t_{C(R)}$ to charge $C_T$. For rise times of 1, 5, and 10 ms, the starter requires 41, 63, and 85 µs respectively to react and 22–25 µs to charge $C_T$. Total startup times, which include reaction time and charge times, are 64, 85, and 110 µs. Startup delay or response time $t_R$ increases with $t_{H(R)}$ because $v_H$ rises less quickly. So by the time $C_T$ charges, $v_H$ reaches a lower level. And with a lower overdrive voltage, the jump starter requires more time to activate the oscillating core.

Charge time $t_{C(R)}$ is consistent at 22–25 µs for 1-, 5-, and 10-ms rise times because $v_H$ and the time $t_E$ across which $L_X$ energizes do not vary much. Charging time is 66% shorter at 8 µs when $t_{H(R)}$ is 100 ns because $v_H$ rises above the minimum threshold $v_{H(MIN)}$

before the starter can respond. As a result, the oscillating core energizes $L_X$ without help from the resetter. In other words, $t_{C(R)}$ excludes reset delays.

When $v_H$ rises to 220–250 mV in the same time span, across 100 ns, charge time $t_{C(R)}$ in Figure 5.17 is fairly constant at 8 µs. This means, reset delays remain absent. Response times $t_R$, however, fall from 32–52 to 6–16 µs with ascending $v_H$ levels, as $v_H$ peaks increase from 220 to 250 mV. The culprit for this rise in $t_R$ is the jump starter. This is because $v_{SW}$ in Figure 5.8 requires more time to bootstrap to $v_{SW(MIN)}$ when $v_H$ is lower.

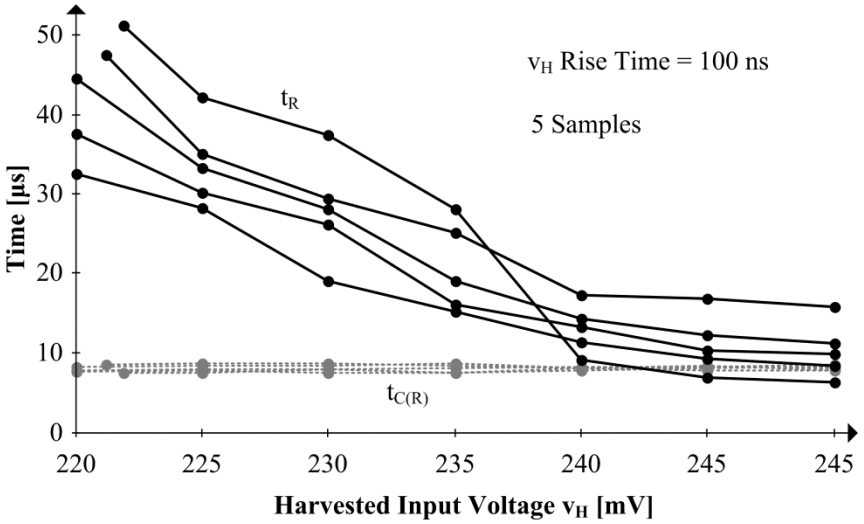


**Figure 5.17. Measured startup times after stepping the input.**

### 5.3.4 Energy Management

Wake time for energy-harvesting microsensors is a critical parameter because ambient sources can vanish and reappear without notice. Charging systems should therefore charge a battery $C_B$ quickly. And for that, $C_B$ should receive as much power as possible. With the temporary supply $C_T$ that the starter in Figure 5.1 and Figure 5.8 establish, the charger can do this: output 80%–90% of the power it harvests [151]. This is possible

because $v_T$ is high enough at 1.8 V, for example, to keep resistances in the network in the milliohm range.

Before the battery can receive power, however, the starter must charge the temporary supply, $C_T$. But with only millivolts provided by the harvesting transducer, starters do not have milliohm transistors with which to switch the inductor $L_X$. So transistors burn a large fraction of the power that could otherwise reach $C_T$. As a result, ohmic losses in the starter extend the time that $C_T$ requires to charge. In the case of the prototyped starter, $M_{FB}$ in the jump starter and $M_{SEN}$ in the energizing path in Figure 5.8 burn the most energy across the charging process. $M_{FB}$'s loss is significant at 4.4–16 nJ when $v_H$ rises to 235–300 mV in 100 ns in Fig. 9. This is because $M_{FB}$ draws substantial current from the harvested input $v_H$ every time $v_{SW}$ rises (as $L_X$ drains).

$M_{SEN}$ dissipates the next highest loss at 0.6–1.2 nJ every time $L_X$ energizes. Because of $M_{SEN}$'s limited gate drive, the inductor energizes into a resistive $M_{SEN}$. This high resistance causes significant losses. The rest of the circuit consumes another 200 pJ. So in delivering 194 pJ to charge $C_T$'s 120 pF to 1.8 V, the starter outputs 1.5%–7% of the power the ambient source supplies when $v_H$ rises to 235–300 mV. However, since startup lasts less than 60 μs, the low efficiency does not significantly affect system performance.

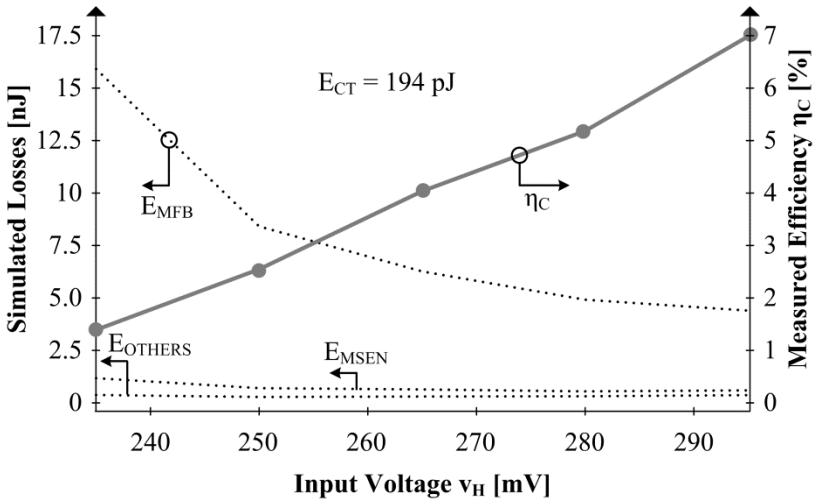


**Figure 5.18. Simulated losses and measured power efficiency.**

### 5.3.5 Relative Performance

*Integration:*

Because microsensors are useful in many more applications when they are smaller, one critical parameter to consider is integration. In this case, the starter requires a 200 × 370-$\mu m^2$ 0.18-µm CMOS die and a 2 × 1.25 × 1.45-$mm^3$ 100-µH inductor. Combined, the starter occupies about 4 $mm^3$, which compares very favorably with the transformer-based oscillator, motion-activated switch starter, and LC oscillator presented in Chapter 3 and summarized in Table 4.1. The size of the starter presented here is comparable with the ring oscillator driven starters, both tuned and natural, also from Chapter 3 and summarized in Table 4.1.

**Table 5.1. Performance summary and the state of the art.**

| | X-Former [149] | MEMS Switch [128] | LC Osc. [152] | Ring Oscillator | | Chapter 4 | This Work |
|---|---|---|---|---|---|---|---|
| | | | | Tuned [145] | Natural [150] | | |
| $V_{H(MIN)}$ | 40 mV | 35 mV | 50 mV | 80 mV | 330 mV | 300 mV | 220 mV |
| $C_T$ | 10 µF | 470 pF | 4.7 nF | 30 pF | – | 100 pF | 120 pF |
| $V_{TAR}$ | 1.2 V | 1 V | 0.8 V | 1.3 V | 1.8 V | 0.55 V | 1.8 V |
| $t_{ST}$ | 4.9 s | 3 ms | 15 ms | 4.8 ms | 1.2 s | 44 µs | 59 µs |
| $I_{EQ}$ | 2.45 µA | 157 nA | 251 nA | 8 nA | – | 1.25 µA | 3.66 µA |
| $\eta_{ST}$ | – | – | – | – | – | 0.50% | 1.50% 7% |
| Other | 1:60 X-Former | 22 µH 22 µH MEMS Switch | 2 µH 2 µH 100 µH 27 µH | 6.8 µH | – | 100 µH | 100 µH |
| Vol. | 175 $mm^3$ | 150 $mm^3$ | **16 $mm^3$ | **4 $mm^3$ | 4 $mm^3$ | 4 $mm^3$ | 4 $mm^3$ |
| Tech. | 0.13 µm | 0.35 µm | 65 nm | 65 nm | – | 0.18 µm | 0.18 µm |

The amplifying transformer-based oscillator requires a 1:60 transformer that, at 175 $mm^3$, occupies 43× more space than the 4 $mm^3$ required here. The motion activated switch uses a MEMS device that switches in response to vibrations. Relying on such a switch is a drawback because the charger can only start when motion is present. Using a motion activated switch also requires two inductors, one for startup and one for steady state, that, at 150 $mm^3$, occupy 38× more volume than the starter presented here. An LC oscillator can be smaller and is not reliant on external forces. Although the size of the inductors is not reported, with four inductors, it still occupies around 16 $mm^3$, which is 4× more space.

At 4 $mm^3$, both tuned and natural ring oscillator starters are comparable in size. The challenge with tuning a ring oscillator is cost. Because to start from 80 mV, P- and N-type transistor threshold voltages in the ring oscillator that start the system must balance *specifically* for that purpose. So tuning requires post-processing steps in the fabrication process to adjust threshold voltages. These steps are costly and time consuming, and without them, the minimum threshold would be that of their less demanding siblings in the natural case: 330 mV.

Capacitor and super capacitors receive and deliver power at any voltage across more than 500k recharge cycles [24]. Lithium- and nickel-based chemistries operate at higher voltages, so $v_{H(MIN)}$ can be higher and $t_{ST}$ longer. They also only recharge 1k–1.2k times [24]. Unfortunately, tiny devices can deplete so often that cycle life must be higher. So although this and others in Table I can charge many types of batteries, capacitors and super capacitors are more likely candidates.

*Startup Time:*

Another equally important parameter is startup time $t_{ST}$. This is because each time the ambient source vanishes and reappears, $t_{ST}$ determines if and what the sensor can accomplish. $t_{ST}$, however, changes with capacitance $C_T$ and target voltage $V_{TAR}$, so comparing $t_{ST}$ alone can be misleading. But since $V_{TAR}$ and $C_T$ will, for the most part, extend $t_{ST}$ in the same way, equivalent $C_T V_{TAR}/t_{ST}$ current $I_{EQ}$ is a better figure of merit (FoM). From this perspective, $I_{EQ}$ for the starter presented here is 3.66 μA, which is 23×, 15×, and 458× higher than a motion-activated switch starter, an LC oscillator, and a tuned ring oscillator. Even without a bulky transformer, the starter presented here charges with $I_{EQ}$ 50% higher than an amplifying transformer-based oscillator.

*Minimum Threshold:*

While the transformer-based oscillator can start from an input voltage as low as 40 mV, more space and higher costs are the ultimate tradeoffs. Similarly, using a MEMS switch is costly and relies on vibrations to start from 35 mV. An LC oscillator requires four inductors to achieve a 50 mV minimum input voltage. To reduce the minimum input voltage of a ring oscillator from 330 mV to 80 mV requires costly post-processing tuning. Therefore, more space, higher cost, and longer starts are the ultimate tradeoffs for lower input threshold $v_{H(MIN)}$ in the state of the art.

Minimum input voltages for these technologies, 35–80 mV, are 16%–36% of the 220 mV that the circuit here requires. But if space and cost are critical constraints, which is the case for many emerging applications with wide-area networks, $v_{H(MIN)}$ is unfortunately a necessary sacrifice. This sacrifice, however, is 50% more severe for a natural ring oscillator at 330 mV than for the starter proposed here.

*Predecessor:*

The starter here differs from its predecessor in Chapter 4 in three basic ways. First, the previous oscillator energizes $L_X$ into a capacitor and the oscillating core here into a resistor $R_E$. Of the two, $R_E$ establishes a higher voltage more quickly and conducts regardless of input rise time. $M_{SEN}$ therefore shuts sooner and more effectively, and as a result, loses less energy. And although the capacitor receives charge it can hold, the previous oscillator nevertheless drains it to ground, which results in a loss of energy.

The feedback transistor, $M_{FB,}$ closes a bootstrapping positive feedback loop that is absent in Chapter 4. This loop starts oscillating and bootstrapping the circuit from a lower input voltage. Plus, the starter incorporates a resetter that restarts the circuit until $L_X$ can

charge $C_T$ fully. Without these improvements, the previous implementation only starts when a non-resistive input rises in less than 300 ns, $C_T$'s final voltage varies with input voltage, conversion efficiency is 3×–14× lower, and the minimum input threshold is 80 mV higher.

## 5.4 Summary

The robust bootstrapping starter presented here addresses and overcomes the limitations of the starter presented in Chapter 4. First, by introducing an additional positive feedback loop, the starter has increased gain between its input and output voltages. This allows the starter to fully charge its output, a temporary supply, with a lower input voltage. Second, by replacing the energizing element in Chapter 4, a capacitor, with a resistor, the starter is able to initialize oscillations regardless of the rise time of the input voltage. Finally, real transducers provide a very limited amount of power which manifests as a decrease in voltage when current is drawn. A resetter circuit was added to the oscillator to handle situations where the input voltage collapses before the output is fully charged. By combining a jump starter and resetter to an oscillating core, the goals of a robust and high gain starter were fulfilled.

The designed starter was then prototyped and tested to validate the theory and compare to the state of the art. By sharing the inductor with the battery charger, it does not add volume to the overall system. Other than the already present inductor, the entire starter and temporary supply are on-chip, so cost remains low. The 0.18-μm CMOS starter prototype charges 120 pF to 1.8 V in 15–59 μs with 1.5%–7% of the power it draws from a 180-Ω, 220–250-mV source. Charging a temporary supply this quickly is important, because with 1–2 V, a charger can deliver 80%–90% of the power it harvests.

This way, the time required to charge both the smaller temporary supply and the larger battery is much faster than charging the larger battery alone with the less efficient starter. A wireless microsensor can therefore wakeup much quicker. And this way, the system can perform many more tasks in the brief time that an ambient source is strong enough to overcome losses and supply power.

# CHAPTER 6

# SELF-STARTING CHARGER SYSTEM

Tiny transducers powering wireless microsensors produce voltages in the range of tens to hundreds of millivolts. Operating from such a low input voltage is challenging because, with low gate drive, transistors are resistive, and as a result, lossy. The charger can therefore consume much of the power drawn, leaving little left for the battery and other blocks. As a result, the battery charges slowly, if at all, and the microsensor must wait for the battery voltage to reach a headroom level that is high enough for system components to perform their prescribed tasks. This is a problem when the source appears across short intervals because the battery voltage may not rise sufficiently to power the sensor, and leakages may drain the battery before the harvesting source is available again. The charger should therefore replenish the battery as quickly as possible, and since space is scarce in a microsystem, do so with as few off-chip components as possible.

The starter circuit presented in Chapter 5 charges a small capacitance to well above the headroom level in under 100 μs. However, because of its low efficiency, charging the battery directly would lead to impractically long startup times. Therefore, the starter should only be used to charge a small capacitor to the headroom level to be used as a temporary supply for the maximum power point (MPP) charger in Figure 6.1. With the temporary supply providing the gate drive and quiescent current requirements of the MPP charger, the battery can be charged with the full efficiency of the charger. As Chapter 2 predicts, charging a smaller capacitor with the starter and then charging the battery with the MPP charger should significantly reduce the wake time of the system

This chapter describes and proposes a maximum power point charger, which uses the starter from Chapter 5 to create a temporary supply with which the system can use for high efficiency battery charging, until the battery is fully charged.

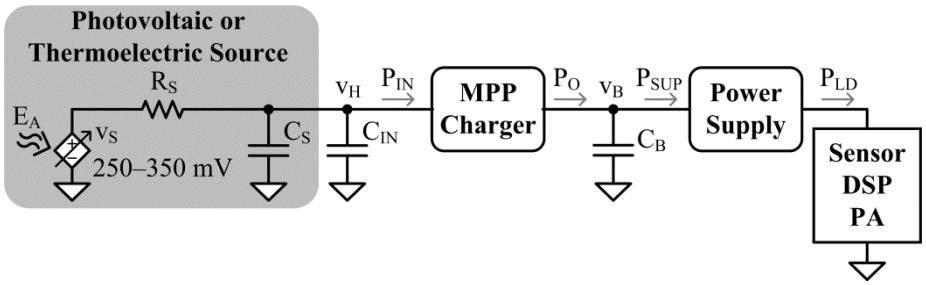


**Figure 6.1. Light- or heat-harvesting microsensor.**

## 6.1 Energy Harvester Operation

The fundamental reason why batteries charge slowly from no-charge conditions is that the only voltage available, the input source, produces low gate drive for the charger. The problem is, with low gate voltages, transistors are resistive and therefore lossy. So, of the power drawn from the transducer, only a small amount reaches the battery. Furthermore, because of the large capacity of the battery, microfarads or millifarads in the case of supercapacitors, the battery voltage climbs slowly. To reduce charge time, the system should start to a smaller temporary supply, which can be used to drive low resistance switches, which can efficiently charge the battery. The temporary supply must be small enough to charge quickly, but hold enough charge to provide gate drive and quiescent current requirements to the battery charger.

### 6.1.1 System Operation

The guiding principles that drive the design here are: small capacitors charge quickly and transistors switch faster and more efficiently when supplied from higher

voltages. So, the basic aim of the proposed system is to charge a very small temporary supply, $C_T$ in Figure 6.2, from which circuits can later draw power. The temporary supply must be charged above the headroom voltage, $V_{HR}$, which transistors need to switch efficiently. This way, with over 0.9 V, for example, the switcher can deliver 80%–90% of the drawn power [151], instead of the 0.1%–7% that a millivolt supply could have supplied [128], [132], [133], [145], [147], [149], [150], [152], [161]. For this, the system should first charge a small on-chip supply capacitor $C_T$ to a level that is high enough to feed the switcher without dropping below $V_{HR}$. To store as much energy as possible with the least capacitance, $C_T$ should charge to the technology's breakdown level $V_{BD}$. And at that level, capacitance should be sufficiently high to store the energy the charger needs to deliver at least two energy packets: one to $C_T$ and another to the battery $C_B$.

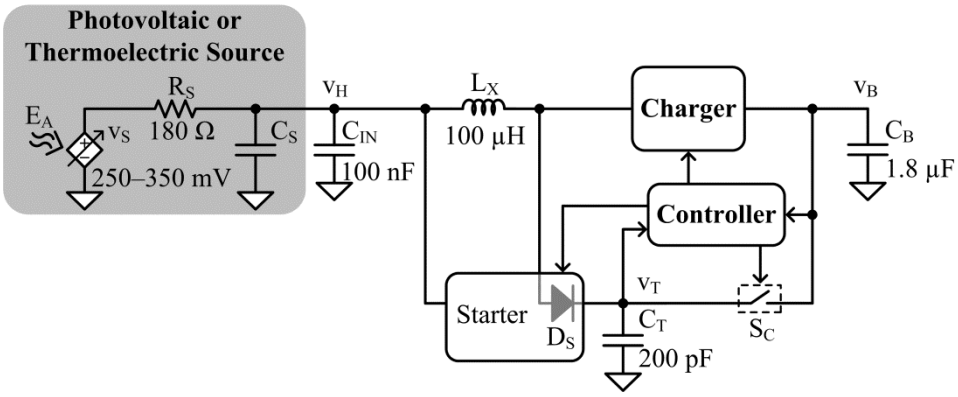


**Figure 6.2. Schematic of harvester system.**

To begin the wakeup process, the starter block from Chapter 5 charges the temporary supply, $C_T$, from a photovoltaic or thermoelectric source using the inductor $L_X$. Although the system is inefficient when first charging $C_T$ with the harvesting input voltage $v_H$, $C_T$ is so low at 200 pF that the process can be fairly short. Once $C_T$ is charged past the headroom level, the controller is enabled and battery charging can begin. The

controller monitors the temporary supply voltage, $v_T$, and the battery voltage, $v_B$ to maintain $v_T$ above $v_{HR}$ and short switch $S_C$ when the battery reaches $V_{HR}$.

The controller uses the charger block to efficiently send energy to the battery by energizing and de-energizing the inductor with low resistance switches. When the temporary supply is discharged to the headroom level, it must be refreshed by energizing the inductor through the charger block and de-energizing the inductor through diode $D_S$ inside the starter block and into $C_T$. $v_T$ should not be allowed to discharge below the headroom level, since this would require the system to return to the inefficient startup phase. Keeping $C_T$'s voltage, $v_T$, above the headroom level throughout this process allows the switcher to supply 80%–90% of the drawn power.

The system delivers energy packets to $C_T$ and $C_B$ this way, in alternating cycles, until the battery charges above the headroom level. Past that point, the controller enables switch $S_C$ and shorts the temporary supply with the battery so, together, both capacitors supply the switcher. So in all, the system is only inefficient when charging $C_T$ to $V_{HR}$ the first time. After that, as $C_T$ supplies the charger and later when $C_B$ supplies the charger, the charger can be 80%–90% efficient. Delivering this much charge to $C_B$ is how the system reduces wake time after harvesting droughts.

### 6.1.2 Wakeup Sequence

While the input source is not available, the system remains in the off phase. As the source returns, and the input voltage surpasses the starter's minimum input voltage, $V_{H(MIN)}$ in Figure 6.3, the system enters the startup phase. The starter block then uses the inductor, $L_X$, to charge the temporary supply, $C_T$, to the headroom level, $V_{HR}$. The low gate drive provided by $v_H$ makes the startup phase inefficient, but, fortunately, because of $C_T$'s

small size, this phase is short and not much energy is consumed to charge $C_T$. The controller, now supplied by $v_T$, detects that $v_T$ has risen above $V_{HR}$, and disables the starter. Before beginning to charge the battery, the controller ensures that $v_T$ is above threshold level $V_{TH}$, and if not sends an additional energy packet to $C_T$. Threshold level $V_{TH}$ is slightly above $V_{HR}$ and is simply meant to provide margin to the system so that $v_T$ does not go below $V_{HR}$ before it is refreshed.

Once the controller begins sending energy packets to the battery, $v_B$ begins to rise and the system enters the charging phase in Figure 6.3. Since $C_T$ supplies the controller and charger with quiescent and gate drive power respectively, $C_T$ discharges and $v_T$ falls. If $v_T$ were to fall below $V_{HR}$, the charger would not operate correctly and the system would return to the startup phase. To prevent this, the controller detects when $v_T$ has fallen below threshold level $V_{TH}$ and sends an energy packet to $C_T$ in between energy packets to $C_B$. This way, the system keeps $v_T$ loosely regulated above $V_{TH}$. The system continues alternating packets while the battery is charging so that $v_B$ rises until $v_B$ reaches $V_{TH}$. Once $v_B$ reaches $V_{TH}$, $v_B$ is high enough so that $C_B$ can now supply the system. Therefore, at this point, $C_T$ and $C_B$ are shorted together. Since $C_B$ is so much greater than $C_T$, $v_T$ in Figure 6.3 falls to $v_B$ while $v_B$ barely changes due to the short. Once $C_T$ and $C_B$ are shorted, energy packets are only sent to $C_B$ and $C_T$ receives energy through the shorting switch $S_C$ in Figure 6.2.

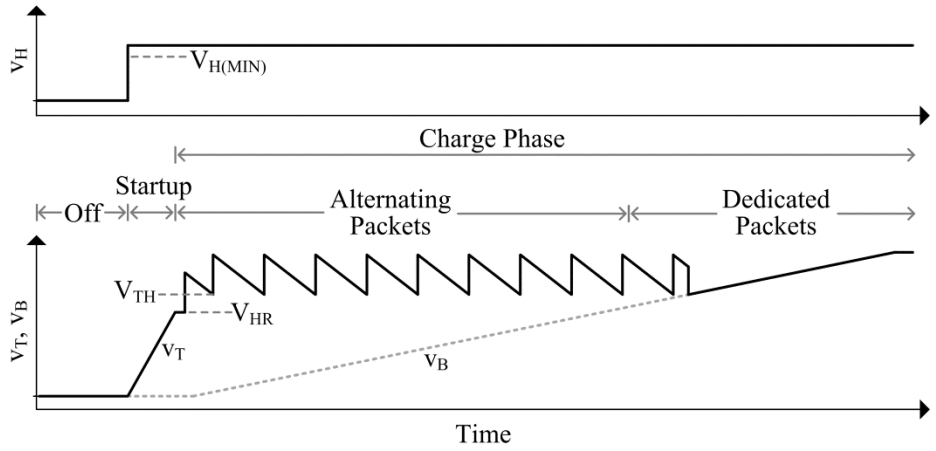


**Figure 6.3. Operational waveforms during wake.**

During the charge phase, the maximum power point tracker sets the frequency at which the battery should be charged. This frequency is dependent on the power available from the energy source. Since ambient power changes slowly, this frequency is essentially constant or slow changing. However, the temporary supply is not charged at a fixed frequency and is instead only charged when $C_T$ requires refreshing. Therefore, the controller may request packets be sent to $C_T$ at any point during the battery's charging frequency. Since $C_T$'s charging events are not synchronized with $C_B$'s charging frequency, conflicts may arise in which the controller requests packets to $C_B$ and $C_T$ at the same time. Since the system in Figure 6.2 reuses $L_X$ to send packets to both $C_T$ and $C_B$, sending simultaneous packets is not possible. Therefore, the controller must be able to handle these conflicts and resolve them appropriately.

The state machine in Figure 6.4 provides the logic required for the controller to prevent such conflicts. If the system is already in the process of sending an energy packet to $C_B$, when the controller receives the command to charge $C_T$, the controller will wait until the packet has been sent to $C_B$ before sending a packet to $C_T$. In other words, if the system is in the state of "Sending to $C_B$" the "Send to $C_B$" signal must clear before the

system changes to the "Sending to $C_T$" state. A similar operation occurs if the system is sending an energy packet to $C_T$ when the controller receives the signal to send to $C_B$. If the system is not actively sending a packet (in the "Not Sending" state) and it receives signals to send to $C_T$ and $C_B$ at the same time, it will give priority to $C_T$, since delaying this energy packet could cause $v_T$ to fall below $V_{HR}$ and disable the system. Note that although "Sending to Both" is not a valid state, the state machine provides an escape path in case a logical error causes the system to move into this state. In this case, regardless of the input signals, the system will move into one of the other three valid states.

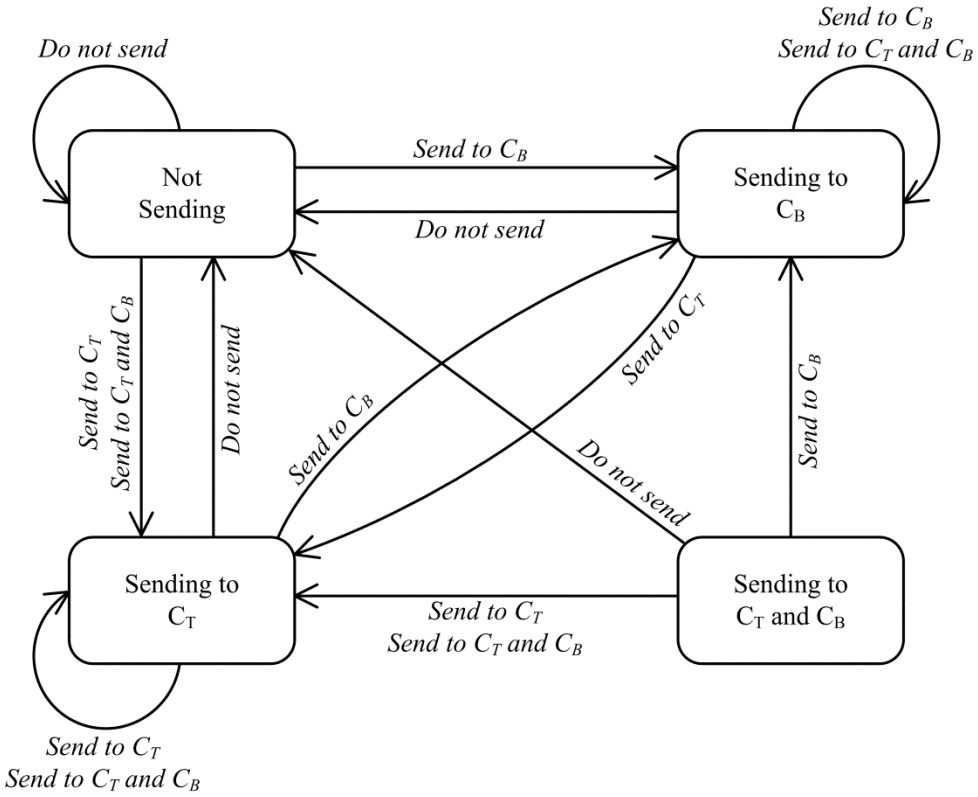


**Figure 6.4. State machine diagram of dual output controller.**

## 6.2 Energy Harvester Prototype

The proposed energy-harvesting charger in Figure 6.5 energizes and drains inductor $L_X$ from the harvesting input $v_H$ into either the small temporary supply $C_T$ or the larger

battery $C_B$. When fully drained, the starter first charges $C_T$ above the headroom level $V_{HR}$ that transistors need to switch efficiently. Then, while supplied by $C_T$, the controller disables the starter and enables the oscillating pulse generator, which with the controller commands ground switch $M_{GND}$ and diode switch $D_B$ to energize and drain $L_X$ from $v_H$ into $C_B$ and $C_T$ in alternating cycles. When $C_B$'s voltage $v_B$ is above a minimum threshold $V_{TH}$, the controller closes $M_{C1}$ and $M_{C2}$ to short $C_T$ and $C_B$, and in so doing, use $C_B$ to supply the charger. The purpose of the starter is to operate the switcher when no other power source than $v_S$ is available. Although inefficient with 250–350 mV at $v_S$, the starter is nevertheless functional, whereas with such a low voltage, the controller is not.

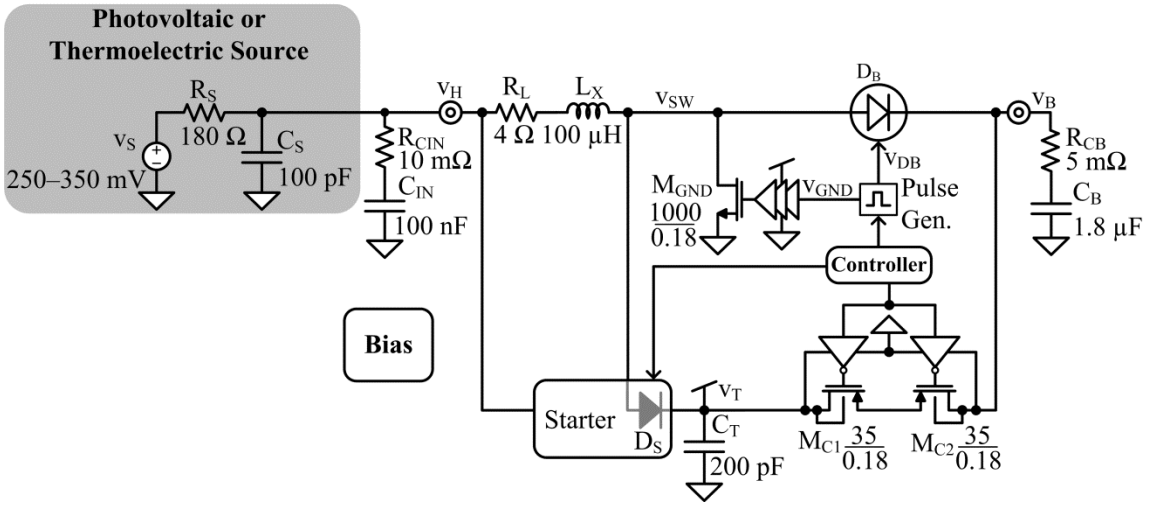


**Figure 6.5. Proposed light/heat-harvesting 0.18-µm CMOS charger.**

### 6.2.1 Controller

The purpose of the controller is to decide when to (*i*) disable the starter and enable the oscillating pulse generator, (*ii*) monitor and replenish the temporary supply $C_T$, and (*iii*) use the battery $C_B$ to supply the system. For this, the controller incorporates three sensing comparators: $CP_{EN}$, $CP_{AID}$, and $CP_B$. $CP_{EN}$, shown in Figure 6.6, monitors $v_T$ and enables the charger by imposing a high voltage on $v_{EN}$ when $v_T$ is higher than the headroom level,

plus some margin. $CP_{AID}$, shown in Figure 6.7, changes state when $v_T$ crosses $V_{TH}$ to indicate when energy must be sent to $C_T$. Since replenishing $C_T$ requires that $v_T$ is high enough to operate the charger, $CP_{AID}$'s $AND_1$ gate does not engage unless $CP_{EN}$'s output $v_{EN}$ is high to indicate $C_T$ is ready to supply. $CP_B$, shown in Figure 6.8, monitors the battery voltage, $v_B$, and sends the signal $v_{SHORT}$ when $v_B$ is above $V_{AID}$ so that $C_B$ and $C_T$ can be shorted. $CP_B$'s $AND_2$ gate similarly keeps $CP_B$ from shorting $C_B$ to $C_T$ until $C_T$ is ready to supply.

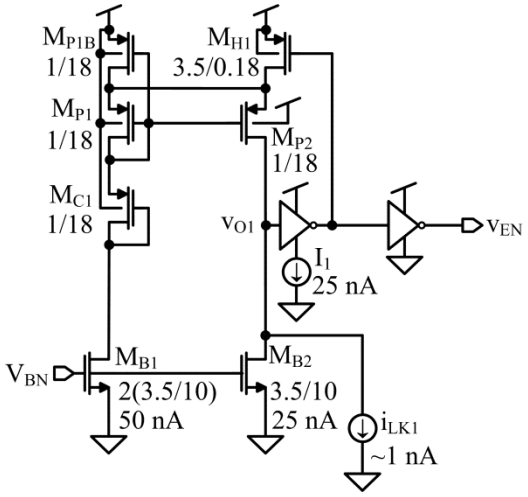


**Figure 6.6. Schematic of the enable comparator $CP_{EN}$.**

The comparators use $V_{BN}$, generated in the bias block, to define currents with which to establish and compare states. These comparators are essentially headroom detectors. When $CP_{EN}$'s supply voltage $v_T$ is low, for example, $M_{P1}$ and $M_{C1}$'s diode connections push $M_{B1}$ into triode, reducing $M_{B1}$'s current below what $V_{BN}$ would otherwise set. $M_{B2}$'s current therefore overwhelms $M_{P2}$'s mirrored reflection of $M_{P1}$–$M_{B1}$'s current to keep $v_{O1}$ and $v_{EN}$ low. When $v_T$ is high enough to pull $M_{B1}$ out of triode, $M_{P2}$'s current surpasses $M_{B2}$'s, so $v_{O1}$ and $v_{EN}$ rise. This way, $CP_{EN}$ trips when $v_T$ rises above $M_{B1}$, $M_{C1}$, and $M_{P1}$'s headroom level $V_{HR}$. To help, $i_{LK1}$ keeps $M_{P2}$'s leakage from

inadvertently tripping $v_{O1}$ when $v_T$ is low. $I_1$ limits the current and power that $v_{O1}$'s first inverter consumes as it transitions. $M_{H1}$ adds headroom to $M_{B1}$ as $v_{O1}$ rises to reinforce (with hysteresis) $v_{O1}$'s rising transition.

$CP_{AID}$ operates the same way, except $M_{C3}$'s and $M_{P3}$'s longer channel lengths raise $M_{B3}$'s headroom level above that of $M_{B1}$ in $CP_{EN}$. $CP_{AID}$ therefore trips at a higher threshold level $V_{TH}$ than $CP_{EN}$'s $V_{HR}$. $V_{TH}$ should be high enough above $V_{HR}$ to keep the switcher from discharging $C_T$ below $V_{HR}$ before the system can recharge $C_T$. This way, $CP_{EN}$ disables the starter when $C_T$ first charges to $V_{HR}$, and with the battery diode $D_B$ still off, the oscillating pulse generator, $M_{GND}$, and $L_X$ can charge $C_T$ after that. When $CP_{AID}$ senses that $v_T$ rises above $V_{TH}$, $v_{AID}$ prompts the oscillating pulse generator to enable $D_B$, and that way, steer $L_X$'s energy into $C_B$. After supplying the switcher across several cycles, $C_T$ discharges below $V_{TH}$, but not below $V_{HR}$, because before that happens, $CP_{AID}$ again disables $D_B$ and allows the diode inside the starter $D_S$ to replenish $C_T$ with the inductor's energy.

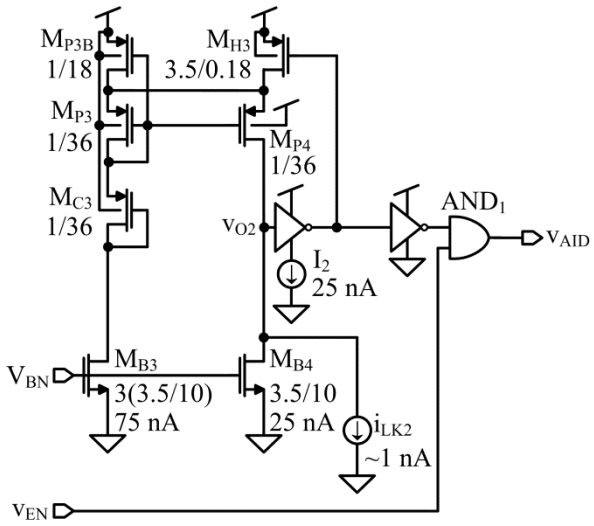


**Figure 6.7. Schematic of the aid comparator $CP_{AID}$.**

The last comparator, $CP_B$, detects when the battery voltage, $v_B$, surpasses $V_{TH}$, to let the system know $C_B$ is ready to be used as a supply. $CP_B$ is a replica of $CP_{AID}$, except $CP_B$ senses $C_B$'s voltage $v_B$. So when $v_B$ rises above $V_{TH}$, the system shorts $C_B$ to $C_T$, and this way, uses $C_B$ to supply the charger. $CP_B$'s $AND_2$ gate ensures that $M_{C1}$ and $M_{C2}$ do not short $C_B$ and $C_T$ unless both are charged near $V_{TH}$. After the supplies are shorted, the system begins sending dedicated packets to $C_B$ and using $v_B$ as its supply. Even after transactions discharge $C_B$ below $V_{TH}$, $V_{TH}$ is high enough above $V_{HR,}$ and transaction losses are low enough fractions of the energy delivered, that $v_B$ does not fall below the headroom level $V_{HR}$.

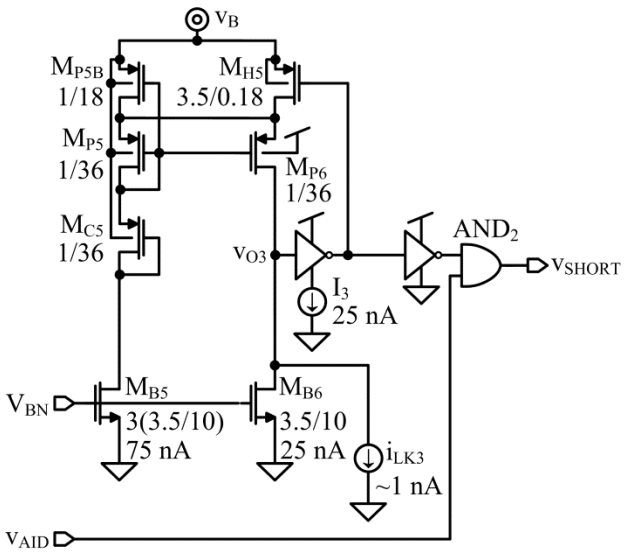


**Figure 6.8. Schematic of the battery comparator $CP_B$.**

### 6.2.2 Oscillating Pulse Generator

The purpose of the oscillating pulse generator in Figure 6.9 is to periodically close $M_{GND}$ long enough to energize $L_X$ with sufficient energy to replenish the temporary supply $C_T$, and when $C_T$ is full, to draw and deliver as much energy as possible from the ambient source to the battery. The frequency at which the charger delivers power to the battery is

set by the oscillator block so that every time that $v_{OSC}$ transitions high, an energy packet is sent to the battery. $v_{AID}$ from $CP_{AID}$ signals the pulse generator to create a packet of energy directed to $C_T$. Although $v_{OSC}$ is periodic and deterministic, $v_{AID}$ may occur at any point in $v_{OSC}$'s period so the pulse generator must resolve race conditions, where both $v_{OSC}$ and $v_{AID}$ arrive near simultaneously, and give proper priority when conflicts arise.

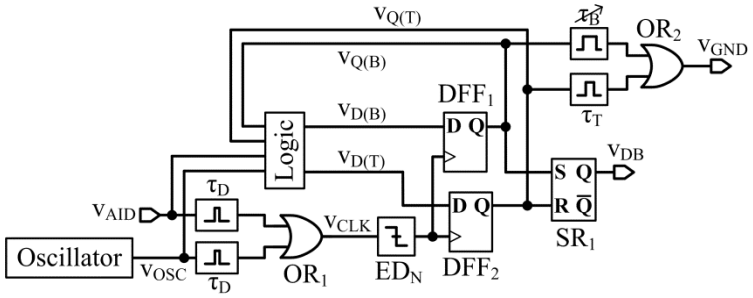


**Figure 6.9. Schematic of the oscillating pulse generator.**

The oscillating pulse generator determines the pulse length that energizes the inductor. When charging the battery, the inductor's energizing pulse width $\tau_B$ is as long as the ambient source $v_S$ can tolerate to remain at or near its maximum power point (MPP). $\tau_B$ is therefore variable and set to a level that draws the most power from $v_S$. However, because the temporary supply's capacitance, $C_T$, is so much lower than the battery's capacitance, $C_B$, $\tau_B$ could easily over-energize the inductor to the extent the inductor overcharges $C_T$ well above the technology's breakdown level $V_{BD}$. So when the controller's $v_{AID}$ indicates the system should replenish $C_T$, the logic chooses an energizing pulse $\tau_T$ that is just long enough to replenish $C_T$ in one cycle.

Every time $v_{OSC}$ rises, the logic's $v_{GND}$ commands $M_{GND}$ to start another energizing event. But since $C_T$ may discharge below $CP_{AID}$'s $V_{TH}$ while charging $C_B$, $v_{CLK}$ in the logic keeps $v_{DB}$ from changing $D_B$'s state and $v_{GND}$ from starting a pulse in the middle of a delivery. When either $v_{OSC}$ or $v_{AID}$ arrive, a pulse of length $\tau_D$ is generated,

which is used as a clock for the D-type flip flops, $DFF_1$ and $DFF_2$. Gate $OR_1$ ensures that if one input arrives and begins to create a $v_{CLK}$ pulse, when the other signal arrives, the pulse length at $v_{CLK}$ is extended to allow the logic to settle with this new information. Once $v_{CLK}$ goes low, $DFF_1$ and $DFF_2$ transfer their input to their outputs, and a change in $v_{AID}$ or $v_{OSC}$ is ignored until the original packet is delivered.

The oscillator in Figure 6.10 establishes the frequency at which the system charges the battery, $C_B$. While $v_T$ is lower than $v_{HR}$, $v_{EN}$ form $CP_{EN}$ is low so that $AND_1$'s output is also low, preventing the SR latch, $SR_{OSC}$, from switching states and preventing oscillations. While the oscillator is disabled, the SR latch output may be high or low, so $AND_2$ keeps $v_{OSC}$ low regardless of $SR_{OSC}$'s state until the oscillator is enabled. Once enabled by the controller's $CP_{EN}$ (when $v_T$ rises above headroom level $V_{HR}$), the current that the gate voltage reference $V_{BP}$ from the bias block establishes with $M_{B1}$ charges $C_1$. When $C_1$ charges above the gate–source voltage that $M_2$ requires to sustain $M_{B2}$'s bias current, $M_2$ overwhelms $M_{B2}$, pulling its drain low and flipping $INV_1$ and setting $SR_{OSC}$. With $SR_{OSC}$'s Q output high, $M_{N1}$ resets $C_1$ to ground, and allows $M_{B3}$ to similarly charge $C_3$. $C_3$ therefore charges until $M_4$ overwhelms $M_{B4}$ to reset the flip-flop and re-start the process. $C_1$ and $C_3$ continue this way, ramping and resetting in alternating cycles, and oscillating $v_{OSC}$ between states at a frequency that $M_{B1}$, $C_1$, $M_2$, $M_{B2}$, $M_{B3}$, $C_3$, $M_4$, and $M_{B4}$ establish.

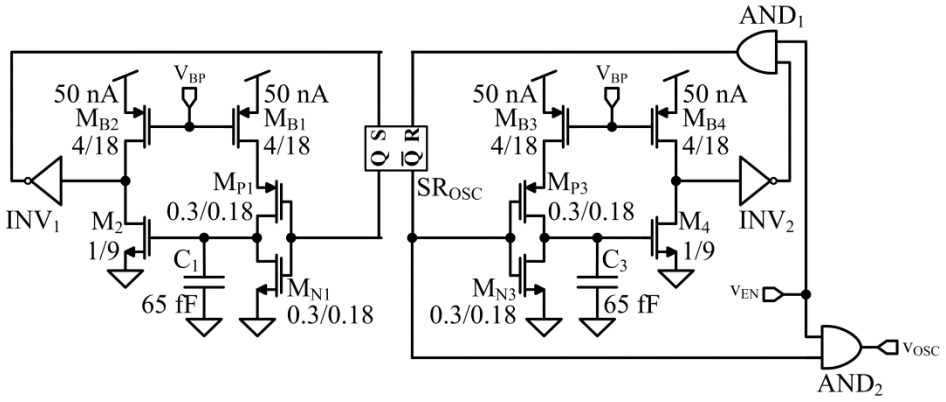


**Figure 6.10. Schematic of the oscillator.**

The logic block in Figure 6.9 implements the state machine presented in Figure 6.4 to determine where to send energy packets. The schematic in Figure 6.11 details the gates used to implement the state machine. The signals $v_{Q(T)}$ and $v_{Q(B)}$ are the states of the system: if $v_{Q(T)}$ is high the system is currently sending a packet to $C_T$, while if $v_{Q(B)}$ is high the system is sending a packet to $C_B$. The output signals of the logic block, $v_{D(T)}$ and $v_{D(B)}$, dictate what the next sate of the system should be. As the state machine dictates, the logic prioritizes the state the system is always in, then sending a packet to the temporary supply, and finally sending a packet to the battery. No combinations of input signals produces a high signal at $v_{D(T)}$ and $v_{D(B)}$ simultaneously and if both $v_{Q(T)}$ and $v_{Q(B)}$ are high, at least one of the outputs is forced low.

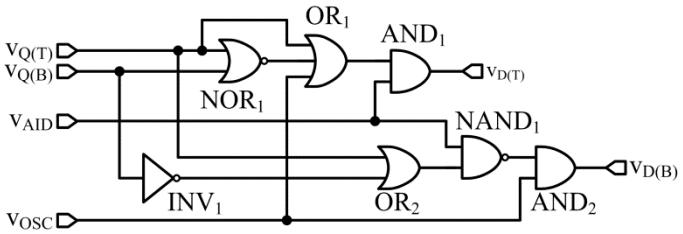


**Figure 6.11. Schematic of the pulse generator logic.**

Four instances of the one-shot pulse generator in Figure 6.12 produce the energizing and filter-delay pulses $\tau_B$, $\tau_T$, and $\tau_D$ in Figure 6.9. When the input $v_I$ is low,

the $AND_1$ gate grounds the output $v_O$, $M_{OFF}$ shuts, and $M_S$ grounds $M_A$'s gate, so $M_B$'s current keeps $v_X$ high. When the input $v_I$ rises, $AND_1$ raises $v_O$, $M_S$ shuts, and $M_{OFF}$ closes to let $I_P$ charge $C_P$. When $C_P$'s voltage is high enough for $M_A$ to overwhelm $M_B$'s current, $v_X$ falls, and with it, $v_O$. In other words, $v_O$ is high only as long as $I_P$ requires to charge $C_P$ above $M_A$'s threshold. Therefore, with different $I_P$ currents, the circuit produces different pulse lengths. Copies of this circuit produce pulse widths of 0.25–1 µs when $I_P$ is 25–100 nA. When $v_I$ goes low, $M_{OFF}$ turns off and prevents $M_P$ from conducting. Similarly, $M_S$ is turned on to pull $M_A$'s gate low so that $M_A$ and $M_B$ do not conduct. Therefore, when $v_I$ is low, the circuit consumes no quiescent current.

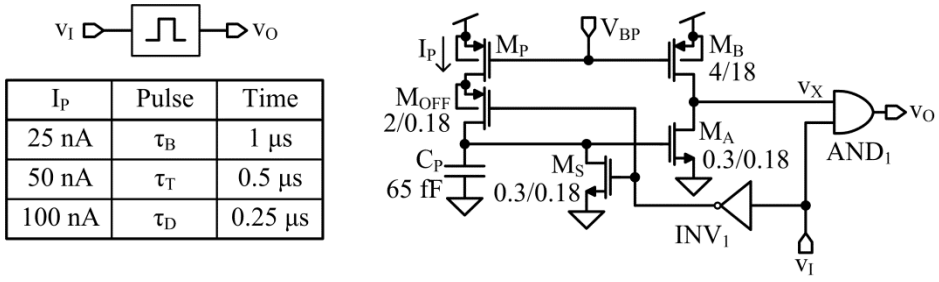


| $I_P$ | Pulse | Time |
|---|---|---|
| 25 nA | $\tau_B$ | 1 µs |
| 50 nA | $\tau_T$ | 0.5 µs |
| 100 nA | $\tau_D$ | 0.25 µs |

**Figure 6.12. Schematic of the one-shot pulse generator.**

### 6.2.3 Battery Diode

The battery diode, $D_B$ in Figure 6.5 is not an ordinary PN-junction diode for several reasons. First, $D_B$ should not direct energy to the battery $C_B$ when the temporary supply $C_T$ needs charge, even if $v_B$ is lower than $v_T$, which would otherwise engage a conventional diode. For this $D_B$ requires a disabling terminal which prevents forward conduction when $v_{SW}$ is higher than $v_B$ if the energy packet is meant for $C_T$. The second reason is that a typical diode would drop 0.6–0.7 V when conducting, which would burn considerably more power than a MOS switch implementation. However, to prevent

reverse battery current, the system must detect when there is a negative voltage across the switch, and ensure the switch is off during this time.

Functionally, MOSFETs $M_{DB1}$ and $M_{DB2}$ in Figure 6.13 should (together) operate like a diode when enabled by $v_{DB}$. When $v_{DB}$ is high, $M_{DB2}$ closes and allows the comparator $CP_{DB}$ to switch $M_{DB1}$ like a diode when $v_{GND}$ opens $M_{GND}$ and an energizing event finishes. After some dead-time, the SR latch is set by a falling edge at $v_{GND}$, and $M_{DB1}$ turns on. When the switching node $v_{SW}$ falls below $v_B$, $CP_{DB}$'s $v_{O2}$ falls to open $M_{DB1}$, and that way, disconnect $v_{SW}$ from $v_B$ like a diode would. $M_{I1}$ and $M_{I2}$, and as a result, their mirroring translations to $v_{O1}$ and $v_{O2}$ source equivalent currents when $v_{SW}$ equals $v_B$. When $v_{SW}$ falls below $v_B$, $M_{I1}$'s translation $M_{M2}$ sinks less current than $M_{I2}$ sources, so $v_{O1}$ rises, $M_O$ strengthens and pulls $v_{O2}$ to ground, to open $M_{DB1}$.

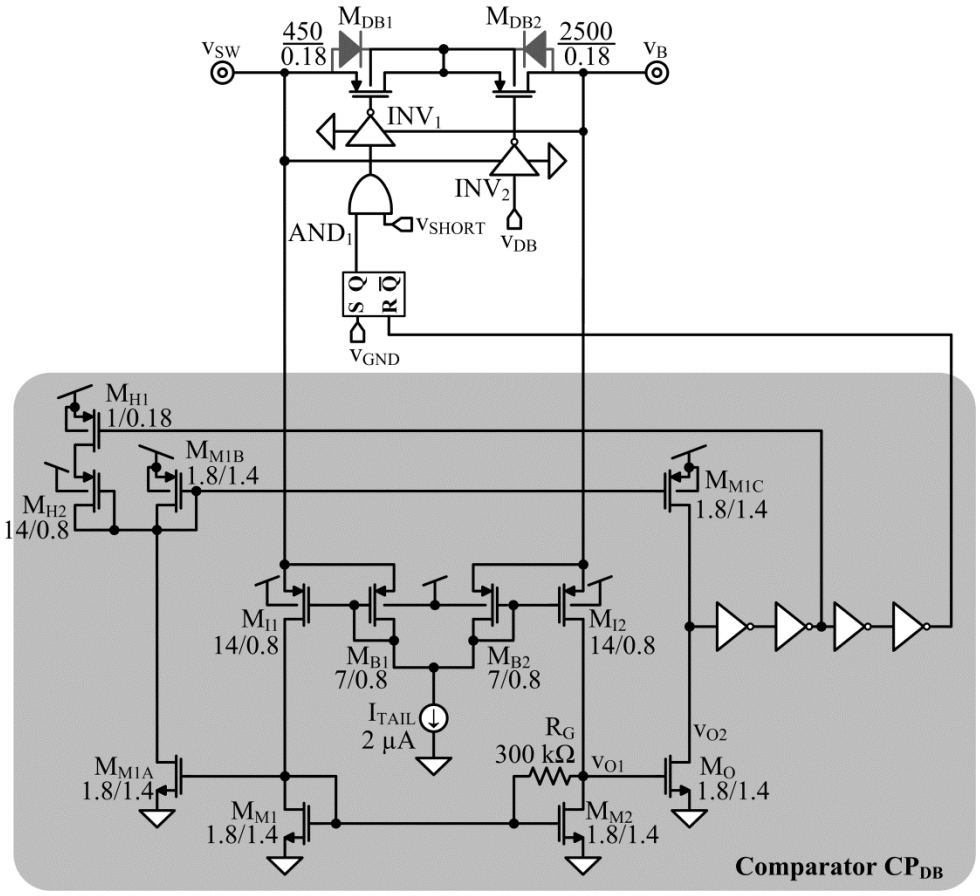


**Figure 6.13. Schematic of the battery diode $D_B$.**

For all this, $M_{B1}$ and $M_{B2}$ split $I_{TAIL}$'s 2 µA (from the bias block) to establish the currents that $M_{I1}$ and $M_{I2}$ and their translations conduct. Splitting the bias between $M_{B1}$ and $M_{B2}$ ensures that neither $M_{I1}$ nor $M_{I2}$ will conduct more than $I_{TAIL}$ thereby reducing the overall power consumption of $CP_{DB}$. $M_{M1C}$ sources a mirrored reflection of $M_{I1}$'s current, so when $M_{I2}$ conducts more current, $M_{M1C}$'s translation allows $v_{O2}$ to fall faster. And as $v_{O2}$ falls, $M_{H1}$ closes to decrease $M_{M1C}$'s mirror gain to $v_{O2}$. This hysteresis allows $M_O$ pull $v_{O2}$ to ground faster and prevent the comparator from tripping again due to switching noise.

When $v_{DB}$ is low, $M_{DB2}$'s driver, $INV_2$, connects $M_{DB2}$'s gate to $v_{SW}$. Although $M_{DB2}$ can still turn on when $v_B$ is greater than $v_{SW}$, $CP_{DB}$ commands $M_{DB1}$'s driver to

connect $M_{DB1}$'s gate to $v_B$ when $v_B$ is above $v_{SW}$ to ensure $M_{DB1}$ stays off. So combined, $M_{DB1}$ and $M_{DB2}$ are off when $v_{DB}$ is low. Otherwise, when $v_{DB}$ is high, $M_{DB1}$ closes only when the SR latch is set, which happens just after the energizing pulse finishes, and $v_{SW}$ is above $v_B$.

### 6.2.4 Starter

The goal of the starter in Figure 6.14 from Chapter 5 is to use the inductor, $L_X$, to charge the temporary supply, $C_T$, once, after the ambient source $v_S$ first recovers from a long drought. As $v_S$ first rises, $M_{SEN}$ energizes $L_X$ and the jump starter and $M_R$ help transfer and exchange the energy drawn between $L_X$ and switching-node capacitance $C_{SW}$. Although the energy swapped is not at first high enough for $M_{DS1}$ and $M_{DS2}$ to steer charge into $C_T$, the oscillations and the energy transferred grow, and with it, so does $v_{SW}$'s peak as it oscillates.

Once $v_{SW}$ is high enough above ground, $M_{DS1}$ and $M_{DS2}$ close to steer $L_X$'s leftover energy into $C_T$. But if $v_T$ does not climb sufficiently high for the controller to shut the starter, $M_{SH}$ resets the jump starter. And to help $M_{DS1}$ and $M_{DS2}$ engage the next time $v_{SW}$ is high, $M_{PLK}$ leaks $C_T$. Since $C_T$ does not altogether deplete, $v_T$ reaches the controller's headroom level $V_{HR}$ the next time $C_T$ receives energy. This prompts the controller's $CP_{EN}$ to shut the starter and enable the oscillating pulse generator. Because $v_{EN}$ grounds $v_{DLY}$, further oscillations from the oscillating core are stopped. Additionally, $M_{PLK}$ is turned off, preventing further leakage from $C_T$ and since $M_{SH}$'s gate voltage, $v_T$, is above its threshold voltage, $M_S$ and therefore the jump starter, also remains off. Turning the starter completely off during the charging phase prevents it from consuming significant amounts of power.

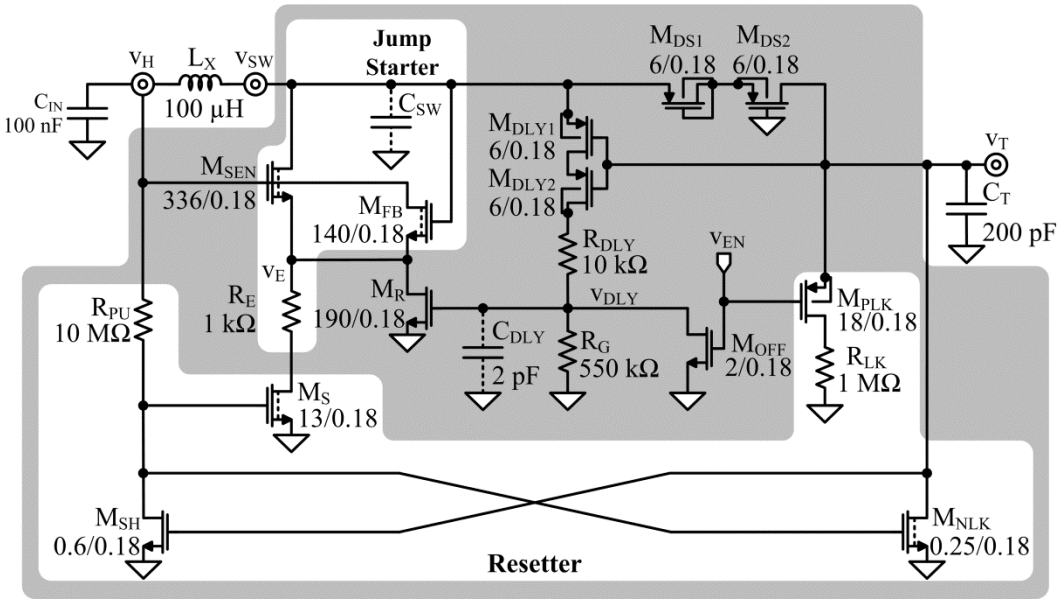


**Figure 6.14. Schematic of the starter circuit described in Chapter 5.**

### 6.2.5 Bias

The bias block in Figure 6.15 establishes the reference gate voltages $V_{BN}$ and $V_{BP}$ for N- and P-channel MOS transistors that all circuits in the system use to establish bias currents. For this, $M_1$ and $M_2$ sink equal currents because $M_3$–$M_{3C}$ mirrors $M_4$–$M_{4C}$'s current. Since $M_2$'s channel width is eight times wider than $M_1$'s, $M_2$'s gate–source voltage $v_{GS2}$ is lower than $M_1$'s $v_{GS1}$. The difference in gate-source voltages, $v_{GS1} - v_{GS2}$, is dropped across $R_B$. In the subthreshold region, this difference is linearly proportional to absolute temperature (PTAT) [162], so $v_{GS1} - v_{GS2}$ across $R_B$ establishes a PTAT current that can be mirrored through $V_{BN}$ and $V_{BP}$ across the system.

When the supply first rises, the circuit can enter and stay in the off state, where $V_{BN}$ remains at ground, $V_{BP}$ remains at the supply, and the drain currents of $M_1$–$M_4$ remain at zero. To remove the bias block from the off state, $M_5$ turns on if $V_{BP}$ is close to the supply, forcing current between $V_{BN}$ and $V_{BP}$ and charging these nodes until $M_1$–$M_4$

turn on. Once the circuit is biased, $M_5$'s current is no longer needed and any current that it pulls introduces an error into the bias circuit. Therefore, to turn $M_5$ off, $M_{BST}$ mirrors $M_4$'s current into a long-channel diode-connected PMOS $M_{RST}$ that behaves like a high-value resistor. So once $M_4$ begins conducting, $M_{BST}$ mirrors its current, pulling its drain and, through two inverters, the gate of M5 to the supply voltage. With M5's gate at the supply, its drain current is zero.

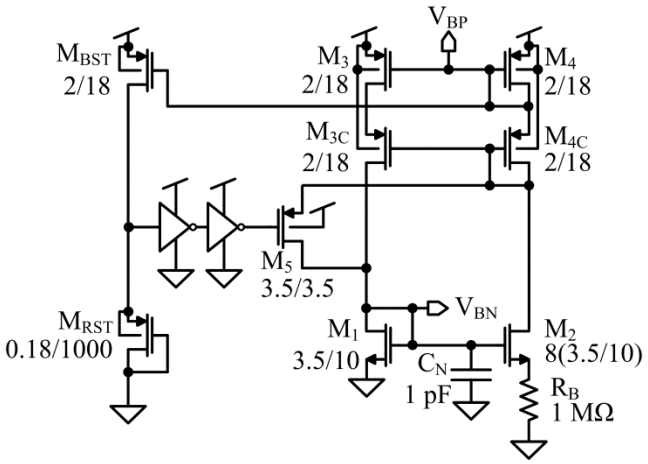


**Figure 6.15. Schematic of the bias block.**

## 6.3 Measured Performance

The prototyped charger was designed and fabricated in a 0.18-µm CMOS process. The die in Figure 6.16a integrates the components in Figure 6.5, except the 70-mV/°C heat-harvesting source $v_S$, the 100-nF input capacitor $C_{IN}$, the 100-µH transfer inductor $L_X$, and the 1.8-µF battery $C_B$, which are off chip on the board shown in Figure 6.16b. The die and board also include replica and monitoring circuits used to isolate and test different parts of the system. The die measures 660 × 370 $\mu m^2$, the packaged die 9.7 × 6.4 × 1.2 $mm^3$, the input capacitor 1.6 × 0.8 × 0.8 $mm^3$, the transfer inductor 2 × 1.25 × 1.45 $mm^3$, the battery 2 × 1.25 × 1.25 $mm^3$, and although emulated for testing purposes, the

thermoelectric generator emulated from [123] measures 3.3 × 2.5 $mm^2$. The series resistances of the input capacitor, transfer inductor, battery, and ambient source are 10 mΩ, 4 Ω, 5 mΩ, and 180 Ω.

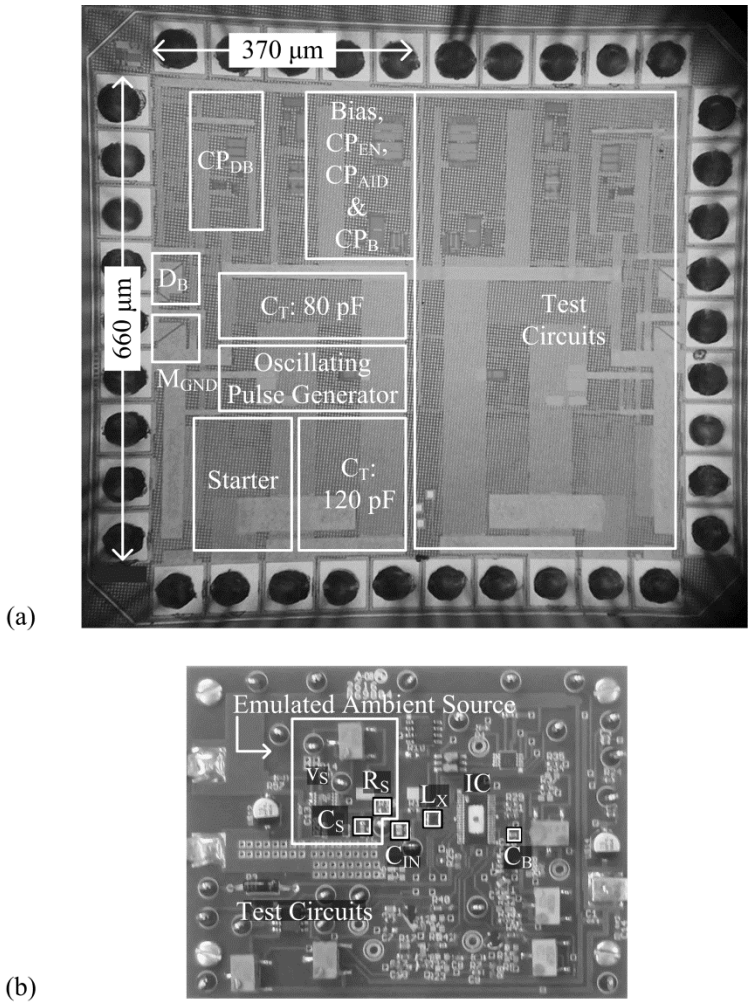


**Figure 6.16. Die and board photographs of the prototyped charger.**

### 6.3.1 Wakeup

Off: Across a prolonged harvesting drought, leakages drain all capacitances in the circuit below the system's headroom level $V_{HR}$. With such low voltages at the supplies, nothing is on. As ambient energy, $E_A$, returns, the ambient source $v_S$ climbs, but as long as $v_S$ remains below the starter's minimum threshold $v_{H(MIN)}$, which, in this case, from Figure

6.17 is 220 mV, the system remains off. So up to about 9.5 ms, the system pulls no current, so the source resistance $R_S$ drops zero volts, and the harvesting input $v_H$ follows the ambient source $v_S$.

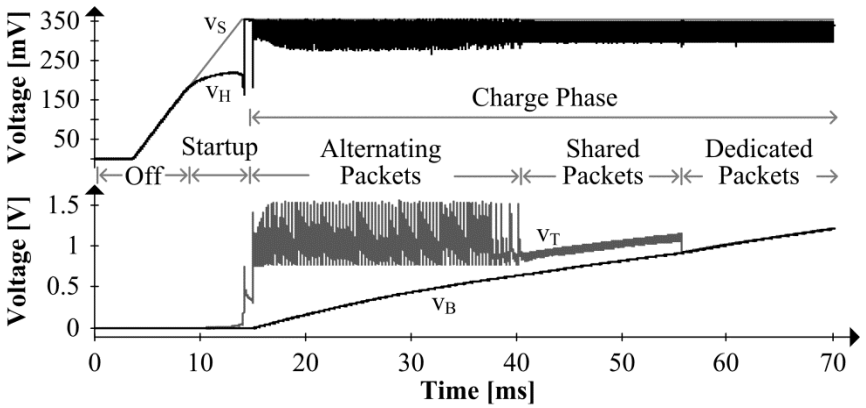


**Figure 6.17. Measured wakeup charge sequence.**

Startup Phase: As $v_S$ reaches 220 mV at 9.5 ms, the starter in Figure 6.14 begins to energize $L_X$ and help $L_X$ drain into the switching-node capacitance $C_{SW}$. $L_X$ and $C_{SW}$ then exchange energy and continue to oscillate this way after that. Except, $L_X$'s energy and current at 13.8–14.2 ms in Figure 6.18 is not enough to raise $v_{SW}$ high enough above $C_T$'s voltage, $v_T$, for the starter's diode, $D_S$ (composed of $M_{DS1}$ and $M_{DS2}$) to steer energy into $C_T$. So, although the starter draws harvested input power from $v_H$, which is why $R_S$ drops voltage at and $v_H$ falls below $v_S$ between 10 and 14 ms in Figure 6.17, $v_T$ does not charge and instead remains near zero.

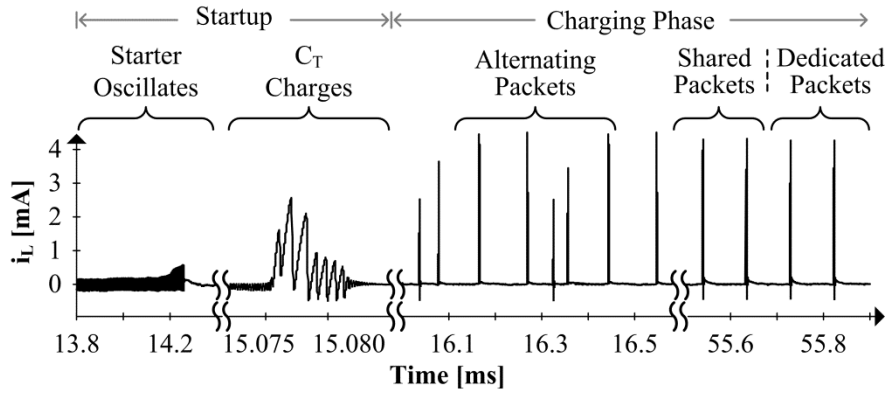


**Figure 6.18. Measured inductor current across wakeup phases.**

At 14.5 ms, however, the inductor draws enough energy to charge the switch node capacitance, $C_{SW}$, and steer leftover charge into $C_T$. However, this energy is not enough to charge $C_T$ above the controller's headroom level, $V_{HR}$, so the starter shuts the jump starter and begins discharging $C_T$. During the starter's next attempt, beginning at 15.075 ms in Figure 6.18, the inductor's energy is high enough to charge $C_T$. So $v_T$ in Figure 6.17 climbs above $V_{HR}$'s 0.8 V at about 15.1 ms. $CP_{EN}$ in the controller senses this, and in response, shuts the starter and enables the oscillating pulse generator. This marks the end of the startup phase.

Charge Phase: Once the controller turns the starter off, the starter no longer loads the input voltage, $v_H$. So at 15.1 ms, all of $R_S$'s current charges $C_{IN}$ so that $v_H$ climbs close to $v_S$. With $v_T$ now above the headroom level, the controller, together with the oscillating pulse generator, close $M_{GND}$ to energize $L_X$ for a time $\tau_T$, and then open $M_{GND}$ to drain $L_X$ into $C_T$ through the starter's $D_S$ (with the rest of the starter off). This transaction charges $C_T$ to just below the chip's breakdown level $V_{BD}$, which, in the CMOS process used, is 1.8 V.

Now that $v_T$ is greater than $CP_{AID}$'s threshold level $V_{TH}$, the controller enables the battery diode $D_B$. After $M_{GND}$ energizes the inductor again, this time for $\tau_B$, $D_B$ drains the

inductor into the battery to begin charging $C_B$. These transactions, however, drain $C_T$ below $V_{TH}$, but not below $V_{HR}$. The controller, therefore, disables $D_B$ and sends an energy packet to $C_T$ through $D_S$. With one energy packet, $v_T$ rises above $V_{TH}$, and the controller again enables $D_B$. The charger alternates packets to $C_B$ and $C_T$ this way between 15 and 40 ms in Figure 6.17 and Figure 6.18.

When $v_B$ is within about 300 mV of $v_T$'s low state and $v_T$ nears threshold level $V_{TH}$ (at about 40 ms in Figure 6.17), $D_S$ begins leaking some of the energy meant for $C_B$ into $C_T$. This leaked energy keeps $C_T$ from discharging below $V_{TH}$, so the controller stops steering packets directly into $C_T$. Specifically, $CP_{AID}$ stops disabling the battery diode $D_B$ so that all the energizing packets last $\tau_B$ and are directed into $C_B$. $v_T$ is higher than $v_B$, however, because $C_T$ is much lower than $C_B$, so $v_T$ rises faster with less energy. $C_B$ and $C_T$ share energy packets this way until $v_B$ reaches $CP_B$'s threshold $V_{TH}$ at 55.7 ms. Past that point, $v_B$ is high enough to supply the system, so the controller shorts $C_B$ and $C_T$. The battery charges more than it supplies through this last phase, so $v_B$ climbs steadily with every switching cycle.

### 6.3.2 Harvesting Efficiency

For the system to charge the battery, $C_B$, quickly, $L_X$ should draw as much power as possible. But as drawn source current, $i_S$, climbs, the source resistance $R_S$ burns more power. While the power that is drawn from the source, $P_S$, rises linearly with $i_S$, the ohmic power lost to $R_S$, $P_{R(S)}$ climbs with the square of the drawn current. This means that initially, harvested input power, $P_H$, increases with source power, $P_S$, but after a point, increases in $P_S$ are offset by increasing losses in $P_{R(S)}$ so that $P_H$ begins to decrease.

Therefore, harvested input power, $P_H$, is at its maximum when the extra loss $\Delta P_{R(S)}$ just cancels the additional gain $\Delta P_S$.

As the source current, $i_S$ in Figure 6.19, increases and the voltage dropped across $R_S$ reduces the input voltage, $v_H$, the source power around 0 mA rises faster (linearly) than $P_{R(S)}$ (quadratically). Since the source power rises faster than the losses, $P_H$ climbs past that point. After 972 µA, with $v_S$ at 350 mV, however, $P_{R(S)}$ outpaces $P_S$, so at 972 µA, $P_H$ is at its maximum at 170 µW and falls after that. Since source power increases quadratically with $v_S$, a larger $v_S$ will quickly increase the maximum source power. Therefore, for higher $v_S$, $P_{R(S)}$ will be higher before $P_H$ peaks. $P_H$'s maximum power point (MPP) $P_{H(MPP)}$ therefore rises with $v_S$.

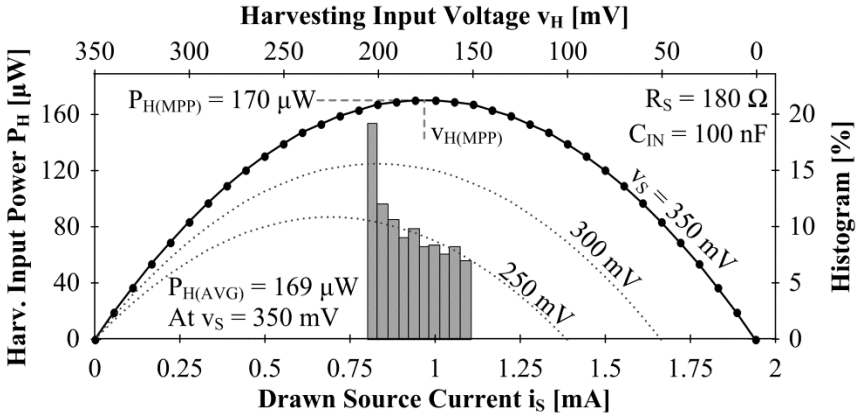


**Figure 6.19. Measured harvested input power and histogram.**

Because the inductor's peak current, about 4 mA, is higher than the 972-µA of current that $v_S$, on average, sources at its maximum power point, source and input capacitors $C_S$ and $C_{IN}$ supply most of the charge $L_X$ draws, and the capacitor voltage, $v_H$, falls. However, whenever the inductor current is less than 972 µA, $v_S$ supplies more charge than the inductor draws, and the excess current recharges $C_S$ and $C_{IN}$ and $v_H$ rises.

So over a complete switching cycle, $C_S$ and $C_{IN}$ supply as much charge as they receive, and their net voltage change is zero.

Unfortunately, the ripple voltage that results at the harvesting input $v_H$ shifts the source from its MPP setting $v_{H(MPP)}$. However, since the input power is already at its maximum, where its slope with respect to $v_H$ is zero, a small enough ripple will have little to no effect on input power. With 100 nF of input capacitance, $C_{IN}$, for example, $v_H$ ripples between 158 and 210 mV. This variation, however, is close enough to $v_{H(MPP)}$'s 175 mV to keep $P_H$ close to $P_{H(MPP)}$ and average 169 μW or 99.4% of the 170 μW that the input source $v_S$ can deliver at 350 mV.

Average input power, $P_{H(AVG)}$, is so close to $P_{H(MPP)}$ that improvements from higher input capacitances are hardly noticeable in Figure 6.20. Lower input capacitances, on the other hand, increase the ripple to such an extent that the effects are apparent. With 10 nF, for example, $v_H$ ripples 280 mV and averages 133 mV, so maximum input power, $P_H$, averages 120 μW or 70.6% of the 170 μW that $v_S$ can deliver. $P_H$ averages less at 22 μW with 1 nF, but not much less below that level because at that point, the ripple is equal to the total voltage available. In other words, input capacitance $C_{IN}$ is so low that each energy packet causes $v_H$ to collapse to zero when the inductor draws energy. Once the inductor stops conducting, $C_{IN}$ is again so low that $v_H$ is charged all the way to $v_S$. This is why $v_H$ does not ripple more than 350 mV when $C_{IN}$ is less than 1 nF.

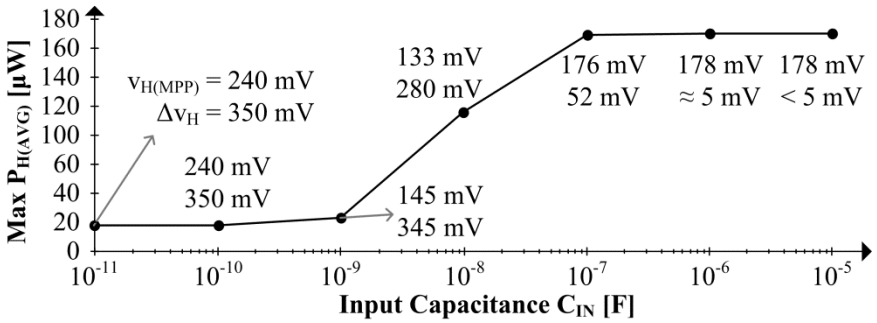


**Figure 6.20. Maximum harvested input power and ripple voltage across input capacitance.**

### 6.3.3 Charging Efficiency

Throughout the charging process, quiescent, $P_{Q(C)}$, gate-drive, $P_{G(C)}$, and ohmic, $P_{R(C)}$, losses in the charger leak power away from the temporary supply $C_T$ and the battery $C_B$. When the source voltage rises, more voltage is applied across the inductor during the energizing phase, resulting in a higher peak current. Since ohmic losses in the inductor equivalent series resistance and in $M_{GND}$'s, $M_{DB1}$'s and $M_{DB2}$'s channel resistances increase with higher inductor peak current, $P_{(R)C}$ increases with $v_S$. Quiescent and gate-drive losses are mostly independent of peak current and, therefore, $v_S$. and $P_{H(MPP)}$. So, as the harvested input power, $P_H$, and output battery power, $P_O$, increase with $v_S$, $P_{R(C)}$ in Figure 6.21 climbs and $P_{G(C)}$ and $P_{Q(C)}$ do not. But since $P_H$ consistently rises more than $P_{R(C)}$ when $v_S$ is below 350 mV, the charger draws 55–168 µW or 98.2%–98.8% of the 56–170 µW that $v_S$ can supply at 200–350 mV and delivers 40–150 µW or 76%–86% of the drawn 55–168 µW.

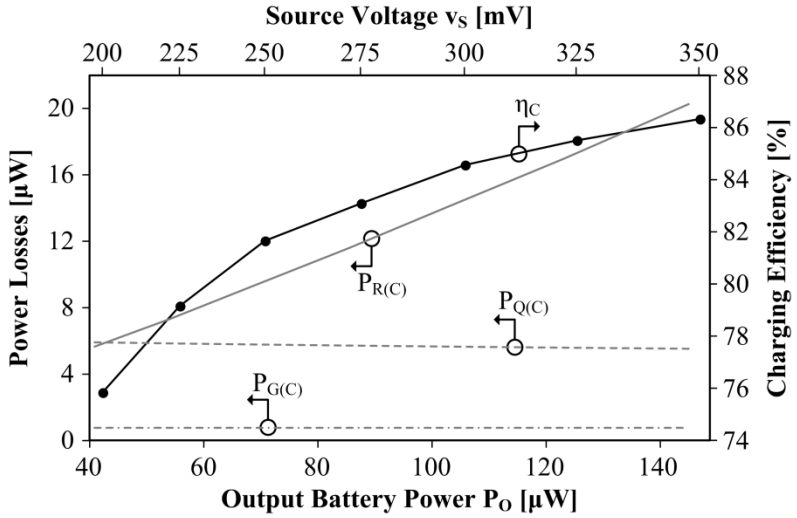


**Figure 6.21. Measured charger losses and charging efficiency.**

The inductor's 4-Ω series resistance, $R_L$, in Figure 6.22 consumes more power, $P_{R(RL)}$, than those of the battery diode $D_B$ and ground switch $M_{GND}$. Although a larger inductor with the same inductance exhibits less resistance, increasing the dimensions of the inductor counter the integration benefits of a smaller board component. $D_B$ burns more power than $M_{GND}$'s resistance $R_{GND}$ because $D_B$'s resistance $R_{DB}$ is, by design, close to 10 Ω. With a lower resistance, the voltage that the inductor current (at less than 4 mA) would drop across $R_{DB}$ would not be sufficiently high to drive $CP_{DB}$ enough. Without enough voltage across its terminals, $CP_{DB}$ would not be able to detect the zero current crossing of the inductor current and $D_B$ would not function as a diode. With 10 Ω, however, $R_{DB}$ does not consume more power than $R_L$ because $D_B$ conducts a small fraction of the time that $L_X$ does. $M_{GND}$'s resistance is considerably lower because, without $R_{DB}$'s limitation, $M_{GND}$'s channel width is wide enough to balance ohmic and gate-drive losses, at which point $M_{GND}$ requires the least power possible to switch across states.

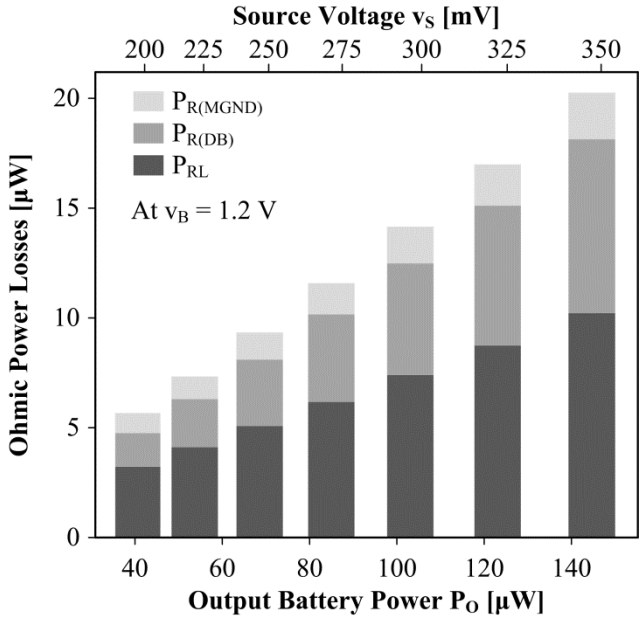


**Figure 6.22. Simulated ohmic power losses.**

When the ambient source $v_S$ is 300 mV, for example, $R_L$, $R_{DB}$, and $R_{GND}$ in Table 6.1 burn 7.40, 5.06, and 1.13 µW respectively. Since $R_{DB}$ is not low enough to balance gate-drive power, the gates of $D_B$'s $M_{DB1}$ and $M_{DB2}$ require (at 100 nW) much less power to switch than the ohmic loss consumes. $M_{GND}$'s gates, however, require about as much as $R_{GND}$ dissipates since $M_{GND}$'s losses are balanced and optimized. At 160 nW, $D_B$'s comparator $CP_{DB}$ requires a little more than what $D_B$ requires to switch. With three comparators to sustain, the controller burns more average power at 330 nW. The bias block consumes 60 nW.

During the startup phase, the starter burns more power because, with only the 250–350 mV that the ambient source $v_S$ avails, efficiency is only 1%–7%. But since the starter operates for only 5 of the 45 ms that the system requires to wake, and it only charges the small temporary supply, the starter consumes, on average, only a little over the 1.86 µW that the starter leaks when disabled. The oscillating pulse generator

consumes more power at 3.01 μW because, once enabled, it never stops switching. As Table 4.1 summarizes, the system delivers 86% of the power it draws to charge a fully depleted 1.8-μF battery to 0.9 V in 45 ms, which is equivalent to charging the battery with 36 μA.

**Table 6.1. Simulated average power losses when the ambient source is 300 mV.**

| Block | | Power Loss |
|---|---|---|
| Controller | | 330 nW |
| Pulse Generator | | 3.01 μW |
| $CP_{DB}$ | | 160 nW |
| Starter | | 1.86 μW |
| Bias | | 60 nW |
| $R_L$ | | 7.40 μW |
| $D_B$ | $R_{DB}$ | 5.06 μW |
| | Gate Capacitance | 100 nW |
| $M_{GND}$ | $R_{GND}$ | 1.13 μW |
| | Gate Capacitance | 650 nW |

### 6.3.4 Relative Performance

*Integration:*

As Chapter 1 highlighted, wireless microsystems are more useful and can be used in more applications when they are smaller. Therefore, each sub-block, including the power management block, must be as small as possible. In this case, the starter requires a 660 × 370-$\mu m^2$ 0.18-μm CMOS die, a 2 × 1.25 × 1.45-$mm^3$ 100-μH inductor, a 1.6 × 0.8 × 0.8 $mm^3$ input capacitor, and a 2 × 1.25 × 1.25 $mm^3$ battery. The inductor, typically the most

critical component in a power management block, occupies about 4 $mm^3$, which compares very favorably with the magnetic components used in the transformer-based oscillator, motion-activated switch starter, and LC oscillator presented in Chapter 3 and summarized in Table 4.1. The size of the inductor used in the prototyped system presented here is comparable with that used in the ring oscillator driven starters, both tuned and natural.

The largest system in the state of the art, the amplifying transformer-based oscillator, requires a 1:60 transformer for startup that, at 175 $mm^3$, occupies 43× more space than the 4 $mm^3$ required here. The motion activated switch uses a MEMS device that switches in response to vibrations, but relying on such a switch is a drawback because the charger can only start when motion is present. Using a motion activated switch also requires two inductors, one for startup and one for steady state, that, at 150 $mm^3$, occupy 38× more volume than the starter presented here. An LC oscillator can be smaller and is not reliant on external forces. Although the size of the inductors is not reported, with four inductors, it still occupies around 16 $mm^3$, which is 4× more space.

Tuned and natural ring oscillator occupy about the same volume, estimated at 4 $mm^3$. Although a ring oscillator could have a minimum input voltage as low as 80 mV, P- and N-type transistor threshold voltages in the ring oscillator that start the system must balance *specifically* for that purpose. To guarantee that the transistors balance, post-processing steps in the fabrication process is required. These steps are costly and time consuming, and without them, the minimum threshold would be much higher, at around 330 mV.

*Wakeup Time:*

Since different technologies are presented that charge a variety of battery sizes, wakeup time itself is not a particularly useful metric. Instead, the equivalent charge current, $I_{EQ}$, which normalizes wakeup time with battery capacitance and target voltage, provides a better comparison across technologies. With 32 μA of equivalent charge current, the LC oscillator is almost, although not quite as efficient as the charger presented, but with three more off-chip inductors: two 2-μH and one 27-μH inductors. At 5.6 μA, with 6.4× less current, the motion activated starter is the next fastest-waking charger, but with one more off-chip inductor and a MEMS switch that operates only in the presence of vibrations. Although the tuned ring oscillator requires as many off-chip components as the system here, at 2.7 μA, its equivalent charge current is 13.3× lower. The amplifying transformer also charges with less current, with 2.4 μA, and requires a bulky off-chip 1:60 transformer.

The advantage of the transformer, MEMS switch, multiple inductors in the LC oscillator, and tuned ring oscillators is that they start with a lower input voltage $v_H$. Replacing the starter in Figure 6.5 with tuned ring oscillators use can reduce the startup voltage of this system to the reported 80 mV. But still, to charge the battery with the equivalent of 36 μA, the system must retain the controller, switching network, oscillating pulse generator, small temporary supply, and operating principles proposed and presented here.

*Efficiency:*

After the battery has been charged, and the system exits the wakeup stage, the system must continue charging the battery at the input source's maximum power point (MPP).

To this end, the proposed system charges the battery with 86% of the available input power. The natural ring oscillator has the second highest efficiency, charging its battery with 80% efficiency at steady state. While the other technologies have lower overall and charge efficiencies, they also operate at lower input voltages, which results in higher ohmic losses. For this reason, a fair comparison of efficiency between technologies is not straightforward. However the proposed system does not introduce any additional significant losses that would make it less efficient under similar conditions.

**Table 6.2. Performance summary and the state of the art.**

| | X-Former [149] | MEMS Switch [128] | LC Osc. [152] | Ring Oscillator | | This Work |
|---|---|---|---|---|---|---|
| | | | | Tuned [145] | Natural [150] | |
| $V_{H(MIN)}$ | 40 mV | 35 mV | 50 mV | 80 mV | 330 mV | 220 mV |
| $C_B$ | 10 µF | 100 nF | 1 µF | 10 nF | – | 1.8 µF |
| $V_{TAR}$ | 1.2 V | 1 V | 0.8 V | 1.3 V | 1.8 V | 0.9 V |
| Charge Time | 4.9 s | 18 ms | 25 ms | 4.8 ms | 1.2 s | 45 ms |
| $I_{EQ}$ | 2.4 µA | 5.6 µA | 32 µA | 2.7 µA | – | 36 µA |
| Charge Efficiency | 40% | – | – | 72% | 80% | 86% |
| $C_{IN}$ | 100 nF | – | – | – | – | 100 nF |
| Harvesting Efficiency | – | – | – | – | – | 99% |
| Overall Efficiency | – | 58% | 73% | – | – | 86% |
| Other | 1:60 X-Former | 22 µH 22 µH MEMS Switch | 2 µH 2 µH 100 µH 27 µH | 6.8 µH | 1 Inductor | 100 µH |
| Inductor Volume | 175 $mm^3$ | 150 $mm^3$ | **16 $mm^3$ | **4 $mm^3$ | 4 $mm^3$ | 4 $mm^3$ |
| Tech. | 0.13 µm | 0.35 µm | 65 nm | 65 nm | – | 0.18 µm |

## 6.4 Summary

This chapter presented an energy harvesting system that quickly wakes from no charge conditions. It integrates the starter presented in Chapter 5 to initially charge a temporary supply that would then allow a maximum power point charger to efficiently deliver power to the battery even when the battery voltage is low. Low power circuits were also described that allow the system to maintain high efficiency, even at low input

power levels. Additionally by substituting the diode in the harvesting system used in Chapter 4 with a MOS switch, efficiency across power levels was improved. With a 100 nF input capacitor and a 100 μH transfer inductor, the 0.18-μm CMOS charger prototyped draws 98.8%–99.7% of the power supplied by a 200–350-mV source and delivers 76%–86% of the 40–150 μW drawn to charge a fully depleted 1.8-μF battery to 0.9 V in 45 ms with an equivalent charge current of 36 μA. This is 13.3× faster than the best reported single-inductor solution, and although only 1.125× faster than the best possible alternative, with three fewer off-chip inductors. The charger is much faster with one inductor because a small on-chip 200-pF power supply, which charges and replenishes quickly, feeds the charger at a voltage that is sufficiently high to switch quickly and keep ohmic and gate-drive losses low. This way, the system can more easily charge the battery and replenish the temporary supply in alternating cycles until the battery is high enough to supply the system. Fast wakeup features of this sort are important because tiny onboard batteries exhaust easily and frequently, and clouds, debris, water, and other factors often interrupt the harvesting action of small photovoltaic and thermoelectric generators.

# CHAPTER 7

# CONCLUSIONS

With their increasingly small size, wireless microsensors can add intelligence to a large infrastructure or the human body by creating a network of tiny, autonomous sensors, which send data to a central processor. Restricting the size of microsensors to the millimeter scale allows them to be numerous yet non-obtrusive. However, the limited space constricts the amount of energy that can be stored on-board the system. Harvesting energy from the environment can help reduce or eliminate this restriction by supplementing or recharging the storage device. The battery, which can be lithium ion, supercapacitor, atomic battery or another high-density storage technology, provides the necessary supply to the DC–DC converter in order to transfer energy to the functional components. However, if the ambient energy disappears during an extended period of time, the battery depletes and can no longer provide enough energy or voltage to the system. When the ambient source returns, the system must wake using the voltage and power from the harvesting source alone.

Operating from such a low input voltage is challenging because with low gate drive transistors are resistive, and as a result, lossy. The charger can therefore consume much of the power drawn, leaving little left for the battery $C_B$ and other blocks. As a result, $C_B$ charges slowly, if at all, and the microsensor must wait for $C_B$'s voltage $v_B$ to reach a headroom level that is high enough for system components to perform their prescribed tasks. This is a problem when the source appears across short intervals because $v_B$ may not rise sufficiently to power the sensor, and leakages may drain $C_B$

before the harvesting source is available again. The charger should therefore replenish $C_B$ as quickly as possible, and since space is scarce in a microsystem, do so with as few off-chip components as possible. To this end, the system should use a starter circuit to charge a small temporary supply quickly that can then enable a high efficiency charger to replenish the battery until its voltage surpasses the headroom level of the system.

## 7.1 Low Voltage Starters

With the abundance of light and heat energy in microsensor applications, harvesting from heat and light becomes an attractive and practical solution to extend lifetime. However, the small size of the transducers limits the voltage and power generated. Photovoltaic cells small enough to be used in microsystems generate 300 – 450 mV of open circuit voltage and 1 – 100 μW of power from indoor light [125], [126]. Tiny thermoelectric generators produce up to 80 mV/K, which generates about 10 μW from one kelvin of temperature difference. With only hundreds of millivolts available at the input, a boosting power converter is required to charge the battery and supply the system.

When light or heat energy disappears for an extended period of time, the system will eventually deplete the battery to a voltage below the headroom level. When the energy source returns, the battery voltage is not enough to supply the charger with the necessary gate drive voltage and power. Therefore, the system requires a starter circuit which draws power directly from the low-voltage input source to charge the battery or a startup capacitor. Because of the low gate drive provided by the input source, starter circuits are inefficient, so charging a large capacitor, such as the battery, would lead to impractically long wakeup times. Alternatively, charging a temporary supply with the starter first, and then supplying a maximum power point (MPP) charger with the

temporary supply would significantly cut down on wake time since the low efficiency starter is only used for a short amount of time.

Today, energy-harvesting chargers use additional bulky components, such as transformers, inductors, or capacitors, which demand considerable space, or fine-tuned devices, which require additional processing steps, to start the system. What is more, state-of-the-art starters are slow and inefficient, which means systems can only harness a fraction of the energy available during startup. In general, the state of the art low voltage chargers can be divided into two main categories: starters that charge the battery and starters that charge a temporary supply through an additional inductor.

The amplifying transformer based starter, with a transformer replacing $L_X$ in Figure 7.1a, charges the battery in startup and steady state with the same transformer. Similarly, a ring oscillator driven starter shares the inductor between the starter and MPP charger, but nevertheless charges the battery during startup, which results in an extended wake time. Using a motion activated switch to charge a temporary supply requires a second inductor, $L_{ST}$ in Figure 7.1b, which increases the overall size and cost of the system. An LC oscillator driven starter also requires an extra startup inductor, in addition to two oscillating inductors inside the starter block. Although these chargers start up to a temporary supply, and therefore have a fast wake time, they nevertheless require at least one additional, bulky inductor. In summary, state-of-the-art chargers are slow to wake because they startup directly to the large battery or rely on bulky additional components to create a temporary supply that speeds up the wake process.

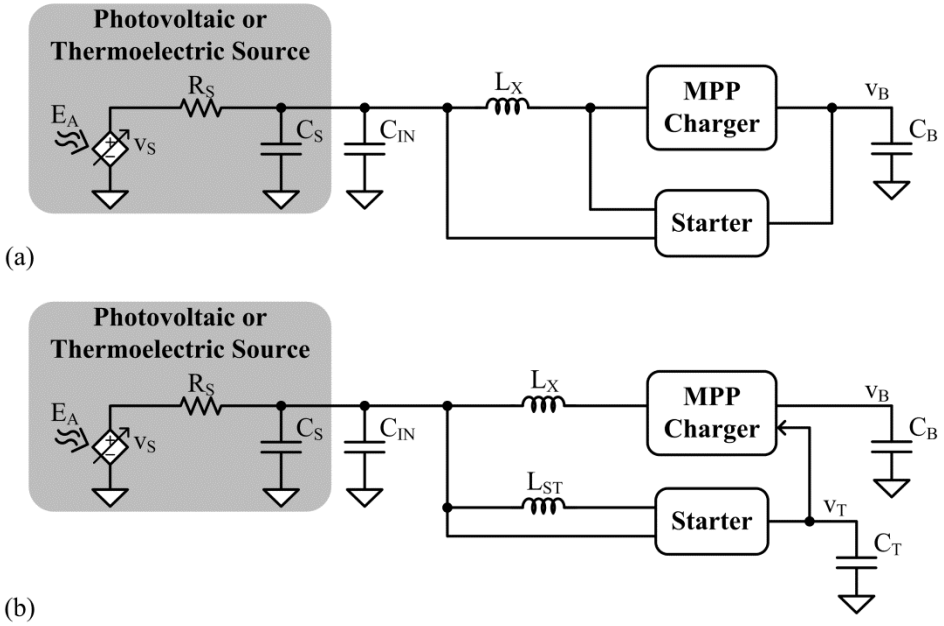


**Figure 7.1. Low-voltage starting chargers (a) without a temporary supply and (b) with additional inductor to charge a temporary supply.**

## 7.2 Research Contributions

### 7.2.1 Self-Starting Charger System

The main contribution of this research is an energy harvesting system, show in Figure 7.2, which achieves a fast wake time using a starter circuit that does not add any off-chip components. The starter begins the wake process by quickly, albeit inefficiently, charging the temporary supply, $C_T$, above the required headroom level. Once the temporary supply, $C_T$ in Figure 7.2 is charged, a control block turns the starter off and begins charging the battery. Whereas the starter uses the low input voltage for gate drive, the battery charger uses the temporary supply initially charged by the starter, so that the battery is charged with high efficiency.

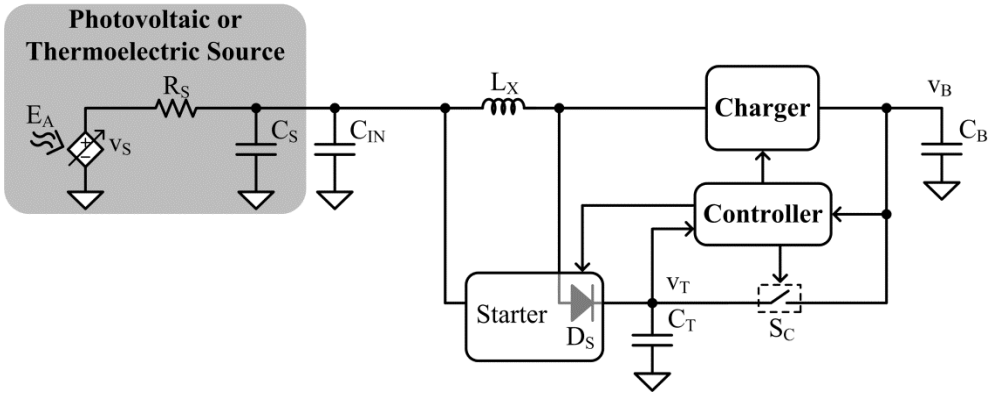


**Figure 7.2. Proposed low-voltage energy harvester with fast wake time.**

To achieve low loss energy transfer, the battery is charged though a diode emulating switch, which drops less voltage when compared to a traditional PN junction diode. Since the temporary supply provides gate drive and quiescent power to the battery charger, the temporary supply will eventually discharge below the headroom level if it is not refreshed. Therefore, the controller monitors the temporary supply's voltage and sends it an energy packet when its voltage nears the headroom level. By momentarily disabling the battery diode, the charger can energize the inductor and then allow it to drain into the temporary supply through the diode, $D_S$, inside the starter block. Once the temporary supply is charged back above the headroom level, the system resumes battery charging.

After the battery is charged to the headroom level of the system, the controller shorts the temporary supply and the battery through switch $S_C$. Since $v_T$ and $v_B$ are now at the same voltage, the charger only needs to send energy through the battery diode, so the starter diode $D_S$ is no longer used. At this point, the wake phase is complete, and the system enters steady state. To summarize, a novel power stage and control scheme allows the system to start up, charge the battery, and refresh the temporary supply with a single

inductor, thereby reducing the system size and decreasing wake time when compared to the state of the art.

To create the complete harvesting system, several low power, low voltage blocks were developed and designed. A novel threshold detector was created that monitored the temporary supply and informed the system if the voltage was above or below the headroom level of the bias generator. A similar threshold detector, but with a shifted threshold, was used to loosely regulate the temporary supply. A copy of this detector monitored the battery and informed the system when the system should use the battery as the main supply. Additionally, a low voltage comparator was designed that quickly detected when the current through the battery diode was zero, so a low loss switch could replace a typical, lossy PN junction diode. Finally, a state machine and a race-condition preventing circuit were developed so that the system could deliver energy to two outputs without conflict.

*Related Publication:*

- A. Blanco and G.A. Rincón-Mora, "Self-Starting and Fast-Waking Light/Heat-Harvesting Single-Inductor 0.18-µm CMOS Charger," IEEE Journal of Solid State Circuits (JSSC), [Submitted for Review: February 2017].

### 7.2.2 Low Voltage Starter

A novel starter circuit was developed, designed, fabricated, and tested that reuses the inductor from the maximum power point charger to initially charge a temporary supply, $C_T$. The oscillating core in the starter energizes the inductor and then, through a diode, charges the output capacitance. The oscillator uses the high amplitudes that it produces to increase the gate drive available to it. An auxiliary oscillator was developed and designed

to jump start the oscillating core when the input voltage rises slowly as is expected in typical wireless microsystem applications. The starter also includes a resetting circuit, which allows the starter to charge the output from a limited-power source, which is also expected in typical applications. When the starter draws power, the input voltage may fall, causing the starter to stall and not charge the output voltage. In this case, the resetting circuit turns the starter completely off so that the input voltage recovers and the starter can attempt to fully charge the output capacitor.

*Related Publications:*

- A. Blanco and G.A. Rincón-Mora, "A 44–93 250–400 mV 0.18-µm CMOS Starter for DC-Sourced Switched-Inductor Energy Harvesters," IEEE Transactions on Circuits and Systems II (TCAS II), vol. 61, no. 12, pp. 1002-1006, Dec 2014.
- A. Blanco and G.A. Rincón-Mora, "Bootstrapping and Resetting CMOS Starter for Thermoelectric and Photovoltaic Chargers," IEEE Transactions on Circuits and Systems II (TCAS II), [Accepted: March 2017].

### 7.2.3 Analysis of Drought Recovery & Low-Energy Task Scheduling

A novel task scheduling algorithm was developed that allows for the minimum size of the system battery. By scheduling only one task at a time, the battery only provides the power requirements of one task, and can therefore be sized so that it can provide power to the highest power consuming task. In between tasks, the battery is charged enough to supply the next task. Minimizing the battery not only saves on system size and cost, but also results in lower wake times, since a smaller battery charges faster. If this algorithm is not used, and tasks can be performed simultaneously, the battery would have to provide

large amounts of power. In this case, the battery would have to be sized to provide the sum of the power requirements of all tasks. Therefore, to minimize system size and minimize wake time, tasks should be completed one at a time.

An analysis was conducted to prove that maintaining the battery charge during energy droughts was unnecessary and led to impractically large systems. Instead, the battery should be allowed to drain, and the system should wake when the energy source returns. The analysis also showed that charging a temporary supply during wake before charging the battery significantly reduces wake time. This reduction is due to the fact that the startup process is generally inefficient since there is not enough gate drive to fully turn on CMOS switches. Therefore, by only using the inefficient process on a small capacitor, the process is quick. Once the small capacitor is charged, it becomes the gate drive supply to the main charger, which can begin delivering energy efficiently to the battery.

*Related Publication:*

- A. Blanco and G.A. Rincón-Mora, "Energy-Harvesting Microsensors: Low-Energy Task Schedule & Fast Drought-Recovery Design," IEEE Midwest Symposium on Circuits and Systems (MWSCAS), Abu Dhabi, United Arab Emirates (UAE), Oct 16 – 19, 2016.

### 7.2.4 Study of the state of the art

One part of validating the presented technology is to compare its performance to the state of the art in low voltage starters. A literature survey was conducted to compare existing technologies and study their strengths and weaknesses. Important performance metrics were selected when designing the proposed starter in order to have the highest impact. A

figure of merit was developed to normalize the charging capabilities of all starter circuits across a range of test conditions.

*Related Publication:*

- A. Blanco and G.A. Rincón-Mora, "On-chip Starter Circuit for Switched-inductor DC–DC Harvester Systems," IEEE International Symposium on Circuits and Systems (ISCAS), Beijing, China, May 19 – 23, 2013.

### 7.2.5 Current measurements

In the process of testing the prototypes, inductor current measurements were taken to validate operation and performance. However, at such low current levels and high frequencies in which the starter operates, measuring these signals can be difficult. Therefore, a study was conducted regarding different methods of measuring inductor currents, and determining which method was the best in terms of noise and maximum bandwidth. Experiments comparing these methods validated the analysis and the determination of the best method. This study not only allows for better measurement for the proposed starter, but future low power measurements can benefit from this analysis.

*Related Publication:*

- A. Blanco and G.A. Rincón-Mora, "Measuring Micro-amp Inductor Currents in Switched-inductor DC–DC Power Supplies," IEEE International Instrumentation and Measurement Technology Conference (I2MTC), Montevideo, Uruguay, May 12 – 15, 2014.

## 7.3 Technological Limitations and Future Research Direction

Although the developed technology provides the fastest wake time along with the best integration in the state of the art, several technological limitations remain. First, the minimum input voltage is not significantly improved when compared to the state of the art and is even much worse when compared to larger solutions. The current system also implements a crude and open-loop maximum power point tracking scheme. While showing good performance in the lab, this loop should eventually be closed so that it can track across process variations and temperature along with more nonlinear sources. Finally, a wireless microsensor requires a regulated voltage that provides power to the functional load components. The system presented here only charges the battery whose voltage varies with the state of charge. Therefore, more research must be conducted to add this final stage to the system.

### 7.3.1 Reduce Minimum Input Voltage of Starter

While the proposed starter had the best integration while maintaining comparable performance, other starters in the state of the art achieve minimum input voltages that are an order of magnitude smaller. To start from these ultra-low voltages, the state of the art requires bulky and expensive components or depends on the presence of motion in the environment. The proposed starter circuit is voltage limited due primarily to two reasons. First, the threshold voltage of the energizing and feedback transistors limits the minimum input voltage, since input voltages below the threshold voltage cause these transistors to be off or highly resistive. Secondly, the energy that can be stored in the inductor is strongly dependent on the voltage across the inductor during the energizing phase. Since

one terminal of the inductor is the input voltage, lower input voltage leads to lower inductor current and energy. If the inductor energy is too low, it cannot charge the switch-node capacitance high enough to engage the oscillating core.

Using a lower or zero threshold transistors would help alleviate the first obstacle since the transistors would remain on for lower input voltages. However, the second obstacle remains regardless of threshold voltage. The inductor energy could also be increased by increasing the inductance value. However, this typically leads to a larger volume device or a larger equivalent resistance. A larger volume inductor would be counter to the integration required by wireless microsensors and a larger series resistance would lead to lower steady state charging efficiency. Therefore, further research is required to either increase the extracted energy from the source or reduce the energy required to charge the output in order to reduce the minimum input voltage.

### 7.3.2 Maximum Power Point Tracking Loop

Because of the low power produced by tiny energy harvesting transducers, the battery charger must extract power at or near the transducer's maximum power point. Extracting power far from this point results in an opportunity loss in which the transducer could produce more power, but the battery does not receive it. For a source that can be modeled by a voltage source in series with a resistor, such as the source in Figure 7.3, a converter with a fixed frequency and fixed energizing time can be designed so that it extracts the maximum power regardless of the open circuit voltage, $v_S$. In other words, for a given source resistance, $R_S$, there exists a frequency and energizing time that extracts the maximum power from a transducer [128]. In discontinuous conduction mode (DCM), the average inductor current rises linearly with input voltage, and since the drawn current

which produces the maximum power, $I_{MPP}$, also rises linearly with input voltage, the charger can be designed so that the inductor current closely matches $I_{MPP}$. The harvesting charger presented in Chapter 6 used this scheme to extract maximum power from an emulated thermoelectric source.

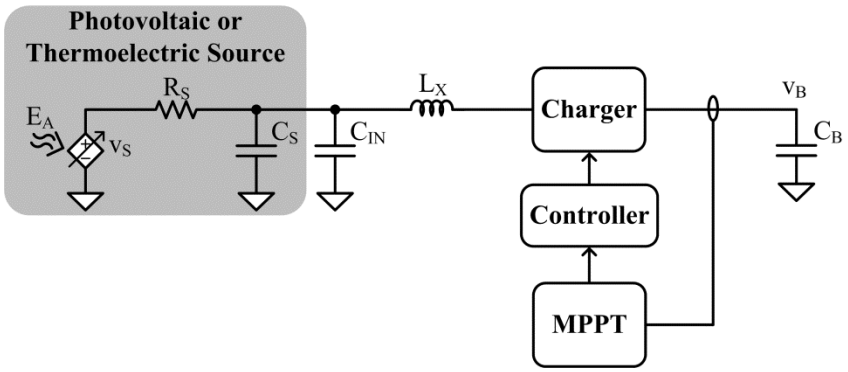


**Figure 7.3. System diagram with maximum power point tracking loop.**

Although the proposed battery charger had a 99% harvesting efficiency when harvesting from a emulated thermoelectric source, the switching frequency was set manually in the lab set-up. Therefore, if there are variations in the source resistance, $R_S$ in Figure 7.3, the harvesting efficiency will fall. The power that the harvester will attempt to draw will differ from the source's maximum power point. Additionally, the switching frequency and energizing time set by design will vary in fabrication and with temperature and time. Therefore, a slow changing maximum power point tracking loop is required to guarantee that the switching frequency and energizing time are set correctly and do not change with time.

For thermoelectric sources, the switching parameters of the battery charger should not change much over time, since the source resistance will remain mostly constant throughout the harvester's lifetime. Photovoltaic sources, however, have a nonlinear relationship between the open circuit voltage and $I_{MPP}$. As a result, as the input voltage

changes, the inductor current will change linearly and will not match the nonlinear $I_{MPP}$. Therefore, photovoltaic sources require a changing switching frequency so that the drawn power matches the maximum available power. In this case, an external maximum power point tracking loop must be included in which the switching frequency is selected in real time to maximize the harvested power. The speed of this loop will depend on the expected time constant of the energy source. Finally, the loop should sense and maximize the battery power instead of the input power, since losses in the charger will slightly vary the maximum power point of the system.

### 7.3.3 Integrated Power Supply for Load

The purpose of the maximum power point battery charger in a wireless microsensor is to provide and store energy in the battery so that the battery in turn can provide power and voltage to the load, which can be sensors, data processors, transmitters, or receivers. As described in Chapter 2, the battery size is minimized when its voltage is allowed to rise as high as the technology break down voltage and fall as low as the headroom voltage during regular operation. Since the battery voltage varies with its stored charge, the battery voltage is not an appropriate supply for the load, which typically requires a constant voltage. Instead, a voltage regulating power supply is used in between the battery and the load to transfer power between the battery and the load while regulating the load voltage, $v_{LD}$ in Figure 7.4.

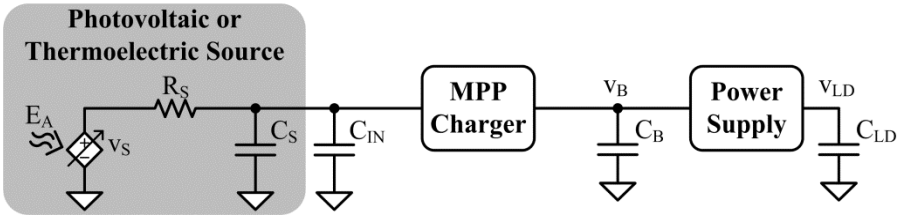


**Figure 7.4. Energy harvesting system with regulated load.**

The voltage-regulating power supply could be a switched-inductor, switched-capacitor or linear regulator. While a switched-inductor power converter would provide the highest efficiency, an additional inductor would significantly increase the size of the energy harvesting system. Fortunately, state of the art power supplies reuse the inductor already in the battery charger to regulate the load voltage [163]. However, these supplies require the inductor be disconnected from the input voltage, which is not compatible with the starter presented in Chapters 4 and 5. Therefore, further research must be done to investigate methods of sharing the inductor between the starter, the charger and the power supply without requiring extra components or special fabrication processes.

Alternatively, a switched-capacitor converter with on-chip capacitors can be used. However, switched-capacitors have high efficiency when the ratio between input and output voltages remains relatively constant. Since the output voltage will be regulated, it is not expected to vary much. However, the input voltage of the power supply, the battery, will vary considerably as it is charged and discharged. Therefore, a switched-capacitor circuit is not an attractive solution since efficiency will be low. Finally, a linear regulator, the simplest and smallest of the three power converter types, has two major drawbacks. First, the loss in a linear regulator is proportional to the voltage difference between its input and output. Therefore, when the battery voltage is at its maximum voltage, the linear regulator will have poor efficiency. The second drawback is that the linear regulator can only produce a voltage lower than its input. This would require that the output voltage always be below the battery voltage, which may not be a practical requirement.

## 7.4 Summary

Harvesting energy from light or temperature differences in the environment provides a practical solution to extend the lifetime of wireless microsystems. Unfortunately, these kinds of ambient sources are not always present. With the limited size available in the system, the on-board battery cannot store enough energy to power the microsystem throughout the drought, even if the system goes into a low power shutdown mode. Therefore, after prolonged energy droughts, the battery completely depletes. When the ambient source returns, the system should resume operation as fast as possible, which requires quickly recharging the discharged battery. Reducing the size and energy capacity of the battery allows for a faster wake time. To this end, an algorithm and design procedure was developed to minimize the required size of the battery. Nevertheless, when the battery is discharged, the charger must be supplied from the low voltage produced by the energy harvester transducer. This low gate drive results in low efficiency charging during startup. Since startup is inefficient, recharging a drained battery impractically extends the wake time. Instead, quickly charging a smaller capacitor first, then using the capacitor as a supply for the charger allows for high efficiency charging and faster wake time.

A novel starter circuit was designed that reuses the battery-charging inductor to minimize the impact on the system's size. This starter circuit quickly charges an on-chip capacitor that serves as a temporary supply to a maximum power point charger. The charger and its controller were designed so that it could manage sharing the inductor between the starter and charger. After the starter charges the temporary supply, the system maintains the temporary supply above the headroom requirements of the charger

as the battery begins charging. After the battery is charged to the system's headroom level, the system shorts the temporary supply with the battery and the system continues charging the battery. Prototypes of the starter and harvesting system showed that wake time could be minimized while keeping the system size small.

# REFERENCES


[1] J. Yoo, L. Yan, S. Lee, Y. Kim, and H. J. Yoo, "A 5.2 mW Self-Configured Wearable Body Sensor Network Controller and a 12 μW Wirelessly Powered Sensor for a Continuous Health Monitoring System," *IEEE Journal of Solid-State Circuits,* vol. 45, pp. 178-188, 2010.

[2] R. F. Yazicioglu, P. Merken, R. Puers, and C. V. Hoof, "A 60 μW 60 nV/√Hz Readout Front-End for Portable Biopotential Acquisition Systems," *IEEE Journal of Solid-State Circuits,* vol. 42, pp. 1100-1110, 2007.

[3] A. C. R. Grayson, R. S. Shawgo, A. M. Johnson, N. T. Flynn, L. I. Yawen, M. J. Cima*, et al.*, "A BioMEMS review: MEMS technology for physiologically integrated devices," *Proceedings of the IEEE,* vol. 92, pp. 6-21, 2004.

[4] L. S. Y. Wong, S. Hossain, A. Ta, J. Edvinsson, D. H. Rivas, and H. Naas, "A very low-power CMOS mixed-signal IC for implantable pacemaker applications," *IEEE Journal of Solid-State Circuits,* vol. 39, pp. 2446-2456, 2004.

[5] G. Chen, M. Fojtik, D. Kim, D. Fick, J. Park, M. Seok*, et al.*, "Millimeter-scale nearly perpetual sensor system with stacked battery and solar cells," in *2010 IEEE International Solid-State Circuits Conference*, 2010, pp. 288-289.

[6] G. Chen, H. Ghaed, R. u. Haque, M. Wieckowski, Y. Kim, G. Kim*, et al.*, "A cubic-millimeter energy-autonomous wireless intraocular pressure monitor," in *2011 IEEE International Solid-State Circuits Conference*, 2011, pp. 310-312.

[7] M. M. Ahmadi and G. A. Jullien, "A Wireless-Implantable Microsystem for Continuous Blood Glucose Monitoring," *IEEE Transactions on Biomedical Circuits and Systems,* vol. 3, pp. 169-180, 2009.

[8] R. Sahai, S. Avadhanula, R. Groff, E. Steltz, R. Wood, and R. S. Fearing, "Towards a 3g crawling robot through the integration of microrobot technologies," in *Proceedings IEEE International Conference on Robotics and Automation*, 2006, pp. 296-302.

[9] A. C. R. Grayson, I. S. Choi, B. M. Tyler, P. P. Wang, H. Brem, M. J. Cima*, et al.*, "Multi-pulse drug delivery from a resorbable polymeric microchip device," *Nature Materials,* vol. 2, pp. 767-772, 2003.

[10] D. A. LaVan, T. McGuire, and R. Langer, "Small-scale systems for in vivo drug delivery," *Nat Biotech,* vol. 21, pp. 1184-1191, 2003.

[11] S. Smith, T. B. Tang, J. G. Terry, J. T. M. Stevenson, B. W. Flynn, H. M. Reekie*, et al.*, "Development of a miniaturised drug delivery system with wireless power transfer and communication," *IET Nanobiotechnology,* vol. 1, pp. 80-86, 2007.

[12] S. Lee, L. Yan, T. Roh, S. Hong, and H. J. Yoo, "A 75 μW Real-Time Scalable Body Area Network Controller and a 25 μW ExG Sensor IC for Compact Sleep Monitoring Applications," *IEEE Journal of Solid-State Circuits,* vol. 47, pp. 323-334, 2012.

[13] J. Yan, R. J. Wood, S. Avadhanula, M. Sitti, and R. S. Fearing, "Towards flapping wing control for a micromechanical flying insect," in *IEEE International Conference on Robotics and Automation*, 2001, pp. 3901-3908

[14] M. Flatscher, M. Dielacher, T. Herndl, T. Lentsch, R. Matischek, J. Prainsack*, et al.*, "A Bulk Acoustic Wave (BAW) Based Transceiver for an In-Tire-Pressure Monitoring Sensor Node," *IEEE Journal of Solid-State Circuits,* vol. 45, pp. 167-177, 2010.

[15] M. Flatscher, M. Dielacher, T. Herndl, T. Lentsch, R. Matischek, J. Prainsack*, et al.*, "A robust wireless sensor node for in-tire-pressure monitoring," in *IEEE International Solid-State Circuits Conference*, 2009, pp. 286-287.

[16] I. F. Akyildiz, W. Su, Y. Sankarasubramaniam, and E. Cayirci, "Wireless sensor networks: a survey," *Computer Networks,* vol. 38, pp. 393-422, 2002.

[17] D. C. Daly, P. P. Mercier, M. Bhardwaj, A. L. Stone, Z. N. Aldworth, T. L. Daniel*, et al.*, "A Pulsed UWB Receiver SoC for Insect Motion Control," *IEEE Journal of Solid-State Circuits,* vol. 45, pp. 153-166, 2010.

[18] J. Marek, "MEMS for automotive and consumer electronics," in *IEEE International Solid-State Circuits Conference*, 2010, pp. 9-17.

[19] R. J. M. Vullers, R. v. Schaijk, H. J. Visser, J. Penders, and C. V. Hoof, "Energy Harvesting for Autonomous Wireless Sensor Networks," *IEEE Solid-State Circuits Magazine,* vol. 2, pp. 29-38, 2010.

[20] D. Puccinelli and M. Haenggi, "Wireless sensor networks: applications and challenges of ubiquitous sensing," *IEEE Circuits and Systems Magazine,* vol. 5, pp. 19-31, 2005.

[21] C. W. Chang, Y. J. Chen, S. H. Hung, and J. C. Chiou, "A wireless and batteryless microsystem with implantable grid electrode/3-dimensional probe array for ECoG and extracellular neural recording on rat," in *International Solid-State Sensors, Actuators and Microsystems Conference*, 2011, pp. 2176-2179.

[22] A. D. DeHennis and K. D. Wise, "A wireless microsystem for the remote sensing of pressure, temperature, and relative humidity," *Journal of Microelectromechanical Systems,* vol. 14, pp. 12-22, 2005.

[23] S. Sudevalayam and P. Kulkarni, "Energy Harvesting Sensor Nodes: Survey and Implications," *IEEE Communications Surveys & Tutorials,* vol. 13, pp. 443-461, 2011.

[24] H. Yang and Y. Zhang, "Analysis of Supercapacitor Energy Loss for Power Management in Environmentally Powered Wireless Sensor Nodes," *IEEE Transactions on Power Electronics,* vol. 28, pp. 5391-5403, 2013.

[25] D. Linden and T. B. Reddy, *Handbook of batteries*, 3rd ed. ed. New York :: McGraw-Hill, 2002.

[26] C. Moore, J. Li, and P. Kohl, "Microfabricated Fuel Cells with Thin-Film Silicon Dioxide Proton Exchange Membranes," *Journal of the Electrochemical Society,* vol. 152, pp. 1606-1612, 2005.

[27] R. Dillon, S. Srinivasan, A. S. Aricò, and V. Antonucci, "International activities in DMFC R&D: status of technologies and potential applications," *Journal of Power Sources,* vol. 127, pp. 112-126, 2004.

[28] S. Kim and G. Rincón-Mora, "Single-inductor fuel cell-Li ion charger-supply IC with nested hysteretic control," *Analog Integrated Circuits and Signal Processing,* vol. 70, pp. 33-45, 2012.

[29] M. Chen and G. A. R.-. Mora, "A Compact Electrical Model for Microscale Fuel Cells Capable of Predicting Runtime and I-V Polarization Performance," *IEEE Transactions on Energy Conversion,* vol. 23, pp. 842-850, 2008.

[30] M. Chen, J. P. Vogt, and G. A. Rincón-Mora, "Design methodology of a hybrid micro-scale fuel cell-thin-film lithium ion source," in *Midwest Symposium on Circuits and Systems (MWSCAS)*, 2007, pp. 674-677.

[31] R. Bogue, "Powering tomorrow's sensor: a review of technologies – Part 1," *Sensor Review,* vol. 30, pp. 182-186, 2010.

[32] R. Duggirala, *Radioisotope Thin-Film Powered Microsystems*. Dordrecht: Springer, 2010.

[33] X. Wei and J. Liu, "Power sources and electrical recharging strategies for implantable medical devices," *Frontiers of Energy and Power Engineering in China,* vol. 2, pp. 1-13, 2008.

[34] P. D. Mitcheson, E. M. Yeatman, G. K. Rao, A. S. Holmes, and T. C. Green, "Energy Harvesting From Human and Machine Motion for Wireless Electronic Devices," *Proceedings of the IEEE,* vol. 96, pp. 1457-1486, 2008.

[35] S. Meninger, J. O. Mur-Miranda, R. Amirtharajah, A. Chandrakasan, and J. H. Lang, "Vibration-to-electric energy conversion," *Very Large Scale Integration (VLSI) Systems, IEEE Transactions on,* vol. 9, pp. 64-76, 2001.

[36] S. Meninger, T. O. Mur-Miranda, R. Amirtharajah, A. Chandrakasan, and J. Lang, "Vibration-to-electric energy conversion," *IEEE Transactions on Very Large Scale Integration (VLSI) Systems,* vol. 9, pp. 48-53, 1999.

[37] M. E. Kiziroglou, C. He, and E. M. Yeatman, "Rolling Rod Electrostatic Microgenerator," *Industrial Electronics, IEEE Transactions on,* vol. 56, pp. 1101-1108, 2009.

[38] M. E. Kiziroglou, C. He, and E. M. Yeatman, "Flexible substrate electrostatic energy harvester," *Electronics Letters,* vol. 46, pp. 166-167, 2010.

[39] M. Miyazaki, H. Tanaka, G. Ono, T. Nagano, N. Ohkubo, T. Kawahara*, et al.*, "Electric-energy generation using variable-capacitive resonator for power-free

LSI: efficiency analysis and fundamental experiment," in *International Symposium on Low Power Electronics and Design*, 2003, pp. 193-198.

[40] Y. Chiu and V. F. G. Tseng, "A capacitive vibration-to-electricity energy converter with integrated mechanical switches," *Journal of Micromechanics and Microengineering,* vol. 18, 2008.

[41] B. C. Yen and J. H. Lang, "A variable-capacitance vibration-to-electric energy harvester," *Circuits and Systems I: Regular Papers, IEEE Transactions on,* vol. 53, pp. 288-295, 2006.

[42] E. O. Torres and G. A. Rincon-Mora, "Electrostatic Energy-Harvesting and Battery-Charging CMOS System Prototype," *Circuits and Systems I: Regular Papers, IEEE Transactions on,* vol. 56, pp. 1938-1948, 2009.

[43] E. O. Torres and G. A. Rincón-Mora, "A 0.7-µm BiCMOS Electrostatic Energy-Harvesting System IC," *IEEE Journal of Solid-State Circuits,* vol. 45, pp. 483-496, 2010.

[44] E. O. Torres and G. A. Rincon-Mora, "Self-Tuning Electrostatic Energy-Harvester IC," *Circuits and Systems II: Express Briefs, IEEE Transactions on,* vol. 57, pp. 808-812, 2010.

[45] P. D. Mitcheson, P. Miao, B. H. Stark, E. M. Yeatman, A. S. Holmes, and T. C. Green, "MEMS electrostatic micropower generator for low frequency operation," *Sensors & Actuators: A. Physical,* vol. 115, pp. 523-529, 2004.

[46] P. Miao, P. Mitcheson, A. Holmes, E. Yeatman, T. Green, and B. Stark, "Mems inertial power generators for biomedical applications," *Microsystem Technologies,* vol. 12, pp. 1079-1083, 2006.

[47] G. Despesse, J. J. Chaillout, T. Jager, F. Cardot, and A. Hoogerwerf, "Innovative Structure for Mechanical Energy Scavenging," in *International Solid-State Sensors, Actuators and Microsystems Conference*, 2007, pp. 895-898.

[48] R. Amirtharajah, S. Meninger, J. O. Mur-Miranda, A. Chandrakasan, and J. Lang, "A micropower programmable DSP powered using a MEMS-based vibration-to-electric energy converter," in *International Solid-State Circuits Conference*, 2000, pp. 362-363.

[49] A. M. Paracha, P. Basset, D. Galayko, F. Marty, and T. Bourouina, "A Silicon MEMS DC/DC Converter for Autonomous Vibration-to-Electrical-Energy Scavenger," *Electron Device Letters, IEEE,* vol. 30, pp. 481-483, 2009.

[50] S. Roundy, P. K. Wright, and J. Rabaey, "A study of low level vibrations as a power source for wireless sensor nodes," *Computer Communications,* vol. 26, pp. 1131-1144, 2003.

[51] H.-B. Fang, J.-Q. Liu, Z.-Y. Xu, L. Dong, L. Wang, D. Chen*, et al.*, "Fabrication and performance of MEMS-based piezoelectric power generator for vibration energy harvesting," *Microelectronics Journal,* vol. 37, pp. 1280-1284, 2006.

[52] S. Roundy, "A piezoelectric vibration based generator for wireless electronics," *Smart Materials and Structures,* vol. 13, pp. 1131-1142, 2004.

[53] P. Glynne-Jones, S. P. Beeby, and N. M. White, "Towards a piezoelectric vibration-powered microgenerator," *IEE Proceedings - Science, Measurement and Technology,* vol. 148, pp. 68-72, 2001.

[54] H. Sodano, D. Inman, and G. Park, "Generation and Storage of Electricity from Power Harvesting Devices," *Journal of Intelligent Material Systems and Structures,* vol. 16, pp. 67-75, 2005.

[55] M. El-Hami, P. Glynne-Jones, N. M. White, M. Hill, S. Beeby, E. James*, et al.*, "Design and fabrication of a new vibration-based electromechanical power generator," *Sensors & Actuators: A. Physical,* vol. 92, pp. 335-342, 2001.

[56] S. P. Beeby, R. N. Torah, M. J. Tudor, P. Glynne-Jones, T. O'Donnell, C. R. Saha*, et al.*, "A micro electromagnetic generator for vibration energy harvesting," *Journal of Micromechanics and Microengineering,* vol. 17, pp. 1257-1265, 2007.

[57] I. Sari, T. Balkan, and H. Kulah, "An Electromagnetic Micro Power Generator for Low-Frequency Environmental Vibrations Based on the Frequency Upconversion Technique," *Microelectromechanical Systems, Journal of,* vol. 19, pp. 14-27, 2010.

[58] H. Kulah and K. Najafi, "Energy Scavenging From Low-Frequency Vibrations by Using Frequency Up-Conversion for Wireless Sensor Applications," *Sensors Journal, IEEE,* vol. 8, pp. 261-268, 2008.

[59] M. Duffy and D. Carroll, "Electromagnetic generators for power harvesting," in *IEEE Annual Power Electronics Specialists Conference*, 2004, pp. 2075-2081.

[60] C. B. Williams, C. Shearwood, M. A. Harradine, P. H. Mellor, T. S. Birch, and R. B. Yates, "Development of an electromagnetic micro-generator," *IEE Proceedings - Circuits, Devices and Systems,* vol. 148, pp. 337-342, 2001.

[61] T. Von Büren and G. Tröster, "Design and optimization of a linear vibration-driven electromagnetic micro-power generator," *Sensors & Actuators: A. Physical,* vol. 135, pp. 765-775, 2007.

[62] P. Glynne-Jones, M. J. Tudor, S. P. Beeby, and N. M. White, "An electromagnetic, vibration-powered generator for intelligent sensor systems," *Sensors & Actuators: A. Physical,* vol. 110, pp. 344-349, 2004.

[63] S. Behrens, J. Ward, and J. Davidson, "Adaptive vibration energy harvesting," *Active and Passive Smart Structures and Integrated Systems,* vol. 6525, 2007.

[64] S. C. L. Yuen, J. M. H. Lee, W. J. Li, and P. H. W. Leong, "An AA-Sized Vibration-Based Microgenerator for Wireless Sensors," *IEEE Pervasive Computing,* vol. 6, pp. 64-72, 2007.

[65] I. Sari, T. Balkan, and H. Kulah, "An electromagnetic micro power generator for wideband environmental vibrations," *Sensors & Actuators: A. Physical,* vol. 145-146, pp. 405-413, 2008.

[66] C. R. Saha, T. O'Donnell, H. Loder, S. Beeby, and J. Tudor, "Optimization of an Electromagnetic Energy Harvesting Device," *IEEE Transactions on Magnetics,* vol. 42, pp. 3509-3511, 2006.

[67] X. Cao, W. J. Chiang, Y. C. King, and Y. K. Lee, "Electromagnetic energy harvesting circuit with feedforward and feedback DC-DC PWM boost converter for vibration power generator system," vol. 22, pp. 679-685, 2007.

[68] E. D. Mantiply, K. R. Pohl, S. W. Poppell, and J. A. Murphy, "Summary of measured radiofrequency electric and magnetic fields (10 kHz to 30 GHz) in the general and work environment," *Bioelectromagnetics,* vol. 18, p. 563, 1997.

[69] T. Salter, K. Choi, M. Peckerar, G. Metze, and N. Goldsman, "RF energy scavenging system utilising switched capacitor DC-DC converter," *Electronics Letters,* vol. 45, pp. 374-376, 2009.

[70] T. Paing, J. Shin, R. Zane, and Z. Popovic, "Resistor Emulation Approach to Low-Power RF Energy Harvesting," *IEEE Transactions on Power Electronics,* vol. 23, pp. 1494-1501, 2008.

[71] T. Paing, E. Falkenstein, R. Zane, and Z. Popovic, "Custom IC for Ultra-low Power RF Energy Harvesting," in *Applied Power Electronics Conference and Exposition*, 2009, pp. 1239-1245.

[72] T. Le, K. Mayaram, and T. Fiez, "Efficient Far-Field Radio Frequency Energy Harvesting for Passively Powered Sensor Networks," *Solid-State Circuits, IEEE Journal of,* vol. 43, pp. 1287-1302, 2008.

[73] H. Nishimoto, Y. Kawahara, and T. Asami, "Prototype implementation of ambient RF energy harvesting wireless sensor networks," *IEEE Sensors,* pp. 1282-1287, 2010.

[74] R. Moghe, Y. Yang, F. Lambert, and D. Divan, "Design of a low cost self powered "Stick-on" current and temperature wireless sensor for utility assets," in *IEEE Energy Conversion Congress and Exposition*, 2010, pp. 4453-4460.

[75] R. Moghe, Y. Yang, F. Lambert, and D. Divan, "A scoping study of electric and magnetic field energy harvesting for wireless sensor networks in power system applications," in *IEEE Energy Conversion Congress and Exposition*, 2009, pp. 3550-3557.

[76] S. A. Bhalerao, A. V. Chaudhary, R. B. Deshmukh, and R. M. Patrikar, "Powering Wireless Sensor Nodes using Ambient RF Energy," in *IEEE International Conference on Systems, Man and Cybernetics*, 2006, pp. 2695-2700.

[77] A. Nimo, D. Grgic, and L. M. Reindl, "Ambient Electromagnetic wireless energy harvesting using multiband planar antenna," in *International Multi-Conference on Systems, Sygnals & Devices*, 2012, pp. 1-6.

[78] H. J. Visser, A. C. F. Reniers, and J. A. C. Theeuwes, "Ambient RF Energy Scavenging: GSM and WLAN Power Density Measurements," in *European Microwave Conference*, 2008, pp. 721-724.

[79] D. Bouchouicha, M. Latrach, F. Dupont, and L. Ventura, "An experimental evaluation of surrounding RF energy harvesting devices," in *The 40th European Microwave Conference*, 2010, pp. 1381-1384.

[80] R. J. M. Vullers, R. van Schaijk, I. Doms, C. Van Hoof, and R. Mertens, "Micropower energy harvesting," *Solid-State Electronics,* vol. 53, pp. 684-693, 2009.

[81] G. S. Smith, *An introduction to classical electromagnetic radiation*: New York, NY, USA : Cambridge University Press, 1997.

[82] D. M. Bennett, R. H. Selfridge, P. Humble, and J. N. Harb, "Hybrid power systems for autonomous MEMS," *Proceedings of SPIE, the International Society for Optical Engineering,* pp. 354-362, 2001.

[83] K. Kobayashi, H. Matsuo, and Y. Sekine, "An excellent operating point tracker of the solar-cell power supply system," *IEEE Transactions on Industrial Electronics,* vol. 53, pp. 495-499, 2006.

[84] T. Esram and P. L. Chapman, "Comparison of Photovoltaic Array Maximum Power Point Tracking Techniques," *IEEE Transactions on Energy Conversion,* vol. 22, pp. 439-449, 2007.

[85] J. Merten, J. M. Asensi, C. Voz, A. V. Shah, R. Platz, and J. Andreu, "Improved equivalent circuit and analytical model for amorphous silicon solar cells and modules," *IEEE Transactions on Electron Devices,* vol. 45, pp. 423-429, 1998.

[86] R. W. Miles, K. M. Hynes, and I. Forbes, "Photovoltaic solar cells: An overview of state-of-the-art cell development and environmental issues," *Progress in Crystal Growth and Characterization of Materials,* vol. 51, pp. 1-42, 2005.

[87] Y. Qiu, C. V. Liempd, B. O. h. Veld, P. G. Blanken, and C. V. Hoof, "5μW-to-10mW input power range inductive boost converter for indoor photovoltaic energy harvesting with integrated maximum power point tracking algorithm," in *2011 IEEE International Solid-State Circuits Conference*, 2011, pp. 118-120.

[88] H. Shao, C. Y. Tsui, and W. H. Ki, "The Design of a Micro Power Management System for Applications Using Photovoltaic Cells With the Maximum Output Power Control," *IEEE Transactions on Very Large Scale Integration (VLSI) Systems,* vol. 17, pp. 1138-1142, 2009.

[89] G. Spiazzi, S. Buso, P. Mattavelli, and P. Tenti, "Low complexity MPPT techniques for PV module converters," in *Power Electronics Conference (IPEC), 2010 International*, 2010, pp. 2074-2081.

[90] B. A. Warneke, M. D. Scott, B. S. Leibowitz, Z. Lixia, C. L. Bellew, J. A. Chediak*, et al.*, "An autonomous 16 $mm^3$ solar-powered node for distributed wireless sensor networks," in *Sensors, 2002. Proceedings of IEEE*, 2002, pp. 1510-1515 vol.2.

[91] R. Enne, M. Nikolic, and H. Zimmermann, "A maximum power-point tracker without digital signal processing in 0.35µm CMOS for automotive applications," in *2012 IEEE International Solid-State Circuits Conference*, 2012, pp. 102-104.

[92] M. Ferri, D. Pinna, E. Dallago, and P. Malcovati, "Integrated micro-solar cell structures for harvesting supplied microsystems in 0.35-µm CMOS technology," in *Sensors, 2009 IEEE*, 2009, pp. 542-545.

[93] N. J. Guilar, T. J. Kleeburg, A. Chen, D. R. Yankelevich, and R. Amirtharajah, "Integrated Solar Energy Harvesting and Storage," *IEEE Transactions on Very Large Scale Integration (VLSI) Systems,* vol. 17, pp. 627-637, 2009.

[94] J. B. Lee, Z. Chen, M. G. Allen, A. Rohatgi, and R. Arya, "A miniaturized high-voltage solar cell array as an electrostatic MEMS power supply," *Journal of Microelectromechanical Systems,* vol. 4, pp. 102-108, 1995.

[95] A. Lingley, B. Otis, T. Shen, and B. Parviz, "A contact lens with integrated micro solar cells," *Microsystem Technologies,* vol. 18, pp. 453-458, 2012.

[96] J. Lu, A. Y. Kovalgin, K. H. M. v. d. Werf, R. E. I. Schropp, and J. Schmitz, "Integration of Solar Cells on Top of CMOS Chips Part I: a-Si Solar Cells," *IEEE Transactions on Electron Devices,* vol. 58, pp. 2014-2021, 2011.

[97] J. Lu, W. Liu, A. Y. Lu, Y. Sun, and J. Lu, "Integration of Solar Cells on Top of CMOS Chips-Part II: CIGS Solar Cells," *IEEE Transactions on Electron Devices,* vol. 58, pp. 2620-2627, 2011.

[98] Y. Lee, S. Bang, I. Lee, Y. Kim, G. Kim, M. H. Ghaed*, et al.*, "A Modular 1 $mm^3$ Die-Stacked Sensing Platform With Low Power $I^2C$ Inter-Die Communication and Multi-Modal Energy Harvesting," *IEEE Journal of Solid-State Circuits,* vol. 48, pp. 229-243, 2013.

[99] R. D. Prabha and G. A. Rincon-Mora, "Drawing the Most Power from Low-Cost Single-Well 1-mm2 CMOS Photovoltaic Cells," *IEEE Transactions on Circuits and Systems II: Express Briefs,* vol. PP, pp. 1-1, 2016.

[100] N. J. Guilar, E. G. Fong, T. Kleeburg, D. R. Yankelevich, and R. Amirtharajah, "Energy harvesting photodiodes with integrated 2D diffractive storage capacitance," in *Low Power Electronics and Design (ISLPED), 2008 ACM/IEEE International Symposium on*, 2008, pp. 63-68.

[101] S. P. Beeby, M. J. Tudor, and N. M. White, "Energy harvesting vibration sources for microsystems applications," *Measurement Science and Technology,* vol. 17, pp. 175-195, 2006.

[102] L. Carrette, K. A. Friedrich, and U. Stimming, "Fuel Cells: Principles, Types, Fuels, and Applications," *ChemPhysChem,* vol. 1, pp. 162-193, 2000.

[103] M. Chen, S.-S. Lu, and B. Liao, "On the Figure of Merit of Thermoelectric Generators," *Journal of Energy Resources Technology,* vol. 127, p. 37, 2005.

[104] K. A. Cook-Chennault, N. Thambi, and A. M. Sastry, "Powering MEMS portable devices—a review of non-regenerative and regenerative power supply systems with special emphasis on piezoelectric energy harvesting systems," *Smart Materials and Structures,* vol. 17, 2008.

[105] H. Li, A. Lal, J. Blanchard, and D. Henderson, "Self-reciprocating radioisotope-powered cantilever," *Journal of Applied Physics,* vol. 92, pp. 1122-1127, 2002.

[106] M. H. Miles, "Recent advances in lithium battery technology," in *Gallium Arsenide Integrated Circuit (GaAs IC) Symposium, 2001. 23rd Annual Technical Digest*, 2001, pp. 219-222.

[107] R. P. Raffaelle, J. D. Harris, D. Hehemann, D. Scheiman, G. Rybicki, and A. F. Hepp, "A facile route to thin-film solid state lithium microelectronic batteries," *Journal of Power Sources,* vol. 89, pp. 52-55, 2000.

[108] G. J. Snyder and E. S. Toberer, "Complex thermoelectric materials," *Nature Materials,* vol. 7, pp. 105-114, Feb. 2008.

[109] A. Harb, "Energy harvesting: State-of-the-art," *Renewable Energy,* vol. 36, pp. 2641-2654, 2011.

[110] J. Bierschenk, "Optimized thermoelectrics for energy harvesting applications," in *IEEE International Symposium on the Applications of Ferroelectrics*, 2008.

[111] E. J. Carlson, K. Strunz, and B. P. Otis, "A 20 mV Input Boost Converter With Efficient Digital Control for Thermoelectric Energy Harvesting," *IEEE Journal of Solid-State Circuits,* vol. 45, pp. 741-750, 2010.

[112] S. Dalola, M. Ferrari, V. Ferrari, M. Guizzetti, D. Marioli, and A. Taroni, "Characterization of Thermoelectric Modules for Powering Autonomous Sensors," *IEEE Transactions on Instrumentation and Measurement,* vol. 58, pp. 99-107, 2009.

[113] J. M. Damaschke, "Design of a low input voltage converter for thermoelectric generator," in *Applied Power Electronics Conference and Exposition*, 1996, pp. 856-860.

[114] F. Disalvo, "Thermoelectric cooling and power generation," *Science,* vol. 285, pp. 703-706, 1999.

[115] P. Dziurdzia, "Simulation tool for virtual estimation of harvested thermoelectric energy supplying wireless sensor nodes," in *International Conference on Software Technology and Engineering*, 2010.

[116] V. Leonov, P. Fiorini, T. Torfs, R. J. M. Vullers, and C. V. Hoof, "Thermal matching of a thermoelectric energy harvester with the environment and its application in wearable self-powered wireless medical sensors," in *Thermal Investigations of ICs and Systems*, 2009, pp. 95-100.

[117] J. A. Paradiso and T. Starner, "Energy scavenging for mobile and wireless electronics," *IEEE Pervasive Computing,* vol. 4, pp. 18-27, 2005.

[118] V. Rama, S. Edward, C. Thomas, and O. Q. Brooks, "Thin-film thermoelectric devices with high room-temperature figures of merit," *Nature,* vol. 413, p. 597, 2001.

[119] S. Percy, *Thermal Energy Harvesting for Application at MEMS Scale*. Dordrecht: Dordrecht : Springer, 2013.

[120] Z. Wang, V. Leonov, P. Fiorini, and C. V. Hoof, "Micromachined Thermopiles for Energy Scavenging on Human Body," in *International Solid-State Sensors, Actuators and Microsystems Conference*, 2007, pp. 911-914.

[121] D. J. Inman, *Energy Harvesting Technologies*. Dordrecht: Dordrecht : Springer, 2008.

[122] J. P. Carmo, L. M. Goncalves, and J. H. Correia, "Thermoelectric Microconverter for Energy Harvesting Systems," *IEEE Transactions on Industrial Electronics,* vol. 57, pp. 861-867, 2010.

[123] *MPG-D655 Thin Film Thermogenerator*. Available: http://micropelt.com/downloads/datasheet_mpg_d655.pdf

[124] S. Dimitrijev, *Principles of Semiconductor Devices*: Oxford University Press, 2012.

[125] G. Chen, S. Hanson, D. Blaauw, and D. Sylvester, "Circuit Design Advances for Wireless Sensing Applications," *Proceedings of the IEEE,* vol. 98, pp. 1808-1827, 2010.

[126] M. Ferri, D. Pinna, M. Grassi, E. Dallago, and P. Malcovati, "Model of integrated micro photovoltaic cell structures for harvesting supplied microsystems in 0.35-μm CMOS technology," in *IEEE Sensors*, 2010, pp. 232-235.

[127] R. F. Pierret, *Semiconductor device fundamentals*. Reading, Mass.: Reading, Mass. : Addison-Wesley, 1996.

[128] Y. K. Ramadass and A. P. Chandrakasan, "A Battery-Less Thermoelectric Energy Harvesting Interface Circuit With 35 mV Startup Voltage," *IEEE Journal of Solid-State Circuits,* vol. 46, pp. 333-341, 2011.

[129] R. Sarpeshkar, *Ultra Low Power Bioelectronics : Fundamentals, Biomedical Applications, and Bio-Inspired Systems*. Cambridge, GB: Cambridge University Press, 2010.

[130] J. D. Meindl and J. A. Davis, "The fundamental limit on binary switching energy for terascale integration (TSI)," *IEEE Journal of Solid-State Circuits,* vol. 35, pp. 1515-1516, 2000.

[131] B. H. Calhoun, A. Wang, and A. Chandrakasan, "Device sizing for minimum energy operation in subthreshold circuits," in *IEEE Custom Integrated Circuits Conference* 2004, pp. 95-98.

[132] G. Schrom, C. Pichler, T. Simlinger, and S. Selberherr, "On the lower bounds of CMOS supply voltage," *Solid-State Electronics,* vol. 39, pp. 425-430, 1996.

[133] T. Niiyama, P. Zhe, K. Ishida, M. Murakata, M. Takamiya, and T. Sakurai, "Dependence of Minimum Operating Voltage (VDDmin) on Block Size of 90-nm CMOS Ring Oscillators and its Implications in Low Power DFM," in *International Symposium on Quality Electronic Design*, 2008, pp. 133-136.

[134] A. Chandrakasan, A. Wang, and B. H. Calhoun, *Sub-threshold Design for Ultra Low-Power Systems*: Springer US, 2006.

[135] A. J. Annema, B. Nauta, R. v. Langevelde, and H. Tuinhout, "Analog circuits in ultra-deep-submicron CMOS," *IEEE Journal of Solid-State Circuits,* vol. 40, pp. 132-143, 2005.

[136] P. R. Gray, P. J. Hurst, S. H. Lewis, and R. G. Meyer, *Analysis and Design of Analog Integrated Circuits*: Wiley, 2001.

[137] H. S. Ruiz and R. B. Perez, *Linear CMOS RF Power Amplifiers*: Springer, 2014.

[138] D. F. Lemmerhirt and K. D. Wise, "Chip-Scale Integration of Data-Gathering Microsystems," *Proceedings of the IEEE,* vol. 94, pp. 1138-1159, 2006.

[139] M. L. Ku, Y. Chen, and K. J. R. Liu, "Data-Driven Stochastic Models and Policies for Energy Harvesting Sensor Communications," *IEEE Journal on Selected Areas in Communications,* vol. 33, pp. 1505-1520, 2015.

[140] P. Lee, Z. A. Eu, M. Han, and H. P. Tan, "Empirical modeling of a solar-powered energy harvesting wireless sensor node for time-slotted operation," in *2011 IEEE Wireless Communications and Networking Conference*, 2011, pp. 179-184.

[141] S. Bader and B. Oelmann, "Short-term energy storage for wireless sensor networks using solar energy harvesting," in *Networking, Sensing and Control (ICNSC), 2013 10th IEEE International Conference on*, 2013, pp. 71-76.

[142] M. Seok, S. Hanson, M. Wieckowski, G. K. Chen, Y. S. Lin, D. Blaauw*, et al.*, "Circuit design advances to enable ubiquitous sensing environments," in *Proceedings of 2010 IEEE International Symposium on Circuits and Systems*, 2010, pp. 285-288.

[143] A. A. Blanco and G. A. Rincón-Mora, "A 44-93- μs 250-400-mV 0.18-μm CMOS Starter for DC-Sourced Switched-Inductor Energy Harvesters," *IEEE Transactions on Circuits and Systems II: Express Briefs,* vol. 61, pp. 1002-1006, 2014.

[144] S. Kim and M. G. A. Rincón, "Efficiency of switched-inductor dc-dc converter ICs across process technologies," in *2012 IEEE International Symposium on Circuits and Systems*, 2012, pp. 460-463.

[145] P. H. Chen, X. Zhang, K. Ishida, Y. Okuma, Y. Ryu, M. Takamiya*, et al.*, "An 80 mV Startup Dual-Mode Boost Converter by Charge-Pumped Pulse Generator and Threshold Voltage Tuned Oscillator With Hot Carrier Injection," *IEEE Journal of Solid-State Circuits,* vol. 47, pp. 2554-2562, 2012.

[146] Y. Lee, G. Chen, S. Hanson, D. Sylvester, and D. Blaauw, "Ultra-low power circuit techniques for a new class of sub-mm³ sensor nodes," in *Custom Integrated Circuits Conference (CICC), 2010 IEEE*, 2010, pp. 1-8.

[147] P. H. Chen, K. Ishida, K. Ikeuchi, X. Zhang, K. Honda, Y. Okuma*, et al.*, "Startup Techniques for 95 mV Step-Up Converter by Capacitor Pass-On Scheme and VTH-Tuned Oscillator With Fixed Charge Programming," *IEEE Journal of Solid-State Circuits,* vol. 47, pp. 1252-1260, 2012.

[148] LTC3108 Data Sheet [Online]. Available: http://linear.com

[149] J. P. Im, S. W. Wang, K. H. Lee, Y. J. Woo, Y. S. Yuk, T. H. Kong*, et al.*, "A 40mV transformer-reuse self-startup boost converter with MPPT control for thermoelectric energy harvesting," in *2012 IEEE International Solid-State Circuits Conference*, 2012, pp. 104-106.

[150] K. Kadirvel, Y. Ramadass, U. Lyles, J. Carpenter, V. Ivanov, V. McNeil*, et al.*, "A 330nA energy-harvesting charger with battery management for solar and thermoelectric energy harvesting," in *2012 IEEE International Solid-State Circuits Conference*, 2012, pp. 106-108.

[151] A. A. Blanco and G. A. Rincon-Mora, "Energy-Harvesting Microsensors: Low-Energy Task Schedule & Fast Drought-Recovery Design," in *IEEE Midwest Symposium on Circuits and Systems (MWSCAS)*, Abu Dhabi, UAE, 2016.

[152] P. S. Weng, H. Y. Tang, P. C. Ku, and L. H. Lu, "50 mV-Input Batteryless Boost Converter for Thermal Energy Harvesting," *IEEE Journal of Solid-State Circuits,* vol. 48, pp. 1031-1041, 2013.

[153] R. D. Prabha, G. A. Rincón-Mora, and S. Kim, "Harvesting circuits for miniaturized photovoltaic cells," in *2011 IEEE International Symposium of Circuits and Systems (ISCAS)*, 2011, pp. 309-312.

[154] N. M. Sze, W. H. Ki, and C. Y. Tsui, "Threshold Voltage Start-up Boost Converter for Sub-mA Applications," in *Electronic Design, Test and Applications, 2008. DELTA 2008. 4th IEEE International Symposium on*, 2008, pp. 338-341.

[155] I. Doms, P. Merken, R. Mertens, and C. V. Hoof, "Integrated capacitive power-management circuit for thermal harvesters with output power 10 to 1000uW," in *2009 IEEE International Solid-State Circuits Conference - Digest of Technical Papers*, 2009, pp. 300-301,301a.

[156] H. Lhermet, C. Condemine, M. Plissonnier, R. Salot, P. Audebert, and M. Rosset, "Efficient Power Management Circuit: From Thermal Energy Harvesting to Above-IC Microbattery Energy Storage," *IEEE Journal of Solid-State Circuits,* vol. 43, pp. 246-255, 2008.

[157] J. W. Kimball, T. L. Flowers, and P. L. Chapman, "Low-input-voltage, low-power boost converter design issues," *IEEE Power Electronics Letters,* vol. 2, pp. 96-99, 2004.

[158] D. Kwon, G. A. Rincón-Mora, and E. O. Torres, "Harvesting Ambient Kinetic Energy With Switched-Inductor Converters," *IEEE Transactions on Circuits and Systems I: Regular Papers,* vol. 58, pp. 1551-1560, 2011.

[159] M. B. Machado, M. C. Schneider, and C. Galup-Montoro, "On the Minimum Supply Voltage for MOSFET Oscillators," *IEEE Transactions on Circuits and Systems I: Regular Papers,* vol. 61, pp. 347-357, 2014.

[160] J. Segura and C. F. Hawkins, *CMOS Electronics: How It Works, How It Fails*: Wiley-IEEE Press, 2004.

[161] A. Richelli, S. Comensoli, and Z. M. Kovacs-Vajna, "A DC/DC Boosting Technique and Power Management for Ultralow-Voltage Energy Harvesting Applications," *IEEE Transactions on Industrial Electronics,* vol. 59, pp. 2701-2708, 2012.

[162] R. Baker, *CMOS: Circuit Design, Layout, and Simulation*. New York: Wiley, 2004.

[163] R. D. Prabha and G. A. Rincón-Mora, "0.18-µm Light-Harvesting Battery-Assisted Charger-Supply CMOS System," *IEEE Transactions on Power Electronics,* vol. 31, pp. 2950-2958, 2016.

# VITA

Andrés Blanco received his Bachelor of Science (BS) degree in 2009 and Master of Science (MS) degree in 2012 in electrical engineering from the Georgia Institute of Technology, Atlanta, GA. He joined the Georgia Tech Analog, Power, and Energy IC Lab in 2011 to pursue his PhD under the guidance of Prof. Gabriel A. Rincón-Mora. He joined Texas Instruments, Inc. in September 2016 as an Analog Design Engineer in Kilby Labs. His research interests include thermoelectric and photovoltaic energy harvesting, switch-mode power ICs, and low power analog circuits.